# Towards a First-Principles Approach to Particle Cosmology

Doctoral dissertation presented by

Yannis Georis

in fulfilment of the requirements for the degree of Doctor in Sciences.

Thesis Jury

| | | |
|---|---|---|
| Prof. Fabio Maltoni | President | Université Catholique de Louvain |
| Prof. Céline Degrande | Secretary | Université Catholique de Louvain |
| Prof. Marco Drewes | Supervisor | Université Catholique de Louvain |
| Prof. Björn Garbrecht | | Technische Universität München |
| Prof. Mikhail Shaposhnikov | | Ecole Polytechnique Fédérale de Lausanne |

*September 2, 2025*

**Acknowledgements/Remerciements**

Far from the cliché of the scientist working alone in his ivory tower, this thesis would never have been possible without the support, direct or indirect, of many individuals, to whom I would like to express my deep gratitude in these few lines.

First and foremost, I would like to thank Marco, my supervisor, without whom this thesis would not have been possible. Working under your supervision for almost five years now not only allowed me to greatly improve my understanding of physics but also to develop the various soft skills necessary to become a physicist. I greatly appreciated the time you took to provide me with numerous (necessary) feedbacks, whether on my presentation skills or on my various applications. Thank you also for allowing me to participate in many conferences and summer schools as well as pushing me to visit different research institutes. These truly were life-changing experiences. I also strongly appreciated the network of collaborators that you put me in contact with over the course of my thesis.

Second, I must address a special thanks to Juraj Klarić, who acted as a second unofficial supervisor during the first part of my thesis and from whom I deeply benefitted.

I would also like to thank all jury members, who kindly agreed to take the time to review this thesis. I am extremely indebted to their insightful comments during the private defence, which greatly improved this thesis.

More generally, I would like to thank the rest of my collaborators (listed here in alphabetical order): Adrian, Antony, Claudia, Inar, Jannis, Jordy, Juraj, Luca, Marco, Michael, Misha, Mubarak, Philipp, Sebastian, Tobias, Vaisakh, Valentin, Yuanzhen and Yvonne. I learned a lot from our discussions and this thesis would definitely have not been possible without all of your contributions. Moreover, I must address a special thank to Misha and Yvonne for kindly hosting me for two months at EPFL and UNSW, respectively. A special thank also to Sebastian for helping with my first postdoc application season.

Outside of the purely scientific aspect, these four years were definitely made much more pleasant by the kind and helpful presence of other members of the institute. Je suis extrêmement reconnaissant à Carinne et Stéphanie de s'être occupées de tout l'aspect administratif et, de manière plus générale, d'avoir veillé en permanence à ce que tout fonctionne sans accroc. Vos chocolats et biscuits quotidiens ont contribué de manière non négligeable à la réussite de cette thèse. Je voudrais aussi remercier de tout cœur l'équipe de nettoyage d'avoir veillé à la propreté de nos bureaux tout au long de ces quatre années.

Thanks also to the cafeteria group (Antoine, Chris, Clémentine, Eliot, Jishnu, Karlijn, Paul, Per, Rogan and many others) for many interesting and "out-of-the-box" discussions over the years as well as to my office mates Mubarak and Valentin.

During this PhD, I had the chance to participate to many interesting activities. I would like to thank the rest of the Young Minds UCLouvain team for their help to organise many events over these years. Additionally, I am grateful to Antoine, Clémentine, Valentin, Morgane, Axel, Maxime and, especially, Oguz for their help organising the visit of CERN facilities for our bachelor students.

En dehors de l'institut, je voudrais aussi remercier tous mes amis pour m'avoir rappelé qu'il n'y a pas que la physique dans la vie et m'avoir fait passer de nombreux excellents moments ces dernières années. Puisse les choses continuer ainsi, même si nous ne serons plus nécessairement dans le même pays.

Enfin, bien entendu, je me dois de remercier ma famille qui aura énormément contribué au succès de cette thèse. En particulier mes parents, par l'éducation qu'ils m'ont apportée mais aussi pour m'avoir supporté (dans mes choix mais aussi tout court) durant ce quart de siècle. Et aussi mes deux frères, Guadon et Sapayas, pour m'avoir gardé les pieds sur terre et tous les moments passés ensemble.

MERCI !

### Funding

I would like to acknowledge the support of the French Community of Belgium through the FRIA grant No. 1.E.063.22F as well as an FSR grant during the first few months of the thesis. Computational resources for various parts of this thesis have been provided by the supercomputing facilities of the Université catholique de Louvain (CISM/UCL) and the Consortium des Équipements de Calcul Intensif en Fédération Wallonie Bruxelles (CÉCI) funded by the Fonds de la Recherche Scientifique de Belgique (F.R.S.-FNRS) under convention 2.5020.11 and by the Walloon Region.

# Associated publications and preprints:

[1] Marco Drewes, Yannis Georis, and Juraj Klarić, “Mapping the Viable Parameter Space for Testable Leptogenesis”, Phys. Rev. Lett., vol. 128, no. 5, pp. 051801, 2022.

**Note:** This paper was already partially discussed in the master thesis of the author.

[2] Marco Drewes, Yannis Georis, Claudia Hagedorn, and Juraj Klarić, “Low-scale leptogenesis with flavour and CP symmetries”, JHEP, vol. 12, pp. 044, 2022.

[3] Marco Drewes, Yannis Georis, Juraj Klarić, and Philipp Klose, “Upper bound on thermal gravitational wave backgrounds from hidden sectors”, JCAP, vol. 06, pp. 073, 2024.

[4] Marco Drewes, Yannis Georis, Michael Klasen, Luca Paolo Wiggering, and Yvonne Y. Y. Wong, “Towards a precision calculation of $N_{\rm eff}$ in the Standard Model. Part III. Improved estimate of NLO contributions to the collision integral”, JCAP, vol. 06, pp. 032, 2024.

[5] Jordy de Vries, Marco Drewes, Yannis Georis, Juraj Klarić, and Vaisakh Plakkot, “Confronting the low-scale seesaw and leptogenesis with neutrinoless double beta decay”, JHEP, vol. 05, pp. 090, 2025.

[6] Marco Drewes, Yannis Georis, Juraj Klarić, and Antony Wendels, “On the collider-testability of the type-I seesaw model with 3 right-handed neutrinos”, JHEP, vol. 03, pp. 176, 2025.

[7] Tobias Binder, Marco Drewes, Yannis Georis, Michael Klasen, Giovanni Pierobon, and Yvonne Y. Y. Wong, “Towards a precision calculation of $N_{\rm eff}$ in the Standard Model IV: Impact of positronium formation”, 11 2024 (submitted to JCAP).

[8] Marco Drewes, Yannis Georis, Claudia Hagedorn, and Juraj Klarić, “Low-scale seesaw with flavour and CP symmetries – from colliders to leptogenesis”, 12 2024 (submitted to Nucl. Phys. B).

# Associated papers in preparation:

[9] Marco Drewes, Yannis Georis, Juraj Klarić, and Inar Timiryasov, “Heavy Fermion Interaction Rates at Finite Temperature in Fermi Theory”, To appear.

# Associated proceedings:

[10] Yannis Georis, “Parameter space for testable leptogenesis”, in 57th Rencontres de Moriond on Electroweak Interactions and Unified Theories, 5 2023.

[11] Yannis Georis, “Recent Developments in Testable Leptogenesis”, Acta Phys. Polon. Supp., vol. 17, no. 2, pp. 2–A22, 2024.

# Contents

# List of Acronyms

| | |
|---|---|
| $0\nu\beta\beta$ | neutrinoless double beta decay. |
| $N_{\rm eff}$ | effective number of neutrinos. |
| **$\nu$MSM** | Neutrino Minimal Standard Model. |
| **1PI** | one-particle-irreducible. |
| **ALP** | axion-like particle. |
| **ARS** | Akhmedov-Rubakov-Smirnov. |
| **BAU** | Baryon Asymmetry of our Universe. |
| **BBN** | Big Bang Nucleosynthesis. |
| **BSM** | beyond-the-Standard-Model. |
| **C.L.** | confidence level. |
| **CKM** | Cabibbo–Kobayashi–Maskawa. |
| **CMB** | Cosmic Microwave Background. |
| **CTP** | Closed-Time-Path. |
| **DM** | Dark Matter. |
| **EFT** | effective field theory. |
| **EoS** | equation of state. |
| **EWSB** | electroweak symmetry breaking. |
| **FLRW** | Friedmann-Lemaître-Robertson-Walker. |
| **GR** | General Relativity. |
| **GUT** | Grand Unified Theory. |
| **GW** | gravitational wave. |
| **GWB** | gravitational wave background. |

| | |
|---|---|
| **HNL** | heavy neutral lepton. |
| **HTL** | Hard Thermal Loop. |
| **IO** | inverted ordering. |
| **IR** | infrared. |
| **KMS** | Kubo-Martin-Schwinger. |
| **LH** | left-handed. |
| **LO** | leading order. |
| **mLRSM** | minimal Left-Right Symmetric Model. |
| **NLO** | next-to-leading order. |
| **NO** | normal ordering. |
| **PMNS** | Pontecorvo–Maki–Nakagawa–Sakata. |
| **QCD** | Quantum Chromodynamics. |
| **QED** | Quantum Electrodynamics. |
| **QFT** | Quantum Field Theory. |
| **QKE** | quantum kinetic equation. |
| **RH** | right-handed. |
| **SM** | Standard Model of particle physics. |
| **SMEFT** | Standard Model effective field theory. |
| **TIC** | thermal initial conditions. |
| **TT** | traceless-transverse. |
| **UV** | ultraviolet. |
| **vev** | vacuum expectation value. |
| **VIC** | vanishing initial conditions. |

# General introduction

> *"On ne fait jamais attention à ce qui a été fait ; on ne voit que ce qui reste à faire."*
>
> Marie Skłodowska-Curie

---

Natural sciences have come a long way since the theory of the four elements of Empedocles. Since then, humanity has refined its understanding of Nature to a point where we can describe an impressively broad range of phenomena, from the quantum behaviour of microscopic particles to the large-scale evolution of our universe. In particular, this understanding is based on the combined successes of

1. the Standard Model of particle physics (SM), which describes the interactions of all fundamental particles, and
2. General Relativity (GR), which describes gravity and the expansion of the universe as a whole.

Over the last few decades however, observational tensions with these two models have emerged. Notably, the SM and GR do not provide a mechanism to explain the extreme homogeneity of our universe, the measured neutrino masses, or the origins of both baryonic and so-called dark matter. All of these observations strongly suggest the existence of so-called beyond-the-Standard-Model (BSM) physics. Over the years, a plethora of such BSM scenarios have been developed to explain various combinations of these observations. In order to discriminate between these scenarios and constrain new physics, it is therefore of extreme importance to improve the accuracy of theoretical predictions for various key observables and leverage the possible interplay between the broad range of cosmological and laboratory experiments searching for such new physics.

In particular, feedback from the early universe plasma can severely alter various cosmological processes, especially those involving light and feebly interacting particles, and need to be properly accounted for. The aim of this

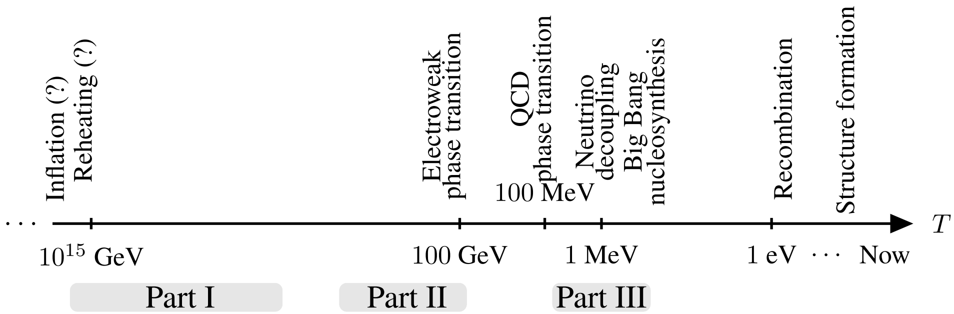


**Figure 1:** Schematic timeline of our universe's history, highlighting the three distinct cosmological epochs examined in the three corresponding parts of this thesis.

thesis is to contribute to that effort. With this objective in mind, we will proceed chronologically through different eras of our universe's history, sketched in Fig. 1, and will refine the theoretical treatment of several key cosmological processes using tools from nonequilibrium Quantum Field Theory (QFT). We will then explore some of their phenomenological implications, specifically how various cosmological and laboratory experiments constrain these new physics scenarios.

## Outline of the thesis:

We now proceed to lay out the general structure of this manuscript. Since it will be used repeatedly throughout the rest of the thesis for estimating the properties and evolution of particles in the early universe, we begin in Chap. 1 by briefly introducing nonequilibrium QFT. The thesis is then divided into three main parts.

**Part I** At the very early times, e.g. immediately after the reheating epoch, the primordial plasma may have been sufficiently hot to emit a detectable amount of gravitational waves through standard thermal processes. In the first part of this thesis, we estimate the cosmological background of gravitational waves emitted by hot hidden sectors in thermal equilibrium. In particular, we focus on the case of feebly interacting hidden sectors, for which such background is enhanced. After a brief introduction to gravitational wave production within an Friedmann-Lemaître-Robertson-Walker (FLRW) universe, Chap. 2 starts with a computation of the production rate for generic feebly interacting fermions. We then extract simplified phenomenological formulae for these rates, allowing us to derive upper bounds on the gravitational wave spectrum. We finish by computing the expected spectrum for two well-motivated benchmark scenarios and compare to experimental sensitivities. The material presented in this part is largely based on Ref. [3] and closely follows its structure.

**Part II** Moving on to lower temperatures, close to the electroweak scale, the production of a sufficient amount of asymmetry between matter and antimatter could also be extremely sensitive to finite-temperature effects. In the second part of this thesis, we focus on so-called low-scale models of leptogenesis and their connection to the neutrino mass problem. We begin in Chap. 3 with a general review of the type-I seesaw mechanism and low-scale leptogenesis. We also briefly explore the connection to the flavour puzzle. In the next chapter, Chap. 4, we then turn to a first-principles computation of the finite-temperature interaction rates of a generic fermion in Fermi-like theories. We then apply these results to the specific case of right-handed neutrinos within the Neutrino Minimal Standard Model and within the minimal Left-Right Symmetric Model. Finally, in Chap. 5, we explore various phenomenological aspects of different incarnations of the type-I seesaw model. In particular, we focus on the interplay between constraints set by leptogenesis and those set by various cosmological and laboratory experiments. The material presented in this part is largely based on Refs. [1,2,5,6,8,9].

**Part III** Taking place much later than the gravitational wave emission and the baryon asymmetry production discussed in the previous two parts, the decoupling of neutrinos from the photon bath at temperatures around 1 MeV provides an extremely powerful cosmological probe of the SM and its extensions. In Chap. 6, we refine the SM prediction for the so-called effective number of neutrinos, $N_{\text{eff}}$, which captures how neutrinos decouple from the QED bath and quantify their contribution to the radiation content of our universe. After a brief introduction, we focus on two key aspects: 1) the impact on $N_{\text{eff}}$ of finite-temperature next-to-leading-order corrections to the neutrino-electron interaction rates, as well as 2) the change in $N_{\text{eff}}$ resulting from positronium formation. The material presented in this part is largely based on Refs. [4,7].

We finish this thesis by summarising our main results and providing a brief outlook in Chap. 7. In addition, we provide multiple appendices with additional technical details on different aspects of each chapter.

**Notations** In this thesis, we will always work, unless explicitly stated otherwise, in natural units setting $\hbar = c = k_B = 1$. Additionally, we will use Greek indices (e.g. $\mu, \nu$) for generic 4-vectors while Latin indices (e.g. $i, j$) will be used for their spatial components. Similarly, we will employ the bolded symbol $\boldsymbol{k}$ to denote the spatial part of the 4-vector $k^\mu$. We will use the *dot* notation for time derivatives, i.e. $\dot{x} \equiv \frac{\mathrm{d}x}{\mathrm{d}t}$.

When drawing Feynman diagrams, scalar particles will be depicted with dashed lines while fermions will be represented with continuous lines. Spin-1 (Spin-2) gauge bosons will on the other hand be drawn with wiggly (double-wiggly) continuous lines. Concerning the metric tensor, we will use the so-called *West Coast convention* in which the Minkowski metric reads $\eta_{\mu\nu} = \mathrm{diag}(1, -1, -1, -1)$. Finally, we will make use of the *Feynman slash notation* when contracting a 4-vector $k_\mu$ with the set of gamma matrices $\gamma^\mu$, i.e. $\not{k} = k_\mu \gamma^\mu$.

Chapter 1

# Introduction to nonequilibrium Quantum Field Theory

The present thesis lies at the interface between the fields of particle physics and cosmology. Very generally, one of its major goals is to characterise the evolution and properties of particles in the early universe. For standard collider settings, the S-matrix approach in vacuum QFT provides a relatively straightforward pipeline to compute particle production rates as well as extract practical observables such as the expected number of detected events. However, this approach fails to describe more complex environments like the early universe. In particular, it heavily relies on the existence of free asymptotic states, whereas the early universe is filled with a hot and dense plasma within which particles are constantly interacting, hence forbidding the existence of such free states. The presence of this plasma can impact the behaviour and properties of particles in multiple ways, e.g. by screening interactions or generating effective thermal masses. Depending on the system, these plasma effects can even be the dominant source of e.g. particle production. Even though the S-matrix approach can still be used to calculate interaction rates at finite-temperature in simple situations by multiplying vacuum matrix elements by a suitable set of distribution functions, this method is not systematic and typically suffers from several issues such as the double counting of some interaction channels [12].

To address these shortcomings, three different formalisms have been developed over the years, listed here in chronological order: 1) the imaginary-time or Matsubara formalism [13], 2) the real-time formalism [14, 15][1] and 3) thermofield dynamics [18, 19]. We will focus in the following on the real-time formalism as it can easily be extended to situations beyond thermal equilibrium where one is interested in the entire time evolution of the system. The connection to the physical processes taking place is also more direct. In this

[1] See also the early works by Julian Schwinger's students, P. Bakshi and K. Mahanthappa [16, 17].

first chapter, we will quickly review this formalism and, more specifically, the so-called[2] Closed-Time-Path (CTP) formalism, sometimes also known as the Schwinger-Keldysh formalism. The material presented here is well known and more details on different aspects of nonequilibrium QFT can be found in Refs. [22–30].

## 1.1 The necessity of the Closed Time Path

In this section, we begin by showing how the Closed-Time-Path formalism naturally arises when considering out-of-equilibrium systems. More details on some aspects of this discussion can be found in chapter 4 of [26], on which our presentation is based.

In standard vacuum QFT, particles can be considered essentially free far from the interaction region. Consequently, one is primarily interested in transition probabilities between well-defined initial and final *asymptotic* states. In practice, such probabilities can be obtained from the vacuum expectation values of various time-ordered operators

$$\langle \Omega | T\{\mathcal{O}\} | \Omega \rangle \ , \tag{1.1}$$

$|\Omega\rangle$ being the ground state of the theory.

In contrast, the early universe is a complex many-particle system that can only be described statistically. As a result, statistical fluctuations arising from our incomplete knowledge of the system need to be accounted for in addition to intrinsic quantum-mechanical fluctuations. These can be captured by tracking the time dependence of ensemble averages of various operators (expressed here in the Heisenberg picture)

$$\langle \mathcal{O}(t) \rangle_\rho = \mathrm{Tr}\left[\hat{\rho}(t_i)\mathcal{O}(t)\right] \ , \tag{1.2}$$

where the Von Neumann density matrix (or density operator)[3] $\hat{\rho}$ captures all statistical properties of the specific quantum mechanical system under study and $t_i$ denotes a reference time at which the initial conditions of the system are

[2] This formalism is also sometimes referred to as the *in-in* formalism in the context of cosmological perturbation theory [20, 21].

[3] For the sake of simplicity, we will not use the *hat notation* to distinguish quantum operators except for the density matrix $\hat{\rho}$, in order to differentiate it from the matrix of densities $\rho$ that typically appears in the evolution equations for particles' number densities.

specified. As an illustration, the density operator takes the well-known form

$$\hat{\rho} = \frac{e^{-\beta(\mathcal{H}-\mu\mathcal{N})}}{\mathrm{Tr}\left[e^{-\beta(\mathcal{H}-\mu\mathcal{N})}\right]}, \tag{1.3}$$

for systems in complete thermodynamic equilibrium with inverse temperature $\beta \equiv \frac{1}{T}$. In this equation, $\mathcal{H}$ denotes the Hamiltonian operator of the system, $\mu$ it chemical potential and $\mathcal{N}$ the number operator. In the following, we omit the index $\rho$ when computing the statistical average (1.2) for the sake of brevity.

In the interaction picture, the operator $\mathcal{O}$ takes the form

$$\mathcal{O}_I(t) = U(t,t_i)\mathcal{O}(t)U^\dagger(t,t_i) \ , \tag{1.4}$$

with

$$U(t_1,t_2) = T\left\{\mathrm{Exp}\left[-i\int_{t_2}^{t_1}\mathcal{H}_I(\tau)\mathrm{d}\tau\right]\right\} \ . \tag{1.5}$$

In the above equation, $\mathcal{H}_I \equiv \mathcal{H} - \mathcal{H}_0$ represents the interacting part of the Hamiltonian $\mathcal{H}$, $\mathcal{H}_0$ being the Hamiltonian of the corresponding free theory. As is well-known [31], in vacuum, it is possible to adiabatically switch off the interacting part of the Hamiltonian in the following way

$$\mathcal{H} \to \mathcal{H}(t) = \mathcal{H}_0 + e^{-\epsilon|t|}\mathcal{H}_I \ , \tag{1.6}$$

such that $\mathcal{H}$ corresponds to the free Hamiltonian infinitely away from the interaction point but reproduces the correct Hamiltonian at $t = 0$ (which we assume is when the interaction takes place). The well-known Gell-Mann and Low theorem then ensures that one can rewrite the correlation function (1.1) in terms of correlation functions with the free vacuum

$$\langle\Omega|T\left\{\mathcal{O}\right\}|\Omega\rangle = \lim_{T\to+\infty(1-i\epsilon)} \frac{\langle 0|T\left\{\mathcal{O}_I\mathrm{Exp}\left(-i\int_{-T}^{T}\mathrm{d}\tau\,\mathcal{H}_I\right)\right\}|0\rangle}{\langle 0|T\left\{\mathrm{Exp}\left(-i\int_{-T}^{T}\mathrm{d}\tau\,\mathcal{H}_I\right)\right\}|0\rangle} \ , \tag{1.7}$$

allowing us to avoid tracking the (in general complicated) time evolution of the interacting theory's ground state $|\Omega\rangle$.

However, in a general nonequilibrium setting, the adiabatic mapping (1.6) does not necessarily exist as $\mathcal{H}(t \to \pm\infty) \neq \mathcal{H}_0$, and, as a result, the Gell-Mann and Low theorem does not hold. Moreover, one is typically also interested in tracking the time dependence of various quantities and not just in in-out transition probabilities. As we will show in the following, one natural

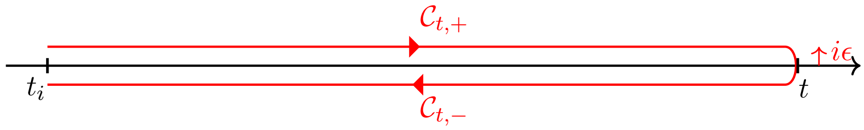


**Figure 1.1:** Closed Time Path.

way out of this conundrum is to rewrite operators in terms of time-ordered products along a *closed time path* $\mathcal{C}_t$

$$\mathcal{O}(t) = U^\dagger(t,t_i)\mathcal{O}_I(t)U(t,t_i) = T_{\mathcal{C}_t}\left\{\mathrm{Exp}\left(-i\int_{\mathcal{C}_t}\mathrm{d}\tau\mathcal{H}_I(\tau)\right)\mathcal{O}_I(t)\right\}\ . \tag{1.8}$$

This contour, displayed in Fig. 1.1, starts in the complex time plane at an initial time $t_i$, slightly off of the real axis by a quantity $+i\epsilon$, with $\epsilon$ an infinitesimal positive number, up to some time $t$ and then returns to $t_i$, again slightly off of the real axis by a quantity $-i\epsilon$. The full contour can be seen as the union $\mathcal{C}_t \equiv \mathcal{C}_{t,+}\cup\mathcal{C}_{t,-}$ of a forward and backward branch, effectively doubling the number of degrees of freedom as fields on each of these branches have to be treated independently. Indeed, the small path connecting these two branches essentially factorises in the partition function in the limit $t_i\to-\infty$ [28], which we will take later, hence contributing only as a global normalisation factor and dropping in all $n$-point correlation functions.[4]

Along this contour, we can define the natural extension $T_{\mathcal{C}_t}$ of the usual time-ordering operator $T$. For example, for a generic scalar field $\varphi$, we have

$$T_{\mathcal{C}_t}\{\varphi(x_1)\varphi(x_2)\} = \begin{cases} T\{\varphi(x_1)\varphi(x_2)\}\ \text{if}\ x_1^0, x_2^0\in\mathcal{C}_{t,+}, \\ \bar{T}\{\varphi(x_1)\varphi(x_2)\}\equiv T\{\varphi(x_2)\varphi(x_1)\}\ \text{if}\ x_1^0,x_2^0\in\mathcal{C}_{t,-}, \\ \varphi(x_2)\varphi(x_1)\ \text{if}\ x_1^0\in\mathcal{C}_{t,+}, x_2^0\in\mathcal{C}_{t,-} \\ \varphi(x_1)\varphi(x_2)\ \text{if}\ x_1^0\in\mathcal{C}_{t,-}, x_2^0\in\mathcal{C}_{t,+}\ . \end{cases} \tag{1.9}$$

Analogous formulae hold for higher-spin fields, up to additional minus signs in case the fields are anticommuting. One can also define in a similar fashion

[4]For systems in thermal equilibrium, it is practical to consider a real-time contour which also includes a path from $t_i$ to $t_i - i\beta$ to make the KMS relation (1.50) manifest. A similar reasoning can be made for this part of the contour, whose contribution factorises and does not affect any $n$-point correlation functions in the limit $t_i\to-\infty$.

the contour-ordered Heaviside function $\Theta_{\mathcal{C}_t}$

$$\Theta_{\mathcal{C}_t}(x_1,x_2)=\begin{cases}\Theta\left(x_1^0-x_2^0\right)\ \text{if}\ x_1^0,x_2^0\in\mathcal{C}_{t,+},\\ \Theta\left(x_2^0-x_1^0\right)\ \text{if}\ x_1^0,x_2^0\in\mathcal{C}_{t,-},\\ 0\ \text{if}\ x_1^0\in\mathcal{C}_{t,+},x_2^0\in\mathcal{C}_{t,-},\\ 1\ \text{if}\ x_1^0\in\mathcal{C}_{t,-},x_2^0\in\mathcal{C}_{t,+}\ ,\end{cases}\tag{1.10}$$

and similarly for the Dirac delta distribution $\delta_{\mathcal{C}_t}$.

In order to demonstrate the relation (1.8), we begin by expanding the right-hand side. It can be explicitly written as

$$\begin{aligned}&T_{\mathcal{C}_t}\left\{\mathrm{Exp}\left(-i\int_{\mathcal{C}_t}\mathrm{d}\tau\mathcal{H}_I(\tau)\right)\mathcal{O}_I(t)\right\}= \qquad (1.11)\\ &\qquad\sum_{n=0}^{+\infty}\frac{(-i)^n}{n!}\int_{\mathcal{C}_t}\mathrm{d}\tau_1\cdots\int_{\mathcal{C}_t}\mathrm{d}\tau_nT_{\mathcal{C}_t}\left\{\mathcal{H}_I(\tau_1)\ldots\mathcal{H}_I(\tau_n)\mathcal{O}_I(t)\right\}.\end{aligned}$$

We can then split these $n$ integrals between $m$ integrals on the forward part and $n-m$ on the backward part of the contour

$$\begin{aligned}&\sum_{n=0}^{+\infty}\frac{(-i)^n}{n!}\sum_{m=0}^{n}\frac{n!}{m!(n-m)!}\int_{\mathcal{C}_{t,-}}\mathrm{d}\tau_{m+1}\cdots\int_{\mathcal{C}_{t,-}}\mathrm{d}\tau_nT_{\mathcal{C}_{t,-}}\left\{\mathcal{H}_I(\tau_{m+1})\ldots\mathcal{H}_I(\tau_n)\right\}\times\\ &\qquad\times\mathcal{O}_I(t)\int_{\mathcal{C}_{t,+}}\mathrm{d}\tau_1\cdots\int_{\mathcal{C}_{t,+}}\mathrm{d}\tau_mT_{\mathcal{C}_{t,+}}\left\{\mathcal{H}_I(\tau_1)\ldots\mathcal{H}_I(\tau_m)\right\}. \qquad (1.12)\end{aligned}$$

Relabelling $n=m+k$, with $k\in\mathbb{N}$, and replacing the sum over $n$ by a sum over $k$, the previous expression reads

$$\begin{aligned}&\sum_{n=0}^{+\infty}\frac{(-i)^k}{k!}\int_{\mathcal{C}_{t,-}}\mathrm{d}\tau_1\cdots\int_{\mathcal{C}_{t,-}}\mathrm{d}\tau_kT_{\mathcal{C}_{t,-}}\left\{\mathcal{H}_I(\tau_1)\ldots\mathcal{H}_I(\tau_k)\right\}\times \qquad (1.13)\\ &\times\mathcal{O}_I(t)\sum_{m=0}^{+\infty}\frac{(-i)^m}{m!}\int_{\mathcal{C}_{t,+}}\mathrm{d}\tau_1\cdots\int_{\mathcal{C}_{t,+}}\mathrm{d}\tau_mT_{\mathcal{C}_{t,+}}\left\{\mathcal{H}_I(\tau_1)\ldots\mathcal{H}_I(\tau_m)\right\}\ .\end{aligned}$$

Therefore, we have

$$\begin{aligned}&T_{\mathcal{C}_t}\left\{\mathrm{Exp}\left(-i\int_{\mathcal{C}_t}\mathrm{d}\tau\mathcal{H}_I(\tau)\right)\mathcal{O}_I(t)\right\}=T_{\mathcal{C}_{t,-}}\left\{\mathrm{Exp}\left(-i\int_{\mathcal{C}_{t,-}}\mathrm{d}\tau\mathcal{H}_I(\tau)\right)\right\}\times\\ &\qquad\times\mathcal{O}_I(t)T_{\mathcal{C}_{t,+}}\left\{\mathrm{Exp}\left(-i\int_{\mathcal{C}_{t,+}}\mathrm{d}\tau\mathcal{H}_I(\tau)\right)\right\}\ . \qquad (1.14)\end{aligned}$$

This equation can easily be mapped into Eq. (1.8) by realising that

$$T_{\mathcal{C}_{t,-}}\left\{\mathrm{Exp}\left(-i\int_{\mathcal{C}_{t,-}}\mathrm{d}\tau\mathcal{H}_I(\tau)\right)\right\}=U(t_i,t)=U^\dagger(t,t_i)\ , \tag{1.15}$$

whereas

$$T_{\mathcal{C}_{t,+}}\left\{\mathrm{Exp}\left(-i\int_{\mathcal{C}_{t,+}}\mathrm{d}\tau\mathcal{H}_I(\tau)\right)\right\}=U(t,t_i)\ . \tag{1.16}$$

From Eq. (1.8), it automatically follows that

$$\langle\mathcal{O}(t)\rangle_\rho=\mathrm{Tr}\left[\hat{\rho}(t_i)T_{\mathcal{C}_t}\left\{\mathrm{Exp}\left(-i\int_{\mathcal{C}_t}\mathrm{d}\tau\mathcal{H}_I(\tau)\right)\mathcal{O}_I(t)\right\}\right]\ . \tag{1.17}$$

This relation has been derived assuming $\mathcal{O}$ depends on one time $t$ only. However, in practice, properties of the early universe plasma are typically encoded in multi-field correlation functions, which depend on more than one argument. Fortunately, it is possible to extend Eq. (1.17) to correlation functions of $\mathcal{C}$-ordered products of operators. Indeed, from the observation that closed contour with no field insertions cancel out, i.e.

$$T_{\mathcal{C}_{x_0,+}}\left\{\mathrm{Exp}\left(-i\int_{\mathcal{C}_{x_0,+}}\mathrm{d}\tau\mathcal{H}_I(\tau)\right)\right\}T_{\mathcal{C}_{y_0,-}}\left\{\mathrm{Exp}\left(-i\int_{\mathcal{C}_{y_0,-}}\mathrm{d}\tau\mathcal{H}_I(\tau)\right)\right\}$$
$$=U(x_0,t_i)U(t_i,y_0)=U(x_0,y_0)\ , \tag{1.18}$$

it is straightforward to prove that

$$T_{\mathcal{C}_t}\left\{\mathrm{Exp}\left(-i\int_{\mathcal{C}_t}\mathrm{d}\tau\mathcal{H}_I(\tau)\right)\varphi_I(x)\varphi_I(y)\right\}= \tag{1.19}$$
$$T_{\mathcal{C}_{x_0}}\left\{\mathrm{Exp}\left(-i\int_{\mathcal{C}_{x_0}}\mathrm{d}\tau\mathcal{H}_I(\tau)\right)\varphi_I(x)\right\}T_{\mathcal{C}_{y_0}}\left\{\mathrm{Exp}\left(-i\int_{\mathcal{C}_{y_0}}\mathrm{d}\tau\mathcal{H}_I(\tau)\right)\varphi_I(y)\right\}\ ,$$

with $t=\max(x_0,y_0)$. Generalising this result to the product of $n$ scalar fields, we obtain

$$\langle T_{\mathcal{C}_t}\left\{\varphi(x_1)\dots\varphi(x_n)\right\}\rangle_\rho= \tag{1.20}$$
$$\mathrm{Tr}\left[\hat{\rho}(t_i)T_{\mathcal{C}_t}\left\{\mathrm{Exp}\left(-i\int_{\mathcal{C}_t}\mathrm{d}\tau\mathcal{H}_I(\tau)\right)\varphi_I(x_1)\dots\varphi_I(x_n)\right\}\right]\ ,$$

with $t=\max(x_1^0,x_2^0,\dots,x_n^0)$. Using a similar argument, it is possible to extend the right end of the contour to $+\infty$ instead of stopping in $t$.

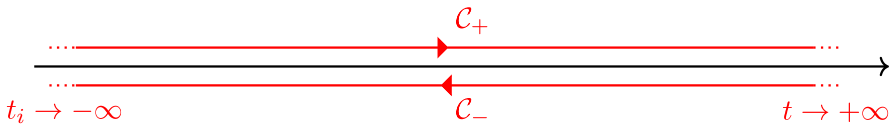


**Figure 1.2:** Schwinger-Keldysh contour.

Finally, we also note that, in this thesis, we will be interested in the time evolution of macroscopic quantities instead of transient microscopic phenomena. In this case, it is justified to send[5] $t_i \to -\infty$ such that the closed time path displayed in Fig. 1.1 effectively turns into the so-called *Schwinger-Keldysh* contour $\mathcal{C}$, see Fig. 1.2. The definition of the time-ordering operator $T_\mathcal{C}$ on this contour follows the same prescription as in Eq. (1.9).

## 1.2 Correlation functions on the Schwinger-Keldysh contour

In the previous section, we have shown that expectation values of contour-ordered products of operators read

$$\langle T_\mathcal{C}\left\{\varphi(x_1)\dots\varphi(x_n)\right\}\rangle_\rho = \mathrm{Tr}\left[\hat{\rho}(t_i)T_\mathcal{C}\left\{\varphi(x_1)\dots\varphi(x_n)\mathrm{Exp}\left(-i\int_\mathcal{C}\mathrm{d}\tau\mathcal{H}_I(\tau)\right)\right\}\right]. \tag{1.21}$$

Many properties of nonequilibrium systems can be understood by tracking the time evolution of these correlation functions. Of particular interest is the contour-ordered 2-point function

$$i\Delta(x_1,x_2) \equiv \langle T_\mathcal{C}\{\varphi(x_1)\varphi(x_2)\}\rangle\,. \tag{1.22}$$

Depending on the exact ordering of $x_1$ and $x_2$ on the Schwinger-Keldysh contour, see Eq. (1.9), Eq. (1.22) simplifies into[6]

$$i\Delta^{++}(x_1,x_2) = i\Delta^F(x_1,x_2) \equiv \langle T\{\varphi(x_1)\varphi(x_2)\}\rangle\,, \tag{1.23a}$$

[5]Formally, this cannot hold strictly, as any system capable of thermalising would already be in equilibrium at any finite time if one takes $t_i \to -\infty$. In practice, one sends $t_i \to -\infty$ only to derive the evolution equation for correlation functions, while keeping the initial time finite when actually solving these equations. We nevertheless leave aside these technical issues in this thesis.

[6]A commonly used alternative convention in the literature labels the different branches in the CTP as $\mathcal{C}_1$ and $\mathcal{C}_2$ instead, with propagators labelled accordingly, e.g. replacing $i\Delta^{++}$ with $i\Delta^{11}$.

$$i\Delta^{--}(x_1,x_2) = i\Delta^{\bar{F}}(x_1,x_2) \equiv \langle \bar{T}\{\varphi(x_1)\varphi(x_2)\}\rangle\,, \tag{1.23b}$$
$$i\Delta^{+-}(x_1,x_2) = i\Delta^{<}(x_1,x_2) \equiv \langle \varphi(x_2)\varphi(x_1)\rangle\,, \tag{1.23c}$$
$$i\Delta^{-+}(x_1,x_2) = i\Delta^{>}(x_1,x_2) \equiv \langle \varphi(x_1)\varphi(x_2)\rangle\,. \tag{1.23d}$$

$i\Delta^F$ ($i\Delta^{\bar{F}}$) corresponds to the usual Feynman propagator (its complex conjugate) while $i\Delta^{<,>}$ are traditionally referred to as the (lesser and greater) *Wightman propagators*. It is interesting to note that, in the case of a homogeneous and isotropic universe, as considered in this work, these propagators depend on the spatial coordinates only through the difference $\mathbf{x}_1-\mathbf{x}_2$. Furthermore, in systems in thermodynamic equilibrium, they depend on the temporal part of $x_1$ and $x_2$ only through $x_1^0 - x_2^0$. Based on the relations (1.23), one can in full generality write

$$i\Delta(x_1,x_2) = \Theta_{\mathcal{C}}(x_1,x_2)i\Delta^{>}(x_1,x_2) + \Theta_{\mathcal{C}}(x_2,x_1)i\Delta^{<}(x_1,x_2). \tag{1.24}$$

Similar definitions can be given for fermions, i.e.

$$iS^{++}_{\alpha\beta}(x_1,x_2) = iS^{F}_{\alpha\beta}(x_1,x_2) \equiv \langle T\{\psi_\alpha(x_1)\bar{\psi}_\beta(x_2)\}\rangle\,, \tag{1.25a}$$
$$iS^{--}_{\alpha\beta}(x_1,x_2) = iS^{\bar{F}}_{\alpha\beta}(x_1,x_2) \equiv \langle \bar{T}\{\psi_\alpha(x_1)\bar{\psi}_\beta(x_2)\}\rangle\,, \tag{1.25b}$$
$$iS^{+-}_{\alpha\beta}(x_1,x_2) = iS^{<}_{\alpha\beta}(x_1,x_2) \equiv -\langle \bar{\psi}_\beta(x_2)\psi_\alpha(x_1)\rangle\,, \tag{1.25c}$$
$$iS^{-+}_{\alpha\beta}(x_1,x_2) = iS^{>}_{\alpha\beta}(x_1,x_2) \equiv \langle \psi_\alpha(x_1)\bar{\psi}_\beta(x_2)\rangle\,, \tag{1.25d}$$

with $\alpha$ and $\beta$ being spinor indices. In lieu of the above Wightman propagators, it is in practice useful to work instead with the following combinations of these

$$\Delta^{\mathcal{A}}(x_1,x_2) = \frac{i}{2}(\Delta^{>}(x_1,x_2) - \Delta^{<}(x_1,x_2)), \tag{1.26a}$$
$$\Delta^{+}(x_1,x_2) = \frac{1}{2}(\Delta^{>}(x_1,x_2) + \Delta^{<}(x_1,x_2)), \tag{1.26b}$$
$$S^{\mathcal{A}}_{\alpha\beta}(x_1,x_2) = \frac{i}{2}(S^{>}_{\alpha\beta}(x_1,x_2) - S^{<}_{\alpha\beta}(x_1,x_2)), \tag{1.26c}$$
$$S^{+}_{\alpha\beta}(x_1,x_2) = \frac{1}{2}(S^{>}_{\alpha\beta}(x_1,x_2) + S^{<}_{\alpha\beta}(x_1,x_2)). \tag{1.26d}$$

The *spectral* (or anti-hermitian) functions $\Delta^{\mathcal{A}}, S^{\mathcal{A}}$ encode the spectrum of (quasi)particles, while the *statistical* functions $\Delta^{+}, S^{+}$ contain information about particle number densities. A very common ansatz for the form of these correlation functions in momentum space is the so-called *Kadanoff-Baym* ansatz, see e.g. Eq. (22) in [32],

$$i\Delta^{<}(k) \equiv 2\Delta^{\mathcal{A}}(k) f_\varphi(k), \qquad i\Delta^{>}(k) \equiv 2\Delta^{\mathcal{A}}(k)\left[1 + f_\varphi(k)\right] \tag{1.27}$$

in the case of scalar fields. It then follows that

$$i\Delta^{+}(k) \equiv \Delta^{\mathcal{A}}(k)\left[1 + 2f_\varphi(k)\right]. \tag{1.28}$$

In the above equations, $f_\varphi$ denotes the scalar field's distribution function. Hence, Eq. (1.28) clearly illustrates the property highlighted above: all information about the scalar field number density is encoded in $\Delta^{+}$ whereas $\Delta^{\mathcal{A}}$ encodes information about the particle spectrum. In particular, $\Delta^{\mathcal{A}}(k) \sim \delta(k^2 - m_\varphi^2)$ for a free particle of mass $m_\varphi$. For these reasons, Eq. (1.28) can be seen as a specific application of the more general fluctuation-dissipation theorem. As shown in the next section, the Kadanoff-Baym ansatz (1.27) is exact in thermal equilibrium. However, it also remains valid for a broad range of nonequilibrium situations for which the quasiparticle picture[7] holds.

Finally, the usual retarded, advanced and Hermitian propagators can also be extracted from the previously defined correlation functions. For scalar particles, for instance, these are respectively defined in position space as

$$i\Delta^{R}(x_1, x_2) = 2\Theta(x_1^0 - x_2^0)\Delta^{\mathcal{A}}(x_1, x_2), \tag{1.29a}$$

$$i\Delta^{A}(x_1, x_2) = -2\Theta(x_2^0 - x_1^0)\Delta^{\mathcal{A}}(x_1, x_2), \tag{1.29b}$$

$$\begin{aligned} i\Delta^{H}(x_1, x_2) &= \frac{i}{2}\left(\Delta^{R}(x_1, x_2) + \Delta^{A}(x_1, x_2)\right), \\ &= \operatorname{sgn}(x_1^0 - x_2^0)\Delta^{\mathcal{A}}(x_1, x_2). \end{aligned} \tag{1.29c}$$

Similar expressions hold for fermions, up to replacing $\Delta \to S_{\alpha\beta}$.

## 1.3 CTP generating functionals and the 1PI effective action

Considering for the moment a pure scalar theory, the aforementioned correlation functions can all be derived by taking derivatives of the generating

[7] Despite their interactions with the early universe plasma, the (dressed) spectral functions of sufficiently weakly-interacting particles will continue to feature narrow resonances and the standard description in terms of propagating degrees of freedom will still hold. This is typically referred to as the quasiparticle picture.

functional

$$Z\left[J\right] = \mathrm{Tr}\left[\hat{\rho}(t_i)T_{\mathcal{C}}\left\{\mathrm{Exp}\left[i\int_{\mathcal{C}}\mathrm{d}^4xJ(x)\varphi(x)\right]\right\}\right], \tag{1.30}$$

where $\hat{\rho}(t_i)$ describes the density matrix of the system at the initial time $t_i$. One can show, see e.g. chapter 3 in [25], that Eq. (1.30) can be rewritten to make the dependence on the classical action of the system $S[\varphi] \equiv \int_{\mathcal{C}}\mathrm{d}^4x\mathcal{L}\left[\varphi\right]$ more explicit, i.e.

$$\begin{aligned} Z\left[J\right] = &\int\mathcal{D}\varphi_1\mathcal{D}\varphi_2\left\langle\varphi_1|\hat{\rho}(t_i)|\varphi_2\right\rangle \times \\ &\times\int_{\varphi(t_i^+,\mathbf{x})=\varphi_1(\mathbf{x})}^{\varphi(t_i^-,\mathbf{x})=\varphi_2(\mathbf{x})}\mathcal{D}\varphi T_{\mathcal{C}}\left\{\mathrm{Exp}\left[i\left(S[\varphi]+\int_{\mathcal{C}}\mathrm{d}^4xJ(x)\varphi(x)\right)\right]\right\}. \end{aligned} \tag{1.31}$$

The first term (on the first line) describes the initial condition of our system while the second (on the second line) characterises its dynamics. Setting $J = 0$, one recovers the partition function of the system. Contour-ordered $n$-point correlation functions are then expressed as

$$\left\langle T_{\mathcal{C}}\left\{\varphi(x_1)\ldots\varphi(x_n)\right\}\right\rangle = \frac{(-i)^n}{Z\left[J\right]}\frac{\delta^n}{\delta J(x_1)\ldots\delta J(x_n)}Z\left[J\right]\Big|_{J=0}. \tag{1.32}$$

The functional derivative $\delta$ is also defined on the Schwinger-Keldysh contour, verifying

$$\frac{\delta J(x_1)}{\delta J(x_2)} = \delta_{\mathcal{C}}^{(4)}(x_1,x_2) \equiv \delta_{\mathcal{C}}(x_1^0,x_2^0)\delta^{(3)}(\boldsymbol{x}_1,\boldsymbol{x}_2). \tag{1.33}$$

As a specific case of interest, the propagator (1.22) reads

$$i\Delta(x_1,x_2) = -\frac{1}{Z\left[J\right]}\frac{\delta^2}{\delta J(x_1)\delta J(x_2)}Z\left[J\right]\Big|_{J=0}. \tag{1.34}$$

As is the case in vacuum QFT, the definition (1.34) also includes contributions from disconnected diagrams. The equivalent generating functional for connected correlators is simply given by

$$W\left[J\right] = -i\ln\left(Z\left[J\right]\right). \tag{1.35}$$

One can indeed straightforwardly extract the 1-point function from Eq. (1.35), yielding

$$\frac{\delta W[J]}{\delta J(x)} = -\frac{i}{Z[J]}\frac{\delta}{\delta J(x)} Z[J] = \langle \varphi(x) \rangle_J \equiv \varphi^{\mathrm{cl}}(x). \tag{1.36}$$

$\varphi^{\mathrm{cl}}$ is the classical field (or 1-point function) in presence of non-zero source $J(x)$. Similarly, for the connected 2-point function, we have

$$\begin{aligned}
\frac{\delta^2 W[J]}{\delta J(x_1)\delta J(x_2)} &= -i\left(\frac{1}{Z[J]}\frac{\delta^2 Z[J]}{\delta J(x_1)\delta J(x_2)} - \left(\frac{1}{Z[J]}\frac{\delta Z[J]}{\delta J(x_1)}\right)\left(\frac{1}{Z[J]}\frac{\delta Z[J]}{\delta J(x_2)}\right)\right), \\
&= i\Big( \langle \varphi(x_1)\varphi(x_2)\rangle - \langle \varphi(x_1)\rangle \langle \varphi(x_2)\rangle \Big), \\
&= i \langle \varphi(x_1)\varphi(x_2)\rangle_{\mathrm{conn}} \equiv -\Delta_{\mathrm{conn}}(x_1, x_2), 
\end{aligned} \tag{1.37}$$

where the index $\mathrm{conn}$ indicates the connected nature of the correlator. Such formula can be generalised to any $n$-point function. We define the resulting one-particle-irreducible (1PI) effective action[8] $\Gamma^{1\mathrm{PI}}$ by taking the Legendre transform of $W$ with respect to $J$

$$\Gamma^{1\mathrm{PI}}\left[\varphi^{\mathrm{cl}}\right] = W[J] - \int_{\mathcal{C}} \mathrm{d}^4x\, \varphi^{\mathrm{cl}}(x) J(x). \tag{1.38}$$

From Eq. (1.38), it is straightforward to verify that

$$\frac{\delta}{\delta \varphi^{\mathrm{cl}}(x)}\Gamma^{1\mathrm{PI}}\left[\varphi^{\mathrm{cl}}\right]\Big|_{J=0} = -J(x)\Big|_{J=0} = 0\,, \tag{1.39}$$

defining the equation of motion for $\varphi^{\mathrm{cl}}$. As a corollary, we have

$$\frac{\delta}{\delta J(x_2)}\frac{\delta}{\delta \varphi^{\mathrm{cl}}(x_1)}\Gamma^{1\mathrm{PI}}\left[\varphi^{\mathrm{cl}}\right] = -\delta^{(4)}_{\mathcal{C}}(x_1, x_2). \tag{1.40}$$

It automatically follows that

$$\begin{aligned}
\delta^{(4)}_{\mathcal{C}}(x_1, x_2) &= -\int_{\mathcal{C}} \mathrm{d}^4z \frac{\delta \varphi^{\mathrm{cl}}(z)}{\delta J(x_2)} \frac{\delta^2}{\delta \varphi^{\mathrm{cl}}(z)\delta\varphi^{\mathrm{cl}}(x_1)}\Gamma^{1\mathrm{PI}}\left[\varphi^{\mathrm{cl}}\right], \\
&= -\int_{\mathcal{C}} \mathrm{d}^4z \frac{\delta^2 W[J]}{\delta J(x_2)\delta J(z)} \frac{\delta^2}{\delta \varphi^{\mathrm{cl}}(z)\delta\varphi^{\mathrm{cl}}(x_1)}\Gamma^{1\mathrm{PI}}\left[\varphi^{\mathrm{cl}}\right], \\
&= \int_{\mathcal{C}} \mathrm{d}^4z \Delta_{\mathrm{conn}}(x_2, z) \frac{\delta^2}{\delta \varphi^{\mathrm{cl}}(z)\delta\varphi^{\mathrm{cl}}(x_1)}\Gamma^{1\mathrm{PI}}\left[\varphi^{\mathrm{cl}}\right].
\end{aligned} \tag{1.41}$$

[8] The 1PI effective action is the analogue of the Gibbs free energy in standard thermodynamics.

Therefore, $\frac{\delta^2}{\delta\varphi^{\rm cl}(z)\delta\varphi^{\rm cl}(x_1)}\Gamma^{\rm 1PI}\left[\varphi^{\rm cl}\right]$ can be seen as the inverse propagator, corresponding to the 1PI two-point correlation function

$$\frac{\delta^2}{\delta\varphi^{\rm cl}(z)\delta\varphi^{\rm cl}(x_1)}\Gamma^{\rm 1PI}\left[\varphi^{\rm cl}\right] = -i\left\langle\varphi(z)\varphi(x_1)\right\rangle_{\rm 1PI}\ . \tag{1.42}$$

Hence,

$$\int_{\mathcal{C}} {\rm d}^4 z \Delta_{\rm conn}(x_2, z)\left\langle\varphi(z)\varphi(x_1)\right\rangle_{\rm 1PI} = -i\delta^{(4)}_{\mathcal{C}}(x_1, x_2). \tag{1.43}$$

At tree level, $\left\langle\varphi(z)\varphi(x_1)\right\rangle_{\rm 1PI}$ is given by $i(\Box_z + m_\varphi^2)\delta^{(4)}_{\mathcal{C}}(z, x_1)$. A similar relation to Eq. (1.42) can be obtained for higher-order correlators [31]. The effective action therefore acts as the generating functional for 1PI correlation functions, which can be obtained by taking derivatives of $\Gamma^{\rm 1PI}$ with respect to $\varphi^{\rm cl}$

$$\left\langle\varphi(x_1)\ldots\varphi(x_n)\right\rangle_{\rm 1PI} = -i\frac{\delta^n}{\delta\varphi^{\rm cl}(x_1)\ldots\delta\varphi^{\rm cl}(x_n)}\Gamma^{\rm 1PI}\left[\varphi^{\rm cl}\right]. \tag{1.44}$$

We can then define the *self-energy* of $\varphi$, denoted $\Pi$, as the difference between the complete 1PI 2-point correlation function and its tree-level limit

$$\Pi(x_1, x_2) \equiv -i\left\langle\varphi(x_1)\varphi(x_2)\right\rangle_{\rm 1PI} - (\Box_{x_1} + m_\varphi^2)\delta^{(4)}_{\mathcal{C}}(x_1, x_2). \tag{1.45}$$

Similarly to the 2-point functions defined in Eq. (1.23), one can define 4 different types of self-energies $\Pi^{++}$, $\Pi^{+-}$, $\Pi^{-+}$ and $\Pi^{--}$ depending on the position of $x_1,\ x_2$ on $\mathcal{C}$.

The definition (1.45) is just another form of the well-known *Schwinger-Dyson* equation. By multiplying Eq. (1.45) by the connected two-point function and integrating over, one can rewrite it in the more conventional form

$$(\Box_{x_1} + m_\varphi^2)\Delta_{\rm conn}(x_1, x_2) + \int_{\mathcal{C}} {\rm d}^4 z\ \Pi(x_1, z)\Delta_{\rm conn}(z, x_2) = -\delta^{(4)}_{\mathcal{C}}(x_1, x_2). \tag{1.46}$$

Note that, in the rest of this thesis, we will always work with fields with null vacuum expectation value (vev) $\varphi^{\rm cl} = 0$ such that Eq. (1.34) also corresponds to the connected 2-point function. We will therefore drop the index $\rm conn$ making the distinction after this subsection.

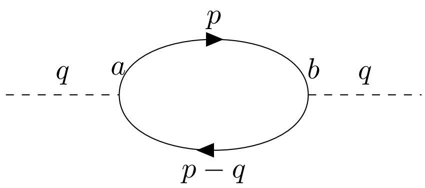


**Figure 1.3:** Scalar one-loop self-energy in the toy model (1.47). $a$ and $b$ are CTP indices, taking values $+$ or $-$.

## 1.4 Feynman rules on the Schwinger-Keldysh contour

Though the derivation has until now been relatively formal, it is possible to define practical Feynman rules, in a relatively similar manner to the zero-temperature situation, to compute the propagators and self-energies defined in the previous subsection. We schematically illustrate the procedure in this subsection, using as toy example the self-energy $\Pi^{ab}$ displayed in Fig. 1.3 and the Lagrangian of a scalar particle coupled to two (Dirac) fermions

$$\mathcal{L} \supset ig\varphi\bar{\Psi}\Psi. \tag{1.47}$$

The main difference with the vacuum case is the doubling of the number of degrees of freedom, which arises from the forward and backward propagating branches of the Schwinger-Keldysh contour. As a consequence, each vertex can be of two different types, a feature which is encoded in the CTP index $+$ or $-$ assigned to it. The coupling associated to a vertex of type $+$ is the same as expected from vacuum QFT, whereas the coupling associated with a vertex of type $-$ is instead its complex conjugate. Propagating in the loop, the zero-temperature Feynman propagators are replaced by the 2-point correlation functions defined in Eq. (1.25). More explicitly, the self-energy displayed in Fig. 1.3 takes the general form

$$i\Pi^{ab}(q) = -\mathrm{sgn}(ab)g^2 \int \frac{\mathrm{d}^4p}{(2\pi)^4} \,\mathrm{Tr}\left[iS^{ab}(p)iS^{ba}(p-q)\right] , \tag{1.48}$$

where $\mathrm{sgn}$ denotes the sign function. In presence of "internal" vertices, i.e. vertices not connected to any external lines, one should typically sum over all possible CTP indices.

## 1.5 The thermodynamic equilibrium limit

In many contexts, particles evolve within a plasma in or close to equilibrium with a slowly evolving temperature $T$. In these situations, explicit expressions for the particles' propagators defined in Sec. 1.2 can be found, see e.g. [33–38]. For instance, for a Dirac fermion in thermal equilibrium and with vanishing chemical potential, the 2-point correlation functions take the following simple form in momentum space

$$iS^{>}(k) = 2\pi \mathrm{sgn}(k_0)\delta(k^2 - m^2)(\not{k} + m)(1 - f_{\mathrm{F}}(k_0)), \tag{1.49a}$$

$$iS^{<}(k) = -2\pi \mathrm{sgn}(k_0)\delta(k^2 - m^2)(\not{k} + m) f_{\mathrm{F}}(k_0)\ , \tag{1.49b}$$

with $f_{\mathrm{F}}(E) = 1/(e^{E/T} + 1)$ the standard Fermi-Dirac distribution. One observes that the two Wightman functions verify the so-called Kubo-Martin-Schwinger (KMS) relation

$$iS^{>}(k) = -e^{k_0/T} iS^{<}(k). \tag{1.50}$$

At the fundamental level, this relation originates from the Hamiltonian $\mathcal{H}$ being the generator of time translations. Indeed, as mentioned earlier, the density matrix $\hat{\rho}$ of systems in thermal equilibrium is directly proportional to $e^{-\beta\mathcal{H}}$ in absence of chemical potential. Identifying $\mathcal{H}$ with the time-evolution operator, it imposes $iS^{>}(x_1^0, x_2^0) = iS^{<}(x_1^0 + i\beta, x_2^0)$, which translates into Eq. (1.50) in momentum space.

The Feynman and anti-Feynman propagators on the other hand reads

$$iS^{F}(k) = \frac{i(\not{k} + m)}{k^2 - m^2 + i\epsilon} - 2\pi\delta(k^2 - m^2)(\not{k} + m) f_{\mathrm{F}}(|k_0|), \tag{1.51a}$$

$$iS^{\bar{F}}(k) = -\frac{i(\not{k} + m)}{k^2 - m^2 - i\epsilon} - 2\pi\delta(k^2 - m^2)(\not{k} + m) f_{\mathrm{F}}(|k_0|). \tag{1.51b}$$

Similarly, for scalar bosons, we have

$$i\Delta^{>}(k) = 2\pi \mathrm{sgn}(k_0)\delta(k^2 - m^2)(1 + f_{\mathrm{B}}(k_0)), \tag{1.52a}$$

$$i\Delta^{<}(k) = 2\pi \mathrm{sgn}(k_0)\delta(k^2 - m^2) f_{\mathrm{B}}(k_0), \tag{1.52b}$$

and

$$i\Delta^{F}(k) = \frac{i}{k^2 - m^2 + i\epsilon} + 2\pi\delta(k^2 - m^2) f_{\mathrm{B}}(|k_0|), \tag{1.53a}$$

$$i\Delta^{\bar{F}}(k) = -\frac{i}{k^2 - m^2 - i\epsilon} + 2\pi\delta(k^2 - m^2) f_{\mathrm{B}}(|k_0|), \tag{1.53b}$$

where $f_{\mathrm{B}}(E) = 1/(e^{E/T} - 1)$ is the usual Bose-Einstein distribution. Finally, one can extend the latter formulae to vector bosons (of mass $m$) by making use of

$$iD^{ab}_{\mu\nu}(k) = i\Delta^{ab}(k) d_{\mu\nu}, \tag{1.54}$$

where $a, b \in \{+, -\}$ are CTP indices and the polarisation tensor $d_{\mu\nu}$ reads

$$d^{\mu\nu}(k) = -g^{\mu\nu} + (1-\xi)\frac{k^\mu k^\nu}{k^2 - \xi m^2} \tag{1.55}$$

in a general $R_\xi$-gauge. In case the chemical potential $\mu$ is non-negligible, it is straightforward to adapt all of the above formulae by making the replacement $f_{\mathrm{F/B}}(k_0) \to f_{\mathrm{F/B}}(k_0 - \mu)$.

From Eqs. (1.52) and (1.53), one can also derive explicit formulae for the (anti-)hermitian, retarded and advanced propagators, which write for scalar bosons

$$\Delta^{\mathcal{A}}(k) = \pi\delta(k^2 - m^2)\mathrm{sgn}(k_0)\,, \tag{1.56a}$$

$$\Delta^{H}(k) = \mathcal{P}\frac{1}{k^2 - m^2}\,, \tag{1.56b}$$

$$i\Delta^{R,A}(k) = \frac{i}{k^2 - m^2 \pm i\mathrm{sgn}(k_0)\epsilon}\,, \tag{1.56c}$$

where $\mathcal{P}$ denotes the Cauchy principal value. Equivalent formulae can be derived for fermions.

Finally, we would like to highlight that, beyond propagators, also (macroscopic) thermodynamic quantities can be extracted from our knowledge of the generating functional (1.30). In particular, the pressure, energy and entropy density $P, \rho$ and $s$ verify

$$P = \frac{T}{\mathcal{V}} \ln Z[0]\,, \tag{1.57a}$$

$$\rho = \frac{T^2}{\mathcal{V}}\frac{\partial}{\partial T} \ln Z[0] = -P + T\frac{\partial P}{\partial T}\,, \tag{1.57b}$$

$$s = \frac{1}{\mathcal{V}}\frac{\partial}{\partial T}\Big(T \ln Z[0]\Big) = \frac{\rho + P}{T} = \frac{\partial P}{\partial T}\,, \tag{1.57c}$$

for systems in thermal equilibrium with thermodynamic volume $\mathcal{V}$. For an ideal gas, i.e. if one neglects interactions between particles, the pressure and energy density take the simple form

$$P = g \int \frac{\mathrm{d}^3\mathbf{p}}{(2\pi)^3} E f_{\mathrm{F/B}}(E) \,, \tag{1.58a}$$

$$\rho = g \int \frac{\mathrm{d}^3\mathbf{p}}{(2\pi)^3} \frac{\mathbf{p}^2}{3E} f_{\mathrm{F/B}}(E) \,, \tag{1.58b}$$

where $E = \sqrt{\mathbf{p}^2 + m^2}$ is the energy of the particle (of mass $m$) and $g$ its number of internal degrees of freedom.

## 1.6 Kadanoff-Baym equations

The main focus of this thesis is the out-of-equilibrium evolution of various particle species. Their dynamics can in general be described by effective kinetic equations, along with a set of interaction rates and Hamiltonians appearing in these. The evaluation of these quantities can typically be carried out from first principles by computing the appropriate self-energies. The major advantage of the CTP formalism is then our ability to derive these kinetic equations, together with the corresponding rates and Hamiltonians, directly from first principles via a controlled set of approximations.

In components, the Schwinger-Dyson equation (1.46) write

$$(\Box_{x_1} + m_\varphi^2)\Delta^{ab}(x_1, x_2) + \sum_c c \int \mathrm{d}^4 z\, \Pi^{ac}(x_1, z)\Delta^{cb}(z, x_2) \tag{1.59}$$
$$= -a\delta^{(4)}(x_1, x_2)\delta^{ab}.$$

Fixing the values of $\{a,\ b\}$ to $\{+, -\}$ and $\{-, +\}$ respectively, Eq. (1.59) yields two independent equations

$$(\Box_{x_1} + m_\varphi^2)\Delta^{<}(x_1, x_2) + \int \mathrm{d}^4 z\, \Pi^{F}(x_1, z)\Delta^{<}(z, x_2) \tag{1.60a}$$
$$- \int \mathrm{d}^4 z\, \Pi^{<}(x_1, z)\Delta^{\bar{F}}(z, x_2) = 0 \,,$$

$$(\Box_{x_1} + m_\varphi^2)\Delta^{>}(x_1, x_2) - \int \mathrm{d}^4 z\, \Pi^{\bar{F}}(x_1, z)\Delta^{>}(z, x_2) \tag{1.60b}$$
$$+ \int \mathrm{d}^4 z\, \Pi^{>}(x_1, z)\Delta^{F}(z, x_2) = 0.$$

The equivalent equations for the $\{+, +\}$ and $\{-, -\}$ components are of less interest for our purposes. Indeed, as highlighted by the Kadanoff-Baym ansatz

(1.28), information about the particle number density and its mass shell is more transparently encoded in the spectral and statistical functions, and it is therefore sufficient to solve for $\Delta^{\mathcal{A}}$ and $\Delta^{+}$. Inverting the relation (1.26) yields $\Delta^{\gtrless} = \Delta^{+} \mp i\Delta^{\mathcal{A}}$. One can then derive the corresponding Schwinger-Dyson equations for these functions, i.e.[9]

$$(\Box_{x_1} + m_\varphi^2)\Delta^{\mathcal{A}}(x_1, x_2) = -2i \int \mathrm{d}^3\boldsymbol{z} \int_{x_1^0}^{x_2^0} \mathrm{d}z^0 \, \Pi^{\mathcal{A}}(x_1, z)\Delta^{\mathcal{A}}(z, x_2), \quad (1.61a)$$

$$(\Box_{x_1} + m_\varphi^2)\Delta^{+}(x_1, x_2) = -2i\Big[ \int \mathrm{d}^3\boldsymbol{z} \int_{-\infty}^{x_2^0} \mathrm{d}z^0 \, \Pi^{+}(x_1, z)\Delta^{\mathcal{A}}(z, x_2) \quad (1.61b)$$
$$- \int \mathrm{d}^3\boldsymbol{z} \int_{-\infty}^{x_1^0} \mathrm{d}z^0 \, \Pi^{\mathcal{A}}(x_1, z)\Delta^{+}(z, x_2)\Big].$$

These two equations are standardly known as the *Kadanoff-Baym* equations, with Eq. (1.61a) referred to as the constraint equation and Eq. (1.61b) as the kinetic equation. A similar set of equations can be derived for fermions. We also note that a similar derivation of the Kadanoff-Baym equations can be done starting instead from the $n$PI effective action [25, 40]. Such a derivation has the advantage of automatically resumming certain classes of diagrams.

## 1.7 From the Kadanoff-Baym to the quantum kinetic equations

In many situations, such as the slow production of a matter-antimatter asymmetry or freeze-in Dark Matter (DM), one is typically more interested in modelling the evolution of a particle's distribution function or number density through effective fluid equations. In this section, we briefly outline how to derive such equations starting from the Kadanoff-Baym equations (1.61), focusing on the freeze-in production of a single scalar field from a thermal bath.

Although it is in principle possible to solve these equations in real time, it is typically easier to work in momentum space. To this end, we rewrite the Kadanoff-Baym equations so that the time component is integrated from $-\infty$ to $+\infty$. Using the definition (1.29c) of the Hermitian propagator, it is possible

[9] These equations typically also rely on the assumption that initial states are Gaussian, an approximation which is not always valid in practice [39], although it is in general justified in freeze-in scenarios.

to rewrite Eq. (1.61) as

$$\left(\Box_{x_1} + m_\varphi^2\right)\Delta^{\mathcal{A}}(x_1,x_2) = -\int \mathrm{d}^4 z \Big(\Pi^H(x_1,z)\Delta^{\mathcal{A}}(z,x_2) + \Pi^{\mathcal{A}}(x_1,z)\Delta^H(z,x_2)\Big), \tag{1.62a}$$

$$\left(\Box_{x_1} + m_\varphi^2\right)\Delta^{+}(x_1,x_2) = -\int \mathrm{d}^4 z \Big[\Big(\Pi^+(x_1,z)\Delta^H(z,x_2) + \Pi^H(x_1,z)\Delta^+(z,x_2)\Big) + \frac{1}{2}\Big(\Pi^>(x_1,z)\Delta^<(z,x_2) - \Pi^<(x_1,z)\Delta^>(z,x_2)\Big)\Big]. \tag{1.62b}$$

As already highlighted in the paragraph below Eq. (1.25), propagators and self-energies only depend on the spatial coordinates through their relative separation in an isotropic and homogeneous universe. It is therefore practical to perform the following change of coordinates

$$\begin{pmatrix} x_1 \\ x_2 \end{pmatrix} \to \begin{pmatrix} \bar{x} \\ r \end{pmatrix} = \begin{pmatrix} \frac{x_1+x_2}{2} \\ x_1 - x_2 \end{pmatrix} . \tag{1.63}$$

Due to their spatial translation invariance, $\Delta$ and $\Pi$ are independent of $\bar{\mathbf{x}}$. In order to express the Kadanoff-Baym equations in momentum space, we perform a Fourier transform of these equations with respect to $r$. Since

$$\partial_{x_1} = \frac{1}{2}\partial_{\bar{x}} + \partial_r \,, \tag{1.64}$$

we can simplify Eq. (1.62) to

$$\left(k^2 + ik_\mu\partial_{\bar{x}}^\mu - \frac{1}{4}\partial_{\bar{x}}^2 - m_\varphi^2\right)\Delta^{\mathcal{A}}(\bar{x},k) = e^{-i\Diamond}\{\Pi^H\}\{\Delta^{\mathcal{A}}\} + e^{-i\Diamond}\{\Pi^{\mathcal{A}}\}\{\Delta^H\}, \tag{1.65}$$

$$\left(k^2 + ik_\mu\partial_{\bar{x}}^\mu - \frac{1}{4}\partial_{\bar{x}}^2 - m_\varphi^2\right)\Delta^{+}(\bar{x},k) = e^{-i\Diamond}\{\Pi^H\}\{\Delta^+\} + e^{-i\Diamond}\{\Pi^+\}\{\Delta^H\} + \frac{1}{2}\left(e^{-i\Diamond}\{\Pi^>\}\{\Delta^<\} - e^{-i\Diamond}\{\Pi^<\}\{\Delta^>\}\right). \tag{1.66}$$

In this equation, the diamond operator $\Diamond$ is a bilinear functional, defined for any functions $f$ and $g$ by

$$\Diamond\{f(\bar{x},k)\}\{g(\bar{x},k)\} \equiv \frac{1}{2}\big(\partial_{\bar{x}}f\cdot\partial_k g - \partial_k f\cdot\partial_{\bar{x}}g\big). \tag{1.67}$$

It verifies

$$\int \mathrm{d}^4 r e^{ikr}\int \mathrm{d}^4 z\, f(x_1,z)g(z,x_2) = e^{-i\Diamond}\{f(\bar{x},k)\}\{g(\bar{x},k)\}\,. \tag{1.68}$$

For a proof of relation (1.68) and a more rigorous definition the diamond operator, see e.g. [41]. Because the system is homogeneous and isotropic, the spatial derivatives in $\bar{x}$ drop, and we can further simplify the Kadanoff-Baym equations to

$$\left(k^2 + ik_0\partial_t - \frac{1}{4}\partial_t^2 - m_\varphi^2\right)\Delta^{\mathcal{A}}(t,k) = e^{-i\diamondsuit}\{\Pi^H\}\{\Delta^{\mathcal{A}}\} + e^{-i\diamondsuit}\{\Pi^{\mathcal{A}}\}\{\Delta^H\}, \tag{1.69}$$

$$\begin{aligned}\left(k^2 + ik_0\partial_t - \frac{1}{4}\partial_t^2 - m_\varphi^2\right)\Delta^{+}(t,k) &= e^{-i\diamondsuit}\{\Pi^H\}\{\Delta^{+}\} \\ &+ e^{-i\diamondsuit}\{\Pi^{+}\}\{\Delta^H\} + \frac{1}{2}\left(e^{-i\diamondsuit}\{\Pi^{>}\}\{\Delta^{<}\} - e^{-i\diamondsuit}\{\Pi^{<}\}\{\Delta^{>}\}\right)\,,\end{aligned} \tag{1.70}$$

where we defined $\bar{x}_0 \equiv t$.

Solving the set of equations (1.69) and (1.70) is in general challenging as they typically involve towers of derivatives. However, in many physical systems, one can exploit the hierarchy between microscopic and macroscopic scales to simplify these equations. This approximation scheme is known as the *gradient expansion scheme*. For the freeze-in production of a scalar particle $\varphi$, $k_0$ encodes the typical energy associated with microscopic processes and is typically of the order of the temperature $T$. On the other hand, $t$ represents the time scale associated with slower, macroscopic processes such as the expansion of the universe or the equilibration of $\varphi$. In the systems considered in this thesis, these scales are typically much larger than the microscopic time scale. Schematically, one has

$$\partial_t \ll k_0. \tag{1.71}$$

As a consequence, one can expand the diamond operator to linear order

$$e^{-i\diamondsuit}\{f\}\{g\} = fg + \mathcal{O}\left(\partial_t f \cdot \partial_k g\right). \tag{1.72}$$

Furthermore, terms quadratic in $\partial_t$ in the left-hand side of Eqs. (1.69) and (1.70) can be neglected for the same reasons. Inserting this approximation into Eqs. (1.69) and (1.70), we finally obtain

$$\left(k^2 + ik_0\partial_t - m_\varphi^2\right)\Delta^{\mathcal{A}}(t,k) = \Pi^H\Delta^{\mathcal{A}} + \Pi^{\mathcal{A}}\Delta^H, \tag{1.73}$$

$$\begin{aligned}\left(k^2 + ik_0\partial_t - m_\varphi^2\right)\Delta^{+}(t,k) &= \Pi^H\Delta^{+} + \Pi^{+}\Delta^H \\ &+ \frac{1}{2}\left(\Pi^{>}\Delta^{<} - \Pi^{<}\Delta^{>}\right)\,.\end{aligned} \tag{1.74}$$

Taking the real and imaginary part of these two equations, we obtain the following four equations

$$\left(k^2 - m_\varphi^2 - \Pi^H\right) \Delta^{\mathcal{A}}(t,k) = \Pi^{\mathcal{A}} \Delta^H, \tag{1.75a}$$

$$ik_0 \partial_t \Delta^{\mathcal{A}}(t,k) = 0, \tag{1.75b}$$

$$\left(k^2 - m_\varphi^2 - \Pi^H\right) \Delta^+(t,k) = \Pi^+ \Delta^H \ , \tag{1.75c}$$

$$ik_0 \partial_t \Delta^+(t,k) = \frac{1}{2} \left(\Pi^> \Delta^< - \Pi^< \Delta^>\right) \ . \tag{1.75d}$$

Eqs. (1.75a) and (1.75c) are referred to as the constraint equations while the remaining two equations are known as the kinetic equations. In particular, as we will see in the following, Eq. (1.75d) captures the evolution of the scalar number density and we will focus on solving this equation in the rest of this section.

As highlighted in the beginning of this section, we focus on the freeze-in production of scalar particles from a bath in complete thermodynamic equilibrium. For simplicity, we assume here that all chemical potentials are vanishing. In this situation, the self-energies $\Pi$ take their equilibrium values $\bar{\Pi}$. Furthermore, it is justified to expand the various propagators around their (known) equilibrium values

$$\Delta^{\gtrless} = \bar{\Delta}^{\gtrless} + \delta\Delta^{\gtrless} \ . \tag{1.76}$$

Equilibrium propagators $\bar{\Delta}^{\gtrless}$ can be obtained as static solutions of Eq. (1.75), with their functional forms given in Eq. (1.56). To leading order in the gradient expansion, Eq. (1.75b) implies

$$\delta\Delta^> = \delta\Delta^< \equiv \delta\Delta \ , \tag{1.77}$$

see also e.g. [32] for explicit solutions for $\delta\Delta$. Inserting this expansion into Eq. (1.75d) and making use of the KMS relation, we obtain[10]

$$\partial_t \delta\Delta = -\partial_t \bar{\Delta} - \frac{\bar{\Pi}^{\mathcal{A}}}{k_0} \delta\Delta \ . \tag{1.78}$$

Using the Kadanoff-Baym ansatz (1.27), we can parametrise

$$\bar{\Delta}^+ = -i\Delta^{\mathcal{A}}(1 + 2f_B), \qquad \delta\Delta = -2i\Delta^{\mathcal{A}}\delta f \ , \tag{1.79}$$

[10]While $\partial_t \bar{\Delta}$ vanishes in Minkowski space, it does not in an FLRW universe, and we therefore need to retain this term.

where $\bar{\Delta}^{\mathcal{A}}(k) = \pi \mathrm{sgn}(k_0)\delta(k^2 - m_\varphi^2)$ and $\delta f(k) \equiv f(k) - f^{\mathrm{eq}}(k) = f(k) - f_B(k)$ denotes the deviation of the scalar distribution function from equilibrium. The kinetic equation describing the time evolution of this distribution function then takes the form

$$\partial_t \delta f = -\partial_t f_B - \frac{\bar{\Pi}^{\mathcal{A}}}{k_0} \delta f \, . \tag{1.80}$$

The approach presented in this section assumes a Minkowski space-time and therefore neglects the expansion of the universe. As shown in [42, 43], it is however straightforward to adapt this approach to an FLRW universe by the use of conformal coordinates. We obtain

$$\partial_t \delta f - H |\mathbf{k}| \partial_{|\mathbf{k}|} \delta f = -\partial_t f_B - \frac{\bar{\Pi}^{\mathcal{A}}}{k_0} \delta f \, . \tag{1.81}$$

If kinetic equilibrium is maintained (and $\frac{\bar{\Pi}^{\mathcal{A}}}{k_0}$ is momentum independent), one can integrate Eq. (1.81) over all momenta to recover the well-known Boltzmann equation

$$(\partial_t + 3H)\, \delta n = -\partial_t n^{\mathrm{eq}} - \frac{\bar{\Pi}^{\mathcal{A}}}{k_0} \delta n \, , \tag{1.82}$$

with $n^{\mathrm{eq}}$ the equilibrium abundance of the scalar field and $\delta n \equiv n - n^{\mathrm{eq}}$. The last two equations make evident that the anti-Hermitian self-energy $\bar{\Pi}^{\mathcal{A}}$ captures the equilibration of the scalar field and can be related to the interaction rates $\Gamma$ appearing in standard Boltzmann equation through

$$\Gamma = \frac{\bar{\Pi}^{\mathcal{A}}}{k_0} = \frac{\mathrm{Im}\left(\bar{\Pi}^{R}\right)}{k_0} \, , \tag{1.83}$$

in agreement with the expectation based on the optical theorem in vacuum. In this thesis, we will therefore focus on computing this quantity for different systems, see e.g. Eqs. (4.18) and (6.14). Beyond the simplified system considered in this section, e.g. in the presence of non-vanishing chemical potentials or multiple generations of scalars, additional terms must be added to Eq. (1.81) in order to account for oscillations, backreactions of the thermal bath, etc. See e.g. appendix B in [44] for the derivation of analogous kinetic equations for (degenerate) right-handed neutrinos during leptogenesis.

# Part I

# Cosmological Gravitational Wave Backgrounds

# Introduction

Our understanding of the universe has for very long solely relied on information transported by light, whether it is seen by our naked eyes or via telescopes. While this already allowed us to unravel some of the most fundamental secrets of Nature, from the seemingly erratic behaviour of planets to the laws of gravity or the evolution of stars, this approach also showed some limits. Indeed, it cannot probe very dense objects or the very early universe due to the large coupling strength of the photon. In recent years however, complementary probes of the cosmos based on neutrinos and gravitational waves (GWs), which are much more feebly interacting, have emerged. GWs in particular form an excellent probe of the very early universe as they are expected to be produced throughout its history and decouple from the rest of its content much earlier.[1] The first direct detection of such waves, emitted by a binary black hole merger, in September 2015 by the LIGO interferometer [46] opened up a new era for the fields of astrophysics, cosmology and particle physics. Since then, there has been rapid experimental progress, with already $\mathcal{O}(100)$ events observed after the third run of LIGO-VIRGO and a few hundred more are expected by the end of its fourth run. Until now, detected events have all been of purely astrophysical origin, excluding a potential hint of a cosmological origin from pulsar timing arrays [47–51]. However, GW searches can also be used to probe a variety of different cosmological gravitational wave backgrounds (GWBs) [52] and in turn constrain particle physics in a manner complementary to traditional laboratory experiments. This tantalizing prospect is one of the major motivation behind the extensive future experimental GW program including planned Cosmic Microwave Background (CMB) experiments such as CMB-S4 [53] or proposed ground-based (e.g. the Einstein telescope [54–56] or the Cosmic Explorer [57]) and space-based (e.g. Taiji [58], TianQin [59], LISA [60] and DECIGO [61, 62] as well as their respective upgrades BBO [63–65] and u-DECIGO [66, 67]) interferometers.

More recently, the possibility of detecting so-called ultra-high-frequency, i.e. frequencies beyond the typical range of GW interferometers (above $\sim 10^4$ Hz), stochastic GWBs has been placed under intense scrutiny, see for instance the recent reviews [68, 69] and references therein for specific examples of proposed searches. While challenging, these searches present the major advantage that the known astrophysical sources of GWBs are not small or dense enough to produce GWs at such high frequencies [68]. Hence, any detection of GWs

[1] Simple estimates [45] place the GW decoupling temperature at the Planck scale.

in this regime would strongly point towards the presence of either exotic astrophysical objects, e.g. primordial black holes or boson stars (see e.g. [70] for additional examples), or of a cosmological GWB. However, even in absence of astrophysical backgrounds, there exist many different cosmological phenomena that can generate sizeable GWBs and it is therefore essential to accurately predict the expected signals for all these mechanisms in order to take full advantage of the discovery potential of the numerous (current and planned) GW experiments. Among the most promising examples of such cosmological sources are for example first-order phase transitions, topological defects or inflation and (p)reheating, see e.g. [52, 71, 72] for reviews on these mechanisms.

All of the aforementioned mechanisms rely on the existence of physics beyond the SM. This is however not necessary. Similarly to a black-body, any viscous plasma, even if in perfect thermodynamic equilibrium, will continuously emit GWs due to the constant interactions between its constituent particles [73–75]. At high frequencies $f \sim \mathcal{O}(10^{11})$ Hz, the production is dominated by microscopic particle collisions while, at lower frequencies, long-range hydrodynamic fluctuations dominate [73]. Generically, one expects the resulting GW background to be much weaker than that of the previously mentioned mechanisms as it does not rely on any deviation from equilibrium and the standard cosmology. However, it is for that precise reason much harder to avoid and practically serves as a cosmic GW floor. In the SM, large deviations from equilibrium are not expected [76] and thermal fluctuations are therefore anticipated to be the primary source of the resulting primordial GWB [73, 74]. Additionally, such background is typically sensitive to the largest temperature of the early universe plasma after inflation and can thus be constrained indirectly from measurements of the effective number of neutrinos ($N_{\rm eff}$) [74,75].[2]

While thermal GWBs have already been investigated in considerable detail within the context of the SM [73, 74, 78, 79], much less is known about their counterparts in generic SM extensions [75]. In particular, the GW production rate from long-range hydrodynamic fluctuations, which dominates in the low

[2]In practice, constraints from Planck on $N_{\rm eff}$ only limit the maximal temperature reached by the SM to be sub-Planckian [74, 75], though an order of magnitude improvement is expected from CMB-S4. These constraints remain nonetheless much weaker than the complementary limits derived by combining the measured amplitude of scalar perturbations and upper bound on the tensor-to-scalar ratio, which restricts the scale of inflation (and therefore the reheating temperature) to be smaller than $\mathcal{O}(10^{16})$ GeV [77] for single-field slow-roll inflationary models. This leads to an upper limit on the reheating temperature $T_{\rm max} \lesssim 6.6 \times 10^{15}$ GeV, assuming a number of degrees of freedom comparable to that of the SM.

frequency tail of the spectrum, is given by the shear viscosity $\eta$ of the early universe plasma. Since the latter generically scales as the mean free path of the most weakly interacting particle in this plasma [73, 80–82], it is expected that this type of GWB can be strongly enhanced in presence of feebly interacting particles. The existence of such feebly interacting particles naturally arises as a solution to the different shortcomings of the SM, such as the origin of Dark Matter and neutrino masses, and is currently under intense experimental scrutiny [83, 84]. Despite their feeble interactions, these particles can nonetheless be abundantly produced in the early universe, either thermally or through non-thermal processes such as (p)reheating or heavy particle decays. Out of equilibrium, a similar enhancement of the GWBs due to the approximate free streaming of feebly interacting particles has been noticed in the context of strong first-order phase-transitions in [85]. Moreover, we note that GW production from hydrodynamic fluctuations has also been studied in the context of axion-like warm inflation in [86, 87] and for a weakly coupled scalar field in [88].

In this part of the thesis, we examine the contribution to the stochastic GWB from a generic plasma in thermal equilibrium during radiation domination. We begin in Sec. 2.1 by reviewing how to model thermal GW backgrounds. Next, in Sec. 2.2, we compute the production rate associated with this type of GW emission, using the first principles of nonequilibrium QFT. From there, we derive general upper bounds on thermal GW spectra. In the next section, Sec. 2.4, we apply our results to two well-motivated benchmarks: right-handed neutrinos and axion-like particles. We then review our assumptions and discuss possible generalisations. Finally, we conclude in Sec. 2.6. The material presented in this part is based on [3] and closely follows its structure.

Chapter 2

# Cosmological Gravitational Wave Background from hidden sectors in thermal equilibrium

## 2.1 Gravitational wave production in an FLRW universe

The early instants of our universe are in good approximation described by the spatially flat, homogeneous and isotropic FLRW metric

$$\mathrm{d}s^2 = \mathrm{d}t^2 - a(t)^2 \delta_{ij} \mathrm{d}x^i \mathrm{d}x^j, \tag{2.1}$$

where $\delta_{ij}$ is the standard 3-dimensional Kronecker delta and $a(t)$ represents the scale factor describing the expansion of our universe. GWs are tensor perturbations $h_{\mu\nu}$ to this FLRW background and, in the traceless-transverse (TT) gauge, verify the properties

$$h^i_i = h^{0\mu} = \partial^i h_{ij} = 0, \tag{2.2}$$

thereby modifying the metric in the following way

$$\mathrm{d}s^2 = \mathrm{d}t^2 - a(t)^2 (\delta_{ij} + h_{ij}) \mathrm{d}x^i \mathrm{d}x^j \ . \tag{2.3}$$

Linearly perturbing the spatial part of the Einstein field equations, one then obtains the well-known evolution equation for GWs

$$\ddot{h}_{ij} + 3H\dot{h}_{ij} - \frac{\boldsymbol{\nabla}^2 h_{ij}}{a^2} = \frac{16\pi\, T^{TT}_{ij}}{a^2 m^2_{\mathrm{Pl}}}. \tag{2.4}$$

In the above equation, $m_{\mathrm{Pl}} \approx 1.22 \times 10^{19}$ GeV is the Planck mass, $H \equiv \dot{a}/a \equiv (\mathrm{d}a/\mathrm{d}t)/a$ is the Hubble rate whereas $T^{TT}_{ij}$ represents the traceless-transverse contribution to the stress-energy tensor of GR

$$T_{\mu\nu} = -\frac{2}{\sqrt{-g}}\frac{\delta S}{\delta g^{\mu\nu}}, \tag{2.5}$$

with $S$ the action and $g = \det(g^{\mu\nu})$. For superhorizon (physical) modes $k$, i.e. modes for which $|\boldsymbol{k}| \ll H$, solutions to Eq. (2.4) are static and tensor perturbations are frozen [89]. In this regime, GWs cannot be produced. Hence, we will focus in the following on subhorizon scales, i.e. $|\boldsymbol{k}| \gg H$. Note that the physical mode $k$ redshifts over time and can be related to the observed GW frequency $f$ through the following relation $2\pi f a_0/a = |\boldsymbol{k}|$, where $a_0$ is the current value of the scale factor. Though experiments are directly sensitive to $h$, a useful quantity to characterise cosmological GW backgrounds is the total energy density carried by the GWs, defined as

$$\rho_{\text{GW}} \equiv \frac{m_{\text{Pl}}^2}{32\pi}\left\langle \dot{h}^{ij}(t,\mathbf{0})\dot{h}_{ij}(t,\mathbf{0})\right\rangle . \tag{2.6}$$

As defined in Eq. (1.2), $\langle \mathcal{O}\rangle \equiv \text{Tr}\left\{\hat{\rho}_{\text{bath}}\, \mathcal{O}\right\}$ denotes the thermal average on the early universe degrees of freedom, with the density matrix $\hat{\rho}_{\text{bath}}$ encoding all the information about the state of the early universe plasma, its temperature in particular. It can then be shown [73] that, for subhorizon modes, $\rho_{\text{GW}}$ evolves according to the equation of motion

$$\frac{\mathrm{d}\dot{\rho}_{\text{GW}}}{\mathrm{d}\ln f} + 4H\frac{\mathrm{d}\rho_{\text{GW}}}{\mathrm{d}\ln f} = 16\pi^2\left(\frac{f a_0}{a}\right)^3 \frac{\Pi(2\pi f a_0/a)}{m_{\text{Pl}}^2} \tag{2.7}$$

where the GW production rate can be extracted from the 2-point correlation function of the stress-energy tensor

$$\Pi(k) = \frac{1}{2}\int \mathrm{d}t\, \mathrm{d}^3\boldsymbol{x}\; e^{i(kt-\boldsymbol{k}\cdot\boldsymbol{x})}\; \mathbb{L}^{ij;kl}\left\langle\{T_{ij}(t,\boldsymbol{x}), T_{kl}(0,\mathbf{0})\}\right\rangle . \tag{2.8}$$

In the above equation, we write $\boldsymbol{k}\cdot\boldsymbol{x} = \delta_{ij}k^i x^j$ and $\boldsymbol{k}^2 = \delta_{ij}k^i k^j$ for the spatial scalar products. The spatial projector $\mathbb{L}_{ij;kl}$ selects the (physical) traceless-transverse components of the tensor perturbations $h_{\mu\nu}$. It reads

$$\mathbb{L}_{ij;kl} = \frac{1}{2}\left(\mathbb{L}_{ik}\mathbb{L}_{jl} + \mathbb{L}_{il}\mathbb{L}_{jk} - \mathbb{L}_{ij}\mathbb{L}_{kl}\right)\,, \qquad \mathbb{L}_{ij} = \delta_{ij} - \frac{k_i k_j}{\boldsymbol{k}^2}. \tag{2.9}$$

### 2.1.1 Connection to the hydrodynamic description

As seen from Eq. (2.5), the stress-energy tensor should in general be extracted directly from the action of GR and depends on all fields in the theory. However, at frequencies $f \ll 10^{11}$ Hz, the graviton momentum is much smaller than the temperature. These frequencies therefore mostly probe the large-scale properties of the system. Assuming the early universe to be close to local thermal equilibrium such as is the case during radiation domination, the stress-energy tensor can be expanded around its perfect fluid ansatz

$$\begin{aligned} T_{00} = \rho \, , \quad T_{0i} = (\rho + P) v_i \, , \\ T_{ij} = \left[P - \zeta(\boldsymbol{\nabla}\cdot\boldsymbol{v})\right]\delta_{ij} - \eta\left[\partial_i v_j + \partial_j v_i - \frac{2}{3}\delta_{ij}(\boldsymbol{\nabla}\cdot\boldsymbol{v})\right] \, , \end{aligned} \tag{2.10}$$

where $\rho$ and $P$ are the local energy and pressure density, $v^i$ the fluid three-velocity and $\zeta$ and $\eta$ the bulk and shear viscosity respectively. We omitted in the above equation higher order terms $\mathcal{O}(v^2)$ and consider the fluid velocity to be small enough. From Eq. (2.10), it is relatively straightforward to show that the traceless component of the stress-energy tensor is directly proportional to the shear viscosity only. To be more specific, one can show [73], see also [90, 91], that the GW production rate $\Pi$ obey the Kubo formula [92, 93]

$$\lim_{|\boldsymbol{k}|\to 0} \Pi = 8T\eta \, . \tag{2.11}$$

The above formula can also be seen as a manifestation of the more well-known fluctuation-dissipation theorem [94, 95].

As already mentioned in the introduction, the shear viscosity is a macroscopic property of the plasma and has been shown to scale as the mean free path $l_{\rm av}$ of its most feebly interacting constituent (of velocity $v_{\rm av}$ and width $\Upsilon$) for many different systems, see e.g. [80–82, 96–99],

$$\eta \sim l_{\rm av} v_{\rm av} T^4 \sim \frac{T^4}{\Upsilon} \, . \tag{2.12}$$

The particle's width $\Upsilon$ is connected to its interaction rates, and therefore to its mean free path, via the optical theorem. While this result might seem surprising at first, it can be understood in a relatively simple way. The shear viscosity quantifies the resistance of a fluid to shear deformation. In particular, if the mean free path of its constituent is large enough, momenta can easily be transported over long distances before being redistributed by collisions. Hence, it will be able to efficiently counteract the application of an external shear force, leading to a larger viscosity. Combining Eqs. (2.11) and (2.12), we find that particles with feeble interactions tend to dominate GW production in the regime of soft graviton momenta. For this reason, high-frequency GWs are potentially promising probes of hidden sectors.

Before moving on, we would like to point out that, taken at face value, Eq. (2.12) seems to imply that the GW production rate diverges in the limit where the hidden sector completely decouples. However, as we will show later, this naive scaling only holds in the limit $|\boldsymbol{k}| \ll \Upsilon$, corresponding to the so-called *hydrodynamic regime*. In the opposite limit of hard momenta $|\boldsymbol{k}| \gg \Upsilon$, the so-called *Boltzmann regime*, one recovers the typical scaling $\Pi \sim \Upsilon$, with no enhancement for feebly interacting particles. This distinction will turn out to be a defining feature of GW spectra from thermal fluctuations as we will see later. It also clearly defines the regime in which feebly interacting particles are expected to enhance the SM signal.

### 2.1.2 Present day spectrum

Ultimately, we are interested in the present-day GW spectrum, typically parametrised by the quantity

$$h^2\Omega_{\rm GW}(f) \equiv \frac{h^2}{\rho_{\rm crit}}\frac{{\rm d}\rho_{\rm GW}}{{\rm d}\ln f}\,, \tag{2.13}$$

where $\rho_{\rm crit}$ is the critical energy density at the present epoch while $h$ is the reduced Hubble constant, respectively defined as

$$\rho_{\rm crit} = \frac{3H_0^2 m_{\rm Pl}^2}{8\pi}\,, \qquad\qquad h = \frac{H_0}{100\ {\rm km\,s^{-1}Mpc^{-1}}}. \tag{2.14}$$

Alternatively, sensitivity to various GWB are sometimes also expressed in terms of the so-called characteristic strain $h_c$, defined through the relation

$$h_c^2 = \frac{3H_0^2}{2\pi^2 f^2}\Omega_{\rm GW} \propto \frac{h^2\Omega_{\rm GW}}{f^2}\,. \tag{2.15}$$

The latter is more directly related to the displacement observed in interferometers. In this paper, we will show results for both quantities.

In order to solve Eq. (2.7) and obtain $h^2\Omega_{\rm GW}(f)$, we need to specify the expansion history considered. As a first approximation, we will assume that the early universe is constituted of the SM, which dominates the energy density and is in thermal equilibrium with a temperature $T$, as well as a hidden sector made out of one single feebly interacting particle. Furthermore, we will assume that one can safely neglect any transfer of entropy between the two sectors, i.e. $\partial_t(a^3 s) = \partial_t(a^3 s_h) = 0$ with $s$ ($s_h$) being the SM (hidden sector) entropy density. In this case, the standard expansion history takes place and we have

$$\frac{\mathrm{d}T}{\mathrm{d}t} = -\frac{g_s}{g_c}\frac{T^3}{m_0}\,, \qquad\qquad \frac{aT}{a_0 T_0} = \left[\frac{g_s(T_0)}{g_s(T)}\right]^{1/3}. \tag{2.16}$$

$T_0 = 2.7255(6)$ K [100], corresponding to the frequency $f_0 = 3.5682(7) \times 10^{11}$ Hz, denotes the current temperature of the CMB. In the above equation, we have defined the effective number of degrees of freedom as measured by the SM entropy density $s$, energy density $\rho$ and heat capacity $c$

$$g_s(T) = \frac{s(T)}{2\pi^2 T^3/45},\quad g_\rho(T) = \frac{\rho(T)}{\pi^2 T^4/30},\quad g_c(T) = \frac{c(T)}{2\pi^2 T^3/15} \tag{2.17}$$

as well as

$$m_0 \equiv m_{\mathrm{Pl}} \left[\frac{4\pi^3 g_\rho}{45}\right]^{-1/2}. \tag{2.18}$$

Plugging Eqs. (2.16), (2.17) and (2.18) into Eq. (2.7) and integrating over time, we obtain the following result

$$h^2\Omega_{\mathrm{GW}}(f) = \frac{2880\sqrt{5\pi}}{\pi^2} h^2\Omega_\gamma \frac{f^3}{T_0^3}\int_{T_{\min}}^{T_{\max}} \frac{\mathrm{d}T'}{m_{\mathrm{Pl}}} \frac{g_c(T')\,[g_s(T_0)]^{1/3}}{[g_\rho(T')]^{1/2}\,[g_s(T')]^{4/3}} \frac{\Pi\,(2\pi f a_0/a')}{8T'^4}. \tag{2.19}$$

$T_{\min}$ ($T_{\max}$) represents the minimal (maximal) temperature at which the plasma under consideration was in equilibrium. In the SM, $T_{\max}$ may, but does not necessarily, correspond to the reheating temperature of our universe. If the reheating epoch was not instantaneous, the SM plasma likely reached equilibrium even earlier, at even larger temperatures [101].[3] Assuming further that the relevant dynamics happen well above the electroweak symmetry breaking (EWSB) (but still during radiation domination, below the reheating tempera-

[3] This statement also depends on the time required for the early universe's bath to thermalise, which may not necessarily be a rapid process [102].

ture) such that $g_c = g_s = g_\rho = 106.75$ at all times and given that [103, 104]

$$h^2\Omega_\gamma = 2.4728(21) \times 10^{-5} \,, \qquad g_s(T_0) = 3.931(4) \,, \tag{2.20}$$

we can further simplify Eq. (2.19) to obtain

$$h^2\Omega_{\text{GW}}(f) \approx 2.02 \times 10^{-38} \times \left(\frac{f}{\text{Hz}}\right)^3 \times \int_{T_{\text{min}}}^{T_{\text{max}}} \frac{\text{d}T'}{m_{\text{Pl}}} \frac{\Pi\,(2\pi f a_0/a')}{8T'^4} \,. \tag{2.21}$$

In case the production rate $\Pi$ as well as the integration bounds $T_{\text{max}}$ and $T_{\text{min}}$ are both independent of the frequency, the emitted GW spectrum features the characteristic $\propto f^3$ frequency shape associated with backgrounds from hydrodynamic fluctuations. Such behaviour was also observed within the context of e.g. GWs from post-inflationary phases stiffer than radiation [105] or axion-like inflation [87]. In the context of the SM, the rate $\Pi$ is well known and is dominated for frequencies $f < \mathcal{O}(10^9)$ Hz by the hydrodynamic fluctuations of the right-handed leptons[4] [73, 97, 99]

$$\Pi^{\text{SM}} = 8\eta_{\text{SM}} T \approx \frac{16T^4}{g^4 \ln(\frac{5T}{m_D})} \approx 400T^4 \,, \qquad m_D^2 = \frac{11}{6} g^2 T^2 \,, \tag{2.22}$$

where $g \approx 0.36$ is the $\text{U}(1)$ hypercharge gauge coupling, $m_D$ the associated Debye mass, and $g_{\text{SM}} = 6$ the relativistic degrees of freedom associated with the right-handed leptons. Plugging this result in Eq. (2.21) and neglecting the potential running of $g$, we obtain

$$h^2\Omega_{\text{GW}}^{\text{SM}}(f) \simeq 1.03 \times 10^{-36} \times \left(\frac{f}{\text{Hz}}\right)^3 \times \frac{T_{\text{max}}}{m_{\text{Pl}}} \,, \tag{2.23}$$

which depends only on $T_{\text{max}}$. As we will see later, different modes cross the Hubble horizon at different times, so $T_{\text{max}}$ is not a constant and introduces an additional dependence on the frequency.

In presence of significant entropy transfer between the hidden sector and the SM or if the SM do not dominate the total energy density of the universe, Eq. (2.21) no longer holds, and it becomes necessary to compute the full time evolution of the SM temperature $T$ and the Hubble rate $H$. As shown in appendix D of [3], if $T$ and $H$ are known monotonous functions of the scale-

[4] As will be shown in Sec. 2.2, in this regime, the hydrodynamic fluctuations from the most weakly interacting particle, right-handed leptons in the case of the SM, dominate the GW production rate.

factor, one can rewrite (2.21) as

$$h^2\Omega_{\rm GW}(f) \approx 2.02\times 10^{-38} \times \left(\frac{f}{\rm Hz}\right)^3 \times \qquad (2.24)$$
$$\times \int_{T_{\rm min}}^{T_{\rm max}} \frac{{\rm d}T'}{m_{\rm Pl}} \frac{\Pi(2\pi f a_0/a)}{8T'^4} \left|\frac{{\rm d}\ln a}{{\rm d}\ln T'}\right| \left(\frac{T'}{\overline{T}'}\right) \left(\frac{\rho_{\rm SM}}{\rho_{\rm tot}}\right)^{\frac{1}{2}},$$

where $\overline{T}$ is what the SM temperature would have been in the absence of entropy transfer, i.e.

$$\overline{T} \equiv \frac{a_0 T_0}{a} \left[\frac{g_s^{\rm SM}(T_0)}{g_s^{\rm SM}(\overline{T})}\right]^{1/3} \qquad (2.25)$$

The term $\left(\frac{\rho_{\rm SM}}{\rho_{\rm tot}}\right)^{\frac{1}{2}}$ accounts for the modification of the Hubble rate from BSM contributions to the total energy density whereas the extra factor $\left|\frac{{\rm d}\ln a}{{\rm d}\ln T'}\right| \left(\frac{T'}{\overline{T}'}\right)$ allows to account for expansion history beyond radiation domination, e.g. early matter domination or reheating.

Finally, we emphasise that Eq. (2.24) makes little assumption about the hidden sector. In particular, it remains valid even if the hidden sector is far from equilibrium. The practical computation of the rate $\Pi$ can however reveal difficult for arbitrary distribution function of the hidden sector. In the rest of this chapter and in particular in Sec. 2.3.2 and 2.4, we will assume the hidden sector to be in thermal equilibrium with the same temperature as the SM. The latter assumption will in general maximise the emitted GWB. Indeed, GWBs from thermalised plasma generically scale with their temperature, see e.g. Eq. (2.23), and observational constraints from e.g. Big Bang Nucleosynthesis (BBN) typically force these hidden sectors to be colder than the SM plasma at late times [106, 107]. Given our focus in this work on feebly interacting particles for which thermalisation is expected to be much slower than for the SM, this assumption might seem overoptimistic. However, feebly interacting hidden sectors can still reach equilibrium early on through ultraviolet (UV) freeze-in in presence non-renormalisable interactions, see e.g. [108], or through non-thermal processes, e.g. via (p)reheating [109, 110] or the decay of heavy new particles, thereby evading this constraint. Moreover, we will focus on the enhancement of the GW spectrum from one feebly interacting particle, for which the simplified Eq. (2.21) is perfectly adequate. In presence of composite hidden sectors, our results can straightforwardly be generalised

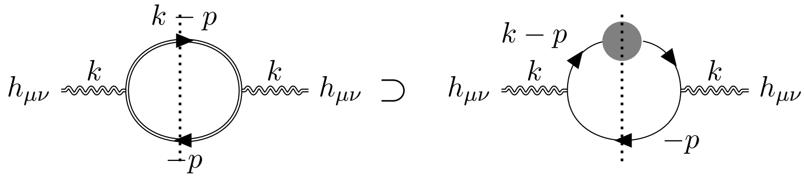


**Figure 2.1:** Feynman diagram representation of the graviton self-energy. The straight double lines represent 1PI-resummed fermionic propagators, which includes an infinite class of diagrams in fixed-order perturbation theory. One such diagram is depicted on the right-hand side, with the grey blob denoting a single self-energy insertion. The dotted lines signal cut propagators, i.e. propagators of the type $+-$ or $-+$. Figure slightly adapted from [3].

(in the enhanced hydrodynamic regime) by summing the contributions of each particle as long as the total energy density remains dominated by the SM.

## 2.2 Computing the graviton production rate

In order to compute the GWB, the main ingredient needed is the production rate (2.8). Its computation for a generic feebly interacting fermion within the CTP formalism is the primary objective of this section. We also show how our results can be readily generalised to different spins using the results of [86,88].

### 2.2.1 GW production rate from fermions

Working within a particle physics framework, the GW production rate can generally be extracted from the graviton self-energy displayed in Fig. 2.1, where the graviton couples to the rest of the plasma through the Lagrangian

$$\mathcal{L} \supset \frac{1}{2}\frac{\sqrt{8\pi}}{m_{\rm Pl}} h_{\mu\nu} T^{\mu\nu}. \tag{2.26}$$

Although we compute graviton self-energies, we nonetheless stress that our computation remains purely at the semi-classical level and does not make any assumption about the quantisation of gravity.

We note that the self-energy 2.1 does not include "vertex-like" contributions, which are shown for illustration in Fig. 2.2. However, these contributions do not exhibit the same enhancement for feebly interacting particles and can therefore be safely neglected in the hydrodynamic regime. In this regime, the GW production rate is dominated by the kinetic contribution to the stress-

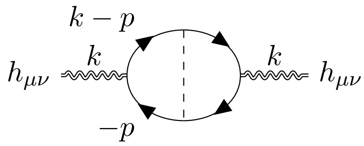


**Figure 2.2:** Illustration of a vertex-type correction to the GW production rate from fermions. Figure taken from [3].

energy tensor

$$T_{ij}(x) \supset \frac{c_X}{4}\overline{\psi}_x i\overleftrightarrow{\partial}_{ij}\psi_x \,, \qquad\qquad i\overleftrightarrow{\partial}_{ij} = \gamma_i i\partial_j + \gamma_j i\partial_i \,, \tag{2.27}$$

where $\psi_x = \psi(x)$ can represent a Dirac or Majorana spinor, evaluated at $x = (t, \boldsymbol{x})$. The coefficient $c_X$ distinguishes Dirac ($c_D = 2$) from Majorana ($c_M = 1$) spinors. For a Dirac fermion, the self-energy displayed in diagram 2.1 can be related to the correlator (2.8) in the following way

$$\begin{aligned}
&\left(\frac{4}{c_D}\right)^2 \langle\{T_{ij}(x), T_{kl}(y)\}\rangle \\
&\qquad = \langle T_C \left\{\overline{\psi}{}^-_x (i\overleftrightarrow{\partial}_{ij}\psi^-_x)\overline{\psi}{}^+_y (i\overleftrightarrow{\partial}_{kl}\psi^+_y) + \overline{\psi}{}^+_x (i\overleftrightarrow{\partial}_{ij}\psi^+_x)\overline{\psi}{}^-_y (i\overleftrightarrow{\partial}_{kl}\psi^-_y)\right\}\rangle \\
&\qquad = -\operatorname{Tr}[(i\overleftrightarrow{\partial}_{ij} iS^>_{xy})(i\overleftrightarrow{\partial}_{kl} iS^<_{yx}) + (\gtrless\leftrightarrow\lessgtr)].
\end{aligned} \tag{2.28}$$

Hence, the production rate $\Pi$ can be written (in momentum space)

$$\Pi(k) = -\frac{c_D^2}{8}\int\frac{\mathrm{d}^3\boldsymbol{p}}{(2\pi)^3}\int\frac{\mathrm{d}p_0}{2\pi}\,\mathbb{L}^{ij;kl}p_i p_k \operatorname{Tr}[\gamma_j iS^>_p \gamma_l iS^<_{p-k} + \gamma_j iS^<_p \gamma_l iS^>_{p-k}]. \tag{2.29}$$

In the case where $\psi$ is a Majorana fermion instead, one should replace $c_D \to c_M = 1$, but the additional possible field contractions result in a further overall prefactor of 2. Using the equivalent of the Kadanoff-Baym ansatz (1.27) for fermions

$$iS^<_p = -2n(p_0)\, S^{\mathcal{A}}_p \,, \qquad\qquad iS^>_p = 2\,(1-n(p_0))\, S^{\mathcal{A}}_p \,, \tag{2.30}$$

we can further simplify the expression (2.29) to

$$\Pi(k) = c_X\int\frac{\mathrm{d}^3\boldsymbol{p}}{(2\pi)^3}\int\frac{\mathrm{d}p_0}{2\pi}\,\mathbb{L}^{ij;kl}p_i p_k \operatorname{Tr}[\gamma_j S^{\mathcal{A}}_{p^+}\gamma_l S^{\mathcal{A}}_{p^-}]\cdot D(p_0^+, p_0^-). \tag{2.31}$$

The function $D(p_0^+, p_0^-)$ encapsulates all the dependence on the (potentially out-of-equilibrium) particle number densities $n(p_0^\pm)$

$$D(p_0^+, p_0^-) = (1 - n(p_0^+))n(p_0^-) + n(p_0^+)(1 - n(p_0^-)) , \tag{2.32}$$

whereas the momenta $p_\mu^\pm = p_\mu \pm k_\mu/2$ are a linear combination of the loop and graviton momenta. As detailed in the introduction, the Kadanoff-Baym ansatz is exact in perfect thermodynamic equilibrium, which is the focus of this chapter. Since it also holds for a broad range of nonequilibrium situations, see footnote 7, in which the quasiparticle picture is valid, Eq. (2.31) could be used as a starting point for future exploration of nonequilibrium systems.

One can easily check using the tree-level thermal propagators (1.49) that Eq. (2.31) vanishes for any $k_0 \neq 0$ and diverges for $k_0 = |\mathbf{k}| = 0$. This is intuitive since, at tree level, Eq. (2.31) essentially captures the rate of graviton bremsstrahlung. Any process of the form $\psi \to \psi + g$, where $g$ is the graviton, is kinematically forbidden for non-zero $k_0$. For $k_0 = 0$ on the other hand, the divergence is related to the mean free path of $\psi$, which is infinite in the absence of interactions. This divergence is regulated by the width of the spectral function $S^{\mathcal{A}}$, hence the need for resummation. One can show, see appendix A.1 for details, that the 1PI-resummed spectral function for a Dirac fermion of mass $m$ takes, at leading order in the coupling, the general form

$$S_p^{\mathcal{A}} = \left(\not{p} + m\right) \frac{\Gamma_p}{\Omega_p^2 + \Gamma_p^2} , \tag{2.33}$$

where we define

$$\Omega_p = p^2 - m^2 , \qquad \Gamma_p \equiv \Gamma(p) = \frac{1}{2} \operatorname{Tr}\left[(\not{p} + m)\Sigma_p^{\mathcal{A}}\right] . \tag{2.34}$$

$\Sigma_p^{\mathcal{A}}$ denotes the anti-hermitian self-energy of $\psi$. As is well known, see e.g. [111], the physical width $\Upsilon_p$ of $\psi$ can be extracted from the on-shell limit of $\Gamma_p$

$$2E_p\Upsilon_p = \lim_{p_0 \to E_p} \Gamma_p , \qquad E_p^2 = \boldsymbol{p}^2 + m^2 . \tag{2.35}$$

Inserting Eq. (2.33) into Eq. (2.31) and defining the transverse momentum $\mathbf{p}_\perp^2 \equiv \mathbb{L}_{ij} p^i p^j$, we find

$$\mathbb{L}^{ij;kl} p_i p_k \, \mathrm{Tr}[\gamma_j S^{\mathcal{A}}_{p^+} \gamma_l S^{\mathcal{A}}_{p^-}] = \frac{4\mathbf{p}_\perp^2 (p_0^+ p_0^- - \boldsymbol{p}_+ \cdot \boldsymbol{p}_- - m^2 + \mathbf{p}_\perp^2) \Gamma_{p^+} \Gamma_{p^-}}{[\Omega^2_{p^+} + \Gamma^2_{p^+}]\,[\Omega^2_{p^-} + \Gamma^2_{p^-}]} \, . \tag{2.36}$$

From the above equation, one can observe that the integrand in Eq. (2.31) features two distinct types of poles:

1. poles associated with the product of distribution functions $D(p_0^+, p_0^-)$, as well as
2. poles associated with the fermionic spectral functions in Eq. (2.36).

In addition, the various spectral functions also feature branch cuts and associated multiparticle continuum contributions. In the limit where the width parameter is small $\Gamma_p \ll \Omega_p$, one can however show that the contribution from the poles dominates over the latter, see e.g. figures 10 and 11 in [112]. Such approximation is typically verified for weakly coupled theories and is related to the common Breit-Wigner approximation [111]. Moreover, given that we are primarily interested in the following by the contribution enhanced as $1/\Upsilon$, we will neglect the poles arising from the distribution functions. Even though these two assumptions can in principle be violated, e.g. for far-from-equilibrium situations where the phase space distribution functions exhibit strong peaks, we nonetheless expect these to remain safe in thermodynamic equilibrium as well as for a broad range of nonequilibrium settings. Then, we can derive from the residue theorem that the enhanced contributions to the GW production rate are generated by the poles located at

$$p_0 \to E_{s,t} = -\frac{sk_0}{2} + t\left[\boldsymbol{p}_s^2 + m^2 + \{it\Gamma_{p^s}\}_{p_0 \to E_{s,t}}\right]^{\frac{1}{2}} \, , \tag{2.37}$$

where $s, t = \pm 1$. In Eq. (2.37), only the four (out of eight possible) poles with positive imaginary part contribute as we choose to close the integration contour along the upper half of the complex plane. Defining $\Gamma'_p \equiv \partial_{p_0} \Gamma_p$ and using the relation $\Omega_{p_-} = \Omega_{p_+} - 2k^\mu p_\mu$, the associated residues write

$$\begin{aligned} &\operatorname*{Res}_{p_0 \to E_{s,t}} \left( \frac{\Gamma_{p^+} \Gamma_{p^-}}{[\Omega^2_{p^+} + \Gamma^2_{p^+}]\,[\Omega^2_{p^-} + \Gamma^2_{p^-}]} \right) \\ &\quad = \lim_{p_0 \to E_{s,t}} \frac{\Gamma_{p^{-s}}}{2i(2E_{s,t} + sk_0 - i\Gamma'_{p^s})\,[(2sk^\mu p_\mu - it\Gamma_{p^s})^2 + \Gamma^2_{p^{-s}}]} , \end{aligned} \tag{2.38}$$

Given that we focus on the soft regime for which $k_0 = |\boldsymbol{k}| \equiv k \ll p \sim \mathcal{O}(T)$ as well as on feebly interacting particles for which $\Gamma_p \ll \Omega_p$, we can separately expand both the numerator and denominator to leading order in these parameters

$$\Gamma_{p^s} \approx \Gamma_{p^{-s}} \approx \Gamma_p \ , \quad E_{s,t} \approx tE_p + i\Upsilon_p - sk\frac{(E_p - tp_{\parallel})}{2E_p} \ , \quad k^\mu p_\mu \approx k(tE_p - p_{\parallel}) \ , \tag{2.39}$$

where $p_{\parallel} = \frac{\boldsymbol{k}\cdot\boldsymbol{p}}{k}$. Hence, Eq. (2.38) simplifies to

$$\begin{aligned}\operatorname*{Res}_{p_0 \to E_{s,t}} \left( \frac{\Gamma_{p^+}\Gamma_{p^-}}{[\Omega^2_{p^+} + \Gamma^2_{p^+}]\,[\Omega^2_{p^-} + \Gamma^2_{p^-}]} \right) &\approx \frac{1}{8i}\frac{\Upsilon_p}{[sk(tE_p - p_{\parallel}) - itE_p\Upsilon_p]^2 + E_p^2\Upsilon_p^2} \\ &\approx \frac{1}{8i}\frac{\Upsilon_p}{k^2(tE_p - p_{\parallel})^2 - 2istk(tE_p - p_{\parallel})E_p\Upsilon_p} \ .\end{aligned} \tag{2.40}$$

Finally, we sum over the residues and set the graviton momentum to zero $k \to 0$ as well as $E_{s,t} \to tE_p$ in the remainder of the integrand in Eq. (2.31). In this limit, we have $p_0^+ p_0^- - \boldsymbol{p}_+ \cdot \boldsymbol{p}_- - m^2 \approx p^2 - m^2 = 0$. Using the invariance of $\Upsilon_p$ under $\mathbf{p} \to -\mathbf{p}$, we then obtain the general result

$$\Pi(k) \simeq \frac{c_X}{2}\int \frac{\mathrm{d}^3\boldsymbol{p}}{(2\pi)^3}\mathbf{p}_\perp^4 \left[D(E_p, E_p) + D(-E_p, -E_p)\right] \frac{2\Upsilon_p}{k^2(E_p - p_{\parallel})^2 + 4E_p^2\Upsilon_p^2} \ . \tag{2.41}$$

In thermal equilibrium, one has $D(E_p, E_p) = D(-E_p, -E_p) = 2f_{\mathrm{F}}(E_p)\times$ $\times\,(1 - f_{\mathrm{F}}(E_p))$ and the above result reduces to

$$\Pi(k) \simeq 2c_X \int_0^\infty \mathrm{d}p\, p^6 \frac{4\, f_{\mathrm{F}}(E_p)\,(1 - f_{\mathrm{F}}(E_p))}{15\pi^2 E_p^2}\frac{1}{2\Upsilon_p}F\left(\frac{k}{2\Upsilon_p}, \frac{p}{E_p}\right) . \tag{2.42}$$

The function $F$ in this equation asymptotically behaves as[5]

$$F(x,v) = \begin{cases} \frac{1}{1+x^2} & v \ll 1 \\ 1 & v = 1 \wedge x \ll 1 \\ \frac{5}{2x^2} & v = 1 \wedge x \gg 1 \end{cases} . \tag{2.44}$$

The hydrodynamic (enhanced) regime corresponds to the limit $x \ll 1$. We note that the result (2.42) is similar to what has already been found in the context of hydrodynamic fluctuations for a unique feebly interacting (pseudo-)scalar [86, 88]

$$\Pi(k) \simeq \int \mathrm{d}p\, p^6 \frac{4\, f_{\mathrm{B}}(E_p)\,(1+f_{\mathrm{B}}(E_p))}{15\pi^2 E_p^2} \frac{1}{2\Upsilon_p} F\left(\frac{k}{2\Upsilon_p}, \frac{p}{E_p}\right) . \tag{2.45}$$

We thus see that the production of GWs from both scalars and fermions can be captured by a single expression, as will be provided in the following subsection. For these reasons, we expect a formula similar to Eq. (2.45) (up to an overall prefactor accounting for the different number of degrees of freedom) to also hold for vector particles.

### 2.2.2 Approximate formulae for phenomenology

Though remarkably simple already, the production rates (2.42) and (2.45) nonetheless still depend on the full momentum-dependence of the hidden particle's width. One can further simplify these results by replacing the momentum-dependent width $\Upsilon_p$ by its thermal average, defined as

$$\Upsilon_{\mathrm{av}} \equiv \frac{1}{2\pi^2 N_{\mathrm{eq}}} \int_0^\infty \mathrm{d}p\, p^2 f_X(E_p)\Upsilon_p \,, \quad N_{\mathrm{eq}} = \frac{1}{2\pi^2} \int_0^\infty \mathrm{d}p\, p^2 f_X(E_p). \tag{2.46}$$

Depending on the hidden particle's spin, $f_X \in \{f_{\mathrm{B}}, f_{\mathrm{F}}\}$ represents either a Bose-Einstein or Fermi-Dirac distribution. The approximation (2.46) is justified as long as the width $\Upsilon_{\mathrm{p}}$ is dominated by the same region in momentum

[5]Beyond the asymptotic limit, the full expression for $F(x,v)$ is given by

$$F(x,v) = \frac{30(4x^2+5x^2(1-v^2)-3)}{48v^4x^4} + \frac{30x(1-x^2(1-v^2))}{16v^5x^5} \ln\frac{1+x^2(1+v)^2}{1+x^2(1-v)^2} + \frac{15(1-x^2(1-v^2))^2-60x^2}{16v^5x^5} \arctan\frac{2vx}{1+x^2(1-v^2)} . \tag{2.43}$$

space as the rest of the integrand $\left(p^6/E_p^2\right) f_X(E_p)\,(1 \pm f_X(E_p))$. This can fail e.g. if the hidden sector is significantly colder than the SM. To the unfamiliar reader, it might be useful to point out that the averaged width defined above can in general be related to the typical cross-sections used in DM studies. For instance, if the width is dominated by $2 \leftrightarrow 2$ scatterings of relativistic particles, it is directly connected to the standard thermally averaged scattering cross-section $\langle \sigma v_{\text{rel}} \rangle$ through the relation [45],

$$\Upsilon_{\text{av}} \propto \langle \sigma v_{\text{rel}} \rangle\, N. \tag{2.47}$$

Here, $N$ denotes the number density of the scattering partner. In the case where the hidden particle also constitutes the DM, Eq. (2.47) provides a direct link between the DM abundance and the GW spectrum.

In the low temperature (non-relativistic) limit, $v \equiv \frac{p}{E_p} \to 0$ and, as highlighted in Eq. (2.43), one can approximate $F$ by the simpler momentum-independent expression

$$F(x,v) \overset{v\to 0}{=} \frac{1}{1+x^2}. \tag{2.48}$$

In the high-temperature regime, $v \to 1$ and the functional form of the function $F$ retains some dependence on the graviton momentum $k$. It can however be reasonably well approximated by interpolating the function between $x \ll 1$ and $x \gg 1$, leading to

$$F(x,v) \overset{v\to 1}{\approx} \frac{5}{5+2x^2}\,. \tag{2.49}$$

Estimating this approximation to be the worst around $x \approx 1$, one can check that it leads to an overestimation of the GW production rate by roughly $30\%$, i.e. $\frac{5/7}{F(1,1)} \approx \frac{0.71}{0.56} \approx 1.27$. This is comparable to other theoretical uncertainties and largely sufficient to obtain an order of magnitude estimate of the GWB as is the goal of the present work. Having made these approximations, we note that $\Upsilon_{\text{av}}$ and $F(x,v)$ are (by definition) independent of the fermion momentum $p$ in both non-relativistic and relativistic regimes and can safely be pulled out of the integrals in Eqs. (2.42) and(2.45). Doing this, we obtain

$$\Pi(k) \overset{m\ll T}{\simeq} g_X \frac{16\pi^2}{225} T^5 \frac{5\Upsilon_{\text{av}}}{k^2+10\Upsilon_{\text{av}}^2}\,, \quad g_X = \begin{cases} 1 & \text{Spin } 0 \\ 2\cdot c_X & \text{Spin } 1/2 \end{cases}\,, \tag{2.50}$$

for the relativistic case. We have further neglected a relative factor of $7/8$ in the fermionic case that originates from the integration over Fermi-Dirac (relative to Bose-Einstein) distribution functions.

The non-relativistic case can be treated in a similar manner with the subtlety that one needs to distinguish two different cases. Assuming that the particle did freeze-out while still relativistic, such as is the case for neutrinos, its distribution function is not Boltzmann suppressed $f_X(E_p) \approx f_{\mathrm{F}}(p)$ at all times (though $E_p \approx m$) and we have

$$\Pi(k) \overset{T \lesssim m \ll T_f}{\simeq} g_X \frac{64\pi^4}{315} \frac{T^7}{m^2} \frac{2\Upsilon_{\text{av}}}{k^2 + 4\Upsilon_{\text{av}}^2}. \tag{2.51}$$

In the above equation, we have now neglected a relative factor of $31/32$ between the fermionic case and bosonic case. Interestingly, this rate is independent of the freeze-out temperature $T_f$. If however the freeze-out happens after the particle became non-relativistic, its distribution function is Boltzmann suppressed and one obtains instead the expression

$$\Pi(k) \overset{T, T_f \lesssim m}{\simeq} g_X \left(\frac{2}{\pi}\right)^{3/2} \left[\frac{T^7}{m^2} \left(\frac{\xi m}{T}\right)^{7/2} e^{-\frac{\xi m}{T}}\right] \frac{2\Upsilon_{\text{av}}}{k^2 + 4\Upsilon_{\text{av}}^2}\,, \tag{2.52}$$

where

$$\xi = \begin{cases} 1 & T > T_f \\ T/T_f & T < T_f \end{cases} \tag{2.53}$$

highlights the explicit dependence on $T_f$. Particles that remains in equilibrium at all times and never freeze-out, e.g. unstable particles with a large width $\Upsilon_{\text{av}} > H$, can be captured by taking the limit $T_f \to 0$. Finally, we note that the rate for a relativistic distribution is always strictly larger than the one for a non-relativistic distribution since $\frac{T}{m} \ll 1$ in this regime, compare Eq. (2.50) with Eqs. (2.51) and (2.52). Hence, we can restrict ourselves to using the former to derive a model-independent upper bound on GW production, as we will see in the next section.

From Eqs. (2.50), (2.51) and (2.52), one can clearly identify the two different regimes discussed earlier. In the hydrodynamic regime, characterised by $k \ll \Upsilon_{\text{av}}$, the contribution from feebly interacting particles is enhanced with $1/\Upsilon_{\text{av}}$. On the other hand, in the Boltzmann regime $k \gg \Upsilon_{\text{av}}$, one recovers the naive scaling $\Pi \sim \Upsilon_{\text{av}}$ characteristic from a production from microphysical collisions in perturbation theory. The transition between these two regimes happens for $k = \sqrt{10}\Upsilon_{\rm av}$ if the particle is relativistic and for $k = 2\Upsilon_{\rm av}$ in the non-relativistic case. As we will see explicitly in the next sections, this typically defines a characteristic frequency at which one can observe a kink in the GW spectrum.

## 2.3 Formulae for phenomenological applications

Using the production rate obtained in the previous section, we now derive explicit formulae for the GW spectrum from hidden sectors in thermal equilibrium, suitable for phenomenological applications. We begin in Sec. 2.3.1 by outlining the main characteristic features of such GW spectra, before setting upper bounds on these spectra that apply to a broad class of scenarios.

### 2.3.1 Generic features of the GW spectrum

As made clear by Eq. (2.7), the GW production rate is directly proportional to $k^3\Pi(k)$. We are interested in the comparison between the SM and hidden sector contribution. In the hydrodynamic regime, the SM GWB is dominated by the contribution from right-handed leptons, see Eq. (2.22), whose width we shall write $\Upsilon_{\ell_{\rm R}}$. In the cases of interest, the hidden sector is much more feebly coupled than the SM and, hence, the GW production rate is dominated by the hidden sector contribution for small momenta $k \lesssim \Upsilon_{\rm av} \ll \Upsilon_{\ell_{\rm R}}$. The general scaling of these two contributions is then:

1. $k \lesssim \Upsilon_{\rm av} \ll \Upsilon_{\ell_{\rm R}}$: Assuming for illustration purposes[6] that both widths are momentum-independent, the SM and hidden sector contributions then both scale as $k^3$ in this regime, with the hidden sector GWB being enhanced by a factor $\Upsilon_{\ell_{\rm R}}/\Upsilon_{\rm av}$.

2. $\Upsilon_{\rm av} < k < \Upsilon_{\ell_{\rm R}}$: For larger momenta, the hidden sector leaves the hydrodynamic regime but not the SM. In this case, the resummation of the hidden particle propagator highlighted in Fig. 2.1 is no longer necessary. A Boltzmann-like picture of the hidden sector as a gas of (interacting) particles becomes more appropriate. In this regime, the new physics contribution scales linearly with the momentum $k$. However, since it is still dominated by hydrodynamics, the SM contribution continues to

[6]We emphasise that this approximation is not used in the remainder of this section and serves solely as an illustrative example for the expected scaling. In particular, the upper bounds derived later do not rely on this assumption.

grow like $k^3$ and eventually overtakes the hidden sector to dominate the overall production rate.

3. $\Upsilon_{\rm av} \ll \Upsilon_{\ell_R} < k$: Finally, at even larger momenta, both the SM and the hidden sector have entered the Boltzmann regime. The corresponding GW spectra then scale linearly with $k$ until they finally peak for momenta $k \sim \pi T$. Beyond this peak, the production rate is Boltzmann-suppressed and the GW spectrum is therefore effectively cut off. During radiation domination, the temperature and graviton momentum redshift in the same way. As a result, the GW spectrum peaks at the frequency

$$f_{\text{peak}} \equiv \frac{T_0}{2}\left[\frac{g_s(T_0)}{g_s(T)}\right]^{1/3} \approx 6 \times 10^{10}\ \text{Hz}. \tag{2.54}$$

Being the only scale, the CMB temperature $T_0$, defined below Eq. (2.16), fixes the position of the peak, which therefore do not depend on the exact composition of the hidden sector. For such high frequencies, the vertex-like contribution 2.2 cannot necessarily be neglected and typically contribute at the same order as their wavefunction equivalent 2.1.

In the following, we will primarily focus on the first two regimes where one can safely neglect vertex-like corrections.

**Hubble suppression:** As highlighted earlier, GW production can only take place for subhorizon modes $k \gtrsim H$. During radiation domination, $k \sim T$ whereas $H \sim T^2$. Hence, the production of GWs with frequency $f$ is delayed until the temperature of the plasma drops below the entry temperature[7]

$$T_{\text{entry}}(f) = m_0 \frac{\pi f}{f_{\text{peak}}}\,, \qquad\qquad H(T = T_{\text{entry}}) = k\,. \tag{2.55}$$

This constraint in general leads to a second visible kink in the GW spectrum. Writing $T_\star$ the temperature at which the plasma under consideration thermalises, the maximal temperature $T_{\max}$ entering Eq. (2.21) then depends on the hierarchy between $T_{\text{entry}}$ and $T_\star$. More precisely,

$$T_{\max} = \min\left(T_{\text{entry}}, T_\star\right) \equiv \frac{\min\left(f, f_\star\right)}{f_\star} T_\star \simeq \frac{f}{f + f_\star} T_\star\,, \tag{2.56}$$

[7] Note that, for $f \lesssim 4 \times 10^{-6}$ Hz, GWs can only be produced after the EWSB. Such frequencies however lie well below the high-frequency band of interest in this work.

where $f_\star$ is defined as the minimal frequency for which GW production is delayed (i.e. for which $T_{\text{entry}} < T_\star$)

$$f_\star = \frac{f_{\text{peak}}}{\pi}\frac{T_\star}{m_0} \approx 3 \times 10^{11}\ \text{Hz}\frac{T_\star}{m_{\text{Pl}}}\,, \qquad T_{\text{entry}}(f_\star) = T_\star\,. \tag{2.57}$$

Similarly, replacing $T_\star$ by $m$ and $f_\star$ by

$$f_{\text{nr}} = \frac{f_{\text{peak}}}{\pi}\frac{m}{m_0} \approx 3 \times 10^{11}\ \text{Hz}\frac{m}{m_{\text{Pl}}} \tag{2.58}$$

in Eq. (2.56) defines the condition under which GW production happens entirely in the non-relativistic regime, i.e. $T_{\text{entry}} < m$.

### 2.3.2 Model-independent upper bounds on cosmological GWBs

Although the production rates (2.50), (2.51) and (2.52) are generally strongly affected by the temperature dependence of the particle's width, these rates can nonetheless be maximised by setting

$$\Upsilon_{\text{av}} = \begin{cases} k/\sqrt{10} & \text{for } T > m \\ k/2 & \text{for } T < m \end{cases}. \tag{2.59}$$

Inserting these values into the relativistic and non-relativistic formulae (2.50) and (2.51), one obtains the two separate bounds

$$h^2\Omega_{\text{GW}}^{T>m}(f) \leq 2.6 \times 10^{-29} \times \left(\frac{f}{\text{Hz}}\right)^2 \times g_X \frac{\max(T_{\text{max}}, m) - \max(T_{\text{min}}, m)}{m_{\text{Pl}}}\,, \tag{2.60a}$$

$$h^2\Omega_{\text{GW}}^{T<m}(f) \leq 1.6 \times 10^{-28} \times \left(\frac{f}{\text{Hz}}\right)^2 \times g_X \frac{\min(T_{\text{max}}^3, m^3) - \min(T_{\text{min}}^3, m^3)}{m^2 m_{\text{Pl}}}\,, \tag{2.60b}$$

on respectively the high- and low-temperature contributions to the final GW energy density. One can then easily see that each contribution is separately maximised by setting $T_{\text{min}} \to 0$, which is equivalent to our assumption that the relevant dynamics happen well before the EWSB. Moreover, for a fixed value of $T_{\text{max}}$, we also observe that the sum of these two contributions is maximised for[8] $m \to T_{\text{max}}$. Subsequently replacing $T_{\text{max}}$ by its definition (2.56), we finally obtain the upper bound

$$h^2\Omega_{\text{GW}}(f) \leq 4.9 \times 10^{-40} \times g_X \left(\frac{f}{\text{Hz}}\right)^2 \min\left(\frac{f}{\text{Hz}}, \frac{f_\star}{\text{Hz}}\right) . \tag{2.61}$$

This last expression depends only on the number of internal degrees of freedom $g_X$ as well as the thermalisation temperature $T_\star$. One can further eliminate the dependence on the latter by trivially noticing that $\min(f, f_\star) \leq f$. This leads to the slightly weaker bound

$$h^2\Omega_{\text{GW}}(f) \leq 4.9 \times 10^{-40} \times g_X \left(\frac{f}{\text{Hz}}\right)^3 , \tag{2.62}$$

where $g_X$ remains now the only model-dependent parameter. At the qualitative level, one can easily understand the origin of this upper bound. For a fixed frequency, decreasing the hidden particle's width $\Upsilon_{\text{av}}$ leads to a stronger enhancement of the GWB. However, the range of enhanced modes also decreases with the width as more and more modes transition from the hydrodynamic to the (non-enhanced) Boltzmann regime.

We note in passing that, at low frequencies $f < f_{\text{nr}}$, $T_{\text{max}} < mf/f_{\text{nr}}$ $(< m)$ and the upper bound (2.62) tightens considerably

$$h^2\Omega_{\text{GW}}(f) \overset{f<f_{\text{nr}}}{\leq} 4.9 \times 10^{-40} \times g_X \left(\frac{f}{\text{Hz}}\right)^3 \frac{f^2}{f_{\text{nr}}^2} . \tag{2.63}$$

Finally, though very robust and model-independent, the upper bound (2.62) nonetheless relies on a number of assumptions such as the complete equilibration of the hidden sector or the absence of entropy transfer. We will review these assumptions in details in Sec. 2.5.

### 2.3.3 Analytic estimates of the high-temperature background

After deriving a model-independent upper bound on GWBs from thermal fluctuations, it remains to be studied how these GWBs change for various particle physics models. Assuming the width is dominated by the contribution of one single operator of dimension $d$ (and scale $\Lambda$) and neglecting the running of the coupling constants, it is expected to scale with the temperature in the

[8] We would like to emphasise that this does not imply that GW production is dominated by the low temperatures. For fixed $m$ and $T_{\text{max}} \gg m$, the relativistic contribution (2.60a) dominates over its non-relativistic counterpart (2.60b).

following way

$$\Upsilon_{\text{av}} \simeq y\, T \left(\frac{T}{\Lambda}\right)^{2(d-4)} \begin{cases} 1 & \text{for } T \gg m \\ (m/T)^n & \text{for } T \lesssim m \end{cases} , \quad n \leq 1 + 2(d-4) \ . \tag{2.64}$$

For particles that are unstable at zero temperature, the power $n$ is exactly $1 + 2(d-4)$. If on the other hand the particle is stable, its value is model-dependent. As it typically dominates the signal (for $T_{\max} \gg m$)[9], we will focus in the following on GW production at high temperatures $T \gg m$ as well as on frequencies $f > f_{\rm nr}$. We will start by considering the case of renormalisable interactions ($d = 4$), which is parametrically simpler, before moving on to non-renormalisable interactions.

### Renormalisable interactions

For renormalisable interactions, the width scales linearly with the temperature. Therefore, it redshifts at the same speed as the physical graviton momentum and the transition between the hydrodynamic and Boltzmann regime happens at a coupling-dependent critical frequency $f_c$ defined below.

$$k = \sqrt{10}\Upsilon_{\text{av}} \quad \Leftrightarrow \quad f = f_c \ , \quad \frac{f_c}{y} \equiv \frac{\sqrt{10}}{\pi} f_{\text{peak}} \simeq 6 \times 10^{10} \text{ Hz} \ . \tag{2.65}$$

For $f < f_c$, GWs are always produced in the hydrodynamic regime, independently of the temperature of the plasma, whereas GWs are always produced in the Boltzmann regime for $f > f_c$. As highlighted earlier, this results in a kink in the GW spectrum located exactly at the frequency $f_c$. Inserting the average width (2.64) into the relativistic GW production rate (2.50) and subsequently in the integral (2.21), we obtain the estimate

$$h^2 \Omega_{\text{GW}}^{T>m}(f) \overset{d=4}{\simeq} 1.6 \times 10^{-40} \times g_X \frac{f f_c}{f_c^2 + f^2} \left(\frac{f}{\text{Hz}}\right)^2 \min\left(\frac{f}{\text{Hz}}, \frac{f_\star}{\text{Hz}}\right) \ . \tag{2.66}$$

The GWB (2.66) saturates the upper bound (2.60a) for $f = f_c$. We also notice that the same process that generates the width (2.64) is also responsible for the production of hidden sector particles and their equilibration. This effectively

[9] In the renormalisable case, this condition imposes a lower bound on the value of $y$, i.e. $y \gtrsim \sqrt{m/m_0}$, if the particle is (perturbatively) produced through the same interaction the generates the width.

puts an lower bound on the thermalisation temperature $T_\star$, which can be estimated from $\Upsilon_{\text{av}}/H = y m_0/T = 1$. This leads to the lower bound $T_\star > y\, m_0$.

Finally, before concluding, we would like to emphasise that the expression (2.66) is not limited to hidden sectors and, in particular, should also capture the SM contribution. In that case, one can show[10]

$$f_c^{\text{SM}} \approx 3.1 \times 10^8 \text{ Hz} . \tag{2.67}$$

Hence, the total GW spectrum emitted by the SM reads

$$h^2 \Omega_{\text{GW}}^{SM}(f) \overset{f<f_c^{SM}}{\simeq} 3.2 \times 10^{-48} \times \left(\frac{f}{\text{Hz}}\right)^3 \min\left(\frac{f}{\text{Hz}}, \frac{f_\star}{\text{Hz}}\right) \tag{2.68}$$

in the hydrodynamic regime. As an illustration, the resulting SM background (computed using the production rate from [73]) is displayed in red for two choices of reheating temperature, i.e. $T_\star = m_{\text{Pl}}$ and $T_\star = 10^{10}$ GeV, in Fig. 2.4. We would like to point out the qualitative difference with the results of earlier works [73–75], which neglected the impact of the Hubble suppression. This suppression leads to a stronger spectral shape at low frequencies, i.e. $f^4$ instead of $f^3$.

### Non-renormalisable interactions

Beyond the renormalisable case, many well-motived scenarios include hidden sectors who primarily interact through non-renormalisable interactions. These models have the additional interesting property that the production rate of hidden sector particles increases much faster with the temperature, potentially leading to a so-called UV freeze-in [108].

Non-renormalisable scenarios present strong qualitative differences with the renormalisable case. In particular, the temperature dependence is very different such that the ratio $\Upsilon_{\text{av}}/k$ now also depends on the temperature. As a consequence, the production of GWs starts in the hydrodynamic regime above a (frequency-dependent) critical temperature

$$T_c(f) = \Lambda \left(\frac{f}{f_c}\right)^{1/2(d-4)} \tag{2.69}$$

[10] The right-handed lepton width is dominated by $2 \leftrightarrow 2$ scatterings with gauge bosons and hence is proportional to $g^4 \ln g$, $g$ being the electroweak coupling. See also Eq. (2.22). The presence of the logarithm highlights the importance of small-angle scatterings. The critical frequency (2.67) is in principle temperature-dependent due to the logarithmic temperature dependence of the viscosity. This however only leads to subleading corrections.

below which the production only takes place in the Boltzmann regime. One can use Eq. (2.69) to associate to each energy scale its corresponding characteristic frequency. For instance, the thermalisation temperature $T_\star$ can be associated with the *Boltzmann frequency*

$$f_{\text{bol}} \equiv f_c \left(\frac{T_\star}{\Lambda}\right)^{2(d-4)} , \qquad T_c(f_{\text{bol}}) = T_\star \, . \tag{2.70}$$

Above $f_{\text{bol}}$, we have $T_c > T_\star$ and GWs are thus only produced in the Boltzmann regime.[11] Similarly, one can associate to the mass $m$ the (characteristic) *hydrodynamic frequency*

$$f_{\text{hyd}} \equiv f_c \left(\frac{m}{\Lambda}\right)^{2(d-4)} , \qquad T_c(f_{\text{hyd}}) = m \, . \tag{2.71}$$

Below this frequency, the GWB is solely produced in the hydrodynamic regime for $T \gtrsim m$. If $m < T_\star$, and therefore $f_{\text{hyd}} < f_{\text{bol}}$, GWs with intermediate frequencies $f_{\text{hyd}} < f < f_{\text{bol}}$ can be produced both in the hydrodynamic and Boltzmann regime as long as $T_c < T_{\text{entry}}$. These two characteristic temperatures are both functions of $f$ and become equal at the crossing frequency

$$f_x \equiv f_c \left(\frac{f_{\text{peak}}\Lambda}{\pi\, f_c\, m_0}\right)^{1+\frac{1}{2(d-4)-1}} , \qquad T_c(f_x) = T_{\text{entry}}(f_x) \, . \tag{2.72}$$

The shape of the present-day GW spectrum is determined by the hierarchy between these three frequencies $f_x$, $f_{\text{hyd}}$ and $f_{\text{bol}}$. A schematic representation of the different possible hierarchies is shown in Fig. 2.3.

We present in appendix A.2 a derivation of the complete GW spectrum for the different regimes of Fig. 2.3 in the high-temperature limit, i.e. neglecting the $m < T$ contribution. In the following, we only list the dominant contribution to these regimes, i.e. assuming sufficient hierarchies between the different scales in the problem.

1. **Left panel of Fig. 2.3:** For $f_{\text{bol}} < f_x$, we have $T_{\text{entry}} < T_c$ whenever the plasma is thermalised. This implies that GW production always proceeds in the Boltzmann regime. The resulting spectrum write

$$h^2\Omega_{\text{GW}}^{T>m}(f) \overset{f_x \geq f_{\text{bol}}}{\simeq} g_X \frac{1.6\times 10^{-40}}{2(d-4)+1} \left(\frac{f}{\text{Hz}}\right)^2 \frac{f_{\text{bol}}}{\text{Hz}} \times \tag{2.73}$$

[11] GWs can of course be emitted at higher temperatures, when the plasma is still out of equilibrium but this is not captured by our calculation.

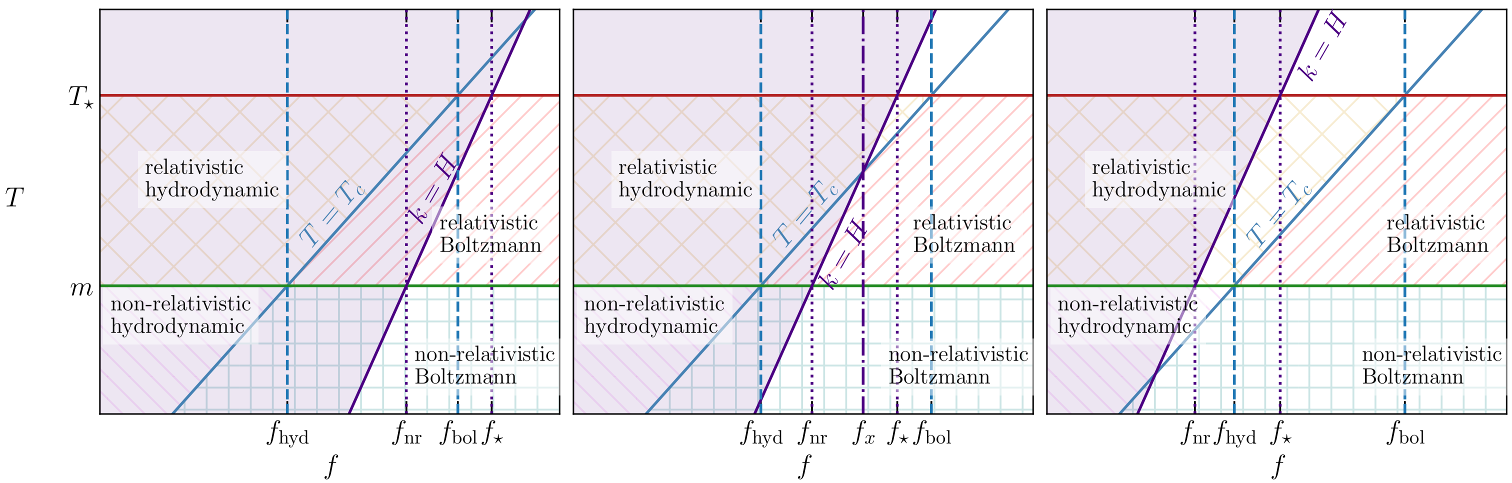


**Figure 2.3:** Schematic representation of the different hierarchies between the characteristic frequencies (2.57), (2.58), (2.70), (2.71) and (2.72). GWs are produced in hydrodynamic (Boltzmann) regime above (below) the blue line. Similarly, the violet line marks the separation between super-Hubble modes (above the line), for which GWs cannot be produced, and sub-Hubble modes (below the line). For $T < m$, the transition between the hydrodynamic and Boltzmann regimes is model-dependent and depends on the index $n$, see Eq. (2.64). In this figure, we display the line for $n = 0$. Figure taken from [3].

$$\times \begin{cases} 0 & \text{for} \quad f < f_{\rm nr}\,, \\ \left(\frac{f}{f_\star}\right)^{2(d-4)} & \text{for} \quad f_{\rm nr} < f < f_\star\,, \\ \frac{f_\star}{f} & \text{for} \quad f_\star < f\,. \end{cases}$$

In particular, it features two kinks, one at $f = f_{\rm nr}$ and one at $f = f_\star$. For this specific scenario, the non-relativistic contribution to the GWB is highly suppressed and bounded by the general upper bound (2.63). Eq. (2.73) corresponds to the first case listed in appendix A.2.

2. **Middle panel of Fig. 2.3:** If on the contrary $f_{\rm hyd} < f_x < f_{\rm bol}$, both the Boltzmann and hydrodynamic regimes contributes to the (total) high-temperature background. At high frequencies $f > f_{\rm bol}$, GWs can only be produced in the Boltzmann regime whereas the intermediate frequencies $f_x < f < f_{\rm bol}$ see contributions from both regimes, given that their critical temperature is smaller than the horizon entry temperature. Finally, since $T_{\rm entry} < T_c$ for $f < f_x$, low frequency GWs are solely produced in the Boltzmann regime. To summarise, the GW spectrum takes the form

$$h^2\Omega_{\rm GW}^{T>m}(f) \overset{f_\star \gg f_{\rm bol}}{\simeq} gX \frac{1.6\times 10^{-40}}{2(d-4)+1}\left(\frac{f}{\rm Hz}\right)^2 \frac{f_{\rm bol}}{\rm Hz}\times \tag{2.74}$$
$$\times \begin{cases} 0 & \text{for} \quad f < f_{\rm nr}\,, \\ \left(\frac{f}{f_\star}\right)^{2(d-4)} & \text{for} \quad f_{\rm nr} < f < f_x\,, \\ \beta \frac{f_x}{f_{\rm bol}} \left(\frac{f}{f_x}\right)^{1/2(d-4)} & \text{for} \quad f_x < f < f_{\rm bol}\,, \\ \frac{f_\star}{f} & \text{for} \quad f_{\rm bol} < f\,. \end{cases}$$

The numerical factor $\beta \in [4/3, 2]$ depends on the dimension $d$ and originates from the integration over $T > T_c$. We note that this expression coincides with Eq. (2.73), except in the range $f_x < f < f_{\rm bol}$ due to the additional contribution from the hydrodynamic regime. This scenario corresponds to the second case described in appendix A.2.

3. **Right panel of Fig. 2.3:** Finally, for the last scenario where $f_x < f_{\rm hyd}$, the GW production always starts in the hydrodynamic regime for $f > f_{\rm hyd}$. Hence, the production of GWs is dominated by the temperatures $T \simeq T_c$ and the Hubble suppression can be safely neglected. The present-day GWB then features two kinks, one at $f = f_{\rm hyd}$ and one

at $f = f_{\rm bol}$.

$$h^2\Omega_{\rm GW}^{T\geq m}(f) \overset{f_{\rm bol}\gg f_\star, f_{\rm hyd}\gg f_{\rm nr}}{\simeq} g_X \frac{1.6\times 10^{-40}}{2(d-4)+1}\left(\frac{f}{\rm Hz}\right)^2 \frac{f_{\rm bol}}{\rm Hz}\times \tag{2.75}$$
$$\times\begin{cases} 0 & \text{for} \quad f < f_{\rm hyd}\,, \\ \beta \frac{f_x}{f_{\rm bol}}\left(\frac{f}{f_x}\right)^{1/2(d-4)} & \text{for} \quad f_{\rm hyd} < f < f_{\rm bol}\,, \\ \frac{f_\star}{f} & \text{for} \quad f_{\rm bol} < f\,. \end{cases}$$

$\beta$ is defined as in Eq. (2.74). This scenario encompasses both cases 3 and 4 described in appendix A.2.

Before moving on to specific examples of GWBs from non-renormalisable interactions, we would like to point out that one should in principle also verify that our effective field theory (EFT) framework remains valid at all times, i.e. that $T_{\rm max} \ll \Lambda$. This condition might however be too restrictive. Indeed, for frequencies below $f_c$, we always have $T_c < \Lambda$. In this case, GWs are always produced in the hydrodynamic regime for temperatures $T_c < T < T_\star$. Given the non-renormalisable nature of the interaction, the production rate entering Eq. (2.21) $\Pi/T^4 \sim T/\Upsilon_{\rm av}$ decreases with the temperature. Hence, the GW spectrum is dominated by the production at $T \simeq T_c < \Lambda$ for which the EFT framework remains valid. A similar reasoning however does not apply for higher frequencies $f > f_c$, for which the largest temperatures $T \simeq T_{\rm max}$ dictate the final GWB.

To illustrate the preceding discussion, we display in Fig. 2.4 the GWB[12] from the SM and from a hidden sector whose interactions are dominated by non-renormalisable operators of various dimensions $d \in \{5, 6, 8\}$. We focus on the most optimistic case choosing the reheating temperature to be equal to the EFT scale $T_\star = \Lambda$. As benchmarks, we also consider two different choices for this reheating temperature: $T_\star = m_{\rm Pl}$ and $T_\star = 10^{10}$ GeV. Finally, we set the coupling $y$ to be $1$. While choosing smaller values of $y$ might enhance the signal and generate additional features at low frequencies, virtual exchanges of gravitons are expected[13] to contribute to the width $\Upsilon_{\rm av}$ at the very least at dimension 8 with $y \sim \mathcal{O}(1)$. This contribution effectively induces a lower bound on the value of $y$, even for lower-dimensional operators.

[12] Although the approximations leading to Eqs. (2.73),(2.74) and (2.75) turn out to hold very well, we emphasise that we do not adopt those to draw Fig. 2.4. We use instead the complete production rate (2.50) along with the width (2.64) before extracting the GW spectrum numerically from (2.21).

[13] This of course neglects any quantum gravity effects at the Planck scale.

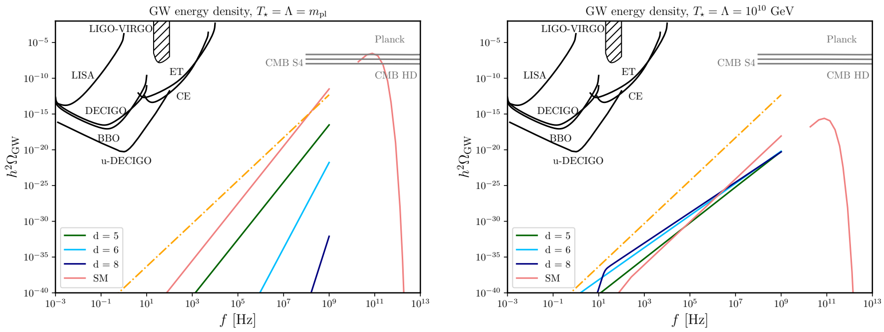


**Figure 2.4:** Estimate of the GWB from non-renormalizable interactions with dimension $d > 4$ for $T_\star = \Lambda = m_{\rm Pl}$ (*Left*) and $T_\star = \Lambda = 10^{10}$ GeV (*Right*), cf. Eqs. (2.73), (2.74) and (2.75). In dashed orange, we highlight the upper bound (2.62) (for $g_X = 1$) while the continuous red line represents the equivalent background for the SM. The continuous black lines are extracted from [113, 114] and show experimental power-law integrated sensitivities [115] of various prospective laser interferometers. In black hatched, we indicate the parameter space already excluded from the third observing run of LIGO and VIRGO [116]. Finally, the grey lines highlight the sensitivity of Planck [117] and a selection of proposed successors, CMB-S4 [53] and CMB-HD [118]. In both plots, we set the hidden particle mass to zero and coupling parameter $y = 1$, cf. Eq. (2.64). Figure slightly adapted from [3].

The first striking feature of Fig. 2.3 is that the GWBs emitted by these different hidden sectors, as well as the general upper bound (2.62), lie at least $\mathcal{O}(15)$ orders of magnitude below the sensitivity of the various proposed interferometers. It seems therefore impossible to observe such GWBs at laser interferometers, even at beyond next-generation experiments such as u-DECIGO.[14] While measurements of $N_{\rm eff}$ seem to probe this background for large values of the reheating temperature, the contributions of the hidden sector is expected to be subdominant to its SM counterpart. Secondly, we also notice that the SM background appears to violate the upper bound (2.62). Note however that 1) the upper bound was drawn for hidden sectors with $g_X = 1$ whereas $g_{\ell_R} = 6$ for right-handed leptons, and 2) this only happens above the critical frequency (2.67) where the validity of (2.68) is questionable. For larger frequencies, vertex-like corrections as well additional diagrams are expected to contribute sizeably. This is also the reason why we do not continue the SM and hidden

[14] Proposals sensitive to GWBs that saturate our upper bound for $f \sim \mathcal{O}(10^7 - 10^9)$ Hz exist, see [119], but they rely on the assumption that the interference term between the signal and the background field in a cavity can be measured with the same level of accuracy as the signal itself. No known method or technology currently enables such a measurement (cf. e.g. [120] for a discussion).

sector spectrum in the gap visible in Fig. 2.4 as well as the slight apparent mismatch between the two regimes of the SM spectrum.

Finally, let us now analyse in more detail the spectral shapes of these GWBs. For both panels, we have $f_{\text{bol}} \approx 6 \times 10^{10}$ Hz, which lies above the range of validity of our approximation. Moreover, in the right panel we set $T_\star = m_{\text{Pl}}$ and, hence, $f_\star \approx 3 \times 10^{11}$ Hz. This in particular implies $f_{\text{bol}} < f_x$. As a consequence, the GW spectrum is captured by Eq. (2.73) and scales as $f^{2(d-3)}$ for all relevant frequencies ($f < f_\star$). On the other hand, the second benchmark $T_\star = 10^{10}$ GeV can be characterised by Eq. (2.74) since $f_\star < f_{\text{bol}} < f_x$ and displays additional features as a result. For instance, we observe that the crossing frequency $f_x$ for dimension-8 operators lies in the LISA frequency band. Therefore, the GWB scales for $f \lesssim 100$ Hz as for the first benchmark, i.e. $h^2\Omega_{\text{GW}} \sim f^{2(d-3)}$, whereas it scales as $f^{2+1/(2(d-4))}$ for larger frequencies. Similar feature could in principle be observed for $d = 5$ and $d = 6$. However, $f_x$ is pushed towards smaller frequencies in that case, beyond the displayed range. The scaling of Eqs. (2.73) and (2.74) also explains the relative suppression of the GWB strength between the first and second benchmark. Indeed, while $T_\star = m_{\text{Pl}}$ in the first case, the maximal temperature $T_{\text{max}}$ for which GWs can be produced remains much lower than the Planck scale and GW production is suppressed by $(T_{\text{entry}}/\Lambda)^{2(d-4)}$ in the Boltzmann regime. Though undetectable with known technologies, it is nonetheless interesting to note that precise measurements of the GWB's shape would reveal extremely useful to pin down the underlying theory. In particular, the slope of the GWB provides direct access to the dimension of the operator generating the width $\Upsilon_{\text{av}}$. Similarly, variations in the slope of the GWB would pinpoint the values of all characteristic frequencies $f_{\text{nr}}$, $f_{\text{hyd}}$, $f_x$, $f_{\text{bol}}$ and $f_\star$ and allow us to extract information on the mass of the particle as well as the the UV scale $\Lambda$ and the reheating temperature $T_\star$.

## 2.4 Application to explicit benchmark scenarios

In this section, we apply the results of the previous section to two well-motivated examples of hidden sectors: right-handed (RH) neutrinos and axion-like particles (ALPs). While [75] already considered GWBs from RH neutrinos (within the $\nu$MSM [121]) and from ALPs (within the SMASH model [122]), they only investigated the impact of the modified reheating temperature predicted by these scenarios, and not the hydrodynamic enhancement originating from the feeble interactions of the plasma constituents.

### 2.4.1 Right-handed neutrinos

The existence of one or several generations of RH neutrinos, which we will write $\nu_R$ in the following, has been proposed to resolve a number of shortcomings of the SM such as the generation of the neutrino masses [123–128], the asymmetry between matter and antimatter [129] or the origin of DM [130,131]. More details on their motivation will be provided in Chap. 3, see also [132–134] for reviews. Of particular interest, RH neutrinos are expected to interact very feebly if their mass lies at a testable scale, well below the Grand Unified Theory (GUT) scale. In the minimal type-I seesaw model, they only interact through the Yukawa coupling $Y$

$$\mathcal{L} \supset Y\overline{\ell_L}\tilde{\Phi}\nu_R + \text{h.c.}\,, \tag{2.76}$$

where $\tilde{\Phi} = i\sigma_2\Phi^*$ is the charge conjugate of the SM Higgs doublet, $\sigma_2 = \left(\begin{smallmatrix} 0 & -i \\ i & 0 \end{smallmatrix}\right)$ being the second Pauli matrix, and $\ell_L$ a left-handed (LH) SM fermion doublet. More details on this scenario can be found in the dedicated section, Sec. 3.2. The momentum-averaged RH neutrino width $\Upsilon_{\text{av}}$ can be extracted from the associated production rate [135] and has been shown [136] to be given by

$$\Upsilon_{\text{av}} = \gamma(z)\frac{F^2 T}{16\pi}. \tag{2.77}$$

$\gamma$ is a dimensionless function of $z \equiv m/T$, whose precise determination is involved. For the level of accuracy needed in this work, using the approximation

$$\gamma \approx \max\left(0.2, z - \frac{3}{2}\right) \tag{2.78}$$

will be sufficient. In particular, the critical frequency $f_c$ reads in the relativistic regime

$$f_c = 2.4 \times 10^8 \text{ Hz} \times F^2\,. \tag{2.79}$$

We display in Fig. 2.5 the expected thermal GWB emitted by RH neutrinos for different choices of the Yukawa coupling as well as for the most optimistic choice of reheating temperature $T_\star = m_{\text{Pl}}$.[15] We display our results for both the GW energy density fraction per logarithmic wave number interval $\Omega_{\text{GW}}$

[15] Such a choice is unrealistic in the case of pure thermal production since $T_\star \approx 4 \times 10^{-3} m_0 F^2 \ll m_{\text{Pl}}$. However, additional production mechanisms at much higher temperature, e.g. from inflaton decay [137, 138], do exist.

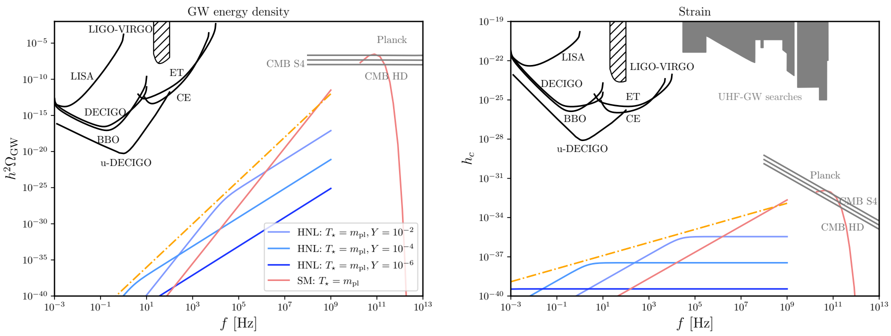


**Figure 2.5:** GWB due to thermal fluctuations of a massless RH neutrino in the early universe plasma, as measured by the energy density $h^2\Omega_{\rm GW}$ (*Left*) and strain $h_c$ (*Right*). The different shades of blue correspond to different choices of the Yukawa coupling. Following a similar colour coding as in Fig. 2.4, the light red line shows the expected SM background for $T_{\rm max} = m_{\rm Pl}$ while the dashed orange line represents the upper bound (2.62) (for $g_X = 1$). For details about the various experimental constraints, see the captions of Fig. 2.4. Additionally, we display in the right plot the sensitivity estimate of various proposed searches[17] for high-frequency GWs [68, 75, 141–146] (cf. also [147]). Figure slightly adapted from [3].

(left panel) and the characteristic strain defined in (2.15) (right panel), and compare to the sensitivities of various planned interferometers as well as recently proposed high-frequency GW searches, see the caption of the figure for more details. Similarly to the non-renormalisable situation, we observe that, while they can overcome the SM background by over 10 orders of magnitude in the LISA frequency band, these GWBs are strongly constrained by the upper bound (2.62) and lie well below experimental sensitivities rendering direct detection impossible at the moment. However, high-frequency GW searches form still a young and very active field of research [68, 69], and it is very well possible that the sensitivity increases by several orders of magnitude in the future.[16] We conclude this subsection by noticing that, as expected for renormalisable interactions, the enhanced hydrodynamic regime ($f < f_c$) is clearly distinct from the Boltzmann regime ($f > f_c$), where the SM quickly dominates.

[16]We however caution that some detector concepts are limited by intrinsic quantum noises [139, 140] that makes it difficult to probe the proposed GWB, independently of technical progresses.

[17]We caution that these searches rely on different sets of assumptions, *e.g.* about the strength of the cosmic magnetic fields, and show different levels of maturity. Hence, the gray region might have to be slightly adapted in the future.

### 2.4.2 Axion-like particles

Beyond RH neutrinos, axions constitute a second very well-motivated benchmark. First proposed in the 70s in the context of Quantum Chromodynamics (QCD) as potential solution to the strong CP-problem [148–151] (see also [152] for a review on QCD axions), it was quickly realised that generalisations of these, so-called ALPs, could also be viable DM candidate [153–155] (for a review, see e.g. [156]) or drive inflation [157–159]. As a result, ALPs gained in popularity in recent years and are currently under intense experimental scrutiny, both in laboratory searches [83, 84, 156, 160–162] or through their inferred effects on astrophysical phenomena [83, 163].

The defining feature of ALPs is their coupling to the (non-abelian) gauge field strength $G_{\mu\nu}$

$$\mathcal{L} \supset \frac{1}{2}\left(\partial_\mu\varphi\partial^\mu\varphi - m^2\varphi^2\right) - \frac{\varphi\,\chi}{\mathrm{f}_\varphi}\,, \qquad \chi = \frac{\alpha}{16\pi}\tilde{G}_{\mu\nu}G^{\mu\nu}. \tag{2.80}$$

$\tilde{G}_{\mu\nu} \equiv \epsilon_{\mu\nu\rho\sigma}G^{\rho\sigma}$, $\epsilon_{\mu\nu\rho\sigma}$ being the Levi-Civita tensor, is the Hodge dual of $G_{\mu\nu}$. If the gauge theory is asymptotically free, the ALP width reads in the relativistic regime [164]

$$\Upsilon_{\text{av}} \overset{m \lll T}{=} \kappa\, n_c^3(n_c^2-1)\frac{\alpha^5 T^3}{\mathrm{f}_\varphi^2}\,, \quad \kappa \approx 1.5\,, \quad \frac{1}{\alpha} \approx \frac{22 n_c}{12\pi}\ln\left(\frac{2\pi T}{\Lambda_{\text{IR}}}\right)\,, \tag{2.81}$$

with $n_c$ the colour number and $\Lambda_{\text{IR}}$ the infrared (IR) confinement scale at which the gauge coupling $\alpha$ exhibits a Landau pole. We emphasise that, contrary to the analytical discussion in Sec. 2.3.3, we account for the logarithmic running of the coupling in our numerical calculation. In the following, we will assume that ALPs are massless and focus on QCD-like scenarios, i.e. setting $n_c = 3$ and $\Lambda_{\text{IR}} = 200$ MeV. To solve the strong CP-problem, axions also need to interact with fermions, which we will neglect.

We display our results in Fig. 2.6. For all chosen benchmarks, we maximise the reheating temperature $T_\star = f_\varphi$. Lower reheating temperatures would only lead to a suppression of the GWB. As one can see, the analytical scaling obtained in Eqs. (2.73) to (2.75) is well reproduced up to minor modifications due to the logarithmic running of the gauge coupling $\alpha$. In particular, the benchmarks $T_\star = m_{\text{Pl}}$ and $T_\star = 10^{15}$ GeV both verify $f_x > f_{\text{bol}}$ and are therefore captured by Eq. (2.73). For the first benchmark $T_\star = m_{\text{Pl}}$, the horizon frequency $f_\star \approx 3 \times 10^{11}$ Hz lies beyond the frequency band of interest. In this case, we have $\Omega_{\text{GW}} \sim f^{2+2(d-4)} = f^4$. For

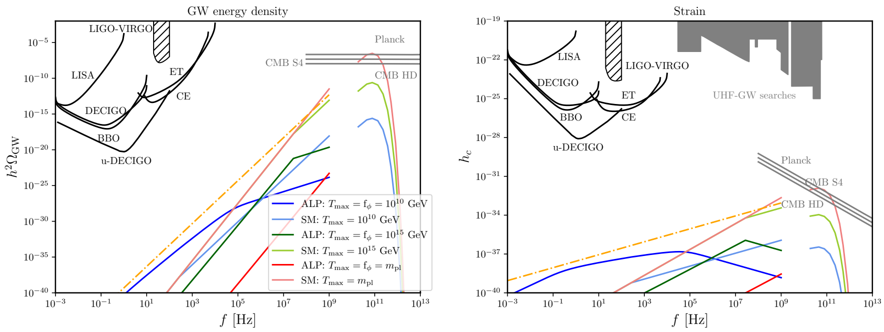


**Figure 2.6:** Equivalent plot to Fig. 2.5 for massless ALPs with decay constants $\mathrm{f}_\varphi \in \{m_{\rm Pl}, 10^{15}\mathrm{GeV}, 10^{10}\mathrm{GeV}\}$. For each line, we choose $T_\star = \mathrm{f}_\varphi$, $\Lambda_{\rm IR} = 200$ MeV and $n_c = 3$. Following a similar colour coding as in Fig. 2.4, the light red (resp. green, blue) line shows the expected SM background for $T_{\rm max} = m_{\rm Pl}$ (resp. $10^{15}\mathrm{GeV},\ 10^{10}\mathrm{GeV}$) while the dashed orange line represents the upper bound (2.62) (for $g_X = 1$). For details about the SM line and the various experimental constraints, see the caption below Figs. 2.4 and 2.5. Figure slightly adapted from [3].

the second benchmark $T_\star = 10^{15}$ GeV, we have instead $f_\star \approx 3 \times 10^7$ Hz. In this case, the spectrum is modified above $f_\star$ and scales, as expected, linearly with the frequency. Finally, the last benchmark $T_\star = 10^{10}$ GeV verifies $f_{\rm hyd} = 0 < f_x \approx 0.1$ Hz $< f_{\rm bol} \approx 6 \times 10^{10}$ Hz and is therefore captured by Eq. (2.74) instead. As expected, the spectrum exhibits two kinks. Below $f_x$, the signal grows as $f^4$, between $f_x$ and $f_{\rm bol}$, it grows as $f^{2+1/2(d-4)} = f^{5/2}$, and above $f_{\rm bol}$, it grows linearly.

## 2.5 How to evade the upper bound on the GWB strength?

In this section, we review the limitations of our approach, discussing how one can lift these restrictions and the expected impact on previous results, on the upper bound (2.62) in particular. Essentially, the assumptions we made can be grouped into three categories:

1. Standard cosmic history.
2. Focus on the hidden-sector-dominated contribution.
3. Equilibrium within and between sectors.

We will now go through each of these assumptions in more detail.

**Standard Cosmic History:** As already highlighted in Sec. 2.1.2, Eq. (2.21), and therefore the upper bound (2.62), assumes standard cosmic history. More specifically, it relies on i) the SM dominating the evolution of the universe in the temperature range of interest, and ii) the absence of (sizeable) entropy transfer between the SM and the hidden sector. Though the generalised result (2.24) capture these two effects, their precise impact on the upper bound (2.62) remains to be explored. We note however that models with more degrees of freedom (such as GUTs)[18] do not necessarily produce a stronger thermal GW signal than the SM. Indeed, while the GW production rate does increase in these models, this enhancement tends to be partially compensated by the subsequent dilution.

**Focus on the hidden-sector-dominated contribution:** In this paper, we focused on the enhanced hydrodynamic contribution from a unique feebly interacting particle. This in practice amounts to two distinct approximation. First, we assume that the hidden sector is not composite. In presence of multiple feebly interacting particles, their individual contribution to the total GWB can be summed and the upper bound (2.62) applies to each species individually (as long as the number of degrees of freedom in the hidden sector remains subdominant to the SM). Moreover, we neglect the vertex-like corrections displayed in Fig. 2.2. While these are not enhanced for feebly interacting hidden sectors, they are expected to contribute at the same order as the wavefunction contribution, displayed in Fig. 2.1, in the Boltzmann regime $k \gg \Upsilon_{\rm av}$. In this regime, we therefore expect $\mathcal{O}(1)$ corrections to our result from these additional diagrams and additional resummations may be needed [73, 74].

**Equilibrium within and between sectors:** Lastly, the derivation of Eq. (2.62) as well as the phenomenological analyses in Secs. 2.3 and 2.4 crucially rely on the following two distinct assumptions

i Thermal equilibrium of both the SM and the hidden sector.

ii Identical temperature between the SM and the hidden sector.

If the hidden sector remains thermalised but with a temperature $T_h$ different[19] from the SM temperature $T$, Eq. (2.42) holds up to a rescaling by the appropri-

[18] However, GUTs are typically accompanied with one or more first-order phase transitions between the UV gauge group and the SM, providing additional mechanisms for GW generation; see e.g. [165, 166].

[19] This is for instance the case if the hidden sector possesses very feeble (or no) interactions with the SM but comparatively strong self-interactions such that it still thermalises with itself.

ate power of $\xi \equiv T_h/T$ of the distribution function's argument. The width is also impacted and depends in general[20] on both $T$ and $T_h$. If the first approximation also fails and the hidden sector is completely out of equilibrium, it is in general difficult to draw any conclusion. Provided the loop is still dominated by the contribution from the propagators' poles, the generalised result (2.41) nonetheless holds for a general product of distribution function (2.32). This assumption can in principle be violated, e.g. if the hidden sector is produced from the decay of a heavy particle and thermalises slowly, but we expect it to hold for a broad range of nonequilibrium situations. Hence, we expect that a generalised version of the upper bound (2.62), where the temperature is replaced by an effective parameter that characterises the hidden sector occupation number, should hold for a variety of nonequilibrium situations provided.

Though it is in general difficult to precisely estimate the impact of relaxing these assumptions on the strength of the GWB, we would like to finish this section by commenting on two phenomenologically relevant situations.

The first is the case of so-called thermal freeze-in, i.e. the slow thermal production of particles from an equilibrated bath. This situation is well-motivated by various DM [130, 167] or baryon asymmetry [121, 168, 169] production scenarios. While the hidden sector strongly deviates from equilibrium during freeze-in, it is also underabundant (compared to equilibrium) such that it is expected[21] that the associated GWB remains constrained by the same upper bound (2.62).

On the other hand, an overabundant hidden sector could lead to a strong enhancement of the GWB. Such overabundance is for instance expected to occur during the reheating of our universe through the decay of the inflaton field. The GW emission in this setup was already studied in a number of works [170–173], see also [174] for the SM contribution during reheating, and seem to severely violate our upper bound (2.62). However, while we expect that our upper bound should be relaxed in this situation due to the inflaton's overabundance, these works neither account for the resummation of wavefunction type corrections (see appendix A.1 for details), necessary in the hydrodynamic regime, nor for the Hubble suppression delaying the onset of GW pro-

[20]If the hidden sector only interacts with itself, one can simply replace $T$ by $T_h$ e.g. in Eq. (2.64) but the general case is more intricate.

[21]As pointed out earlier, the averaged width $\Upsilon_{\rm av}$ can also be sensitive to the hidden sector abundance. An underabundant hidden sector would then decrease the width and, therefore, enhance the production rate. We however do not expect this effect to compensate the reduction in $D(p_0, q_0)$.

duction, see Eq. (2.55) and discussions around it, when estimating the current GWB.

## 2.6 Conclusion and outlook

In this first part of the thesis, we examined the cosmological GWB from thermal fluctuations of hidden sectors during radiation domination. While this type of background is generically suppressed compared to GWBs from violent out-of-equilibrium phenomena such as first-order phase transitions or preheating, it is also much harder to avoid as it does not rely on deviations from the standard cosmic history, acting in this sense as a cosmic GW floor.

We started by evaluating the GW production rate from feebly interacting particles using tools of the CTP formalism. We performed this computation explicitly for a generic fermionic species, noticing a striking similarity with previously obtained results for scalar particles and consequently postulating equivalent formulae should hold for vector particles. This allowed us to write compact formulae for the GW production rates that encompass these different cases.

We then made use of these rates to derive useful phenomenological formulae describing thermal GWBs emitted during radiation domination. In particular, we estimated the strength of these backgrounds for generic (non-)renormalisable interactions and derived universal upper bounds that place strong constraints on their magnitude. These upper bounds include both the hydrodynamic enhancement from the feebly interacting nature of the plasma constituents as well as the suppression of the GW production rate at super-Hubble scale. Applying these result to well-motivated benchmarks, we additionally computed the expected GWBs from RH neutrinos as well as ALPs. We found that a precise measurement of this background would in principle give access to many different model parameters, e.g. the mass of the particle or the EFT scale. Unfortunately, while the presence of hidden sectors can enhance this type of background by $\mathcal{O}(10)$ orders of magnitudes in the high-frequency range, the upper bound (2.62) effectively precludes detection in the interferometer frequency band. The same in principle applies to higher frequencies, though high-frequency GW searches is a very recent and active field, where significant improvements can still be expected.

Finally, we concluded by quickly reviewing the assumptions underlying our estimate and the impact of relaxing them. In particular, while it is relatively straightforward to account for deviations from radiation domination, see

Eq. (2.24), we expect that our upper bound can be strongly violated when thermodynamic equilibrium breaks down. In the future, it would be particularly interesting to investigate such scenarios, in particular GW production during reheating for which key aspects of the dynamics have been neglected in previous works. In this case, the different expansion history can help evade our upper bound. Moreover, the evolution and decay of the inflaton condensate can lead to the presence of peaks in the decay product distribution functions or even non-perturbative particle production, all of which are expected to modify our conclusions.

# Part II

# Low-scale leptogenesis and the generation of the baryon asymmetry

# Introduction

In 1928, after solving the relativistic generalisation of the Schrödinger equation, Paul Dirac famously predicted the existence of a new type of matter, the so-called *antimatter*, of opposite charges compared to ordinary matter. Its detection in 1932 by Carl D. Anderson immediately raised the obvious question of its virtual absence in our surrounding universe, which, to this day, remains one of the most intriguing unresolved issue in cosmology. This problem has since then been made more pressing by the advent of precision cosmology and, in particular, measurements of the CMB by Planck [117] as well as of the light element abundances [175, 176]. The leading constraints on the asymmetry between baryons and antibaryons, or Baryon Asymmetry of our Universe (BAU), currently give

$$Y_B^{\rm obs} = \frac{n_b - n_{\bar{b}}}{s} = (8.6 \pm 0.06) \times 10^{-11} \,, \tag{3.1}$$

with $n_b$ ($n_{\bar{b}}$) the (anti)baryon number density and $s$ the present-day entropy density. Assuming that the initial conditions of our universe were not already matter-antimatter asymmetric, Andrei Sakharov derived three necessary conditions for a successful generation of a matter-antimatter asymmetry [177]

1. Violation of the C and CP symmetries,
2. Violation of baryon number conservation,
3. Deviation from equilibrium dynamics.

Interestingly, these conditions are all fulfilled within the SM: The C and CP symmetries are violated by the weak interaction as can be observed in $\beta$ and meson decays [178–180], baryon number conservation is violated by the sphaleron process [181–184] and the expansion of the universe provides a natural source of deviation from thermodynamic equilibrium [185,186]. However, the amount of baryon asymmetry produced within the SM, assuming a standard cosmological history, is too small by at least $\sim 12$ orders of magnitude [184, 187–192]. Such a large discrepancy between the observed and theoretically predicted asymmetry strongly points towards the presence of additional physics beyond the SM. Many mechanisms have been proposed over the years, including GUT baryogenesis [193, 194], the Affleck-Dine mechanism [195], electroweak baryogenesis [196–198] or so-called leptogenesis. In the second part of this thesis, we will concentrate on the latter option.

Baryogenesis through leptogenesis, or more simply leptogenesis, offers an elegant mechanism to connect the production of a matter-antimatter asymmetry to another long-standing unresolved issue in particle physics: the origin of neutrino masses. The observation of neutrino flavour oscillations in a variety of different systems, including solar, atmospheric, reactor and beam neutrinos, clearly indicates that neutrinos must be massive. As neutrinos have until now only been observed with left-handed chirality, it also constitutes the only clear evidence of BSM physics tested in laboratory experiments.

The existence of neutrinos with right-handed chirality could resolve these two problems simultaneously. As briefly highlighted in Sec. 2.4.1 already, these RH neutrinos can generate the neutrino masses through the so-called type-I seesaw mechanism. They can also explain the BAU through leptogenesis, providing the necessary additional C- and CP-violation via their complex Yukawa coupling, as well as departure from thermal equilibrium, either during freeze-out or freeze-in. As they are pure gauge singlets, these RH neutrinos can possess a Majorana mass beyond the standard Dirac mass given by the interaction with the Higgs field. This additional mass scale is however poorly constrained from a theoretical perspective and its magnitude critically affects the phenomenology associated with these new particles.

So-called low-scale seesaw models, where the Majorana mass lies below the TeV scale, are particularly attractive from a phenomenological viewpoint, as they are within reach of laboratory experiments. Such models are currently the subject of an intensive experimental research program, including direct searches at a broad range of fixed target experiments (e.g. at NA62 [199, 200] and the T2K near detector [201]) and collider facilities (e.g. at ATLAS [202], Belle [203] and CMS [204–208]). Looking ahead, this experimental program is set to expand further in the near future with the upcoming DUNE near detector [209–211], SHiP experiment [212–214] as well as the High Luminosity LHC (HL-LHC) [215, 216]. Beyond direct searches, the existence of RH neutrinos could also be signalled by the observation of e.g. lepton number or flavour violation. Current and upcoming experiments targeting neutrinoless double beta decay ($0\nu\beta\beta$) (see e.g. [217–220]) or $\mu$ to $e$ conversion (see e.g. [221–229]) may therefore provide decisive insights into their properties.

In view of this extensive program, it is essential to explore the parameter space of these models consistent with the requirement to reproduce neutrino masses and the BAU so as to single out the most promising regions and provide guidelines for experiments but also to maximize the insight gained from experimental results in the event of a detection. The second part of this thesis aims to take steps in this direction. In Chap. 3, we first briefly review the type-I seesaw mechanism, leptogenesis and various neutrino mass models. Then, in Chap. 4, we compute from first principles of nonequilibrium QFT the finite-temperature interaction rates of a generic fermion in Fermi-like theories. We apply our results to the specific case of RH neutrinos within the Neutrino Minimal Standard Model ($\nu$MSM) and in the minimal Left-Right Symmetric Model (mLRSM). Finally, we explore different phenomenological aspects of various neutrino mass models, focusing on the interplay between constraints set by leptogenesis and by various cosmological and laboratory experiments.

Chapter 3

# Models of neutrino masses and leptogenesis

In this third chapter, we will review the prerequisites necessary for the rest of this part II. We begin with a brief overview of light neutrino oscillation data. Next, we present the well-known type-I seesaw mechanism, followed in Sec. 3.3 by a brief review of leptogenesis. Finally, we finish in Secs. 3.4 and 3.5 by describing two possible extensions of the standard *vanilla* type-I seesaw model: one involving discrete symmetries, and another featuring additional gauge interactions. Different aspects of these scenarios will be examined in more detail in the next two chapters, Chap. 4 and Chap. 5.

## 3.1 Light neutrino oscillation data

First predicted by Pauli in 1930 [230] and discovered by Reines and Cowan a little more than 25 years later [231], neutrinos are the most elusive SM particles and extensive experimental efforts have been deployed to characterise their properties. It has since been established that they primarily interact through the weak interaction, with the corresponding Lagrangian given by

$$\mathcal{L}_{\text{weak}} \supset -\frac{g}{\sqrt{2}}\left(\overline{\nu_{L\alpha}}\gamma^\mu e_{L\alpha}W_\mu^+ + \overline{e_{L\alpha}}\gamma^\mu \nu_{L\alpha}W_\mu^- + \frac{1}{\sqrt{2}\cos\theta_W}\overline{\nu_\alpha}\gamma^\mu\nu_{L\alpha}Z_\mu\right) , \tag{3.2}$$

where $\theta_W \simeq 29°$ is the so-called Weinberg angle. The later observations of neutrino oscillations [232–235] entail that at least two (out of three) neutrinos are massive and that the (propagating) mass eigenstates $\nu_i,\ i \in \{1,2,3\}$ are linear combinations of the flavour eigenstates $\nu_{L\alpha}$ appearing in Eq. (3.2). This mixing is usually parametrised via the so-called Pontecorvo–Maki–Nakagawa–Sakata

(PMNS) matrix

$$\nu_i = \sum_\alpha \left(U_\nu\right)_{i\alpha} \nu_{L\alpha}. \tag{3.3}$$

This $3 \times 3$ matrix contains 6 free parameters and is typically parametrised in the following way

$$U_\nu = V^{(23)} U_\delta V^{(13)} U_{-\delta} V^{(12)} \mathrm{diag}(1, e^{i\alpha_1/2}, e^{i\alpha_2/2})\,, \tag{3.4}$$

with $U_{\pm\delta} = \mathrm{diag}(e^{\mp i\delta/2}, 1, e^{\pm i\delta/2})$. $\delta, \alpha_1$and $\alpha_2$ are the standard Dirac and Majorana CP-phases respectively. The non-zero entries of the matrices $V^{(ij)}$ are given by

$$\begin{gathered} V_{ii}^{(ij)} = V_{jj}^{(ij)} = \cos\theta_{ij}, \qquad V_{ij}^{(ij)} = -V_{ji}^{(ij)} = \sin\theta_{ij}, \\ V_{kk}^{(ij)} = 1 \quad \text{for } k \neq i, j\ , \end{gathered} \tag{3.5}$$

where $\theta_{ij}$ are the light neutrino mixing angles. As these phases could be rotated away in the limit of mass-degenerate neutrinos, neutrino oscillation experiments are also sensitive to the mass differences between neutrinos. Until now, these experiments have been able to constrain the so-called *solar mass splitting*, i.e. $\Delta m_{21}^2 = m_2^2 - m_1^2 > 0$. This leaves two possible orderings of the mass: 1) $m_1 < m_2 < m_3$, usually referred to as normal ordering (NO) or, equivalently, normal hierarchy, and 2) $m_3 < m_1 < m_2$, usually referred to as inverted ordering (IO) or, equivalently, inverted hierarchy. The splitting between the lightest and heaviest neutrinos ($\Delta m_{31}^2$ for NO, $\Delta m_{32}^2$ for IO) has also been accurately determined at various neutrino oscillation experiments and is usually known as the *atmospheric mass splitting*. A summary of the (experimental) best-fit values for all the above-mentioned parameters is provided in Tab. 3.1. We note the absence of constraints on the Majorana phases $\alpha_i$, which cannot be accessed at traditional neutrino oscillation experiments but could potentially by observing $0\nu\beta\beta$ processes.

Finally, we close this section by mentioning that, while it cannot be measured at neutrino oscillation experiments, the lightest neutrino mass $m_0 = \min(m_1, m_3)$ can be determined by studying the energy content of our universe. Currently, the best limit is set by Planck which constraint the sum of neutrino masses to be smaller than $0.12$ eV (at $95\%$ confidence level (C.L.)) [117]. This in turn yields the following upper limit on $m_0$

$$m_0 \equiv m_1 < 0.030 \text{ eV (NO)}, \qquad m_0 \equiv m_3 < 0.016 \text{ eV (IO)}\,. \tag{3.6}$$

| Parameter | Best-fit value (NO) | Best-fit value (IO) |
|---|---|---|
| $\sin^2\theta_{12}$ | $0.307$ | $0.308$ |
| $\sin^2\theta_{23}$ | $0.561$ | $0.562$ |
| $\sin^2\theta_{13}$ | $0.02195$ | $0.02224$ |
| $\Delta m^2_{21}$ [eV$^2$] | $7.49\times10^{-5}$ | $7.49\times10^{-5}$ |
| $\Delta m^2_{3l}$ [eV$^2$] | $2.534\times10^{-3}$ | $-2.510\times10^{-3}$ |
| $\delta$ [°] | $177$ | $285$ |

**Table 3.1:** Best-fit values for different light neutrino oscillation parameters, as obtained by the global fit $\nu$FIT [236]. The exact definition of the atmospheric mass splitting $\Delta m^2_{3l}$ depends on the neutrino mass ordering, see main text for details. We separate the constraint on $\delta$ from the rest as the measurement's accuracy is much weaker.

## 3.2 The type-I seesaw model

As emphasised in the introduction, RH neutrinos can explain the origin of both the neutrino masses and the BAU. Guided by a principle of minimality, the type-I seesaw model [123–128] constitutes the most general renormalisable extension of the SM that includes only a number $n_s$ of RH neutrino generations, which we will label $\nu_{Ri}$, $i\in\{1,\dots,n_s\}$. The corresponding Lagrangian reads

$$\mathcal{L}\supset \mathrm{i}\,\overline{\nu_{Ri}}\,\partial\!\!\!/\,\nu_{Ri}-\frac{1}{2}\overline{\nu^c_{Ri}}\,M_{Mij}\,\nu_{Rj}-Y_{\alpha i}\overline{\ell_{L\alpha}}\tilde{\Phi}\nu_{Ri}+\text{h.c.}\,, \tag{3.7}$$

where we define the charge-conjugated fields $\bar{\psi}^c=\overline{(\psi^c)}=\overline{C\bar{\psi}^T}$, with $C=-C^\dagger$ the unitary charge conjugation matrix, and write $\ell_{L\alpha}\equiv(\nu_{L\alpha},e_{L\alpha})^T$ for the lepton doublet of flavour $\alpha\in\{e,\mu,\tau\}$. In this expression, repeated indices are summed over. The $n_s\times n_s$ matrix $M_M$ is the so-called Majorana mass of the RH neutrinos while $Y$ is a $3\times n_s$ matrix of complex Yukawa couplings. In Eq. (3.7), we can always rotate the RH neutrino fields such that $M_M$ is diagonal.

Below the EWSB, the Higgs field acquires a vev which, in vacuum, takes the value $\langle\Phi\rangle=(v_{\text{ew}},0)^T$, with $v_{\text{ew}}\simeq 174.1$ GeV [104]. As a result, the neutrino mass term reads

$$\frac{1}{2}\begin{pmatrix}\bar{\nu}_L & \bar{\nu}^c_R\end{pmatrix}\begin{pmatrix}0 & m_D\\ m_D^T & M_M\end{pmatrix}\begin{pmatrix}\nu^c_L\\ \nu_R\end{pmatrix}+\text{h.c.} \tag{3.8}$$

where the Dirac mass term reads $m_D = v_{\rm ew} Y$. In the so-called *seesaw limit* $m_D \ll M_M$, one can diagonalise the mass term (3.8) and we find the eigenstates

$$\nu_i = \Big[V_\nu^\dagger \nu_L - U_\nu^\dagger \theta \nu_R^c + V_\nu^T \nu_L^c - U_\nu^T \theta^* \nu_R\Big]_i \,, \tag{3.9a}$$

$$N_i = \Big[V_N^\dagger \nu_R + \Theta^T \nu_L^c + V_N^T \nu_R^c + \Theta^\dagger \nu_L\Big]_i \,, \tag{3.9b}$$

where the mixing matrix between LH and RH neutrinos can be written

$$\theta = v_{\rm ew} Y M_M^{-1} \ll 1 \,. \tag{3.10}$$

The corresponding mass eigenvalues reads

$$m_\nu = -\theta M_M \theta^T = -v_{\rm ew}^2 Y M_M^{-1} Y^T \tag{3.11}$$

for the light eigenstate $\nu$ whereas they read

$$M_N = M_M + \frac{1}{2}(\theta^\dagger \theta M_M + M_M^T \theta^T \theta^*) \tag{3.12}$$

for the heavy eigenstates. In Eq. (3.9), the matrix $V_\nu = (1 - \frac{1}{2}\theta\theta^\dagger)U_\nu$ diagonalise $m_\nu$ whereas $V_N = (1 - \frac{1}{2}\theta^T\theta^*)U_N$ diagonalises $M_N$, i.e.

$$V_\nu^\dagger \, m_\nu \, V_\nu^* = \mathrm{diag}\,(m_1, m_2, m_3), \quad V_N^\dagger \, M_N \, V_N^* = \mathrm{diag}\,(M_1, \dots, M_{n_s}) \,. \tag{3.13}$$

Eq. (3.11) is commonly referred to as the *seesaw* relation. We note in passing that $U_\nu$ is always unitary, so that any non-unitarity in neutrino oscillations is entirely captured by $V_\nu$. In the seesaw limit, we have $M_N \simeq M_M \gg m_\nu$. Hence, we will refer in the follow to the $\nu_i$'s as the light neutrinos while the $N_i$'s will be known as *heavy neutrinos* or also heavy neutral leptons (HNLs).[1]

From the seesaw relation (3.11), it is evident that at least two RH neutrino generations are required to account for the two observed neutrino mass splittings. While $n_s$ is not bounded from above, we will focus in the rest of this work on the two most minimal scenarios: $n_s = 2$ and $n_s = 3$. In the minimal case $n_s = 2$, the lightest neutrinos is necessarily massless ($m_0 = 0$) and only one linear combination of the Majorana phases remains physical, which we usually write $\eta \equiv \frac{1}{2}(\alpha_{21} - \alpha_{31})$ for NO and $\eta \equiv \frac{1}{2}\alpha_{21}$ for IO.

[1] While these terms are not strictly equivalent, we will use them interchangeably throughout the remainder of this thesis.

Finally, we also note that the mixing

$$\Theta = \theta\, U_N^* \tag{3.14}$$

captures the suppression of the weak interaction undergone by the HNLs. Below the EWSB, HNL interactions are indeed captured by the Lagrangian

$$\mathcal{L} \supset -\frac{m_W}{v_{\rm ew}}\overline{N}_i\Theta^*_{\alpha i}\gamma^\mu e_{L\alpha}W^+_\mu - \frac{m_Z}{\sqrt{2}v_{\rm ew}}\overline{N}_i\Theta^*_{\alpha i}\gamma^\mu \nu_{L\alpha}Z_\mu - \frac{M_i}{v_{\rm ew}}\Theta_{\alpha i}\varphi\overline{\nu_L}_\alpha N_i + \text{h.c.}\,, \tag{3.15}$$

with $\varphi$ the Higgs field. Because $\theta \ll 1$, we can in general neglect the $\mathcal{O}(\theta^2)$-corrections to the mixing matrices $V_\nu$ and $V_N$. However, as we will see later, this might not be the case for the HNL mass matrix (3.12) if the Majorana mass matrix is close to diagonal, which is typical in the collider-testable region of the parameter space. We will go back to this aspect later. In the limit where HNL productions and decays are independent, the number of events at accelerator-based experiments is mostly sensitive to the derived quantities

$$U^2_{\alpha i} = |\Theta_{\alpha i}|^2\ ,\ U_i^2 = \sum_\alpha U^2_{\alpha i}\ ,\ U^2_\alpha = \sum_i U^2_{\alpha i}\ \text{ and }\ U^2 = \sum_i U_i^2 = \sum_\alpha U^2_\alpha\ . \tag{3.16}$$

Ignoring the matrix structure in flavour space of $\theta$, these quantities can naively be estimated from the seesaw relation (3.11), yielding

$$U_i^2 \sim \frac{\sum_j m_j}{M_i} \sim 10^{-10}\frac{\text{GeV}}{M_i}\ , \tag{3.17}$$

We will later refer to this limit as the *naive seesaw limit*.

### 3.2.1 Low-scale seesaw models and approximate $B-L$ symmetry

While the requirement to reproduce the neutrino masses constrain the form of the Yukawa coupling, see Sec. 3.2.2 for more details, the Majorana mass scale is barely limited from an experimental viewpoint. Assuming that the Yukawa couplings remain perturbative, the seesaw relation (3.11) translates into an upper bound on the Majorana mass scale

$$M_M \lesssim v^2_{\rm ew}/m_\nu \lesssim \mathcal{O}(10^{15})\ \text{GeV}\ \ , \tag{3.18}$$

but it can otherwise range from zero, in which case neutrinos are Dirac particles, all the way up to this canonical seesaw scale. Additional constraints do exist from a theoretical perspective. Unitarity requirements on neutrino annihilations into $W$ and $Z$ bosons yield a similar upper bound of $\mathcal{O}(10^{15})$ GeV on $M_M$ [237]. Moreover, the existence of RH neutrinos generate additional contributions to the Higgs mass and potential. Constraints from naturalness yield the upper bound $M_M \lesssim 10^7$ GeV [238, 239] whereas electroweak vacuum metastability puts a bound on a combination of $M_M$ and $Y$, see e.g. [240–246]. We however caution that these bounds assume the absence of additional new physics beyond RH neutrinos, which is far from certain.

Motivated by testability prospects, we will in the following focus on low-scale models, where $M_M \lesssim \mathcal{O}(10^4)$ GeV. In this regime, the naive estimate (3.17) would, if taken at face value, severely limit the possibility of RH neutrino direct detection in the near future. However, low-scale seesaw models can be endowed with a (generalised) approximate $B-L$ symmetry[2] [247–249] for which the lightness of the neutrino masses does not arise from the large Majorana mass $M_M$ but from the smallness of the $B-L$ symmetry breaking. In such scenarios and taking as illustration the minimal case with two generations of RH neutrinos, the Yukawa coupling and Majorana mass matrices would typically take the schematic form

$$Y = \begin{pmatrix} y_e(1+\epsilon_e) & iy_e(1-\epsilon_e) \\ y_\mu(1+\epsilon_\mu) & iy_\mu(1-\epsilon_\mu) \\ y_\tau(1+\epsilon_\tau) & iy_\tau(1-\epsilon_\tau) \end{pmatrix}, \quad M_M = \bar{M}\mathrm{diag}(1-\mu, 1+\mu) \tag{3.19}$$

in the mass basis. In the $B-L$ symmetric limit $\epsilon_\alpha, \mu \to 0$, the two RH neutrinos combine into a pseudo-Dirac pair and cancellations in the seesaw relation (3.11) ensure that all neutrino masses vanish exactly, regardless of the size of the Yukawa coupling $y_\alpha$. Slightly deviating from this symmetric limit, the smallness of the light neutrino masses can therefore be made consistent with active-sterile mixing angles much larger than the estimate (3.17) in a technically natural way. In fact, one can even show [250] that Eq. (3.17) merely acts as a lower bound on the value of the HNL mixing angles. Beyond the minimal field content of Lagrangian (3.7), specific examples where such symmetry-protected scenarios appear include the inverse [251–253] and linear [254, 255] seesaw mechanisms.

[2] Here, $L$ denotes a generalised lepton number, which encompasses the RH neutrinos.

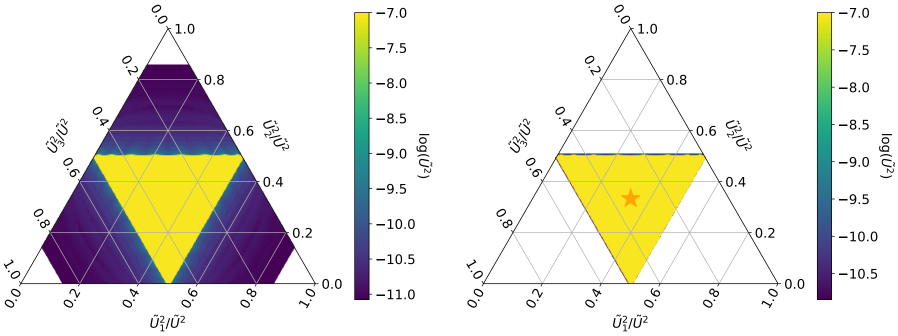


**(a)** **(b)**

**Figure 3.1:** Range of allowed[3] $\tilde{U}_i^2/\tilde{U}^2$ for $m_0 = 0$ eV, shown for both normal ordering (left) and inverted ordering (right). The orange star indicates the first benchmark listed in Tab. 5.1, see Chap. 5 for details. The colour bar indicates the maximal value of $\tilde{U}^2$ that can be reached for specific flavour ratios. Figure taken from [6].

For $n_s = 3$, the situation differs slightly. The Yukawa coupling matrix (3.19) can be extended to

$$Y = \begin{pmatrix} y_e(1+\epsilon_e) & iy_e(1-\epsilon_e) & \epsilon'_e \\ y_\mu(1+\epsilon_\mu) & iy_\mu(1-\epsilon_\mu) & \epsilon'_\mu \\ y_\tau(1+\epsilon_\tau) & iy_\tau(1-\epsilon_\tau) & \epsilon'_\tau \end{pmatrix}, \tag{3.20}$$

which approximately conserves $B-L$ as long as $\epsilon'_\alpha \ll 1$. In this limit, two RH neutrinos again combine into a pseudo-Dirac pair, each carrying half of the total mixing, i.e. $U_i^2/U^2 \simeq 1/2$ for $i \in \{1,2\}$, while the third one effectively decouples. However, we emphasise that the form (3.20) is not universal. If all three RH neutrinos are nearly degenerate, the Yukawa couplings do not necessarily exhibit the same hierarchical pattern in the $B-L$-symmetric limit. Fig. 3.1 displays the fraction of the total mixing carried by each of the three RH neutrinos for various values of $U^2$. The $B-L$-symmetric limit is highlighted in yellow. As can be seen, in the large-$U^2$ limit, all three RH neutrinos can have comparable Yukawa couplings, with the only restriction being that none carries more than $50\%$ of the total mixing.

### 3.2.2 Casas-Ibarra parametrisation

Until now, we have considered the Yukawa coupling to be a generic $3 \times n_s$ complex matrix. In order to reproduce the observed light neutrino mixing

[3]The $\tilde{U}_i^2$ reduce to the standard $U_i^2$ in the mass-degenerate limit, see e.g. Eq. (5.1) and the discussion below.

parameter, it should however fulfil the seesaw relation (3.11). In the Majorana mass basis, the so-called *Casas-Ibarra parametrisation* [256][4]

$$Y \simeq \frac{i}{v_{\rm ew}} U_\nu \sqrt{m_\nu^{\rm diag}} \mathcal{R} \sqrt{M_M} \tag{3.21}$$

provides a convenient way to automatically accommodate light neutrino oscillation data at tree level. In this equation, $m_\nu^{\rm diag} = {\rm diag}(m_1, m_2, m_3)$ and $\mathcal{R}$ is a complex $3 \times n_s$ matrix verifying $\mathcal{R}\mathcal{R}^T = \mathbb{1}_{3\times 3}$. In the minimal scenario $n_s = 2$, this matrix can be parametrised as[5]

$$\mathcal{R}_{\rm NO} = \begin{pmatrix} 0 & 0 \\ \cos(\omega + i\gamma) & \sin(\omega + i\gamma) \\ -\sin(\omega + i\gamma) & \cos(\omega + i\gamma) \end{pmatrix} \tag{3.22}$$

in the case of NO, and as

$$\mathcal{R}_{\rm IO} = \begin{pmatrix} \cos(\omega + i\gamma) & \sin(\omega + i\gamma) \\ -\sin(\omega + i\gamma) & \cos(\omega + i\gamma) \\ 0 & 0 \end{pmatrix} , \tag{3.23}$$

for IO. In these expressions, $\omega$ and $\gamma$ are both real numbers. In the next-to-minimal scenario $n_s = 3$, different parametrisations of $\mathcal{R}$ exist. We find convenient to use the parametrisation introduced in [1]

$$\mathcal{R} = {\rm O}_\nu {\rm R}_{\rm C} {\rm O}_{\rm N} , \tag{3.24}$$

where we define

$${\rm O}_\nu = \begin{pmatrix} {\rm c}_{\nu 2} & 0 & {\rm s}_{\nu 2} \\ 0 & 1 & 0 \\ -{\rm s}_{\nu 2} & 0 & {\rm c}_{\nu 2} \end{pmatrix} \cdot \begin{pmatrix} 1 & 0 & 0 \\ 0 & {\rm c}_{\nu 1} & {\rm s}_{\nu 1} \\ 0 & -{\rm s}_{\nu 1} & {\rm c}_{\nu 1} \end{pmatrix} , \tag{3.25}$$

$${\rm O}_{\rm N} = \begin{pmatrix} 1 & 0 & 0 \\ 0 & {\rm c}_{\rm N1} & {\rm s}_{\rm N1} \\ 0 & -{\rm s}_{\rm N1} & {\rm c}_{\rm N1} \end{pmatrix} \cdot \begin{pmatrix} {\rm c}_{\rm N2} & 0 & {\rm s}_{\rm N2} \\ 0 & 1 & 0 \\ -{\rm s}_{\rm N2} & 0 & {\rm c}_{\rm N2} \end{pmatrix} , \tag{3.26}$$

[4]Beyond the seesaw limit, generalisations of the Casas-Ibarra parametrisation can be found [257,258].

[5]For $n_s = 2$, only a submatrix of $\mathcal{R}\mathcal{R}^T$ corresponds to the identity matrix since rank of the light neutrino mass matrix is 2. In the following, the sign of the determinant of this submatrix has been set to $+1$. While in principle the opposite sign is also compatible with the orthogonality condition, one can show, see e.g. footnote 6 of [259], that it can be absorbed by shifting other parameters and is therefore unphysical.

and

$$\mathrm{R_C} = \begin{pmatrix} \cos(\omega + i\gamma) & \sin(\omega + i\gamma) & 0 \\ -\sin(\omega + i\gamma) & \cos(\omega + i\gamma) & 0 \\ 0 & 0 & 1 \end{pmatrix} . \tag{3.27}$$

As a shorthand notation, we introduced the quantities $\mathrm{c}_{\nu i}$, $\mathrm{s}_{\nu i}$, $\mathrm{c}_{\mathrm{N}i}$ et $\mathrm{s}_{\mathrm{N}i}$ to denote the cosine and sine of the angles $\theta_{\nu i}$ and $\theta_{\mathrm{N}i}$ respectively. The parametrisation (3.24) possesses the appealing property that the overall size of the active-sterile mixing $U_{\alpha i}^2$ can be expressed in terms of a single parameter, namely

$$\epsilon = e^{-2\gamma} . \tag{3.28}$$

Moreover, the dependence on the two real angles $\theta_{N1}, \theta_{N2}$ approximately drops out of the mixing angles $U_\alpha^2$ (assuming small HNL mass splittings), which greatly facilitates parameter space scans such as those performed in Sec. 5.1. We note that the Casas-Ibarra exhausts the entire parameter space of the type-I seesaw model and, in particular, captures the $B-L$-symmetric limit discussed above. The latter corresponds to the limit $\gamma \gg 1$ or, equivalently, $\epsilon \ll 1$. In this regime, we have

$$\mathrm{R_C} \simeq \frac{e^{-i\omega}}{2} e^{\gamma} \begin{pmatrix} 1 & i & 0 \\ -i & 1 & 0 \\ 0 & 0 & 0 \end{pmatrix} . \tag{3.29}$$

As an illustration, it is straightforward to show that, in the large-$\gamma$ limit, the structure of the Yukawa matrix in Eq. (3.20) can be recovered for $\theta_{N1} = \theta_{N2} = \pi/2$.

Before concluding this subsection, we briefly highlight two additional points of interest. First, the Casas-Ibarra parametrisation (3.21) makes the number of free parameters in the type-I seesaw model apparent. For an arbitrary number of generations $n_s$, $7n_s - 3$ parameters are needed to accommodate the light neutrino oscillation data. Considering that 5 of these are fixed by experiments, see Tab. 3.1,[6] we conclude that 6 and 11 free parameters are required for $n_s = 2$ and $n_s = 3$ respectively. Second, as briefly highlighted in footnote 5, different transformations of these parameters keep the Yukawa matrix invariant. Using these redundancies, one can reduce the fundamental domain

[6] The Dirac CP-phase $\delta$ is not yet measured precisely enough to be treated as a fixed parameter.

| $\theta_{\nu 1}$ | $\theta_{\nu 2}$ | $\theta_{\mathrm{N}1}$ | $\theta_{\mathrm{N}2}$ | $\omega$ | $\gamma$ | $\alpha_{1,2}$ |
|---|---|---|---|---|---|---|
| $[0,\pi]$, | $[0,\pi]$, | $[0,2\pi]$, | $[0,2\pi]$, | $[0,\pi]$, | $\mathbb{R}_+$, | $[0,4\pi]$ |
| $[0,\pi]$, | $[0,\pi]$, | $[0,\pi/2]$, | $[0,2\pi]$, | $[0,2\pi]$, | $\mathbb{R}$, | $[0,4\pi]$ |
| $[0,\pi]$, | $[0,\pi]$, | $[0,2\pi]$, | $[0,2\pi]$, | $[0,\pi/2]$, | $\mathbb{R}$, | $[0,4\pi]$ |
| $[0,\pi]$, | $[0,\pi]$, | $[0,\pi]$, | $[0,\pi]$, | $[0,2\pi]$, | $\mathbb{R}$, | $[0,4\pi]$ |
| $[0,\pi]$, | $[0,\pi]$, | $[0,\pi]$, | $[0,2\pi]$, | $[0,\pi]$, | $\mathbb{R}$, | $[0,4\pi]$ |

**Table 3.2:** Possible choices for the fundamental domains of parameters entering the Casas-Ibarra parametrisation (3.21) that cover all values of $Y$. We assume $\delta$ to be fixed. Table taken from [6].

of these free parameters. In Tab. 3.2, we list possible choices for their fundamental domain for the case $n_s = 3$ (and assuming $\delta$ is fixed).

### 3.2.3 Radiative corrections to the light neutrino masses

While the Casas-Ibarra parametrisation (3.21) ensures that the type-I seesaw model reproduces the light neutrino oscillation data at tree level, loop corrections could in principle spoil this agreement. At the one-loop level, the radiative correction to $m_\nu$ is given by [260]

$$m_\nu^{1-\text{loop}} = -\frac{2}{(4\pi v_{\text{ew}})^2}\theta\, l(M_N^2) M_N \theta^T\,, \tag{3.30}$$

where we define the loop function

$$l(x) = \frac{x}{2}\left(\frac{3\ln(x/m_Z^2)}{x/m_Z^2 - 1} + \frac{\ln(x/m_H^2)}{x/m_H^2 - 1}\right)\,. \tag{3.31}$$

$m_Z$ and $m_H$ denote the $Z$ boson and Higgs masses, respectively. Due to the relatively simple structure of these one-loop corrections, the Casas-Ibarra parametrisation can be straightforwardly generalised to include them, see [261].

## 3.3 Introduction to low-scale leptogenesis

We now briefly review the leptogenesis mechanism and how the evolution of RH neutrinos in the early universe can be modelled. We refer the interested reader to Refs. [262–270] for more detailed reviews on various aspects of leptogenesis.

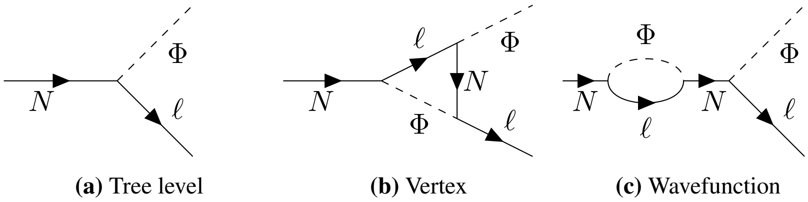


**Figure 3.2:** (Left) Feynman diagram representing the tree-level decay of an HNL into a Higgs and a lepton doublet. (Middle) Vertex correction to this decay at the one-loop level. (Right) Wavefunction correction to this decay at the one-loop level.

## 3.3.1 Leptogenesis in a nutshell

As highlighted in the introduction, right-handed neutrinos could also generate the BAU in addition to explaining the origin of the neutrino masses. This was first realised in [129].

In its most simple incarnation, leptogenesis essentially relies on the decay of the lightest HNL into a Higgs and a lepton doublet. Because the RH neutrino Yukawa couplings can be complex, the interference between the tree-level HNL decay amplitude and the so-called (one-loop) vertex correction to this amplitude can provide the necessary CP-violation. Both diagrams are represented in Fig. 3.2, see diagrams (a) and (b). Assuming at first the HNL mass spectrum to be hierarchical, one can safely neglect the contribution from different RH neutrino generations as well as the so-called *wavefunction* contribution, see diagram (c) in Fig. 3.2. The HNL decay rate into leptons then differs from that into anti-leptons, an asymmetry which is typically parametrised via the so-called decay asymmetry parameter

$$\epsilon_N \equiv \frac{\Gamma_{N\to\ell+\Phi} - \Gamma_{N\to\bar{\ell}+\Phi^*}}{\Gamma_{N\to\ell+\Phi} + \Gamma_{N\to\bar{\ell}+\Phi^*}} \,. \tag{3.32}$$

If the Yukawa couplings of the RH neutrinos are sufficiently weak for their decays to occur out of equilibrium, this will result a non-zero asymmetry in the lepton sector. Assuming the relevant dynamics happens in the unflavoured regime ($T \gtrsim \mathcal{O}(10^{12})$ GeV), i.e. assuming the different SM flavours cannot be distinguished, the evolutions of the HNL number density $n_N$ as well as of the abundance of $B-L$ asymmetry $n_{B-L}$ in this minimal framework are captured by the set of coupled Boltzmann equations

$$\frac{\mathrm{d}}{\mathrm{d}z} n_N = -\frac{\Gamma_D + \Gamma_S}{Hx}(n_N - n_N^{\mathrm{eq}}) \,, \tag{3.33a}$$

$$\frac{\mathrm{d}}{\mathrm{d}z} n_{B-L} = \epsilon_N \frac{\Gamma_D}{Hz}(n_N - n_N^{\mathrm{eq}}) - \frac{\Gamma_W}{Hz} n_{B-L} \,, \tag{3.33b}$$

with $z \equiv M/T$ the ratio between the HNL mass and the bath temperature. In the above equation, $\Gamma_D$ and $\Gamma_S$ denote the HNL decay and scattering rates respectively while $\Gamma_W$ captures the rate at which the asymmetry is washed out by inverse decays and lepton number violating scatterings.

Because the processes represented in Fig. 3.2 can only lead to a non-zero lepton asymmetry, the last ingredient needed is a violation of the baryon number. As mentioned in the introduction, this is naturally provided by the sphaleron process, which is a non-perturbative, $B-L$-conserving process associated with the anomalous violation of the global $B+L$ symmetry in the SM. While the rate at which such $B+L$ violation proceeds is heavily suppressed in vacuum [271, 272], the energy provided by a surrounding thermal bath facilitates the crossing of the potential barrier between different gauge vacua and therefore drastically enhances the sphaleron rate [184]. The precise calculation of this rate has been the subject of intensive studies, see e.g. [273–277], which have shown this process to be relevant in the temperature range $T_{\text{sph}} \equiv 131.7\text{ GeV} \lesssim T \lesssim 10^{12}$ GeV.

This minimal framework, however, is severely constrained. The decay asymmetry (3.32) is indeed bounded from above, which, combined with estimates for the strength of the washout [278], leads to a lower bound on the HNL mass [279]

$$M_N \gtrsim 2 \times 10^9 \text{ GeV} , \tag{3.34}$$

as well as an upper bound on the lightest neutrino mass [280–282]. More comprehensive analyses of the leptogenesis parameter space, including the full impact of flavour effects, have since then shown that this bound can be lowered by up to three orders of magnitude [283,284]. RH neutrinos would nonetheless remain out of reach of direct searches in this scenario. Fortunately, there exist two ways to circumvent this lower bound, dubbed *resonant leptogenesis* and *leptogenesis from neutrino oscillations*, which we briefly describe below.

**Resonant leptogenesis:** The lower bound (3.34) only accounts for the contribution of the vertex diagram to the decay asymmetry. While this is a good approximation for hierarchical HNLs, the wavefunction diagram shown in Fig. 3.2 is enhanced for close-to-degenerate HNLs. Its contribution to the decay asymmetry (3.32) is resonantly enhanced [285–288] and peaks for HNL mass splittings comparable to their decay widths. As first pointed out in Refs. [289–292], this observation can be used to lower the scale of leptogenesis. Detailed numerical studies [1, 293] have found this enhancement to be sufficient for leptogenesis to remain viable for HNL masses as low as $\mathcal{O}(1)$ GeV.

**Leptogenesis from neutrino oscillations:** Instead of producing the asymmetry during the HNL freeze-out, an alternative approach [121, 168], sometimes also known as Akhmedov-Rubakov-Smirnov (ARS) leptogenesis, consists in producing the asymmetry during the HNL approach to equilibrium by CP-violating oscillations between the different flavours. This mechanism typically also requires a mild degeneracy between the HNL masses, although it has been shown to work with $\mathcal{O}(1)$ mass splittings [294]. In this scenario, the lower bound on the HNL mass is further pushed to masses $M_N \sim \mathcal{O}(100)$ MeV [1, 293].[7]

It was recently shown [1, 169, 293] that the temperature ranges at which these mechanisms are effective widely overlap and cover the entire experimentally accessible range. In practice, the two scenarios can be described by the same set of evolution equations [269, 296] which we will describe in the next subsection.

### 3.3.2 Right-handed neutrino quantum kinetic equations

The quest for an accurate, first-principles description of the RH neutrino time evolution has been a long-standing focus of many theoretical investigations, most of which are rooted in the CTP formalism, as highlighted by the references [43, 135, 169, 267, 296–313]; see also [266, 269] for reviews. While the evolution of HNLs can still be precisely described by Boltzmann equations in the limit of fast oscillations [169, 266, 308, 314], these in general cannot consistently describe RH neutrino oscillation which are essential for HNL masses within reach of direct searches. In this case, one needs to keep track of the time dependence of the entire matrix of densities $\rho$ ($\bar{\rho}$) of HNLs with positive (negative) helicities. In the rest of this work, we will work with the following

[7] While leptogenesis itself remains viable below 100 MeV, the interplay between constraints from BBN and direct experimental searches tends to rule out lower masses [295].

set of quantum kinetic equations (QKEs) which includes all relevant effects[8]

$$i\frac{\mathrm{d}\delta\rho}{\mathrm{d}t} = -i\frac{\mathrm{d}\rho_{\mathrm{eq}}}{\mathrm{d}t} + [H_N, \delta\rho] - \frac{i}{2}\{\Gamma, \delta\rho\} - i\sum_{\alpha\in\{e,\mu,\tau\}} \frac{\mu_\alpha}{T}\tilde{\Gamma}_\alpha f_N^{\mathrm{eq}}(1-f_N^{\mathrm{eq}}), \tag{3.35a}$$

$$i\frac{\mathrm{d}\delta\bar{\rho}}{\mathrm{d}t} = -i\frac{\mathrm{d}\rho_{\mathrm{eq}}}{\mathrm{d}t} - [H_N, \delta\bar{\rho}] - \frac{i}{2}\{\Gamma, \delta\bar{\rho}\} + i\sum_{\alpha\in\{e,\mu,\tau\}} \frac{\mu_\alpha}{T}\tilde{\Gamma}_\alpha f_N^{\mathrm{eq}}(1-f_N^{\mathrm{eq}}), \tag{3.35b}$$

$$i\frac{\mathrm{d}}{\mathrm{d}t}n_{\Delta_\alpha} = -\frac{2i\mu_\alpha}{T}\int\frac{\mathrm{d}^3\mathbf{k}}{(2\pi)^3}\mathrm{Tr}[\Gamma_\alpha f_N^{\mathrm{eq}}(1-f_N^{\mathrm{eq}})] + i\int\frac{\mathrm{d}^3\mathbf{k}}{(2\pi)^3}\mathrm{Tr}[\tilde{\Gamma}_\alpha(\delta\bar{\rho}-\delta\rho)], \tag{3.35c}$$

with $\delta\rho \equiv \rho - \rho_{\mathrm{eq}}$ the deviation from the equilibrium heavy neutrino matrix of density $\rho_{\mathrm{eq}}$. $\rho_{\mathrm{eq}}$ is diagonal and reads $f_N^{\mathrm{eq}}\mathbb{1}_{n_s\times n_s}$ in the high-temperature regime where $f_{N_1}^{\mathrm{eq}} = f_{N_2}^{\mathrm{eq}} = \cdots \equiv f_N^{\mathrm{eq}}$. The coefficients $\mu_\alpha$ are the SM chemical potentials, which can be related to the matter-antimatter flavour asymmetries $n_{\Delta_\alpha}$ by a susceptibility matrix $\mu_\alpha = \chi_{\alpha\beta}n_{\Delta_\beta}$. This matrix captures the impact of spectator processes [315, 316], i.e. SM processes redistributing charges during leptogenesis. While this matrix is in general temperature-dependent [317, 318], it is a reasonable approximation for[9] $T_{\mathrm{sph}} \lesssim T \lesssim 10^5$ GeV to use the temperature-independent result

$$\chi = -\frac{2}{711}\begin{pmatrix} 257 & 20 & 20 \\ 20 & 257 & 20 \\ 20 & 20 & 257 \end{pmatrix}. \tag{3.36}$$

We note in passing that the susceptibility matrix displayed above includes the impact of the sphaleron process assuming it is in equilibrium at all times. Therefore, this approach neglects the impact of non-instantaneous sphaleron decoupling, which can lead to sizeable errors in case the baryon asymmetry is produced close to $T = T_{\mathrm{sph}}$ [318]. In Eq. (3.35), $H_N$ denotes the effective Hamiltonian of the model while $\Gamma$ and $\tilde{\Gamma}$ represent the different interaction rates. These coefficients and, in particular, their finite-temperature behaviour, have been already extensively studied within the type-I seesaw model in pre-

[8] Some debate remains about whether mixing and oscillations inherently constitute two distinct phenomena, see [309], or not, see [296, 311, 313]. In what follows, we adopt the approach developed in the latter works.

[9] Above $T \simeq 30$ TeV, the RH electron stops being in chemical equilibrium [319] and the susceptibility matrix should be modified in consequence. See e.g. [44, 315] for an explicit form of this matrix in different temperature regimes.

vious works, see e.g. Refs. [135, 269, 320] for reviews. We use in the rest of this thesis the Hamiltonian and rates provided by Ref. [169], which extrapolates to the non-relativistic regime the results of [311]. Finally, we note that, at a technical level, the derivation of the set of equations (3.35) assumes that i) all HNLs have the same energy. This assumptions breaks down in the non-relativistic regime for large HNL mass splittings $\frac{\Delta M}{M} \sim 1$, and ii) that one can expand to linear order in $\delta\rho$ and $\mu$. In particular, it neglects term proportional to $\mu\delta\rho$ which are not necessarily parametrically small during freeze-in and can lead to $\mathcal{O}(1)$ errors. For a step-by-step derivation of the set of equations (3.35) from the Kadanoff-Baym equations (1.61), we refer the reader to e.g. appendix B of [44].

Though not explicitly displayed, the set of equations (3.35) is momentum-dependent. While it is possible to retain the full momentum-dependence for specific benchmarks [321–324], it is in general too expensive numerically to do so when performing large parameter space scans. For this reason, we approximate the HNL matrix of densities with the ansatz

$$\delta\rho \approx \frac{\delta n}{n_N^{\mathrm{eq}}} f_N^{\mathrm{eq}} \,. \tag{3.37}$$

This ansatz can be justified by the observation that HNLs are produced from (or freeze out of) a thermal bath with temperature $T$, and are therefore expected to approximately retain its momentum distribution. Besides, the set of equations (3.35) can only describe the time evolution of HNLs and of the baryon asymmetry in a Minkowski background. In order to incorporate the expansion of the universe, we use the approach detailed in [43]. Defining the yield

$$\delta Y_N = \frac{\delta n}{s} \,, \qquad \delta \bar{Y}_N = \frac{\delta \bar{n}}{s} \,, \qquad Y_{\Delta_\alpha} = \frac{n_{\Delta_\alpha}}{s} \tag{3.38}$$

as well as $z = T_{\mathrm{sph}}/T$, we obtain the momentum-averaged QKEs

$$\begin{aligned} i\, z\mathcal{H} \frac{\mathrm{d}\delta Y_N}{\mathrm{d}z} &= -i\, z\mathcal{H} \frac{\mathrm{d}Y_N^{\mathrm{eq}}}{\mathrm{d}z} && \text{(3.39a)} \\ &\quad + [\langle H_N \rangle_S, Y_N] - \frac{i}{2} \{\langle \Gamma \rangle_S, \delta Y_N\} - \frac{i}{2} \sum_\alpha \langle \tilde{\Gamma}_\alpha \rangle_W \, 2\frac{\mu_\alpha}{T} \frac{n_\nu^{\mathrm{eq}}}{s}, \\ i\, z\mathcal{H} \frac{\mathrm{d}\delta \bar{Y}_N}{\mathrm{d}z} &= -i\, z\mathcal{H} \frac{\mathrm{d}Y_N^{\mathrm{eq}}}{\mathrm{d}z} && \text{(3.39b)} \\ &\quad - [\langle H_N \rangle_S, \bar{Y}_N] - \frac{i}{2} \{\langle \Gamma \rangle_S, \delta \bar{Y}_N\} + \frac{i}{2} \sum_\alpha \langle \tilde{\Gamma}_\alpha \rangle_W \, 2\frac{\mu_\alpha}{T} \frac{n_\nu^{\mathrm{eq}}}{s}, \end{aligned}$$

$$iz\mathcal{H}\frac{\mathrm{d}Y_{\Delta_\alpha}}{\mathrm{d}z} = -2i\frac{n_\nu^{\mathrm{eq}}}{s}\frac{\mu_\alpha}{T}\mathrm{Tr}[\langle\Gamma_\alpha\rangle_W] + i\,\mathrm{Tr}[\langle\tilde{\Gamma}_\alpha\rangle_S\,(\delta\bar{Y}_N - \delta Y_N)]\,. \quad (3.39c)$$

In this equation, we define the two averages

$$\langle X\rangle_W = \frac{1}{n_\nu^{\mathrm{eq}}}\int\frac{\mathrm{d}^3\mathbf{k}}{(2\pi)^3}X f_N^{\mathrm{eq}}(1-f_N^{\mathrm{eq}})\,, \langle X\rangle_S = \frac{1}{n_N^{\mathrm{eq}}}\int\frac{\mathrm{d}^3\mathbf{k}}{(2\pi)^3}X f_N^{\mathrm{eq}}\,. \quad (3.40)$$

We in general expect this momentum-averaging procedure, which may introduce $\mathcal{O}(1)$ errors [321, 324], to be the leading source of uncertainty. In Eq. (3.39), $\mathcal{H} \equiv 3c_s^2 H$, $c_s$ being the speed of sound in the early universe plasma [325, 326], denotes the effective Hubble parameter and accounts for the temperature-dependence of the number of relativistic degrees of freedom. However, $c_s^2 = 1/3$ at all relevant times up to (at most) an $\mathcal{O}(4\%)$ deviation during the electroweak crossover [325, 326]. Hence, given the relative size of the remaining uncertainties, it is in practice safe to set $\mathcal{H} = H$.[10]

### 3.3.3 The Neutrino Minimal Standard Model

As highlighted before, the number of RH neutrino generations $n_s$ should be larger than (or equal to) 2 to reproduce the observed neutrino masses. Leptogenesis do not impose any further constraints and is viable for any $n_s \geq 2$. Within the minimal setup $n_s = 2$, low-scale leptogenesis has already been extensively studied [328–330] (see also [169, 293, 331] for recent studies) especially because it can be straightforwardly embedded in the so-called $\nu$MSM [121, 332]. The $\nu$MSM distinguishes itself by its minimality, predictivity and testability. In this scenario, three generations of RH neutrinos are added to the SM particle content, two of which lie at the GeV-scale and are responsible for the origin of both the neutrino masses and the BAU. In contrast, the third RH neutrino generation has a much smaller mass, $\mathcal{O}$(keV), almost decouples and can therefore serve as a viable DM candidate [130, 131]. To make the distinction with the two heavier HNLs, we typically refer to the lightest HNL as the *sterile neutrino*. Due to its small mass, it could potentially explain the excess observed at $\sim 3.5$ keV in the X-ray spectra of galaxy clusters [333, 334].[11] In

[10] Close to equilibrium, this is not necessarily the case as the varying number of degrees of freedom provides an additional contribution to $\mathrm{d}Y_N^{\mathrm{eq}}/\mathrm{d}z$, which survives even in the massless limit $M_N \to 0$, and thus offers another way to move the HNLs out of equilibrium [327]. We expect however this effect to be negligible during freeze-in. During freeze-out, the exact magnitude of this effect remains to be precisely assessed.

[11] The existence of this excess has been questioned in more recent works, see e.g. [335], but more data will be needed to definitely clarify this question.

absence of additional interactions, sterile neutrinos can be produced through their mixing with SM neutrinos. This process can be resonantly enhanced if the pre-existing lepton asymmetry, generated by the two heavier right-handed neutrinos, is large enough [336] and could account for the entirety of the DM content of our universe [337]. For more details on the possible production mechanisms and experimental constraints on the mass and mixing of sterile neutrino DM, we refer the reader to the reviews [338–340].

## 3.4 Discrete flavour and CP symmetries

When introducing the type-I seesaw mechanism in Sec. 3.2, only its vanilla version, where no constraints are imposed on the Yukawa couplings and Majorana masses beyond the requirement to reproduce light neutrino oscillation data, was discussed. In this section, we motivate and examine the impact of imposing flavour and CP symmetries on the type-I seesaw model. Phenomenological consequences of these symmetries will be studied in Chap. 5.

### 3.4.1 Motivations

The vanilla type-I seesaw mechanism presented in Sec. 3.2 offers a minimal framework for generating neutrino masses. However, it does not provide a dynamical explanation for the origin of the observed flavour structure in the neutrino sector. While this pattern is in principle consistent with neutrino mass anarchy [341–344], i.e. assuming the PMNS matrix is described by a random draw from an unbiased distribution of unitary $3 \times 3$ matrices, different aspects of the so-called *flavour puzzle* are sufficiently intriguing to warrant further investigations. It is indeed curious that all fermions come in three generations, in the lepton sector as well as in the quark sector. Moreover, it was noticed early on [345] that the PMNS matrix

$$|U_{\mathrm{PMNS}}| \simeq \begin{pmatrix} 0.82 & 0.55 & 0.15 \\ 0.29 & 0.59 & 0.75 \\ 0.49 & 0.59 & 0.64. \end{pmatrix} \tag{3.41}$$

is numerically reasonably close[12] to a tri-bimaximal mixing

$$U_{\mathrm{TB}} \equiv \begin{pmatrix} \sqrt{2/3} & \sqrt{1/3} & 0 \\ -\sqrt{1/6} & \sqrt{1/3} & \sqrt{1/2} \\ -\sqrt{1/6} & \sqrt{1/3} & -\sqrt{1/2} \end{pmatrix} , \tag{3.42}$$

in stark contrast with the large hierarchies observed in the Cabibbo–Kobayashi–Maskawa (CKM) matrix.

In order to understand these peculiar flavour structures in the quark and lepton sectors, different approaches have been examined over the years, see e.g. [351–358] for reviews. Endowing the theory with a flavour symmetry, i.e. a symmetry acting on flavour space, can explain (some of) these features if it possesses at least one irreducible three-dimensional representation so as to unify all three lepton generations. The underlying symmetry group is therefore typically a subgroup of $U(3)$. In particular, the form (3.42) of the neutrino mixing matrix is reminiscent of non-abelian discrete symmetries.[13] Breaking this symmetry in specific ways imposes severe constraints on the neutrino mixing angles. This predictive power is further enhanced by the presence of (generalised) CP symmetries [362–370], which, in particular, generally impose strong constraints on the values taken by the Dirac and Majorana phases. When combined with the type-I seesaw framework discussed earlier (with $n_s = 3$ as required to unify all three lepton generations), flavour and CP symmetries also lead to strong constraints on the RH neutrino properties. In particular, they generally induce a drastic reduction of the number of free parameters compared to the *agnostic*, i.e. without assuming any specific pattern for the Yukawa coupling and Majorana mass beyond the requirement to reproduce the observed light neutrino oscillation data, scenario. This opens up the possibility of an analytic understanding of the RH neutrino phenomenology and BAU production within such scenarios, which is in general difficult for $n_s = 3$ [6].

For these reasons, we will examine in this chapter, as well as in Chap. 5, a particular incarnation of these flavour symmetries based on the symmetry

[12] While this observation predates the measurement of $\theta_{13} \neq 0$ [346–350], the approach developed in the following can also accommodate such non-zero mixing.

[13] Abelian symmetries are more limited, typically leading to texture zeros [359], and can only account for the smallness of $\theta_{13}$ [360]. These are in general more appropriate to explain large hierarchies in the mixing matrix using Froggatt-Nielsen-like scenarios [361]. Moreover, while continuous non-abelian symmetry groups can also explain the neutrino mixing pattern, using discrete symmetries turned out to be much simpler to implement [354]; see e.g. section IV.B of [355] and references therein for realistic examples based on continuous symmetries.

group $\Delta(6n^2)$ [371] as well as an additional CP symmetry following the approach developed in [372]. We will focus on the analytical understanding of the parameter space and the difference with the agnostic type-I seesaw. In the next subsection, we will outline the exact framework before detailing the possible qualitatively different cases. Various aspects of its phenomenology will then be explored in Chap. 5.

### 3.4.2 Type-I seesaw framework with flavour and CP symmetries

In this section, we summarise the framework considered. As briefly mentioned in the previous section, the starting point of this approach is to assume that, in the UV, leptons transform under the symmetry group $\mathcal{G}_f$. In this work, we choose

$$\mathcal{G}_f = \Delta(6n^2) \sim ((\mathbb{Z}_n \times \mathbb{Z}_n) \rtimes \mathcal{S}_3) \ , \tag{3.43}$$

with $n \in \mathbb{N}$, $n \geq 2$ and even but not divisible by 3.[14] This set of group is particularly interesting and comprises well-studied, simpler examples such as $S_3$ (see e.g. [374,375]) and $S_4$ (see e.g. [376,377]), corresponding respectively to $n = 1$ and $n = 2$. In our scenario, both the Higgs field and the RH charged leptons are assumed to transform as singlets of $\mathcal{G}_f$. On the other hand, the three generations of lepton doublets are unified into a triplet of $\mathcal{G}_f$, and similarly for the RH neutrinos. Since $\Delta(6n^2)$ possesses two distinct 3-dimensional irreducible representations, we assign, following the notations of [2], the lepton doublets to the (complex) representation $\mathbf{3}$, whereas the three RH neutrinos are assigned to the real representation $\mathbf{3}'$. For more details on these representations, see [371]. Moreover, in order to distinguish between the different charged RH leptons and accommodate the observed hierarchical mass spectrum, we assume the existence of an auxiliary $\mathbb{Z}_3$ symmetry, which we write $\mathbb{Z}_3^{(\mathrm{aux})}$, under which the RH electron, muon and tau carry charges $1, e^{2\pi i/3}$ and $e^{4\pi i/3}$, respectively, while the remaining leptons do not transform under this symmetry.

Then, in order to construct invariant operators, it is necessary to introduce additional scalar fields $\varphi$, so-called *flavons*, which are charged under the same group and couple directly to leptons. For instance, the mass of the charged

[14] For $n \in 3\mathbb{N}$ or $n$ odd, the structure of the group differs slightly, and this case must be treated separately; see e.g. [371,373].

leptons can originate from non-renormalisable couplings of the form

$$\mathcal{L} \supset y_e(\bar{\ell}\Phi)\frac{\varphi_e}{\Lambda_F}e_R + y_\mu(\bar{\ell}\Phi)\frac{\varphi_\mu}{\Lambda_F}\mu_R + y_\tau(\bar{\ell}\Phi)\frac{\varphi_\tau}{\Lambda_F}\tau_R \,, \tag{3.44}$$

with the $\varphi_\alpha$ carrying charges $1, e^{4\pi i/3}$ and $e^{2\pi i/3}$ under the auxiliary $\mathbb{Z}_3$ symmetry, and with $\Lambda_F$ denoting the cut-off scale of the theory.[15] On the other hand, the neutrino properties are encoded in e.g. couplings of the form

$$\mathcal{L} \supset y_\nu(\bar{\ell}\Phi)\frac{\varphi_\nu}{\Lambda_F}\nu_R + a\varphi_\xi(\bar{\nu}_R^c\nu_R) \tag{3.45}$$

with $a$ a constant and $\varphi_\xi$ a scalar singlet. As the temperature decreases, the flavour symmetry is spontaneously broken,[16] and these flavons acquire a vev. As a result, charged and neutral leptons acquire a mass term, whose structure depends on the specific values taken by these vevs. It is possible to choose the vev of these flavons in such a way that the charged lepton sector remains invariant under a residual symmetry $\mathcal{G}_l \subset \mathcal{G}_f$ while the neutrino sector instead remains invariant under $\mathcal{G}_\nu \subset \mathcal{G}_f$. The mismatch between $\mathcal{G}_l$ and $\mathcal{G}_\nu$ will then determine the exact form of the PMNS matrix $U_\nu$. Although it is strictly speaking not necessary that any residual symmetry remains after the flavour symmetry breaking, the theory's predictive power is significantly reduced in absence of such symmetry.

As an illustration, let us briefly look at the charged lepton sector. Assuming the fields $\varphi_\alpha$ respectively take the vevs

$$\langle\varphi_e\rangle = v_e\begin{pmatrix}1\\0\\0\end{pmatrix}, \quad \langle\varphi_\mu\rangle = v_\mu\begin{pmatrix}0\\1\\0\end{pmatrix}, \quad \langle\varphi_\tau\rangle = v_\tau\begin{pmatrix}0\\0\\1\end{pmatrix}, \tag{3.46}$$

with $v_\alpha \in \mathbb{R}$, we immediately see that a residual symmetry $\mathcal{G}_l$, corresponding to the diagonal subgroup of the cartesian product between a $\mathbb{Z}_3$ symmetry contained in $\mathcal{G}_f$ and $\mathbb{Z}_3^{(\mathrm{aux})}$, survives. A similar procedure can be done for the neutrino sector, the Yukawa coupling and Majorana mass of the RH neutrinos being obtained by considering the most general matrix structures compatible with $\mathcal{G}_\nu$. We refer the reader to e.g. [378–381] for more detailed illustrations of this procedure using different symmetry groups.

[15] It is nonetheless straightforward to generate this mass term using only renormalisable couplings. For instance, one may assume that the charged RH leptons couple directly to heavy flavons $\varphi_{F_\alpha}$, which in turn couple to $\Phi$ and $\varphi_\alpha$.

[16] An unbroken flavour symmetry common to both charged and neutral leptons would lead to unacceptable neutrino mixings, see section III.C of [355].

Dynamically generating the correct alignment of the flavon vevs is in general challenging [354], see e.g. [378, 382, 383] for explicit examples of how this can be realised in practice. However, in this rest of this work, we will assume that the correct flavon alignment can be found and limit ourselves to considering its low-energy phenomenological consequences. We will furthermore assume that the flavour symmetry breaking happens at a scale well above that relevant for leptogenesis, so that one can safely neglect the direct impact of the flavon fields on the BAU generation.

In addition to the flavour symmetry, we endow the theory with a CP symmetry, which corresponds to an automorphism of $\Delta(6n^2)$ [368–370], to constrain the CP phases of the theory. In the rest of this work, we assume the residual symmetry in the charged lepton sector to be chosen as before, namely the diagonal subgroup of the cartesian product between a $\mathbb{Z}_3$ symmetry contained in $\mathcal{G}_f$ and $\mathbb{Z}_3^{(\mathrm{aux})}$, while the residual symmetry in the neutrino sector $\mathcal{G}_\nu$ is taken to be $\mathbb{Z}_2 \times CP$, where the $\mathbb{Z}_2$ symmetry is a subgroup of $\mathcal{G}_f$.

We further assume that the symmetry is broken in such a way that the Majorana mass does break neither $\mathcal{G}_f$ nor CP.[17] In this case, working in the basis where the charged lepton mass matrix is diagonal, it reads

$$M_M = M \begin{pmatrix} 1 & 0 & 0 \\ 0 & 0 & 1 \\ 0 & 1 & 0 \end{pmatrix} , \tag{3.47}$$

which has degenerate eigenvalues $M$ and can be diagonalised by

$$U_R = \frac{1}{\sqrt{2}} \begin{pmatrix} \sqrt{2} & 0 & 0 \\ 0 & 1 & i \\ 0 & 1 & -i \end{pmatrix} , \quad \text{i.e.} \;\; \hat{M}_M = U_R^T \, M_M \, U_R \, . \tag{3.48}$$

In contrast, we will assume that the Yukawa coupling matrix $Y$ instead only preserves the residual symmetry $\mathcal{G}_\nu$. As discussed in [2, 381], the matrix $Y$ then can be written as

$$Y = \Omega(\mathbf{3}) \, R_{ij}(\theta_L) \, \mathrm{diag}(y_1, y_2, y_3) \, P_{kl}^{ij} \, R_{kl}(-\theta_R) \, \Omega(\mathbf{3}')^\dagger \, , \tag{3.49}$$

where the matrices $\Omega(\mathbf{3})$ and $\Omega(\mathbf{3}')$ are determined by the CP transformation in the representation $\mathbf{3}$ and $\mathbf{3}'$ of $\mathcal{G}_f$, respectively. Their explicit form depends on the case under consideration and will be specified in the next subsection. The

[17] For alternative scenarios where the Majorana mass matrix only preserves the residual symmetry $\mathcal{G}_\nu$ while the Yukawa coupling matrix is trivial, see e.g. [381].

coefficients $y_i$ are real Yukawa couplings whereas the matrix $R_{ij}(\theta_L), i < j$ ($R_{kl}(-\theta_R), k < l$) represents a rotation in the $(ij)$-plane ($(kl)$-plane) with real angle $\theta_L$ $-\theta_R$). Again, the exact values taken by the indices $i, j, k, l$ depend on the case under consideration and will be specified in the next subsection along with the permutation matrix $P_{kl}^{ij}$. The index $L/R$ refers to whether these rotations act on the LH or the RH leptons. In the RH neutrino mass basis, the Yukawa coupling (3.49) reads

$$\hat{Y} = Y\, U_R\,. \tag{3.50}$$

If the combination

$$R_{kl}(-\theta_R)\, \Omega(\mathbf{3}')^\dagger\, M_M^{-1}\, \Omega(\mathbf{3}')^*\, R_{kl}(\theta_R) \tag{3.51}$$

is diagonal, the PMNS mixing matrix then takes the simple form

$$U_\nu = \Omega(\mathbf{3})\, R_{ij}(\theta_L)\, K_\nu\,. \tag{3.52}$$

In this equation, the matrix $K_\nu$ captures the CP parities of the light neutrino mass eigenstates and is a diagonal matrix whose non-vanishing elements take values in $\{\pm 1, \pm i\}$. Even if the matrix product (3.51) is not diagonal, Eq. (3.52) still holds if one replaces the angle $\theta_L$ by an effective angle $\widetilde{\theta}_L$ which is the sum of $\theta_L$ and an additional angle that depends on both the couplings $y_i$ and the angle $\theta_R$. More details will be provided below, see also [2,8].

We finish by noting that Eq. (3.47) predicts the complete absence of mass splitting at the Lagrangian level in the RH neutrino sector. While leptogenesis can still remain viable in this case due to thermal and Higgs corrections to the RH neutrino mass [384, 385], this would nonetheless drastically reduce the viable parameter space as will be explicitly verified later. Moreover, in concrete models, additional corrections to the Majorana mass are expected to arise at higher order in $1/\Lambda_F$, see e.g. [352, 354, 355].[18] For this reason, we will consider the following two corrections to the Majorana mass (3.47). The first one reads

$$\delta M_M = \kappa\, M \begin{pmatrix} 2 & 0 & 0 \\ 0 & 0 & -1 \\ 0 & -1 & 0 \end{pmatrix}, \tag{3.53}$$

[18] While these higher-order corrections can be expected to also affect the form of the Yukawa couplings $Y$ and charged lepton mass matrix, we will assume in the following that these effects are sufficiently small to be safely neglected.

while the second one can be written

$$\Delta M_M = \lambda\, M \begin{pmatrix} 0 & 0 & 0 \\ 0 & 1 & 0 \\ 0 & 0 & 1 \end{pmatrix} . \tag{3.54}$$

$\kappa$ and $\lambda$ are both real parameters. Interestingly, the correction (3.53) remains invariant under $\mathcal{G}_l$ and can therefore be motivated from symmetry considerations. In general, these two corrections completely remove mass degeneracies in the RH neutrino spectrum, which reads

$$M_1 = M\,(1{+}2\,\kappa)\;, \quad M_2 = M\,(1{-}\kappa{+}\lambda) \;\text{ and }\; M_3 = M\,(1{-}\kappa{-}\lambda)\,. \tag{3.55}$$

We note however that, for the specific choices $\lambda = 0$ and $\lambda = \pm 3\kappa$, two out of the three RH neutrinos remain mass-degenerate.

### 3.4.3 The different cases

While the symmetry-breaking pattern was already highlighted in the previous subsection, some freedom remains in the choice of the specific group element in $\mathcal{G}_f$ acting as generator of the subgroups $\mathcal{G}_l$ and $\mathcal{G}_\nu$. This choice will determine the exact shape of the matrices appearing in the Yukawa coupling (3.49). The different possible choices have already been comprehensively studied in [372], which has shown the existence of four qualitatively different group settings. These possibilities are traditionally labelled Case 1), Case 2), Case 3 a) and Case 3 b.1) respectively. In the following, we do not aim to exhaustively detail the phenomenology of each case, but rather to highlight the key qualitative features of this class of flavour symmetries. To that end, we focus on Case 1) and Case 3 b.1), which are representative of the main phenomenologically relevant behaviours, while the remaining cases do not introduce qualitatively new aspects. For a comprehensive study of the different cases, we refer the reader to Refs. [2, 8]. In this subsection, we give explicit formulae for the different matrices appearing in Eq. (3.49). To keep the discussion concise, we refrain from proving these results. More details can be found in [2, 372].

**Case 1):** In this first case, the CP symmetry is parametrised by a discrete parameter $s \in \mathbb{N}$. One can then show [372] that the matrix $\Omega(s)(\mathbf{3})$ appearing in Eq. (3.49) takes the form

$$\Omega(\mathbf{3}) = e^{i\,\varphi_s}\,U_{\rm TB} \begin{pmatrix} 1 & 0 & 0 \\ 0 & e^{-3\,i\,\varphi_s} & 0 \\ 0 & 0 & -1 \end{pmatrix} , \tag{3.56}$$

where we defined

$$\varphi_s \equiv \frac{\pi\,s}{n} \, . \tag{3.57}$$

On the other hand, the form of $\Omega(s)(\mathbf{3}')$ depends on whether $s$ is even or odd. If $s$ is even, we have

$$\Omega(\mathbf{3}') = U_{\rm TB} \, , \tag{3.58}$$

whereas

$$\Omega(\mathbf{3}') = U_{\rm TB} \begin{pmatrix} i & 0 & 0 \\ 0 & 1 & 0 \\ 0 & 0 & i \end{pmatrix} \tag{3.59}$$

if $s$ is odd. One can also show that both rotations $R_{ij}(\theta_L)$ and $R_{kl}(-\theta_R)$ act in the $(13)$-plane [368].

The Yukawa couplings should also be fixed to explain the observed neutrino mass splittings.[19] As a first step, we neglect the mass splittings (3.53) and (3.54). The range of validity of this approximation will be investigated in Sec. 3.4.4. In this case, one can directly relate the second Yukawa coupling $y_2$ to $m_2$ through

$$m_2 = \frac{y_2^2\,v_{\rm ew}^2}{M} \, , \tag{3.60}$$

independently of whether the product of matrices (3.51) is diagonal or not. Expressions for the first and third Yukawa couplings are more complex for a generic choice of light neutrino mass spectrum. They verify

$$m_{1,3} = \frac{v_{\rm ew}^2}{2\,M} \left| (y_1^2 - y_3^2)\,\cos 2\,\theta_R \pm \sqrt{4\,y_1^2\,y_3^2 + (y_1^2 - y_3^2)^2\,\cos^2 2\,\theta_R} \right| . \tag{3.61}$$

[19]Compared to the generic case, Case 1) presents the additional constraint that the group index $n$ should not be divisible by $4$. One can show [2] that $n \in 4\mathbb{N}$ can only lead to one non-vanishing light neutrino mass.

In this general case, the combination (3.51) is not diagonal and is diagonalised by the PMNS matrix

$$U_\nu = \Omega(\mathbf{3})\, R_{13}(\widetilde{\theta}_L)\, K_\nu \tag{3.62}$$

instead of Eq. (3.52), where $\widetilde{\theta}_L$ can be obtained in terms of $\theta_L$ by solving the trigonometric equation

$$\tan 2\,(\widetilde{\theta}_L - \theta_L) = -\frac{2\, y_1\, y_3}{y_1^2 + y_3^2}\, \tan 2\,\theta_R\, . \tag{3.63}$$

Nonetheless, these expressions can be simplified for vanishing lightest neutrino masses $m_0 = 0$ eV. For NO, we obtain

$$m_1 = y_1 = 0 \;\text{ and }\; m_3 = \frac{y_3^2\, v_{\text{ew}}^2}{M}\, |\cos 2\,\theta_R|\; , \tag{3.64}$$

whereas, for IO, we get

$$m_1 = \frac{y_1^2\, v_{\text{ew}}^2}{M}\, |\cos 2\,\theta_R| \;\text{ and }\; m_3 = y_3 = 0\; . \tag{3.65}$$

These equations highlight an important feature of this scenario. Large Yukawa couplings, and therefore the $B-L$-symmetric limit, can be obtained by taking the limit[20] $\theta_R = \pi/4 + k\pi/2,\ k \in \mathbb{Z}$. Moreover, these equations also make the counting of free parameters transparent. As will be seen later in Chap. 5, $\widetilde{\theta}_L$ is fixed as it directly enters the PMNS matrix whereas the Yukawa couplings are fixed by the requirement to reproduce light neutrino oscillation data. Then, the only free parameters are the lightest neutrino mass $m_0$, the group theory parameter $\varphi_s$, the angle $\theta_R$ parametrising the overall strength of the RH neutrino mixing angles and the three RH neutrino masses.

**Case 3 b.1):** In this case, the generator of the residual $Z_2$ symmetry in the neutrino sector is parametrised by a discrete parameter $m \in \mathbb{N}$ while the CP symmetry remains parametrised by the same discrete parameter $s \in \mathbb{N}$. One can then show [372] that the matrix $\Omega(s)(\mathbf{3})$ appearing in Eq. (3.49) takes the

[20]While one might wonder about the naturalness of these choices, it is possible to show, see section 7 of [2], that the residual symmetry of $Y^\dagger Y$ is enhanced at these special values for most of the cases considered. Therefore, the smallness of the deviation of $\theta_R$ from such a special value can be protected by this enhanced symmetry and should not be considered as a tuning of the angle $\theta_R$.

form

$$\Omega(\mathbf{3}) = e^{i\,\varphi_s} \begin{pmatrix} 1 & 0 & 0 \\ 0 & \omega & 0 \\ 0 & 0 & \omega^2 \end{pmatrix} U_{\mathrm{TB}} \begin{pmatrix} 1 & 0 & 0 \\ 0 & e^{-3\,i\,\varphi_s} & 0 \\ 0 & 0 & -1 \end{pmatrix} R_{13}\,(\varphi_m) \quad (3.66)$$

with

$$\omega = e^{2\pi i/3}, \quad \varphi_s = \frac{\pi s}{n} \quad \text{and} \quad \varphi_m = \frac{\pi\, m}{n}\,. \qquad (3.67)$$

Similarly to Case 1), the form $\Omega(\mathbf{3}')$ depends on the parity of $s$. If $s$ is even, we have

$$\Omega(\mathbf{3}') = \begin{pmatrix} 1 & 0 & 0 \\ 0 & \omega & 0 \\ 0 & 0 & \omega^2 \end{pmatrix} U_{\mathrm{TB}} \begin{pmatrix} 1 & 0 & 0 \\ 0 & 1 & 0 \\ 0 & 0 & -1 \end{pmatrix} \qquad (3.68)$$

whereas, for $s$ odd, we obtain

$$\Omega(\mathbf{3}') = \begin{pmatrix} 1 & 0 & 0 \\ 0 & \omega & 0 \\ 0 & 0 & \omega^2 \end{pmatrix} U_{\mathrm{TB}} \begin{pmatrix} i & 0 & 0 \\ 0 & -1 & 0 \\ 0 & 0 & -i \end{pmatrix}\,. \qquad (3.69)$$

Furthermore, the rotation associated with the LH leptons always acts in the $(12)$-plane. Regarding $R_{ij}(\theta_R)$, the plane on which this rotation acts depend on the parity of $m$. For $m$ even, it also acts in the $(12)$-plane. However, if $m$ is odd, it then acts in $(23)$-plane such that the permutation matrix $P^{ij}_{kl}$ appearing in Eq. (3.49) differs from the identity matrix and reads

$$P^{12}_{23} = P_{13} = \begin{pmatrix} 0 & 0 & 1 \\ 0 & 1 & 0 \\ 1 & 0 & 0 \end{pmatrix}\,. \qquad (3.70)$$

We note in passing that these results also hold for Case 3 a). Regarding the Yukawa couplings, similar expressions to Case 1) hold for $m$ even and $s$ odd or vice-versa. For instance, for $m$ even and $s$ odd, the light neutrino masses read $m_1 = \frac{y_3^2\, v_{\mathrm{ew}}^2}{M}$ and

$$m_{2,3} = \frac{v_{\mathrm{ew}}^2}{2\,M} \left|(y_1^2 - y_2^2)\,\cos 2\,\theta_R \pm \sqrt{4\,y_1^2\,y_2^2 + (y_1^2 - y_2^2)^2\,\cos^2 2\,\theta_R}\right|\,, \quad (3.71)$$

whereas $\widetilde{\theta}_L$ can be obtained by solving

$$\tan 2\,(\widetilde{\theta}_L - \theta_L) = -\frac{2\,y_1\,y_2}{y_1^2 + y_2^2}\,\tan 2\,\theta_R\,. \tag{3.72}$$

We again observe that large Yukawa couplings are obtained in the limit $\theta_R \to \pi/4 + k\pi/2,\ k \in \mathbb{Z}$. For the case where $s$ and $m$ are both odd or both even however, we have

$$m_1 = \frac{y_3^2\,v_{\mathrm{ew}}^2}{M}\ ,\ \ m_2 = \frac{y_1^2\,v_{\mathrm{ew}}^2}{M}\quad \text{and}\quad m_3 = \frac{y_2^2\,v_{\mathrm{ew}}^2}{M}\ , \tag{3.73}$$

i.e. the mixing angle is forced to lie at the seesaw line $U^2 \sim m_\nu/M$. We will therefore focus on the cases $m$ even, $s$ odd and $m$ odd, $s$ even. Finally, we note that the free parameters are the same as in Case 1) with the addition of $\varphi_m$.

### 3.4.4 Stability of the light neutrino masses and PMNS mixing matrix with respect to the RH neutrino mass splittings

As already mentioned, we have neglected in the previous subsection the impact of the mass splittings $\kappa$ and $\lambda$. We here assess under which conditions this approximation is justified. Naively, we expect this approximation to hold well at the seesaw line but not in the limit of large Yukawa couplings where large cancellations between different elements in the seesaw relation (3.11) could be spoiled by the presence of large mass splitting. To be more precise, we evaluate the leading correction to the light neutrino masses due to the finite size of the mass splitting for Case 1). In this case, we have

$$m_3 \approx \frac{y_3^2\,v_{\mathrm{ew}}^2}{M}\left|\kappa + \frac{2}{3}\,\lambda + \cos 2\,\theta_R\right|. \tag{3.74}$$

Hence, the corrections to light neutrino oscillation data can be kept small as long as

$$|\kappa|\ ,\ |\lambda| \ll |\cos 2\,\theta_R|\,. \tag{3.75}$$

This constraint can equivalently be formulated in terms of the total mixing angle $U^2$ in the following way

$$U^2 \ll \frac{1}{M}\left(m_2 + \frac{m_3}{|\kappa|, |\lambda|}\right)\ . \tag{3.76}$$

We checked that similar constraints hold for the remaining cases, Case 2) to Case 3 b.1), up to permutations of the light neutrino masses $m_i$.

## 3.5 The minimal Left-Right Symmetric Model

The previous sections have focused on scenarios where RH neutrinos are pure gauge singlets and only interact with the SM through their Yukawa couplings. While the type-I seesaw model could in principle be a valid theory all the way up to the Planck scale [386], RH neutrinos also naturally appear in various gauge extensions of the SM. One of the most minimal gauge extensions of this kind is the mLRSM [387, 388]. In its usual setup, it extends the SM with an SU(2)$_R$ gauge symmetry, its gauge group being $\mathrm{SU}(3)_C \otimes \mathrm{SU}(2)_L \otimes \mathrm{SU}(2)_R \otimes \mathrm{U}(1)_{B-L}$. Besides the existence of three additional gauge bosons, labelled as $W_R^{\pm}$ and $Z'$, the mLRSM also predicts an extended scalar sector with the presence of 2 scalar triplets $\Delta_L(1,3,1,2)$ and $\Delta_R(1,1,3,2)$ in addition to a complex Higgs bidoublet $\Phi(1,2,2,0)$

$$\Delta_{L/R} = \begin{pmatrix} \frac{1}{\sqrt{2}}\delta^+_{L/R} & \delta^{++}_{L/R} \\ \delta^0_{L/R} & -\frac{1}{\sqrt{2}}\delta^+_{L/R} \end{pmatrix} \text{ and } \Phi = \begin{pmatrix} \Phi_1^0 & \Phi_2^+ \\ \Phi_1^- & \Phi_2^0 \end{pmatrix}. \tag{3.77}$$

This field content puts right- and left-handed particles on the exact same footing. Above the $\mathrm{SU}(2)_R$ symmetry-breaking scale, the mLRSM Lagrangian includes the following terms[21]

$$\mathcal{L} \supset i\left(\bar{Q}_L \not{D}_L Q_L + \bar{Q}_R \not{D}_R Q_R\right) + i\left(\bar{\psi}_L \not{D}_L \psi_L + \bar{\psi}_R \not{D}_R \psi_R\right) \tag{3.78}$$
$$-f_{L,\alpha\beta}\,\bar{\psi}^c_{L,\alpha}\widetilde{\Delta}_L\psi_{L,\beta} - f_{R,ij}\;\bar{\psi}^c_{R,i}\widetilde{\Delta}_R\psi_{R,j} + F^{(1)}_{\alpha i}\overline{\psi}_{L,\alpha}\Phi\psi_{R,i} + F^{(2)}_{\alpha i}\overline{\psi}_{L,\alpha}\widetilde{\Phi}\psi_{R,i} + \text{h.c.}$$

where the left- and right-handed covariant derivatives are defined as

$$D^\mu_L = \partial^\mu + ig_L\frac{\boldsymbol{\tau}}{2}\cdot\mathbf{W}^\mu_L + ig'\frac{B-L}{2}B^\mu, \tag{3.79a}$$
$$D^\mu_R = \partial^\mu + ig_R\frac{\boldsymbol{\tau}}{2}\cdot\mathbf{W}^\mu_R + ig'\frac{B-L}{2}B^\mu. \tag{3.79b}$$

[21] In the mLRSM, one additionally imposes a discrete Left-Right symmetry on the Lagrangian (3.78), which relates $g_L$ with $g_R$, $f_L$ with $f_R$ and similarly for the Yukawa coupling. This symmetry is however typically broken at the SU(2)$_R$-breaking scale (or above, see e.g. [389]), and it is therefore reasonable to consider all left- and right-handed couplings to be independent. In any case, we emphasise that these technicalities do not affect the validity of our results.

$Q_{L/R}$ and $\psi_{L/R}$ represent the LH and RH quark and lepton doublets respectively. In addition to their usual Yukawa interactions with LH neutrinos, RH neutrinos therefore undergo gauge interactions with the gauge bosons from the RH sector. From the Lagrangian (3.78), we observe however that these additional interactions are similar to the LH neutrino gauge interactions in the SM.

Finally, it is interesting to note that, because the LH scalar field $\Delta_L$ also develops a vev at low temperature, the mLRSM generate an additional contribution to the light neutrino masses beyond the (standard) type-I seesaw contribution (3.11). This contribution is in particular reminiscent of the so-called type-II seesaw mechanism. Which of these 2 contributions dominate will depend on the choice of model parameters.

Chapter 4

# Heavy fermion interaction rate within effective Fermi theories

## 4.1 Introduction

In the previous chapter, we reviewed different aspects of neutrino mass and BAU generation. Below the EWSB, the RH neutrinos introduced in the type-I seesaw model (3.7) can only interact through their mixing with the LH neutrinos and therefore indirectly feel the SU(2) gauge interaction. Beyond the type-I seesaw, a broad range of SM extensions features similar characteristics, introducing additional fermions that couple to the rest of the early universe bath through vector gauge interactions. These gauge interactions may involve the known SM $W^{\pm}$ and $Z$ bosons, or yet-undiscovered vector bosons [390, 391]. Motivated examples of such BSM theories include the $\nu$MSM discussed earlier or various SM gauge extensions such as $\mathrm{U}(1)_{B-L}$ [392–395], SO(10) [396, 397], Pati-Salam and more general Left-Right symmetric models [387, 388, 398].

At low energies, well below their mass, gauge bosons can be integrated out and fermionic interactions in the aforementioned theories can effectively be described by a *Fermi-like theory*, whose Lagrangian generically reads[1]

$$\mathcal{L}_{\text{Fermi}} = 2\sqrt{2}\mathcal{G}\left(\bar{\Psi}_1\gamma^{\mu}(g_L P_L + g_R P_R)\Psi_2\right)\left(\bar{\Psi}_3\gamma_{\mu}(g'_L P_L + g'_R P_R)\Psi_4\right) + \text{h.c.} \tag{4.1}$$

In this equation, the fields $\Psi_i$, with $i \in \{1, 2, 3, 4\}$, represent generic fermions whose chiral structure (e.g. Weyl, Dirac or Majorana) is encoded in the (complex) coefficients $g_{L/R}$ and $g'_{L/R}$. We emphasise that no further assumptions

[1] More general dimension-6 operators, see e.g. [399] for examples within the $N_R$SMEFT, can in principle also be captured by our analysis, up to slight modifications of the matrix elements. However, we will not investigate such scenarios in this work.

are made about these fields, i.e. they may refer to different or identical fields, and may be part of the SM or not. $\mathcal{G} \propto 1/\Lambda^2$ is an overall dimensionful coupling constant related to the mass scale $\Lambda$ of the integrated-out mediators. It can be identified with the usual Fermi constant $G_F$ when the fields interact via the SM weak interaction, as is the case in the $\nu$MSM. While the Lagrangian (4.1) only describes the interaction between one specific combination of fermion species, it is straightforward to generalise it to multiple four-fermion processes. In this case, $g_{L/R}$ and $g'_{L/R}$ are promoted to complex matrices encoding the flavour structure and CP-violating nature of the fermion gauge interactions.

The fermions $\Psi_i$ appearing in the aforementioned theories can potentially serve as DM candidate or explain the asymmetry between matter and antimatter. Therefore, accurately tracking their evolution in the early universe is of crucial importance. For that purpose, it is necessary to precisely derive their interaction rates, which appear in effective kinetic equations (see e.g. Eq. (3.35)) describing their behaviour in the early universe. If the relevant processes occur at temperatures that exceed the involved particles' masses, thermal effects can drastically affect dark or baryonic matter abundances and a first-principles computation of these interaction rates rooted in the CTP formalism is desirable. Notable examples where thermal effects matter include low scale leptogenesis [1, 168, 169, 290], sterile neutrino dark matter production [121, 131, 332, 400], and other freeze-in dark matter scenarios [84, 167]. At the same time, the relevant dynamics may occur in a regime where these fermions primarily interact via the Fermi interaction (4.1). A well-known example of this is the production of sterile neutrino DM within the $\nu$MSM, which typically peaks at $T \sim \mathcal{O}(100\text{ MeV}) \ll m_W$ [130].

The primary goal of this work is to derive the leading order (LO) finite-temperature interaction rates of heavy[2] fermions $N$ within the general Fermi-like theory (4.1). We further apply our calculations to two well-motivated models: the $\nu$MSM and the mLRSM. While the rates in the former have been studied previously in the Fermi-dominated regime in [401, 402], we here provide an explicit derivation of the rates and display their dependence on the SM lepton flavours. We also retain the helicity dependence of the rates as well as

[2]The word *heavy* is here used in analogy with heavy neutrinos. We however stress that we do not limit ourselves to scenarios where $M \gtrsim T$. Our results can also be used in the ultra-relativistic limit $M \to 0$.

the finite fermion masses. For the mLRSM, this is to the best of our knowledge the first time that such computation is performed.[3]

The present work is largely based on Ref. [9] and is structured as follows. In Sec. 4.2, we first describe the exact system under consideration, set up our notation, and outline the technical steps needed to derive the fermionic interaction rates. The main objective of this section is to provide the building blocks that can be used to compute interaction rates for any type of Fermi theory. As a concrete application, we compute, in Sec. 4.3, these rates for heavy neutrinos within the $\nu$MSM and the mLRSM. In Sec. 4.4, we summarise our main results. In addition, we provide an appendix (appendix C), where we show explicit expressions for the fundamental integrals required for the derivation of interaction rates in a general Fermi theory.

## 4.2 Imaginary part of heavy fermion self-energies in Fermi theory

As highlighted in the introduction, we search to compute the in-medium interaction rate of a heavy fermion $N$, interacting with the rest of the early universe plasma through the 4-fermion contact term (4.1). For a general out-of-equilibrium situation, this turns out to be a non-trivial task. However, in many cases, it is reasonable to assume that $N$ is the only out-of-equilibrium species. In addition, we also assume that the heavy fermion interaction rate $\Gamma$ is approximately independent of the distribution function of $N$, which we write $f_N$. While this is not necessarily the case in general, e.g. in presence of self-interactions, this is nonetheless verified in various well-motivated models. In the $\nu$MSM considered in Sec. 4.3.1 for instance, $N$ represents a heavy neutrino that primarily interacts with SM fields, while cross-sections for processes involving several sterile neutrinos are suppressed by powers of the (small) mixing angle $\theta$. Moreover, in the mLRSM considered in Sec. 4.3.2, interactions involving several $N$ are not suppressed by a small parameter (relative to those involving only one $N$). However, precisely because the $N$'s are not sterile in that model, one can expect their phase space distribution functions to be close to equilibrium, $\delta f_N/f_N \equiv (f_N - f_N^{\text{eq}})/f_N \ll 1$, at relevant temperatures such that $\Gamma$ remains independent of $f_N$ at LO.

[3] We note that the rates associated with $W_R$-mediated $1 \to 3$ decays and $2 \to 2$ scatterings have been computed in [403, 404], see also [268]. However, quantum statistical effects were neglected in these studies.

With this in mind, it is instructive to separate the out-of-equilibrium field $N$ from the equilibrium ones and rewrite the Lagrangian (4.1) as

$$\begin{aligned}\mathcal{L}_{\text{Fermi}} = 2\sqrt{2}\mathcal{G}\Big(c_{\mathcal{J}_R}\left(\bar{N}\gamma^\mu P_R \Psi_3\right)\left(\bar{\Psi}_2\gamma_\mu(a_R + b_R\gamma^5)\Psi_1\right) \\ + c_{\mathcal{J}_L}\left(\bar{N}\gamma^\mu P_L \Psi_3\right)\left(\bar{\Psi}_2\gamma_\mu(a_L + b_L\gamma^5)\Psi_1\right)\Big) + \text{h.c.},\end{aligned} \tag{4.2}$$

We emphasise that the Lagrangian (4.2) does not forbid vertices involving higher powers of the fermion $N$ whose interaction rate we compute, as the fields $\Psi_1$, $\Psi_2$ and $\Psi_3$ can also represent $N$. It only assumes that their distribution function is in equilibrium.

In addition to explicitly labelling one fermion as $N$, we have also partially changed the notation from the chiral coefficients $g_{L/R}$ in (4.1) to the vector and axial-vector coefficients $a_{L/R}$ and $b_{L/R}$ in (4.2) for convenience and easier comparison with previous references such as [401]. As highlighted in the introduction, different types of fermions can be captured by the Lagrangian (4.2) by absorbing their chiral structure into the (interaction-dependent) coefficients $a_{L/R}$ and $b_{L/R}$. For the sake of definiteness, we choose the convention that $\Psi_1$, $\Psi_2$ and $\Psi_3$ are arbitrary Dirac fields of mass $m_1, m_2$ and $m_3$. Finally, we introduce here the (in principle redundant) prefactors $c_{\mathcal{J}_{L/R}}$ so that $a_{L/R}$ and $b_{L/R}$ take their standard values if (4.2) is applied to the SM weak interaction.

In the rest of this section, we compute the (momentum-dependent) $1 \leftrightarrow 3$ and $2 \leftrightarrow 2$ heavy fermion interaction rates assuming that the system is described by the Lagrangian (4.2). It is then straightforward to numerically obtain the relevant momentum-averaging rates, see Eq. (3.40).

### 4.2.1 Deriving the momentum-dependent interaction rates

Similarly to Chap. 2, the approach we follow in this section consists in computing the imaginary part of the heavy fermion retarded self-energy[4] $\Sigma^{\text{ret}}$ within the real-time formalism, which we then relate to the heavy fermion interaction rates through the optical theorem and the associated cutting rules [405, 406]. The Feynman diagram associated to the considered process is displayed in Fig. 4.1. "Internal" fermions, i.e. fermions within the loop in Fig. 4.1, are left completely arbitrary.

[4] Note that we change notation for the retarded self-energy compared to Chap. 1 in order to avoid confusion with the index $R$ indicating the chirality of $N$.

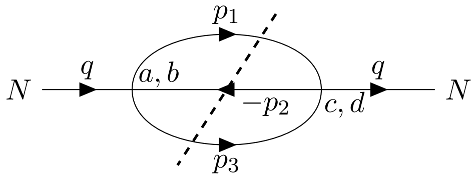


**Figure 4.1:** Diagrammatic representation of the heavy fermion self-energy at leading order in Fermi theory. The coefficients $a, b, c$ and $d$ encode the chiral structure of $N$, see text for details. Interaction rates are obtained via the optical theorem by cutting through the internal propagators; the cut is indicated by the black dashed line.

In general, the chiral structure of any particle's retarded self-energy arising from the effective Fermi Lagrangian (4.2) can be factorised as follows:

$$\Sigma^{\text{ret}} = \mathcal{C}^V_{\mathcal{J}_R} P_L \hat{\Sigma}^V_R P_R + \mathcal{C}^V_{\mathcal{J}_L} P_R \hat{\Sigma}^V_L P_L + \mathcal{C}^S_{\mathcal{J}_R} \hat{\Sigma}^S_R P_R + \mathcal{C}^S_{\mathcal{J}_L} \hat{\Sigma}^S_L P_L \,, \tag{4.3}$$

see e.g. appendix A.1. The upper indices $V$ and $S$ refer to the vector and scalar nature of the self-energy, respectively. The coefficients $\mathcal{C}^{V,S}_{\mathcal{J}_{L/R}}$ are specific to each interaction channel and can be expressed as a combination of $c_{\mathcal{J}_{L/R}}$, symmetry factors $\mathcal{S}$ and multiplicity factors $n$ accounting for indistinguishable channels (e.g. summing over quark colours) in the following way[5]

$$\mathcal{C}^V_{\mathcal{J}_{L/R}} = |c_{\mathcal{J}_{L/R}}|^2 \frac{n}{\mathcal{S}} \text{ and } \mathcal{C}^S_{\mathcal{J}_{L/R}} = c^*_{\mathcal{J}_{L/R}} c_{\mathcal{J}_{R/L}} \frac{n}{\mathcal{S}}. \tag{4.4}$$

As examples, their numerical values for each channel within the $\nu$MSM and the mLRSM are listed in the next section, in Tab. 4.1 and Tab. 4.2 respectively. Assuming $N$ is a Majorana particle in thermal equilibrium and all chemical potentials vanish, $\hat{\Sigma}^{V,S}_R = \hat{\Sigma}^{V,S}_L$. In general, however, the left- and right-handed part of the self-energy are completely unrelated.

We start by deriving the contribution to the rates resulting from the vector term in the self-energy (4.3). The scalar case proceeds analogously. Depending on how one contracts the fermionic currents, two different types of retarded self-energies can be formed, which we call $\hat{\Sigma}^{V,1}_{L/R}$ (type-1) and $\hat{\Sigma}^{V,2}_{L/R}$ (type-2) in the following.[6] The total self-energy is given by the sum of both $\hat{\Sigma}^V_{L/R} = \hat{\Sigma}^{V,1}_{L/R} + \hat{\Sigma}^{V,2}_{L/R}$. Using the momentum convention from Fig. 4.1, the imaginary

[5]In case more than one heavy fermion flavour is present, off-diagonal damping terms $\Gamma_{ij}$ are instead proportional to $c^*_{\mathcal{J}_{L/R},i} c_{\mathcal{J}_{L/R},j}$, where $c_{\mathcal{J}_{L/R},i/j}$ are the coefficients $c_{\mathcal{J}_{L/R}}$ associated to $N_{i/j}$.

[6]The origin of these two types of self-energies is clear in the UV-theory where gauge bosons have not yet been integrated out. See e.g. Fig. 4.2 in Sec. 4.3 for a diagrammatic representation of these two self-energies within the specific case of the $\nu$MSM.

parts of the self-energies $\hat{\Sigma}^{V,1}_{L/R}$ and $\hat{\Sigma}^{V,2}_{L/R}$ read

$$P_{R/L}\,\mathrm{Im}\hat{\Sigma}^{V,1}_{L/R}(q)P_{L/R} = 4\mathcal{G}^2 P_{R/L}\Bigg[\int \frac{\mathrm{d}^4p_1}{(2\pi)^4}\frac{\mathrm{d}^4p_2}{(2\pi)^4}\frac{\mathrm{d}^4p_3}{(2\pi)^4}(2\pi)^4\times$$
$$\times\delta^{(4)}(p_1+p_2+p_3-q)\gamma^\mu \mathrm{Tr}\Big[\gamma_\mu\left(a_{L/R}+b_{L/R}\gamma^5\right)S^>(p_1)\gamma_\nu$$
$$\left(a^*_{L/R}+b^*_{L/R}\gamma^5\right)S^<(-p_2)\Big]S^>(p_3)\gamma^\nu - S^> \leftrightarrow S^<\Bigg]P_{L/R}, \quad (4.5a)$$

$$P_{R/L}\,\mathrm{Im}\hat{\Sigma}^{V,2}_{L/R}(q)P_{L/R} = -4\mathcal{G}^2 P_{R/L}\Bigg[\int \frac{\mathrm{d}^4p_1}{(2\pi)^4}\frac{\mathrm{d}^4p_2}{(2\pi)^4}\frac{\mathrm{d}^4p_3}{(2\pi)^4}(2\pi)^4\times$$
$$\times\delta^{(4)}(p_1+p_2+p_3-q)\Bigg(\gamma^\mu S^>(p_3)\gamma^\nu\left(a_{L/R}+b_{L/R}\gamma^5\right)S^<(-p_2)\gamma_\mu$$
$$\left(c_{L/R}+d_{L/R}\gamma^5\right)S^>(p_1)\gamma_\nu\Bigg) - S^> \leftrightarrow S^<\Bigg]P_{L/R}. \quad (4.5b)$$

The coefficients $c_{L/R}$ and $d_{L/R}$ represent the values of $a_{L/R}$ and $b_{L/R}$ respectively at the right vertex of the self-energy in Fig. 4.1. Note that, for self-energies of type-1, we always have $c_{L/R} = a^*_{L/R}$ and $d_{L/R} = b^*_{L/R}$. As already mentioned, they encode the chiral structure of the heavy neutrino interactions and are in general different for each interaction channels; in the SM, for instance, they differ between charged and neutral currents. As concrete examples, their numerical value for the $\nu$MSM and the mLRSM can be found in the next section in Tab. 4.1 and Tab. 4.2 respectively. We emphasise that, while type-1 self-energies are present in any Fermi-like theory, type-2 self-energies encode interference between different amplitudes and, as such, are not necessarily present. Their existence depends on the presence of identical particles or of mixing between different terms in the Lagrangian that share the same field content.[7]

Factorising the fermionic distribution functions in the above equations, we can reformulate these expressions as

$$P_{R/L}\,\mathrm{Im}\,\hat{\Sigma}^{V,1}_{L/R}(q)P_{L/R} = 4\mathcal{G}^2 P_{R/L}\int \frac{\mathrm{d}^4p_1}{(2\pi)^4}\frac{\mathrm{d}^4p_2}{(2\pi)^4}\frac{\mathrm{d}^4p_3}{(2\pi)^4}(2\pi)^4\times \quad (4.6a)$$

[7] Even in that case, it is sometimes possible, e.g. when considering $e-\nu$ scattering in the SM, to use Fierz identities [31,407] on the Lagrangian (4.2) to express the rates in terms of type-1 self-energies only. This however relies on particles being either all left- or all right-handed. In case both right- and left-handed particles are present, this simplification does not work as well since Fierz identities will generate scalar currents in addition to the fermionic ones.

$$
\begin{aligned}
&\times \delta^{(4)}(p_1+p_2+p_3-q)\Big[(1-f_1)(1-f_2)(1-f_3)+f_1f_2f_3\Big]\gamma^\mu \\
&\mathrm{Tr}\Big[\gamma_\mu\left(a_{L/R}+b_{L/R}\gamma^5\right)\rho_1(p_1)\gamma_\nu\left(a^*_{L/R}+b^*_{L/R}\gamma^5\right)\rho_2(-p_2)\Big]\rho_3(p_3)\gamma^\nu P_{L/R},
\end{aligned}
$$

$$
\begin{aligned}
P_{R/L}\,\mathrm{Im}\,\hat{\Sigma}^{V,2}_{L/R}(q)P_{L/R} &= -4\mathcal{G}^2 P_{R/L}\int\frac{\mathrm{d}^4p_1}{(2\pi)^4}\frac{\mathrm{d}^4p_2}{(2\pi)^4}\frac{\mathrm{d}^4p_3}{(2\pi)^4}(2\pi)^4\times \qquad (4.6b)\\
&\times \delta^{(4)}(p_1+p_2+p_3-q)\Big[(1-f_1)(1-f_2)(1-f_3)+f_1f_2f_3\Big] \\
&\left(\gamma^\mu\rho_3(p_3)\gamma^\nu\left(a_{L/R}+b_{L/R}\gamma^5\right)\rho_2(-p_2)\gamma_\mu\left(c_{L/R}+d_{L/R}\gamma^5\right)\rho_1(p_1)\gamma_\nu\right)P_{L/R}.
\end{aligned}
$$

The function $\rho_i(k) = 2\pi\,\mathrm{sign}(k_0)\delta(k^2-m_i^2)(\not{k}+m_i)$ is the (equilibrium) spectral function of the fermion $\Psi_i$, whose distribution function we write $f_i$.

Because we are interested, e.g. in the context of leptogenesis, in the helicity dependence of the rates, both traces $\mathrm{Tr}\left[\not{q}\,\mathrm{Im}\,\hat{\Sigma}^{V,\omega}_{L/R}(q)\right]$ and $\mathrm{Tr}\left[\not{u}\,\mathrm{Im}\,\hat{\Sigma}^{V,\omega}_{L/R}(q)\right]$ are necessary. Here, the index $\omega\in\{1,2\}$ indicates the type of self-energy, while $u=(1,\mathbf{0})$ is the plasma four-velocity in its rest frame. These two traces serves as the basic building blocks from which the rates can be reconstructed. They can be expressed in a form similar to the convention from Kolb and Turner [45]

$$
\begin{aligned}
\mathrm{Tr}\left[\not{K}\,\mathrm{Im}\,\hat{\Sigma}^{V,\omega}_{L/R}(q)\right] &= (-1)^{1+\omega}(2\pi)^4\int\frac{\mathrm{d}^3\mathbf{p}_1}{(2\pi)^3 2E_1}\int\frac{\mathrm{d}^3\mathbf{p}_2}{(2\pi)^3 2E_2}\int\frac{\mathrm{d}^3\mathbf{p}_3}{(2\pi)^3 2E_3}\times\\
&\times\Big[\delta^{(4)}(p_1+p_2+p_3-q)|\mathcal{M}^\omega_K(m_1,-m_2,m_3)|^2\times\\
&\qquad\times\left[(1-f_1)(1-f_2)(1-f_3)+f_1f_2f_3\right]\\
&+\delta^{(4)}(p_1+p_2-p_3-q)|\mathcal{M}^\omega_K(m_1,-m_2,-m_3)|^2\times\\
&\qquad\times\left[(1-f_1)(1-f_2)f_3+f_1f_2(1-f_3)\right]\\
&+\delta^{(4)}(p_1+p_3-p_2-q)|\mathcal{M}^\omega_K(m_1,m_2,m_3)|^2\times\\
&\qquad\times\left[(1-f_1)f_2(1-f_3)+f_1(1-f_2)f_3\right]\\
&+\delta^{(4)}(p_2+p_3-p_1-q)|\mathcal{M}^\omega_K(-m_1,-m_2,m_3)|^2\times\\
&\qquad\times\left[f_1(1-f_2)(1-f_3)+(1-f_1)f_2f_3\right]\\
&+\delta^{(4)}(p_3-p_1-p_2-q)|\mathcal{M}^\omega_K(-m_1,m_2,m_3)|^2\times\\
&\qquad\times\left[f_1f_2(1-f_3)+(1-f_1)(1-f_2)f_3\right]\\
&+\delta^{(4)}(p_2-p_1-p_3-q)|\mathcal{M}^\omega_K(-m_1,-m_2,-m_3)|^2\times\\
&\qquad\times\left[f_1(1-f_2)f_3+(1-f_1)f_2(1-f_3)\right]
\end{aligned}
$$

$$
\begin{aligned}
&+\delta^{(4)}(p_1-p_2-p_3-q)|\mathcal{M}^{\omega}_{K}(m_1,m_2,-m_3)|^2\times\\
&\qquad\qquad\times\left[(1-f_1)\,f_2f_3+f_1\,(1-f_2)\,(1-f_3)\right]\\
&+\delta^{(4)}(-p_1-p_2-p_3-q)|\mathcal{M}^{\omega}_{K}(-m_1,m_2,-m_3)|^2\times\\
&\qquad\qquad\times\left[f_1f_2f_3+(1-f_1)\,(1-f_2)\,(1-f_3)\right]\Big]\,, \qquad (4.7)
\end{aligned}
$$

where we define the squared S-matrix element[8]

$$
\begin{aligned}
|\mathcal{M}^{\omega}_{K}(m_1,m_2,m_3;p_1,p_2,p_3,q)|^2 &\equiv |\mathcal{M}^{\omega}_{K}(m_1,m_2,m_3)|^2\\
&=4\mathcal{G}^2\mathcal{T}^{\omega}_{K}\,(m_1,m_2,m_3) \qquad (4.8)
\end{aligned}
$$

and $E_i\equiv\sqrt{\mathbf{p}_i^2+m_i^2}$. For the sake of brevity, we omit the dependence with the particles' momenta as well as the subscript $L/R$ in these matrix elements. The functions $\mathcal{T}^{\omega}_{K}$ encode the spinor structure of the amplitude. Explicit expressions for these traces are displayed hereunder.

$$
\begin{aligned}
\mathcal{T}^{1}_{K}(m_1,m_2,m_3) &= 32\Big[(|a_{L/R}|^2+|b_{L/R}|^2)\Big((p_2\cdot p_3)(p_1\cdot K)\\
&\quad+(p_1\cdot p_3)(p_2\cdot K)\Big)+\Big(|b_{L/R}|^2-|a_{L/R}|^2\Big)\,m_1m_2(p_3\cdot K)\Big], \qquad (4.9a)\\
\mathcal{T}^{2}_{K}(m_1,m_2,m_3) &= 16\Big[-2(a_{L/R}\mp b_{L/R})(c_{L/R}\mp d_{L/R})(p_1\cdot p_3)(p_2\cdot K)\\
&\quad+(a_{L/R}\pm b_{L/R})(c_{L/R}\pm d_{L/R})m_1m_3(p_2\cdot K)\\
&\quad+(a_{L/R}\mp b_{L/R})(c_{L/R}\pm d_{L/R})m_1m_2(p_3\cdot K)\\
&\quad+(a_{L/R}\pm b_{L/R})(c_{L/R}\mp d_{L/R})m_2m_3(p_1\cdot K)\Big], \qquad (4.9b)
\end{aligned}
$$

where the $-/+$ signs distinguish between the left- and right-handed self-energies.

Using the KMS relation, one can then simplify Eq. (4.7) into the more synthetic form

$$
\begin{aligned}
\mathrm{Tr}\left[\not{K}\,\mathrm{Im}\,\hat{\Sigma}^{V,\omega}_{L/R}(q)\right] &= 4(-1)^{1+\omega}\mathcal{G}^2 f_{\mathrm{F}}^{-1}(-q_0)\int\frac{\mathrm{d}^3\mathbf{p}_1}{(2\pi)^3 2E_1}\int\frac{\mathrm{d}^3\mathbf{p}_2}{(2\pi)^3 2E_2}\int\frac{\mathrm{d}^3\mathbf{p}_3}{(2\pi)^3 2E_3}\times\\
&\times\Big[(2\pi)^4\delta^{(4)}(p_1+p_2+p_3-q)\times\\
&\qquad\times(1-f_{\mathrm{F}}(E_1))\,(1-f_{\mathrm{F}}(E_2))\,(1-f_{\mathrm{F}}(E_3))\,\mathcal{T}^{\omega}_{K}(m_1,-m_2,m_3)\\
&+(2\pi)^4\delta^{(4)}(p_1+p_2-p_3-q)\times
\end{aligned}
$$

[8] This constitutes a slight abuse of notation, as the conventional S-matrix element technically corresponds only to $\mathcal{M}_K$ for $K=q$. Moreover, the quantities $|\mathcal{M}^{\omega}_{K}|^2$ do not include either certain numerical factors, such as CKM matrix elements, which are instead captured in $\mathcal{C}^{V}_{\mathcal{J}_{L/R}}$.

$$
\begin{aligned}
&\times (1 - f_{\mathrm{F}}(E_1))\,(1 - f_{\mathrm{F}}(E_2))\, f_{\mathrm{F}}(E_3) \mathcal{T}_K^{\omega}(m_1, -m_2, -m_3) \\
&+ (2\pi)^4 \delta^{(4)}(p_1 + p_3 - p_2 - q) \times \\
&\qquad \times (1 - f_{\mathrm{F}}(E_1))\, f_{\mathrm{F}}(E_2)\,(1 - f_{\mathrm{F}}(E_3))\, \mathcal{T}_K^{\omega}(m_1, m_2, m_3) \\
&+ (2\pi)^4 \delta^{(4)}(p_2 + p_3 - p_1 - q) \times \\
&\qquad \times f_{\mathrm{F}}(E_1)\,(1 - f_{\mathrm{F}}(E_2))\,(1 - f_{\mathrm{F}}(E_3))\, \mathcal{T}_K^{\omega}(-m_1, -m_2, m_3) \\
&+ (2\pi)^4 \delta^{(4)}(p_3 - p_1 - p_2 - q) \times \\
&\qquad \times f_{\mathrm{F}}(E_1) f_{\mathrm{F}}(E_2)\,(1 - f_{\mathrm{F}}(E_3))\, \mathcal{T}_K^{\omega}(-m_1, m_2, m_3) \\
&+ (2\pi)^4 \delta^{(4)}(p_2 - p_1 - p_3 - q) \times \\
&\qquad \times f_{\mathrm{F}}(E_1)\,(1 - f_{\mathrm{F}}(E_2))\, f_{\mathrm{F}}(E_3) \mathcal{T}_K^{\omega}(-m_1, -m_2, -m_3) \\
&+ (2\pi)^4 \delta^{(4)}(p_1 - p_2 - p_3 - q) \times \\
&\qquad \times (1 - f_{\mathrm{F}}(E_1))\, f_{\mathrm{F}}(E_2) f_{\mathrm{F}}(E_3) \mathcal{T}_K^{\omega}(m_1, m_2, -m_3) \Big] \,. \qquad (4.10)
\end{aligned}
$$

For the specific case of the $\nu$MSM, similar expressions can be found in multiple papers, see e.g. Eq. (3.9) in [401] but also related formulae in [312, 408]. We stress that, although we will assume throughout the rest of this section that all chemical potentials vanish, Eq. (4.10) remains valid even for non-zero chemical potentials. Even though the integrals in Eq. (4.10) are formally 9-dimensional, they can be analytically reduced to 3-dimensional integrals by exploiting 4-momentum conservation and the isotropy of the problem. More details on how to perform this reduction are provided in appendix B.

Instead of working directly with the traces (4.10), it is in practice more convenient to express the rates in terms of the following two combinations [169]

$$
\begin{aligned}
\mathrm{Im}\,\hat{\Sigma}^{V,\omega}_{L/R,\pm} &\equiv \mathrm{Im}\,\hat{\Sigma}^{V,\omega}_{L/R,0} \pm \frac{\mathbf{q}}{|\mathbf{q}|} \cdot \mathrm{Im}\,\hat{\mathbf{\Sigma}}^{V,\omega}_{L/R} \qquad (4.11) \\
&= \frac{1}{4}\,\mathrm{Tr}\left[\not{u}\,\mathrm{Im}\,\hat{\Sigma}^{V,\omega}_{L/R}\right] \pm \frac{q_0\,\mathrm{Tr}\left[\not{u}\,\mathrm{Im}\,\hat{\Sigma}^{V,\omega}_{L/R}\right] - \mathrm{Tr}\left[\not{q}\,\mathrm{Im}\,\hat{\Sigma}^{V,\omega}_{L/R}\right]}{4|\mathbf{q}|}.
\end{aligned}
$$

Factoring out the chiral coefficients $a, b, c$ and $d$, these self-energies can be expressed, for a generic Fermi theory, in terms of four (dimensionless) functions $\mathcal{I}_h, \mathcal{J}_h(m_1, m_2, m_3; M_N, |\mathbf{q}|, T)$, with $h \in \{-1, +1\}$, as follows:

$$
\begin{aligned}
&\mathrm{Im}\,\hat{\Sigma}^{V,1}_{L/R,h}(m_1, m_2, m_3; M_N, |\mathbf{q}|, T) = 128\mathcal{G}^2 T^5 \times \qquad (4.12a) \\
&\times \Big[ (|a_{L/R}|^2 + |b_{L/R}|^2)(\mathcal{I}_h(m_1, m_2, m_3) + \mathcal{I}_h(m_2, m_1, m_3))
\end{aligned}
$$

$$
\begin{aligned}
&\qquad\qquad + (|b_{L/R}|^2 - |a_{L/R}|^2)\mathcal{J}_h(m_3,m_2,m_1)\Big],\\
&\mathrm{Im}\,\hat{\Sigma}^{V,2}_{L/R,h}(m_1,m_2,m_3;M_N,|\mathbf{q}|,T) = -64\mathcal{G}^2T^5\times \qquad (4.12\text{b})\\
&\times\Big[-2(a_{L/R}\mp b_{L/R})(c_{L/R}\mp d_{L/R})\mathcal{I}_h(m_2,m_1,m_3)\\
&\qquad\qquad + (a_{L/R}\pm b_{L/R})(c_{L/R}\pm d_{L/R})\mathcal{J}_h(m_2,m_1,m_3)\\
&+ (a_{L/R}\mp b_{L/R})(c_{L/R}\pm d_{L/R})\mathcal{J}_h(m_3,m_2,m_1)\\
&\qquad\qquad + (a_{L/R}\pm b_{L/R})(c_{L/R}\mp d_{L/R})\mathcal{J}_h(m_1,m_2,m_3)\Big].
\end{aligned}
$$

To keep expressions compact, we have omitted the explicit dependence of $\mathcal{I}_h$ and $\mathcal{J}_h$ on $M_N, |\mathbf{q}|$ and $T$. The momenta $q_h \equiv q_\pm$ are defined following Eq. (4.11), i.e. $q_\pm = q_0 \pm |\mathbf{q}|$. These functions satisfy the symmetry properties:

$$\mathcal{I}_h(m_1,m_2,m_3) = \mathcal{I}_h(m_1,m_3,m_2), \qquad (4.13\text{a})$$

$$\mathcal{J}_h(m_1,m_2,m_3) = \mathcal{J}_h(m_1,m_3,m_2). \qquad (4.13\text{b})$$

Explicit integral representations of $\mathcal{I}_\pm$ and $\mathcal{J}_\pm$ are provided in appendix C.

The derivation of the scalar contributions to the total interaction rate proceeds analogously, up to minor differences. We therefore only quote the final result

$$
\begin{aligned}
&\mathrm{Im}\,\hat{\Sigma}^{S,1}_{L/R}(m_1,m_2,m_3;M_N,|\mathbf{q}|,T) = -128\mathcal{G}^2T^5\times \qquad (4.14)\\
&\times\big[(a_{L/R}a^*_{R/L} + b_{L/R}b^*_{R/L})\mathcal{K}(m_1,m_2,m_3)\\
&\qquad\qquad + 2(b_{L/R}b^*_{R/L} - a_{L/R}a^*_{R/L})\mathcal{L}(m_1,m_2,m_3)\big],\\
&\mathrm{Im}\,\hat{\Sigma}^{S,2}_{L/R}(m_1,m_2,m_3;M_N,|\mathbf{q}|,T) = -64\mathcal{G}^2T^5\times \qquad (4.15)\\
&\times\big[-2(a_{L/R}-b_{L/R})(c_{L/R}+d_{L/R})\mathcal{L}(m_1,m_2,m_3)\\
&\qquad\qquad + (a_{L/R}+b_{L/R})(c_{L/R}+d_{L/R})\mathcal{K}(m_3,m_2,m_1)\\
&\quad + (a_{L/R}+b_{L/R})(c_{L/R}-d_{L/R})\mathcal{K}(m_1,m_3,m_2)\\
&\qquad\qquad + (a_{L/R}-b_{L/R})(c_{L/R}-d_{L/R})\mathcal{K}(m_1,m_2,m_3)\big].
\end{aligned}
$$

Explicit expressions for $\mathcal{K}$ and $\mathcal{L}$ are provided in appendix C. Importantly, since the coefficients $\mathcal{C}^V_{\mathcal{J}_{L/R}}$, $a_{L/R}$, $b_{L/R}$, $c_{L/R}$ and $d_{L/R}$ have been factorised out, the functions $\mathcal{I}_\pm$, $\mathcal{J}_\pm$, $\mathcal{K}$ and $\mathcal{L}$ depend only on the mass spectrum of the theory and kinematic quantities, not on its chiral structure or specific couplings. Thus, they provide a universal basis to compute interaction rates for any Fermi-like theory by summing over the relevant interaction channels.

To illustrate this, we can assume that $N$ is much heavier than its interaction partners, and all share the same temperature $T$ and have vanishing chemical potential $\mu_i = 0$. In this case, the rates depend only on twelve functions, independently of the chiral structure of the theory:

1. When $N$ couples only to massless particles, its interaction rates depend solely on the function $\mathcal{I}_\pm(0,0,0)$.
2. If vertices involving 2 heavy fermions are allowed, one can show, using the symmetries (4.13), that the rates depend only on three functions: $\mathcal{K}(0,0,M_N)$, $\mathcal{I}_\pm(M_N,0,0)$ and $\mathcal{I}_\pm(0,0,M_N)$.
3. In the presence of a $3N$-vertex, the symmetries (4.13) imply that only the functions $\mathcal{K}(0,M_N,M_N)$, $\mathcal{I}_\pm(M_N,0,M_N)$, $\mathcal{I}_\pm(0,M_N,M_N)$ and $\mathcal{J}_\pm(0,M_N,M_N)$ are necessary.
4. Finally, if $N$ self-interactions are possible (i.e. a $4N$-vertex), the rates can be expressed in terms of $\mathcal{K}(M_N,M_N,M_N)$, $\mathcal{L}(M_N,M_N,M_N)$, $\mathcal{I}_\pm(M_N,M_N,M_N)$ and $\mathcal{J}_\pm(M_N,M_N,M_N)$.

The dependence of these functions with $\frac{|\mathbf{q}|}{T}$, $\frac{M_N}{T}$ will be made available in an online repository at a later time, along with Python and Mathematica code snippets illustrating how to extract interaction rates from this set of functions. In appendix C, we provide explicit formulae for $\Gamma$, the interaction rates of $N$, in terms of $\mathcal{I}_h$, $\mathcal{J}_h$, $\mathcal{K}$ and $\mathcal{L}$. In particular, we show that we recover the standard neutrino-neutrino scattering rates in the case where all particles are massless and left-handed, see Eq. (C.12).

## 4.3 Applications to specific scenarios

Until now, we have remained relatively generic in our study. In particular, Eqs. (4.7) and (4.9) can be applied to any Fermi-like interactions. The objective of this section is therefore to apply these general results to compute the heavy fermion interaction rates in two well-motivated scenarios: the $\nu$MSM, in Sec. 4.3.1, and the mLRSM, in Sec. 4.3.2.

### 4.3.1 HNL interaction rates in the $\nu$MSM

Over the years, the $\nu$MSM, described in Sec. 3.3.3, has been studied in great detail. In particular, the helicity-conserving and helicity-violating HNL interaction rates have already been computed both above [44, 169, 312, 328, 409–

416] and below the electroweak crossover [312, 317, 328, 402, 408, 417–419]. At low temperatures, i.e. $T \lesssim 5$ GeV, one can effectively neglect the Born contributions from on-shell W and Z bosons [317] and the weak gauge bosons can be safely integrated out in the Lagrangian (3.15). Moreover, direct interactions mediated by the Higgs boson are suppressed by the smallness of the SM fermion Yukawa couplings, or — in the specific case of the top quark — severely Boltzmann suppressed. Hence, the HNL interactions are dominated by the effective Fermi interaction[9]

$$\begin{aligned}\mathcal{L}_{\text{Fermi}} &= 2\sqrt{2}G_F \theta^{\dagger}_{i\alpha}\left(\bar{N}_i\gamma^{\mu}e_{L\alpha}\right)\mathcal{J}_{\mu} + \text{h.c.}\,,\\ &= 2\sqrt{2}G_F \frac{v_{\text{ew}}}{M_i} Y^{\dagger}_{i\alpha}\left(\bar{N}_i\gamma^{\mu}e_{L\alpha}\right)\mathcal{J}_{\mu} + \text{h.c.}\,,\end{aligned} \tag{4.16}$$

where $\mathcal{J}_{\mu} \equiv \bar{\Psi}_2\gamma_{\mu}(a_L + b_L\gamma^5)\Psi_1$ is a neutral or charged fermionic current, see Tab. 4.1 for the possible particle content of this current, and $G_F = \frac{g^2}{4\sqrt{2}m_W^2}$ is the usual Fermi constant. Given that the DM abundance [131] crucially relies on the amount of lepton asymmetry at $T \lesssim \mathcal{O}(1)$ GeV, an accurate calculation of the HNL interaction rates in this regime was therefore desirable. Late-time lepton asymmetries may also indirectly influence other quantities such as the order of the QCD phase transition [425] and the resulting primordial black hole abundance [426]. We note that these rates were also computed in [317, 402], which show good qualitative agreement with our results.

Due to their Majorana nature, the HNL Hamiltonian $H_N$ and interaction rates $\Gamma, \tilde{\Gamma}$ appearing in the QKEs (3.35) depend on both $Y^{\dagger}Y$ and its complex conjugate $Y^tY^*$. Their flavour structure can therefore be decomposed as

$$(H_{N\alpha})_{ij} = h_{+,\alpha}Y^{\dagger}_{i\alpha}Y_{\alpha j} + h_{-,\alpha}Y^{t}_{i\alpha}Y^{*}_{\alpha j}, \tag{4.17a}$$

$$(\Gamma_{\alpha})_{ij} = \gamma_{+,\alpha}Y^{\dagger}_{i\alpha}Y_{\alpha j} + \gamma_{-,\alpha}Y^{t}_{i\alpha}Y^{*}_{\alpha j}, \tag{4.17b}$$

$$\left(\tilde{\Gamma}_{\alpha}\right)_{ij} = -\gamma_{+,\alpha}Y^{\dagger}_{i\alpha}Y_{\alpha j} + \gamma_{-,\alpha}Y^{t}_{i\alpha}Y^{*}_{\alpha j}\,, \tag{4.17c}$$

where $h_{\pm}, \gamma_{\pm}$ and $\delta\gamma_{\pm}$ are temperature- and momentum-dependent coefficients. The total interaction $\Gamma$ in Eq. (3.35) is obtained by summing over the

[9] Below the QCD phase transition, i.e. for $T < T_{\text{QCD}} \simeq 155$ MeV [420] (assuming vanishing chemical potentials), the Lagrangian (4.16) is no longer accurate, as heavy neutrinos interact directly with mesons rather than quarks. We nevertheless neglect this effect in the present work. Indeed, the interaction rates of heavy neutrinos with mesons are well known in vacuum, see e.g. [210, 421–424]. For a benchmark $M_N \simeq 2$ GeV, we checked that considering interactions with quarks instead of mesons only leads to a $\mathcal{O}(10\%)$ underestimation of the zero-temperature rates, see Fig. 4.3.

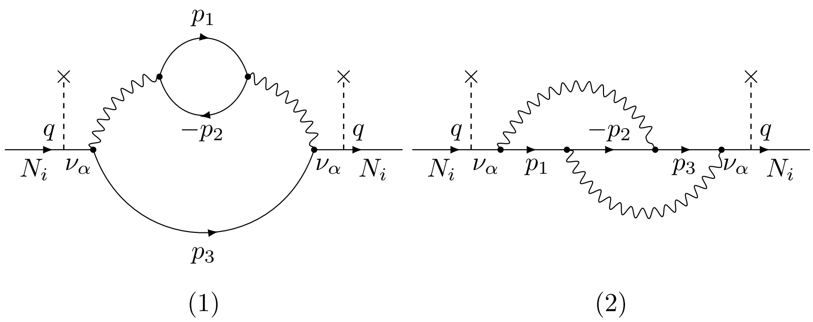


**Figure 4.2:** Diagrams contributing to the heavy neutrino self-energy at low temperature within the $\nu$MSM. Both diagrams have the same representation, equivalent to Fig. 4.1, in Fermi theory after integrating out the $W$ and $Z$ bosons but respectively corresponds to the traces $\mathcal{T}^1$ and $\mathcal{T}^2$. Higgs vev insertions are represented by dashed lines ended by crosses.

SM flavours $\alpha$, i.e. $\Gamma = \sum_\alpha \Gamma_\alpha$. The index $+$ ($-$) refers to the helicity-conserving (helicity-violating) nature of the interaction. Note that, while our motivations are clearly arising from the $\nu$MSM, the coefficients $\gamma_\pm$ are independent of the number of RH neutrino generations as long as their masses remain approximately degenerate and therefore our computation also apply to non-minimal models with e.g. three degenerate RH neutrinos.

Below the EWSB, HNLs only interact through their θ-suppressed mixing with the LH neutrinos. The relevant HNL self-energies are displayed in Fig. 4.2. Following a similar derivation as in [44], one can show the helicity-conserving and helicity-violating coefficients $\gamma_\pm$ can be extracted from the active neutrino retarded self-energy

$$\gamma_\pm = \frac{v_{\mathrm{ew}}^2 \tilde{\mathcal{C}}_{\mathcal{J}}}{M_N^2 |q_0|} q_\mp \mathrm{Im}\hat{\Sigma}^V_{\nu,\pm}. \tag{4.18}$$

where $q$ is the HNL 4-momentum and we define $\hat{\Sigma}^V \equiv \hat{\Sigma}^V_L = \hat{\Sigma}^V_R$. Because there exists no vertex involving multiple heavy neutrinos at leading order in the Yukawa coupling, we can safely neglect scalar contributions to the self-energy. Note that, as highlighted by Eq. (4.17), we also factor out the dependence on the Yukawa coupling from $\mathcal{C}^V_{\mathcal{J}_{L/R}}$, i.e.

$$\mathcal{C}^V_{\mathcal{J}_L} = \tilde{\mathcal{C}}_{\mathcal{J}} Y^\dagger_{i\alpha} Y_{\alpha j} \quad \text{and} \quad \mathcal{C}^V_{\mathcal{J}_R} = \tilde{\mathcal{C}}_{\mathcal{J}} Y^t_{i\alpha} Y^*_{\alpha j}. \tag{4.19}$$

| Channel | $\tilde{\mathcal{C}}_{\mathcal{J}}$ | $m_1$ | $m_2$ | $m_3$ | $\mathcal{T}^{\omega}$ | $a_L$ | $b_L$ | $c_L$ | $d_L$ |
|---|---|---|---|---|---|---|---|---|---|
| *W-only channels* | | | | | | | | | |
| WW + quarks | $3\lvert V_{ij}\rvert^2$ | $m_i$ | $m_j$ | $m_{l_\alpha}$ | $\mathcal{T}^1$ | $\frac{1}{2}$ | $-\frac{1}{2}$ | | |
| WW + leptons | 1 | $m_{l_\beta}$ | 0 | $m_{l_\alpha}$ | $\mathcal{T}^1$ | $\frac{1}{2}$ | $-\frac{1}{2}$ | | |
| *Z-only channels* | | | | | | | | | |
| ZZ + up-like quarks | $\frac{3}{4}$ | $m_q$ | $m_q$ | 0 | $\mathcal{T}^1$ | $\frac{1}{2}-\frac{4}{3}s_W^2$ | $-\frac{1}{2}$ | | |
| ZZ + down-like quarks | $\frac{3}{4}$ | $m_q$ | $m_q$ | 0 | $\mathcal{T}^1$ | $-\frac{1}{2}+\frac{2}{3}s_W^2$ | $\frac{1}{2}$ | | |
| ZZ + charged leptons | $\frac{1}{4}$ | $m_{l_\alpha}$ | $m_{l_\alpha}$ | 0 | $\mathcal{T}^1$ | $-\frac{1}{2}+2s_W^2$ | $\frac{1}{2}$ | | |
| ZZ + 3 LHN | $\frac{3}{4}$ | 0 | 0 | 0 | $\mathcal{T}^1$ | $\frac{1}{2}$ | $-\frac{1}{2}$ | | |
| ZZ + 3 LHN | $\frac{1}{4}$ | 0 | 0 | 0 | $\mathcal{T}^2$ | $\frac{1}{2}$ | $-\frac{1}{2}$ | $\frac{1}{2}$ | $-\frac{1}{2}$ |
| *Mixed channels* | | | | | | | | | |
| ZW + charged leptons | $\frac{1}{2}$ | $m_{l_\alpha}$ | $m_{l_\alpha}$ | 0 | $\mathcal{T}^2$ | $-\frac{1}{2}+2s_W^2$ | $\frac{1}{2}$ | $\frac{1}{2}$ | $-\frac{1}{2}$ |
| WZ + charged leptons | $\frac{1}{2}$ | 0 | $m_{l_\alpha}$ | $m_{l_\alpha}$ | $\mathcal{T}^2$ | $\frac{1}{2}$ | $-\frac{1}{2}$ | $-\frac{1}{2}+2s_W^2$ | $\frac{1}{2}$ |

**Table 4.1:** Overview of the possible HNL interaction channels and their characteristics in the $\nu$MSM (in the Fermi-dominated regime). Table taken from [401] up to small modifications, see erratum of [401], and different conventions for the momenta. We did split the channels in 3 categories depending on whether the rates would be present if only the $W$ or the $Z$ boson were present in the UV-theory or if both needs to be present. We abbreviate $\sin^2\theta_W \to s_W^2$.

As explained in Sec. 4.2, in order to obtain $\mathrm{Im}\,\hat{\Sigma}^V$, it is sufficient to evaluate the integrals (4.10) using the traces (4.9). The specific values taken by the coefficients $a_L, b_L, c_L, d_L$ entering these traces are listed for all possible interaction channels within the $\nu$MSM in the following Tab. 4.1.

To illustrate our results, we display in Fig. 4.3 the temperature-dependence of the flavoured HNL interaction rates, restricting ourselves to temperatures below 5 GeV such that contributions from $1 \to 2$ Born decays of $W$ and $Z$ bosons and direct interactions with the Higgs boson remain negligible. Given that the electron and muon masses are negligible compared to the HNL mass, the difference between $\gamma_{+,e}$ and $\gamma_{+,\mu}$ is unobservable in this plot. At these temperatures, there is also no need to resum the light neutrino propagator. For $T \sim 5$ GeV and $M_N = 2$ GeV, we cross-checked our rates against the one used in [414] and found agreement at the percent level. While we display these rates down to temperature as low as 50 MeV, these should only be regarded as indicative below $T_{\mathrm{QCD}}$, where QCD becomes non-perturbative and one should instead use an effective Lagrangian to describe heavy neutrino interaction with mesons. In dotted, the LO vacuum contribution taken from [423] is displayed.

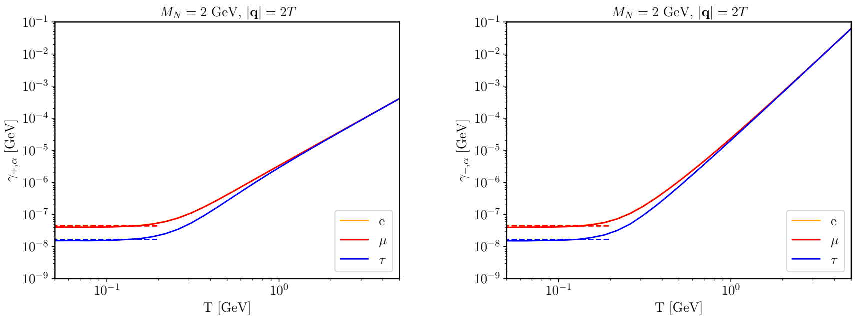


**Figure 4.3:** The left (right) panel displays the helicity-conserving (helicity-violating) heavy neutrino interaction rates for different SM flavours. In dotted, we display the zero-temperature limit obtained using the HNL decay rates from [423], including decays into mesons. We stop this line at $T = 200$ MeV as quarks are the propagating degrees of freedom above that threshold. The heavy neutrino mass was chosen to be 2 GeV while the momentum modes were chosen such that $|\mathbf{q}| = 2T$.

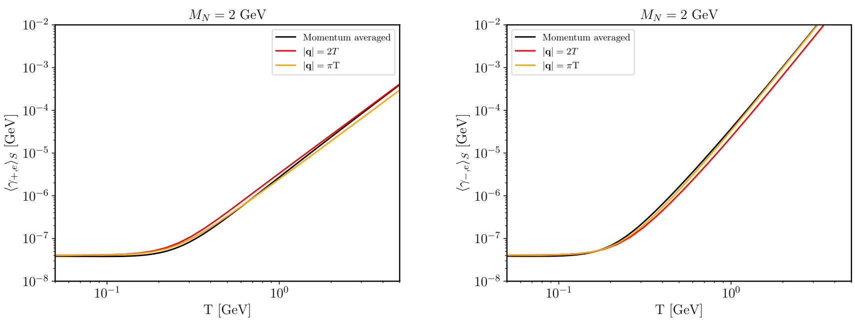


**Figure 4.4:** The left (right) panel displays (in black) the momentum averaged helicity-conserving (helicity-violating) heavy neutrino interaction rates in the electron flavour. Specific momentum modes ($|\mathbf{q}| = 2T$ and $|\mathbf{q}| = \pi T$) are displayed for comparison in red and orange respectively. The heavy neutrino mass was chosen to be 2 GeV.

We observe that the effect of neglecting quark confinement on the total interaction rate is relatively mild, of $\mathcal{O}(10)\%$ at zero temperature.

In Fig. 4.4, we compare the momentum-averaged rates entering the source term in Eq. (3.39) to the rates evaluated at two different averaged modes, i.e. $|\mathbf{q}| = 2T$ and $|\mathbf{q}| = \pi T$. We observe that, for $\gamma_-$, choosing $|\mathbf{q}| = \pi T$ approximates very well the momentum-averaged rate, as is commonly expected. In contrast, the helicity-conserving rate $\gamma_+$ is infrared-enhanced and is thus better approximated by $|\mathbf{q}| = 2T$.

### 4.3.2 HNL interaction rates in the mLRSM

We now turn to the mLRSM. As the universe cools down, the Left-Right symmetry is spontaneously broken when $\Delta_R$ develops a vev $v_R$ [391, 427]. The exact value of $v_r$ is determined by the scalar potential $V(\Delta_L, \Delta_R, \Phi)$, which can be quite involved in full generality, see e.g. [428], and is not considered here. Below the SU(2)$_R$-breaking scale (but above the EWSB), both the RH neutrinos and the associated SU(2)$_R$ gauge bosons acquire a mass proportional to $v_R$

$$M_N = f_R v_R,\; m_{W_R} = g v_R \text{ and } m_{Z'} = \frac{\sqrt{2} m_{W_R}}{\cos\theta_R}. \tag{4.20}$$

$\theta_R$ is the right-handed equivalent of the Weinberg angle $\theta_W$ and verifies $\cos\theta_R = \frac{\sqrt{\cos 2\theta_w}}{\cos\theta_w}$ [391, 427]. Given that $v_R$ is typically much larger than the electroweak scale, the $W_R$ and $Z'$ bosons can be integrated out in Eq. (3.78) to obtain the Fermi-like interaction

$$\mathcal{L}_{\text{Fermi}} = 2\sqrt{2} G_{F,R} \left( \bar{N}_i \gamma^\mu l_{R,i} \right) \mathcal{J}_\mu + \text{h.c.}\,, \tag{4.21}$$

with $l_{R,i}$ the $i^{\text{th}}$ flavour of charged right-handed leptons and $G_{F,R} = \frac{g_R^2}{4\sqrt{2} m_{W_R}^2}$ the equivalent Fermi constant for the mLRSM. The latter is typically much weaker than its SM counterpart given that the right-handed gauge boson masses have been constrained by ATLAS and CMS to lie at least an order of magnitude above those of the SM gauge bosons [429–431].

The rates are then computed in a manner analogous to the $\nu$MSM. From Eq. (4.21), we can see that $W_R^{\pm}$- and $Z'$-mediated interactions are essentially flavour-blind, since, above the EWSB and neglecting thermal masses, all particles except the RH neutrinos are massless. Owing to the Majorana nature of the heavy neutrinos, one can expand the retarded self-energy as

$$\Sigma^{\text{ret}} = \mathcal{C}_{\mathcal{J}} \hat{\Sigma}^V \left( P_R + P_L \right) \,. \tag{4.22}$$

Given the flavour-blindness of the 4-fermion interactions, we have $\mathcal{C}_{\mathcal{J}_L} = \mathcal{C}_{\mathcal{J}_R} \equiv \mathcal{C}_{\mathcal{J}}$ and the total interaction rate $\Gamma$ simply reads

$$\Gamma = \gamma_+ + \gamma_- = \mathcal{C}_{\mathcal{J}} q \cdot \text{Im}\, \hat{\Sigma}^V / |q_0|. \tag{4.23}$$

$\Gamma$ therefore depends on $\mathcal{C}_{\mathcal{J}}$, $m_i$ and $a_R, b_R, c_R, d_R$. The values taken by these coefficients are listed for the mLRSM below in Tab. 4.2. We note in passing

| Channel | $\mathcal{C}_{\mathcal{J}}$ | $m_1$ | $m_2$ | $m_3$ | $\mathcal{T}^{\omega}$ | $a_R$ | $b_R$ | $c_R$ | $d_R$ |
|---|---|---|---|---|---|---|---|---|---|
| *$W_R$-only channels* | | | | | | | | | |
| $W_RW_R$ + quarks | $3\lvert V_{R,ij}\rvert^2$ | 0 | 0 | 0 | $\mathcal{T}^1$ | $\frac{1}{2}$ | $\frac{1}{2}$ | | |
| $W_RW_R$ + leptons | 3 | 0 | $M_N$ | 0 | $\mathcal{T}^1$ | $\frac{1}{2}$ | $\frac{1}{2}$ | | |
| *Z'-only channels* | | | | | | | | | |
| Z'Z' + up-like quarks | $\frac{9}{16}$ | 0 | 0 | $M_N$ | $\mathcal{T}^1$ | $\frac{1}{2}-\frac{5}{6}s_R^2$ | $\frac{1}{2}c_R^2$ | | |
| Z'Z' + down-like quarks | $\frac{9}{16}$ | 0 | 0 | $M_N$ | $\mathcal{T}^1$ | $-\frac{1}{2}+\frac{1}{6}s_R^2$ | $-\frac{1}{2}c_R^2$ | | |
| Z'Z' + charged leptons | $\frac{3}{16}$ | 0 | 0 | $M_N$ | $\mathcal{T}^1$ | $-\frac{1}{2}+\frac{3}{2}s_R^2$ | $-\frac{1}{2}c_R^2$ | | |
| Z'Z' + 2 LHN + 1RHN | $\frac{3}{16}$ | 0 | 0 | $M_N$ | $\mathcal{T}^1$ | $\frac{1}{2}s_R^2$ | $-\frac{1}{2}s_R^2$ | | |
| Z'Z' + 3 RHN | $\frac{3}{16}$ | $M_N$ | $M_N$ | $M_N$ | $\mathcal{T}^1$ | $\frac{1}{2}$ | $\frac{1}{2}$ | | |
| Z'Z' + 3 RHN | $\frac{1}{16}$ | $M_N$ | $M_N$ | $M_N$ | $\mathcal{T}^2$ | $\frac{1}{2}$ | $\frac{1}{2}$ | $\frac{1}{2}$ | $\frac{1}{2}$ |
| *Mixed channels* | | | | | | | | | |
| Z'$W_R$ + charged leptons | $\frac{1}{4}$ | 0 | 0 | $M_N$ | $\mathcal{T}^2$ | $-\frac{1}{2}+\frac{3}{2}s_R^2$ | $-\frac{1}{2}c_R^2$ | $\frac{1}{2}$ | $\frac{1}{2}$ |
| $W_R$Z' + charged leptons | $\frac{1}{4}$ | $M_N$ | 0 | 0 | $\mathcal{T}^2$ | $\frac{1}{2}$ | $\frac{1}{2}$ | $-\frac{1}{2}+\frac{3}{2}s_R^2$ | $-\frac{1}{2}c_R^2$ |

**Table 4.2:** List of interaction channels for heavy neutrinos and their characteristics within the mLRSM in Fermi theory. The temperature is chosen to be above the EWSB scale such that all fermions are massless except for the RH neutrinos whose mass we label as $M_N$. Hence, the coefficient $\mathcal{C}_{\mathcal{J}}$ already includes the possible summation over the different flavours, except in the first channel. $V_R$ is the RH equivalent of the CKM matrix and coincides with the latter in the limit where the Higgs bidoublet's vev $\langle\Phi\rangle$ is purely real [432]. We abbreviate $\sin^2\theta_R, \cos^2\theta_R \to s_R^2, c_R^2$.

that we assumed three nearly degenerate heavy neutrino species to keep the table relatively compact. A generalisation to a different heavy neutrino mass spectrum is nonetheless straightforward.

In Fig. 4.5, we display the momentum and mass dependence of the HNL interaction rate above the EWSB for a specific benchmark. For the sake of simplicity, we chose a purely real vev for the Higgs bidoublet such that the CKM matrix remains identical to its SM form [432]. We also neglected any interactions beyond the 4-fermion ones, which are expected to dominate.

In addition to the rates themselves, it is also interesting to examine at the ratio $\Gamma/H$ as function of both the temperature and HNL mass, which we display in Fig. 4.6. We observe that, for $m_{W_R} < \mathcal{O}(10^6)$ GeV, we have $\Gamma/H > 1$ at all temperatures above the sphaleron freeze-out temperature $T_{\rm sph}$. Hence, in this regime, HNLs are expected to remain close to equilibrium at least until $T = T_{\rm sph}$, thereby limiting the generation of a baryon asymmetry. Deriving a precise bound on the value of $m_{W_R}$ would however require a more careful analysis. In particular, it would entail solving the complete set of HNL QKEs in the mLRSM. Previous studies [403] suggest a weaker bound of $m_{W_R} > 1.8\times 10^4$ GeV.

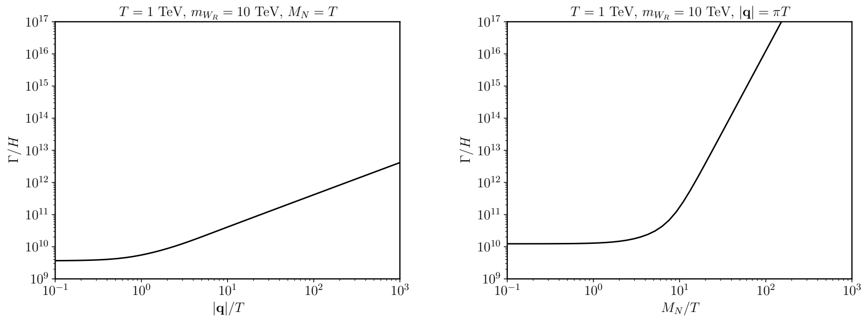

**Figure 4.5:** HNL interaction rates at $T = 1$ TeV as a function of the dimensionless momentum $\frac{|\mathbf{q}|}{T}$ for $\frac{M_N}{T} = 1$ (left figure) and the dimensionless mass $\frac{M_N}{T}$ for $\frac{|\mathbf{q}|}{T} = \pi$ (right figure). We chose as benchmark a mass for the right-handed $W$ boson of 10 TeV, beyond the current collider bounds.

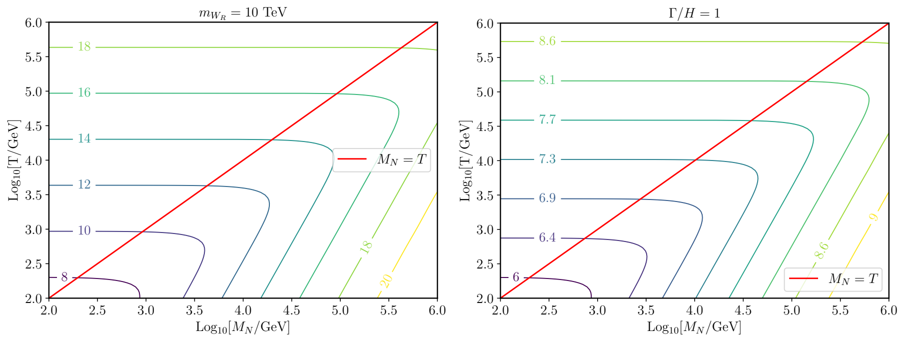

**Figure 4.6:** (*Left*) 2D contour plot displaying the value of $\mathrm{Log}_{10}(\Gamma/H)$ in the $M_N - T$ plane for a benchmark $m_{W_R} = 10$ TeV, beyond the current collider bounds. (*Right*) 2D contour plot displaying the value of $\mathrm{Log}_{10}(m_{W_R}/\mathrm{GeV})$ for which $\Gamma = H$ in the $M_N - T$ plane. For both figures, the momentum was set to $|\mathbf{q}| = \pi T$.

As highlighted at the beginning of this chapter, the rates are computed under the assumption that all interaction partners are in thermal equilibrium. Contrary to the $\nu$MSM where these were suppressed by additional powers of the mixing angle, interactions between multiple HNLs come at leading order in the mLRSM. We expect however heavy neutrinos to deviate from equilibrium only for $T \lesssim M_N$. At such low temperatures, these channels will be anyway kinematically suppressed compared to the interactions of heavy neutrinos with the massless SM particles. Nonetheless, this should in principle be taken into account for accurate predictions of the RH neutrino evolution. Additionally, the QKEs (3.35) describing the RH neutrino evolution would also need to be modified. We leave such study for future works.

Finally, we note that our computation does not capture 1) the standard Yukawa interactions between LH and RH neutrinos, and 2) the non-renormalisable interactions mediated by the scalar triplets $\Delta_L$ and $\Delta_R$.[10] Regarding 1), these are well known and can be easily implemented as they do not differ from the $\nu$MSM. Regarding 2), we expect these processes to be kinematically suppressed in the non-relativistic regime and for small heavy neutrino mass splittings, which are typically required for successful leptogenesis. This is because the scalar triplets can only mediate decays of a given heavy neutrino species into a different heavy neutrino flavour.

## 4.4 Summary

Fermi-like interactions typically appear in several BSM scenarios. In order to correctly predict the DM abundance or baryon asymmetry within such scenarios, it is of crucial importance to accurately determine fermionic interaction rates in these systems. In this chapter, we compute at leading order the finite-temperature interaction rates of fermions within a generic effective Fermi theory, retaining their helicity dependence. We factor out the fermion chiral structure and coupling from the interaction rates so as to easily reconstruct the rates of any given Fermi-like scenario.

We then apply our results to the Neutrino Minimal Standard Model and the minimal Left-Right Symmetric Model, for which we have computed both the momentum-dependent and momentum-averaged heavy neutrino interaction rates. For the $\nu$MSM, we observe percent-level agreement with the results of [402,414] for a selected benchmark. For the mLRSM, this was to the best of our knowledge the first time such a calculation (retaining all quantum statistical effects) was performed. Interestingly, we find that gauge interactions keep HNLs close to equilibrium across the entire temperature range relevant for low-scale leptogenesis as long as $m_{W_R} \lesssim 10^6$ GeV, although a more comprehensive analysis would be necessary to precisely determine the lower bound on $m_{W_R}$ imposed by leptogenesis. We also note that the precise impact that out-of-equilibrium HNL distributions have on the rates and QKEs remains to be properly investigated. The (momentum-dependent and momentum-averaged) rates corresponding to these two models will be made available for specific choices of the HNL mass in an online repository at a later time.

[10] Below the breaking scale of the $SU(2)_R$ symmetry, the scalar triplets can get a large mass, proportional to $v_R$. Integrating out these fields in principle leads to additional dimension 5 and 6 operators.

Likewise, in addition to these two examples, we intend to provide tables compiling the momentum-dependent rates of a generic heavy fermion in the limit where it is much more massive than its interaction partners, along with example code snippets in Python and Mathematica illustrating how to use these results.

# Chapter 5

# Testing the seesaw and leptogenesis mechanisms

In this chapter, we examine various phenomenological consequences of the type-I seesaw mechanism and leptogenesis. While the minimal scenario with $n_s = 2$ RH neutrino generations has already been thoroughly investigated, see e.g. [259, 384, 411], where it was shown that all 11 model parameters can, at least in principle, be constrained from a combination of different experiments[1] and leptogenesis further restricts their viable range, much less is known about the next-to-minimal scenario with $n_s = 3$. However, as highlighted in Chap. 3, this scenario is typical in many SM extensions, e.g. the mLRSM or in presence of flavour symmetries. We therefore mostly focus on the case $n_s = 3$ in this chapter (with the sole exception of Sec. 5.2.3). Sec. 5.1 focuses on the constraints imposed on model parameters by the requirement to reproduce neutrino masses. We also explore how flavour symmetries affect the testability of this scenario. Then, in Sec. 5.2, we study the additional constraints set by the requirement to reproduce the observed baryon asymmetry. We summarise our results in Sec. 5.3 and finish with a brief outlook. This chapter is heavily based on Refs. [1, 2, 5, 6, 8].

## 5.1 Testing the seesaw mechanism

Assuming RH neutrinos exist, are responsible for the origin of neutrino masses and can be produced in sufficient numbers at colliders, it is interesting to ask how much information about the 18 model parameters can be retrieved. More specifically, this question can be addressed at several levels:

[1] Although, in practice, this may require experiments capable of reaching the seesaw line. This is in general challenging, even though it might be reached in a limited mass range by DUNE [209–211], SHiP [212–214] or FCC-ee [162, 433, 434].

1. Does a given set of observables *in theory* contain enough information to reconstruct all type-I seesaw model parameters assuming they can all be measured with arbitrary precision?

2. Will any experiment in the near future be able to produce a sufficient number of events to allow for this reconstruction, assuming an idealised detector and the absence of systematic errors?

3. How much information can be extracted with realistic detectors?

The last question requires detailed simulations of the collisions but also of the detector and goes beyond the scope of this work. We thus focus in this section on the first two questions. To answer these, many different sets of observables can be considered. In this work, we focus on the RH neutrino branching ratios into the different SM flavours, parametrised through

$$\frac{\tilde{U}^2_{\alpha i}}{\tilde{U}^2} \equiv \frac{\left|\left(V_\nu \sqrt{m_\nu^{\rm diag}} \mathrm{O}_\nu \mathrm{R_C}\right)_{\alpha i}\right|^2}{\mathrm{Tr}\left[V_\nu \sqrt{m_\nu^{\rm diag}} \mathrm{O}_\nu \mathrm{R_C} \mathrm{R_C}^\dagger \mathrm{O}_\nu^\dagger \sqrt{m_\nu^{\rm diag}} V_\nu^\dagger\right]}. \tag{5.1}$$

Compared to the standard mixing angles defined in Eq. (3.16), this definition has the advantage of being completely independent of the HNL mass and mass splittings. In the limit $\Delta M \to 0$, these two definitions coincide. In the regimes where HNLs can be kinematically resolved experimentally, these flavour ratios can be directly extracted from the flavour content of semi-leptonic HNL decay products. While more complicated observables could also be used, such as angular and energy distributions or lepton number violation, their simulation requires non-standard tools [435] and goes beyond the scope of this work.

We start by investigating this question for the agnostic scenario with $n_s = 3$. Subsequently, we examine how the picture changes in the presence of the flavour and CP symmetries introduced in Sec. 3.4. Lastly, we briefly discuss the possibility to access model parameters by measuring the lifetimes of the HNLs.

### 5.1.1 How much information can we retrieve in the event of a discovery?

Firstly, it is important to notice that the range of flavour ratios $\tilde{U}^2_\alpha/\tilde{U}^2 \equiv \sum_i \tilde{U}^2_{\alpha i}/\tilde{U}^2$ consistent with light neutrino oscillation data is limited and strongly depends on the mass $m_0$ of the lightest SM neutrino as well as the neutrino mass ordering. Accurately measuring the flavour ratios could therefore give us access to the entire light neutrino mass spectrum. Alternatively, independent measurements of $m_0$ — from $\beta$ decays [436] or from cosmological observations [117,437,438] — combined with collider measurements of the flavour ratios provide a consistency check of the type-I seesaw model. As an illustration, we display in Fig. 5.1 the allowed range of $\tilde{U}_\alpha^2/\tilde{U}^2$ for both mass orderings and different choices of $m_0$, see also [439, 440] for similar figures. While the two leftmost panels were obtained by fixing light neutrino oscillation parameters to their best-fit values (except $\delta$, which is marginalised over), we also assess (in the rightmost panel) the uncertainty related to the light neutrino oscillation data by varying all parameters within their $3\sigma$ ranges (assuming $m_0 = 0$).

As discussed earlier, the $n_s = 3$ scenario possesses 18 parameters, 5 of which are already fixed by light neutrino oscillation data. This leaves 13 free parameters to reconstruct. If all three HNLs are kinematically distinguishable,[2] it is in theory possible to measure all nine $\tilde{U}_{\alpha i}/U^2$ branching ratios. Combining these observables with the three HNL masses, one clearly sees that, at best, 12 model parameters can be reconstructed. However, as we have seen, some of these parameters can be determined from complementary low-energy measurements. In particular, the Dirac CP phase $\delta$ is expected to be measured in the foreseeable future by DUNE [442] or T2HyperK [443–445] whereas $0\nu\beta\beta$ experiments are sensitive to a combination of the Dirac and Majorana CP phases. In the following, we therefore consider $\delta$ fixed[3] and freely vary the remaining parameters.

This simple parameter counting is however not sufficient to ensure that every model parameters can be reconstructed as degeneracies might remain, even if one assumes that the $\tilde{U}_{\alpha i}^2/U^2$ can be measured with arbitrary precision. In the following, we will numerically verify this is not the case. For this purpose, it is useful to organise the discussion in powers of $\epsilon$, defined in Eq. (3.28), which is the main parameter governing the expected number of events observed at colliders. In the minimal model with $n_s = 2$ for instance, the branching ratios $U_{\alpha i}^2$ can be expressed as Laurent polynomials in $\epsilon$, involving only integer powers of $\epsilon$, specifically $\epsilon^1$, $\epsilon^0$ and $\epsilon^{-1}$ [259, 446, 447]. Note that, for the sake of brevity, we will only show a limited number of formulae. More

[2] Preliminary studies [434] showed that the expected relative mass resolution at FCC-ee could be of $\mathcal{O}(1\%)$ for HNLs.

[3] For $m_0 = 0$, one of the Majorana CP phases becomes unphysical, rendering this assumption in principle unnecessary in this case.

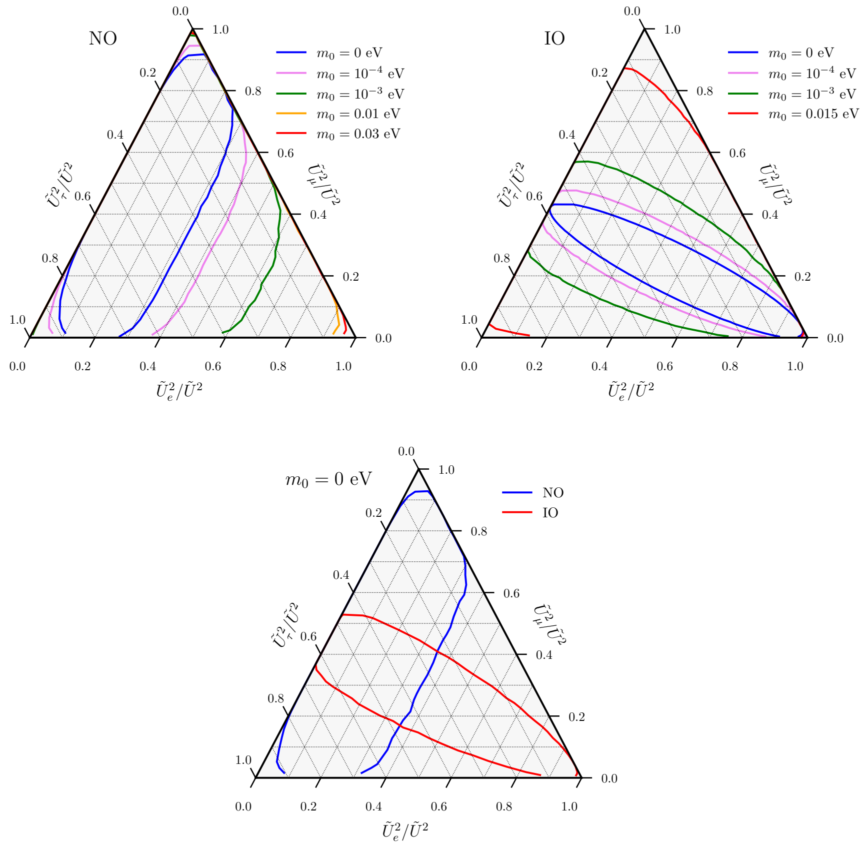


**Figure 5.1:** Range of flavour ratios $\tilde{U}_\alpha^2/\tilde{U}^2$ consistent with light neutrino oscillation data for both NO (left panel) and IO (middle panel), assuming different values of $m_0$. The three PMNS angles and 2 observed neutrino mass splittings are fixed to their best fit values [441] but $\delta$ is completely marginalised over. The right panel underscores (for $m_0 = 0$) the impact of marginalising over the light neutrino parameters. Figure and caption slightly adapted from [6].

details and explicit expressions can be found in [6], in particular in appendix A.

**Order $1/\epsilon$.** Starting with the leading order, one can show that the branching ratios $U_{\alpha i}^2$ factorises

$$U_{\alpha i}^2 = \frac{U_i^2 U_\alpha^2}{U^2} + \mathcal{O}(1/\sqrt{\epsilon}) \tag{5.2}$$

in this limit. This factorisation can easily be understood by looking at the relations between the different $U^2_{\alpha i}$

$$M_i U^2_{\alpha i} = \bar{M}\tilde{U}^2_\alpha \times \begin{cases} \frac{1}{2}(1 - \mathrm{c}^2_{\mathrm{N}1}\mathrm{s}^2_{\mathrm{N}2}) & \text{for } i = 1, \\ \frac{1}{2}\mathrm{c}^2_{\mathrm{N}1} & \text{for } i = 2, \\ \frac{1}{2}(1 - \mathrm{c}^2_{\mathrm{N}1}\mathrm{c}^2_{\mathrm{N}2}) & \text{for } i = 3\ . \end{cases} \tag{5.3}$$

Summing over the SM flavour $\alpha$, one obtains the same relation between the $\tilde{U}^2_i$. Therefore, only 5 parameters are accessible at leading order. To illustrate the sensitivity to each model parameter, we display the parametric dependence of the total mixing angle, which takes the particularly simple form

$$\bar{M}\tilde{U}^2 = \frac{e^{2\gamma}}{2}\left(m_1[1 - \mathrm{c}^2_{\nu 1}\mathrm{s}^2_{\nu 2}] + m_2\mathrm{c}^2_{\nu 1} + m_3[1 - \mathrm{c}^2_{\nu 1}\mathrm{c}^2_{\nu 2}]\right). \tag{5.4}$$

This expression shows that, at leading order and up to discrete degeneracies, one possible set of reconstructible parameters includes $\theta_{\mathrm{N}1}$, $\theta_{\mathrm{N}2}, \theta_{\nu 1}, \theta_{\nu 2}$ and $\alpha_2$. These can be expressed in terms of other model parameters, assuming the latter have been independently measured. Note that, in this subsection, we use the convention in which the Majorana mass matrix reads $\mathrm{diag}(e^{i\alpha_1/2}, e^{i\alpha_2/2}, 1)$, which can be easily mapped onto the convention used in Eq. (3.4).

**Order $1/\sqrt{\epsilon}$.** Genuinely new is the appearance of contributions at $\mathcal{O}(1/\sqrt{\epsilon})$, which vanish for $n_s = 2$. Mathematically, this is simply a consequence of the fact that the parametrisation (3.27) of $R_C$ involves only terms proportional to $\sqrt{\epsilon}$ and $1/\sqrt{\epsilon}$ for $n_s = 2$, whereas the third RH neutrino generation gives rise to $\mathcal{O}(\epsilon^0)$ terms. This can also be understood by examining the combinations

$$d_{\alpha i} = \sum_{j,k} \epsilon_{ijk} U^2_{\beta j} U^2_{\gamma k} = \bar{M}^2 \sum_{j,k} \epsilon_{ijk} \frac{\tilde{U}^2_{\beta j}\tilde{U}^2_{\gamma k}}{M_j M_k}\ , \tag{5.5}$$

which all vanish at LO because of the factorisation (5.2) and are therefore directly sensitive to next-to-leading order (NLO) contributions. Indeed, these combinations scale differently depending on the number of RH neutrino generations. In particular,

$$d_{\alpha i} \sim \mathcal{O}(U^4\epsilon) \quad \text{for } n_s = 2, \tag{5.6}$$

| Benchmark | $\bar{M}$ | $\theta_{\nu 1}$ | $\theta_{\nu 2}$ | $\omega$ | $\gamma$ | $\theta_{\mathrm{N}1}$ | $\theta_{N2}$ | $\delta$ | $\alpha_1$ | $\alpha_2$ | $m_0$ |
|---|---|---|---|---|---|---|---|---|---|---|---|
| 1 | 7 GeV | $\pi/14$ | $\pi/3.2$ | 1 | 5 | $\pi/5.1$ | $\pi/4$ | $1.3\pi$ | 0 | $\pi/10$ | 0 eV |
| 2 | 7 GeV | $\pi/2.57$ | $\pi/3.2$ | 1 | 5 | $\pi/5.1$ | $\pi/4$ | $1.3\pi$ | 0 | $\pi/10$ | 0.01 eV |

**Table 5.1:** Benchmarks chosen for our numerical analyses. In Figs. 5.2 and 5.3, we further assume that both mass splittings are 1 GeV, i.e. $M_i \in \{6, 7, 8\}$ GeV. Inverted ordering is assumed.

whereas these combinations scale as

$$d_{\alpha i} \sim \mathcal{O}(U^4\sqrt{\epsilon}) \quad \text{for } n_s = 3\,. \tag{5.7}$$

Remarkably, we found that, for the benchmarks listed in Tab. 5.1, all remaining model parameters are accessible at this order. Hence, we expect that the fact that all model parameters are, in principle, accessible at $\mathcal{O}(1/\sqrt{\epsilon})$, rather than at $\mathcal{O}(\epsilon^0)$, partially compensates for the larger dimensionality of the $n_s = 3$ parameter space.

**The full picture.** Using the complete expressions for the flavour ratios $\tilde{U}^2_{\alpha i}/\tilde{U}^2$, we then perform a numerical scan of the model parameter space to check whether the sets of parameters listed in Tabs. 5.1 are unique (within the fundamental domain defined in Tab. 3.2) or whether different choices of model parameters lead to the same flavour ratios. For these two benchmarks (as well as for a few benchmarks with NO), we find that the mapping between the $\tilde{U}^2_{\alpha i}$ and the model parameters is indeed bijective (provided that $\delta$ is determined in low-energy experiments). Therefore, we can answer positively to the first question posed at the beginning of this section. We must however caution that this bijectivity was only established with certainty for a few benchmarks and it cannot be concluded that it holds across the entire model parameter space. Moreover, it also relies on using the complete expression for the $\tilde{U}^2_{\alpha i}/\tilde{U}^2$. When considering only the LO terms, the system exhibits a higher degree of symmetry, e.g. under $\theta_{N1} \to \pi - \theta_{N1}$, and there exist discrete degeneracies. This raises the question of how much information can be retrieved in practice for semi-realistic experiments, which will be the focus of the remainder of this subsection.

### Parameter reconstruction in semi-realistic experiments

We now evaluate whether near futures experiments can realistically measure the flavour ratios $\tilde{U}^2_{\alpha i}$ with sufficient precision. The expansion parameter $\epsilon$ essentially determines the distance to the seesaw line (3.17). Several experiments can get close or reach the seesaw line, including DUNE and SHiP. In this work, we focus on FCC-ee (or equivalently CEPC) because of its sensitivity but also because the number of events that can be seen in an idealised detector of given dimensions can be computed analytically [448] and formulae to estimate the sensitivities to the $\tilde{U}^2_{\alpha i}$ have already been derived in [384].

The statistical approach followed in the rest of this work is strongly inspired by the approach taken in [384]. Essentially, we focus on displaced vertex searches such that one can safely neglect the SM background [449]. In this regime, the analytical estimates for the event numbers provided by [448] fit reasonably well results from more comprehensive simulations [162]. We also assume that all charged particles in all final states can be seen with $100\%$ detector efficiencies and focus on semi-leptonic final states, for which the extraction of the $\tilde{U}^2_{\alpha i}$ is most straightforward.

Because the number of observed semi-leptonic events is expected to follow a Poisson distribution [384], we can use the $\chi^2$-function

$$\chi^2 = \sum_{\alpha,i} \left[ \frac{(U^2_{\alpha i})_{\rm ms} - (U^2_{\alpha i})_{\rm ev}}{\Delta (U^2_{\alpha i})_{\rm ms}} \right]^2 \tag{5.8}$$

in order to estimate the statistical significance of the measurements. In this equation, $(U^2_{\alpha i})_{\rm ms}$ is the measured value of $U^2_{\alpha i}$ (with a standard deviation $\Delta (U^2_{\alpha i})_{\rm ms}$), corresponding to one of the benchmark listed in Tab. 5.1, whereas $(U^2_{\alpha i})_{\rm ev}$ denotes the fiducial value, i.e. the true value of $U^2_{\alpha i}$. Assuming a Poisson distribution for the event numbers in each channel, the mixing angles $U^2_{\alpha i}$ can be obtained from the number of measured events $\mathrm{N}_{\alpha i}$ arising from the decay of the HNL $N_i$ into a charged lepton of flavour $\alpha$. The total number of semi-leptonic events accordingly reads $\mathrm{N} = \sum_{\alpha,i} \mathrm{N}_{\alpha i}$. In this case, the statistical uncertainties on the measured quantities can be estimated as

$$\frac{\Delta U^2_{\alpha i}}{U^2_{\alpha i}} \simeq \frac{\sqrt{\mathrm{N}_{\alpha i}}}{\mathrm{N}_{\alpha i}} \, , \quad \frac{U^2_{\alpha i}}{U^2} \simeq \frac{\mathrm{N}_{\alpha i}}{\mathrm{N}} \quad . \tag{5.9}$$

Therefore, we can express the standard deviation as

$$\Delta U^2_{\alpha i} = \sqrt{\frac{U^2_{\alpha i} U^2}{\mathrm{N}}} . \tag{5.10}$$

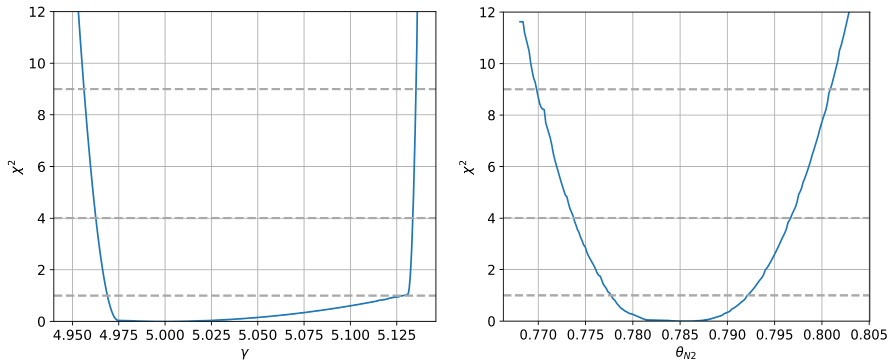


**Figure 5.2:** (*Left panel*) Dependence of the $\chi^2$-function on $\gamma$. (*Right panel*) Equivalent plot for $\theta_{N2}$. In both panels, all other model parameters are marginalised over. Event numbers in each channel correspond to the first benchmark in Tab. 5.1. Figures taken from [6].

Inserting this result in Eq. (5.8), we obtain

$$\chi^2 = \mathrm{N} \sum_{\alpha,i} \frac{\left[(U_{\alpha i}^2)_{\mathrm{ms}} - (U_{\alpha i}^2)_{\mathrm{ev}}\right]^2}{(U_{\alpha i}^2 U^2)_{\mathrm{ms}}}. \tag{5.11}$$

Using the analytical formulae provided in [448], we obtain that N $\simeq 10^5$ for the two benchmarks listed in Tab. 5.1, assuming an IDEA-type detector [433].

In Fig. 5.2, we illustrate the potential sensitivity of FCC-ee/CEPC to $\gamma$ and $\theta_{N2}$ for the first benchmark in Tab. 5.1, using the method described above and marginalising over all remaining parameters. In this figure, the $1\sigma$, $2\sigma$ and $3\sigma$ intervals correspond to the regions where the blue curve remains below the dashed lines corresponding to $\chi^2 = 1, 4$ and 9, respectively. As can be clearly seen, these parameters could be measured with a reasonably good accuracy.

Unfortunately, this is not the case for every parameter. In particular, the Majorana phase $\alpha_2$ as well as the angle $\theta_{\nu 2}$ cannot be precisely constrained and only correlations between these two parameters can be extracted for this benchmark choice. This can be seen in the left panel of Fig. 5.3. In the right panel on the other hand, we focus on the second benchmark in Tab. 5.1, which has a non-zero value for $m_0$. Remarkably, a measurement at FCC-ee/CEPC could exclude $m_0 = 0$ (and, hence, scenarios with $n_s = 2$). This illustrates well the complementarity between measurements at colliders and cosmological as well as low-energy experiments. Our capacity to exclude $m_0 = 0$ however largely depends on the values taken by the flavour ratios, i.e. it is significantly improved if the fiducial value for these ratios falls outside of the

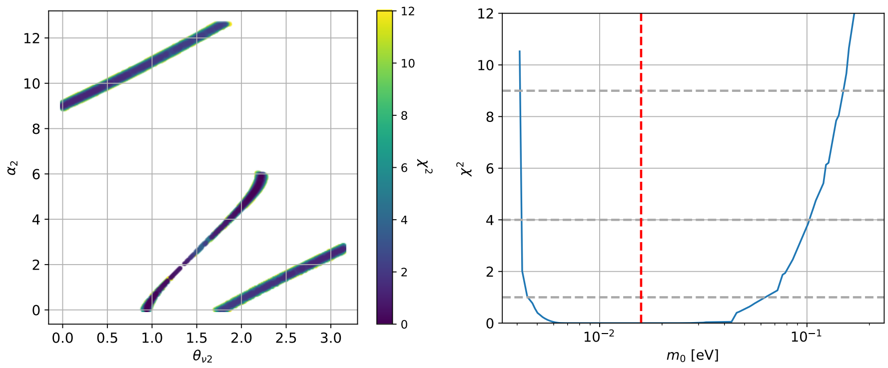


**Figure 5.3:** (*Left panel*) Two-dimensional $\chi^2(\theta_{\nu 2}, \alpha_2)$, represented by the colours as indicated in the legend. (*Right panel*) Dependence of the $\chi^2$-function on $m_0$. Event numbers in the left (right) panel correspond to the first (second) benchmark in Tab. 5.1. In both panels, all remaining model parameters are marginalised over. Figures taken from [6].

standard $m_0 = 0$ region delimited in Fig. 5.1. For the first benchmark (with $m_0 = 0$), we find that FCC-ee could exclude at the $3\sigma$-level values of $m_0$ larger than $\approx 0.08$ eV. It is therefore unlikely that colliders will be competitive with cosmological bounds. Nonetheless, having complementary laboratory probes of $m_0$ would be extremely valuable. In this context, collider searches could potentially be more sensitive than the KATRIN experiment, which currently constrains $m_0 \lesssim 0.45$ eV at $90\%$ C.L. [436], with a projected sensitivity of $0.2$ eV in the future [450]. We should, however, caution that the proposed measurement is indirect and significantly model-dependent, whereas KATRIN is based directly on kinematics and is therefore far less model-dependent. Moreover, in contrast to the sensitivity estimates of KATRIN, our analysis does not account for realistic detector simulations.

### 5.1.2 Impact of flavour symmetries

We now turn to the phenomenology of type-I seesaw models endowed with flavour and CP symmetries. These scenarios can in general be constrained on several fronts. The flavour and CP symmetries indeed tend to predict specific values for various light neutrino oscillation parameters, but also severely restricts the viable range of HNL flavour ratios. In the remainder of this subsection, we will neglect the HNL mass splittings and thus identify $\tilde{U}_\alpha^2/\tilde{U}^2$ with $U_\alpha^2/U^2$.

**Case 1)** Starting with Case 1), we find numerically that constraints from the global fit data [441][4] on the lepton mixing angles essentially fix $\theta_L$ (or $\widetilde{\theta}_L$ if $m_0 > 0$) to

$$\theta_L \approx 0.183\,(0.184)\ . \tag{5.12}$$

for NO (IO). This yields the following prediction for the PMNS angles:

$$\sin^2\theta_{13} \approx 0.0220\,(0.0222)\ \ ,\ \ \sin^2\theta_{12} \approx 0.341\ \ ,\ \ \sin^2\theta_{23} \approx 0.605\,(0.606)\ . \tag{5.13}$$

The best-fit value quoted above corresponds to a $\Delta\chi^2$ value of approximately $11.9$ $(11.2)$, thereby remaining consistent with experimental data at the $3\sigma$ level. Interestingly, Case 1) is highly predictive with respect to the various low-energy CP phases. In particular, the group theory parameter $s$, see Eq. (3.57) for a definition, fixes the value of the Majorana phase $\alpha_1$ through the relation $\sin\alpha_1 = |\sin 6\,\varphi_s|$. In this case, this Majorana phase is the only source of low-energy CP violation as the sine of the other two CP phases, the Dirac phase $\delta$ and the second Majorana phase $\beta \equiv \alpha_2 - 2\delta$, are forced to vanish, i.e. $\sin\delta = 0$ and $\sin\beta = 0$. For this reason, future experimental results from DUNE [442] or Hyper-Kamiokande [443–445] are expected to provide valuable insights about the viability of this first case.

In addition to their impact on light neutrino oscillation data, flavour and CP symmetries also limit the possible flavour ratios $U_\alpha^2/U^2$. In the large-$U^2$ limit, we find for these ratios

$$\frac{U_\alpha^2}{U^2} \approx \begin{cases} \frac{2}{3}\sin^2\,\theta_{L,\alpha} & \text{for NO}\ , \\ \frac{2}{3}\cos^2\,\theta_{L,\alpha} & \text{for IO}\ , \end{cases} \tag{5.14}$$

where we have defined the quantity

$$\theta_{L,\alpha} = \theta_L + \rho_\alpha\,\frac{4\,\pi}{3} \quad \text{with} \quad \rho_e = 0,\ \rho_\mu = +1,\ \rho_\tau = -1\ . \tag{5.15}$$

It is interesting to note that there exists a direct connection between some of these flavour ratios and the light neutrino mixing angles, e.g. we have

$$\frac{U_e^2}{U^2} = \sin^2\theta_{13} \approx 0.022\ , \tag{5.16}$$

for NO and $m_0 = 0$.

[4]Throughout this study we use the global fit results v5.1 of $\nu$FIT. These are (very) similar to the updated results v6.0 [236].

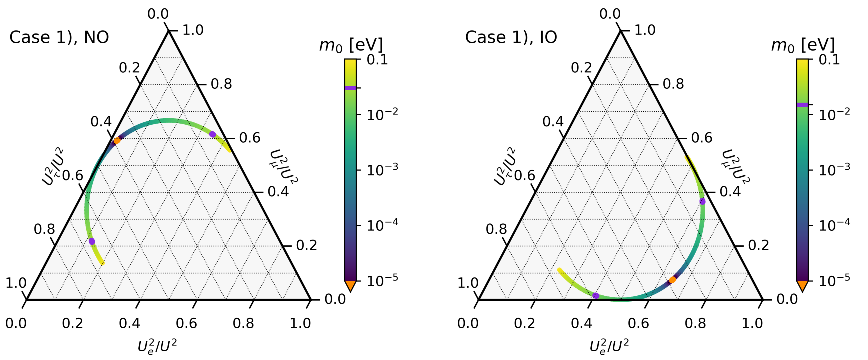


**Figure 5.4: Case 1)** Range of viable flavour ratios $\frac{U_\alpha^2}{U^2}$ assuming NO (left plot) and IO (right plot). The different colours indicate different values of the lightest neutrino mass $m_0$. The point shown in orange corresponds to the choice $m_0 = 0$, while the points in violet correspond to the current upper bound (3.6) on $m_0$ from Planck. Figure taken from [8].

For a general choice of $m_0$ and mass ordering, we display these flavour ratios in Fig. 5.4. It is clear that the viable parameter is very reduced for this first case. Moreover, there is no overlap between the flavour ratios for NO and IO. Therefore, a sufficiently accurate measurement of these flavour ratios at colliders or other laboratory experiments would give us a direct access to the light neutrino mass ordering as well as to the lightest neutrino mass $m_0$, thereby highlighting the complementarity with cosmological and $\beta$ decay constraints. For indicative purposes, we note, see Fig. 5.6, that $U^2$ should be about two orders of magnitude larger than the naive seesaw limit (3.17) in order to achieve at least $10\%$ relative accuracy on the flavour ratio $U_e^2/U^2$ at FCC-ee, assuming $M = 10$ GeV. With such precision, we for instance expect to be able to distinguish between the different mass orderings.

While scenarios with flavour and CP symmetries are in general more predictive than the agnostic scenario discussed in the previous subsection, Case 1) is particularly predictive and may not be representative of all cases. For this reason, we also consider a second incarnation of this flavour and CP symmetric scenario, namely Case 3 b.1).

**Case 3 b.1)** In this case, $\theta_L$ is not as constrained and can take a broad range of values. Interestingly, the ratio $m/n$ is forced to be close to $1/2$, i.e. $0.44 \lesssim m/n \lesssim 0.56$. For $m/n = 1/2$ exactly, we can relate the Majorana phases to the group theory parameter $\varphi_s$ via $\sin\alpha_1 = \sin\beta = |\sin 6\,\varphi_s|$. In

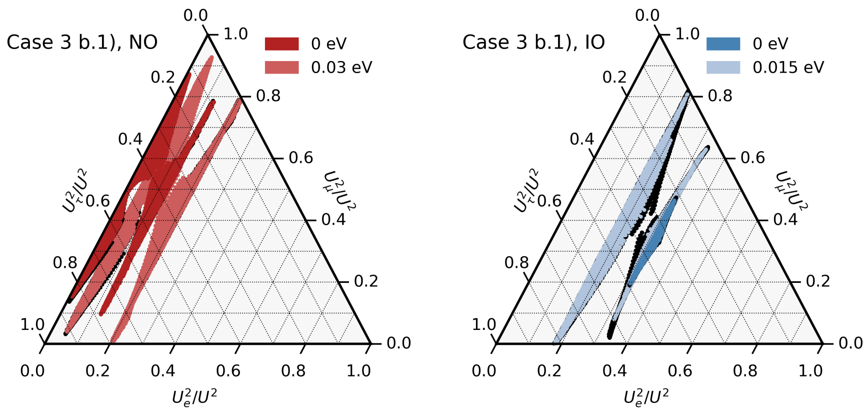


**Figure 5.5: Case 3 b.1)** Range of viable flavour ratios $\frac{U_\alpha^2}{U^2}$ assuming NO (left plot) and IO (right plot). We compare two different values of $m_0$: $m_0 = 0$ (darker red area) and $m_0 = 0.03$ eV (lighter red) for NO as well as $m_0 = 0$ (darker blue area) and $m_0 = 0.015$ eV (lighter blue) for IO. We marginalise over $\varphi_m$ and $\varphi_s$ in their allowed intervals. The black regions correspond to regions of parameter space in which only the lepton mixing angles can be fitted at the $3\sigma$ level or better, but not the CP phase $\delta$ [441]. Figure taken from [8].

general, however, the relations between the model parameters and the light neutrino oscillation parameters are more complicated.

Regarding the HNL flavour ratios, they read, in the large-$U^2$ limit,

$$\frac{U_\alpha^2}{U^2} \approx \begin{cases} \frac{1}{3}\left(1+\sin^2\theta_L\,\cos 2\,\varphi_{m,\alpha}+\sqrt{2}\,\sin 2\,\theta_L\,\cos\varphi_{m,\alpha}\,\cos 3\,\varphi_s\right) & \text{for NO}\,, \\ \frac{1}{3}\left(1+\cos^2\theta_L\,\cos 2\,\varphi_{m,\alpha}-\sqrt{2}\,\sin 2\,\theta_L\,\cos\varphi_{m,\alpha}\,\cos 3\,\varphi_s\right) & \text{for IO}\,. \end{cases} \tag{5.17}$$

In this equation, we have defined

$$\varphi_{m,\alpha} = \frac{\pi\, m}{n} + \rho_\alpha\,\frac{4\,\pi}{3} = \varphi_m + \rho_\alpha\,\frac{4\,\pi}{3}\,, \tag{5.18}$$

with $\rho_\alpha$ defined as in Eq. (5.15).

The viable range of flavour ratios for both NO and IO as well as two different (extremal) choices for $m_0$ is displayed in Fig. 5.5. It is clear that the predictive power is reduced compared to Case 1). In particular, depending on where we sit in the parameter space, it is not necessarily possible to distinguish the different mass orderings and values of $m_0$. Nonetheless, comparing with Fig. 5.1, we observe that flavour and CP symmetries still drastically reduce the viable parameter space. Assuming, for illustrative purposes, a similar precision as discussed for Case 1), it may also be possible to distinguish not only between certain cases, but also between different choices of the relevant group theory parameters. However, this conclusion strongly depends on the underlying model parameters. For instance, while Case 1) and Case 3 b.1) can be readily distinguished in the case of IO, doing so becomes significantly more challenging in the case of NO. A detailed comparison of the flavour ratios in all four cases, Case 1) to Case 3 b.1), along with a more in-depth analytical study of the boundaries of the parameter space is provided in [8].

Before closing this subsection, we briefly comment on the validity of using the large-$U^2$ limit. While the flavour ratios can deviate from the expectation in (5.14) and (5.17) for values of the mixing angle close to the seesaw line, we have verified that this remains a good approximation in the region where a sufficient number of events can be observed at colliders. This is illustrated in Fig. 5.6. Based on the simplified analytical formulae provided in [448], the left (right) panel of this figure displays the expected number of observed HNL semi-leptonic decays during the $Z$-pole run of FCC-ee/CEPC as function of the flavour ratio $\frac{U_e^2}{U^2}$ for Case 1) (Case 3 b.1)). We assumed a Majorana mass of $M = 10$ GeV and $10^{12}$ produced $Z$ bosons. More details about the considered benchmarks are provided in the caption. In the figure, black points correspond to fewer than one expected event, while the colour bar indicates that semi-leptonic event numbers as large as $10^5$ could be attained. Using Eq. (5.9), it is possible to estimate the expected statistical uncertainty on $U_e^2/U^2$. The iso-uncertainty contours corresponding to relative statistical uncertainties of $10\%$ and $1\%$ are shown in green and blue, respectively. Fig. 5.6 clearly demonstrates that, in the region where FCC-ee and CEPC could detect multiple events, the approximations (5.14) and (5.17) are expected to hold. Moreover, it highlights that the ratios $\frac{U_\alpha^2}{U^2}$ could indeed be measured with high precision, potentially enabling to discriminate between the different cases, to distinguish among the light neutrino mass orderings, and to determine of the lightest neutrino mass $m_0$.

### 5.1.3 Heavy neutrino lifetime

In Sec. 5.1.1, we focused on scenarios where all three HNLs can be kinematically distinguished. While such a situation is possible, it is by no means a requirement. For near-degenerate RH neutrinos, the total number of events in each channel depends solely on the ratios $U_\alpha^2/U^2 = \sum_{i=1}^{3} U_{\alpha i}^2/U^2$. As a

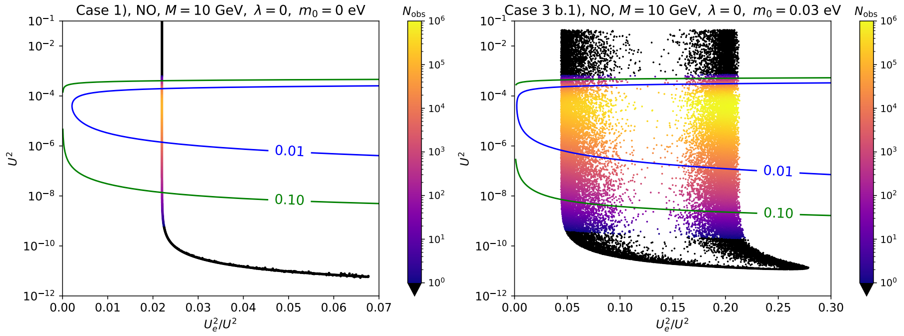


**Figure 5.6: Event numbers displayed in the $\frac{U_e^2}{U^2} - U^2$-plane** for semi-leptonic decays expected at FCC-ee/CEPC for $10^{12}$ produced $Z$ bosons. The Majorana mass $M$ is set to $M = 10$ GeV, the splitting $\lambda$ to $\lambda = 0$ and we assume light neutrino masses follow NO, while marginalising over $\kappa$. The left plot refers to Case 1) with the lightest neutrino mass being zero, $m_0 = 0$, while in the right plot results for Case 3 b.1) and $m_0 = 0.03$ eV are displayed. For both cases we marginalise over $\frac{s}{n}$, and for Case 3 b.1) also over $\frac{m}{n}$. The colour bar indicates the obtained event numbers; in particular, black points refer to numbers smaller than one. The green (blue) contour highlights the region in which $\frac{U_e^2}{U^2}$ can be measured with $10\%$ ($1\%$) relative accuracy. For further details see text. Figure taken from [8].

result, all experimental[5] sensitivity to the number of RH neutrino generations is lost. However, the potentially large number of events that can be observed at FCC-ee/CEPC opens up the possibility of measuring the differential distribution of heavy neutrino decays as a function of the distance from the collision point, and therefore accessing their lifetime. In the presence of multiple HNLs, the lifetime distribution is expected to deviate from a simple exponential decay law, *even if these HNLs are kinematically indistinguishable.*

For simplicity, we illustrate this point using Case 1), discussed earlier. In collider settings, the physical mass splittings receive a contribution from the interaction with the Higgs boson

$$\Delta\hat{M}_{\theta\theta} \approx \frac{v_{\rm ew}^2}{M}\mathrm{Re}\Big(\hat{Y}^\dagger\,\hat{Y}\Big) \tag{5.19}$$

$$= \frac{v_{\rm ew}^2}{M}\,\mathrm{Re}\Big(U_R^\dagger\,\Omega(\mathbf{3}')\,R_{kl}(\theta_R)\,(P_{kl}^{ij})^T\,\mathrm{diag}(y_1^2,y_2^2,y_3^2)\,P_{kl}^{ij}\,R_{kl}(-\theta_R)\,\Omega(\mathbf{3}')^\dagger\,U_R\Big)$$

[5]As discussed in the previous subsections, imposing *a posteriori* the requirement to reproduce the light neutrino oscillation data effectively introduces constraints on these ratios that depend on $n_s$, but these are purely theoretical.

in addition to the Lagrangian mass splittings (3.53) and (3.54); see also Eq. (3.12). For Case 1), the full mass matrix takes the form

$$\hat{M}_N \approx \begin{pmatrix} M & 0 & 0 \\ 0 & M & 0 \\ 0 & 0 & M \end{pmatrix} + M \begin{pmatrix} \frac{U^2}{3} + 2\kappa & -\frac{U^2}{3\sqrt{2}} & 0 \\ -\frac{U^2}{3\sqrt{2}} & \frac{U^2}{6} - \kappa + \lambda & 0 \\ 0 & 0 & \frac{U^2}{2} - \kappa - \lambda \end{pmatrix} . \tag{5.20}$$

To determine the expected HNL lifetimes in this scenario, one must first diagonalise the mass matrix (5.20). This yields the following hierarchy among the mixings of the three HNL generations

$$U_1^2 : U_2^2 : U_3^2 = \cos^2 \alpha_N : \sin^2 \alpha_N : 1 \, , \tag{5.21}$$

where the angle $\alpha_N$ is given by

$$\tan 2\,\alpha_N = -\frac{4\sqrt{2}\,(3\,\kappa - \lambda)}{3\,U^2 + 2\,(3\,\kappa - \lambda)} \, . \tag{5.22}$$

In two relevant limiting cases — when the HNLs are either completely mass-degenerate or exhibit large mass splittings at the Lagrangian level — these simplify to:

$$U_1^2 : U_2^2 : U_3^2 = \begin{cases} 1 : 0 : 1 \text{ for } U^2 \gg |3\,\kappa - \lambda| \, , \\ 2 : 1 : 3 \text{ for } U^2 \ll |3\,\kappa - \lambda| \, . \end{cases} \tag{5.23}$$

Tab. 5.2 summarises the values taken by these ratios in various cases and limiting regimes, see also [8] for a more comprehensive analysis. We note that, for $U^2$ much larger than the vacuum mass splittings, two RH neutrinos always combine to form a pseudo-Dirac pair, as is the case for $n_s = 2$. This observation holds even in non-flavour-symmetric scenarios. Moreover, we would like to emphasise that, in the limit $U^2 \gg |3\,\kappa - \lambda|$, $U_2^2$ is not necessarily vanishing, as it receives small contributions from the mass splittings $\kappa$ and $\lambda$ as well as from $m_0$.

In Fig. 5.7, we illustrate the expected differential distribution of HNL decays as a function of the distance from the collision point in various limiting cases. In the limit of large $U^2$, the factorisation (5.2) implies that all three HNLs have the same flavour ratio $U_{\alpha i}^2/U_i^2$. As a result, the shape of this distribution depends only on the ratios $U_1^2 : U_2^2 : U_3^2$. Fig. 5.7 highlights that a large number of observed events at FCC-ee/CEPC could allow these ratios

| Case | $\lvert\lambda\rvert \gg U^2$ | $\lvert\kappa\rvert \gg U^2 \gg \lvert\lambda\rvert$ | $U^2 \gg \lvert\kappa\rvert, \lvert\lambda\rvert$ |
|---|---|---|---|
| Case 1) | $2:1:3$ | $2:1:3$ | $1:0:1$ |
| Case 3 b.1), $m$ even and $s$ odd | $4:1:3$ | $1:0:1$ | $1:0:1$ |
| Case 3 b.1), $m$ odd and $s$ even | $4:11:9$ | $1:3:2$ | $0:1:1$ |

**Table 5.2: Ratios of heavy neutrino mixing, $U_1^2 : U_2^2 : U_3^2$,** for the different cases, Case 1) through Case 3 b.1), depending on the relative size of the splittings $\kappa$ and $\lambda$ and the total mixing $U^2$. These results are valid for both light neutrino masses with NO and with IO. Note that the heavy neutrino corresponding to 0 does not completely decouple, but has a negligible coupling compared to the other two. Table slightly adapted from [8].

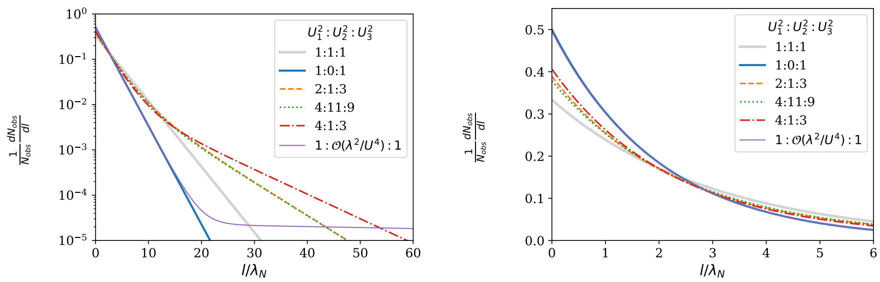


**Figure 5.7: Expected differential distribution of heavy neutrino decays as a function of $l/\lambda_N$** assuming the different ratios from Tab. 5.2. We show the distribution both on a log scale (left) and on a linear scale (right). The following ratios of heavy neutrino mixing are considered: $2:1:3$ (orange, dashed), $4:11:9$ (green, dotted), $4:1:3$ (red, dot-dashed) as well as $1:0:1$ (blue, solid), all found in Tab. 5.2, together with $1:1:1$ (gray, solid). For comparison, we also include a case with an almost decoupled state, whose lifetime is determined by $\kappa = 0$ and $\lambda \approx 0.2 \cdot U^2$ (violet, solid). Figure taken from [8].

to be measured and, in particular, make it possible to infer the presence of more than one HNL species even if HNLs are kinematically indistinguishable. While a precise determination of each lifetime would generally require a detailed statistical analysis, it is instructive to note that the presence of an almost decoupled state could manifest as a long-lifetime tail in the distribution. For sufficiently large event numbers, this tail could be clearly separated from the bulk of the decays.

## 5.2 Testing leptogenesis

Until now, we have limited ourselves to understanding how strongly the type-I seesaw model parameters are constrained by the requirement to reproduce the light neutrino oscillation data alone. It is interesting to examine next how this picture changes when the additional requirement to reproduce the observed BAU is imposed. As before, we begin by assessing the size of the viable parameter space in the vanilla $n_s = 3$ type-I seesaw model before turning to scenarios endowed with flavour and CP symmetries. We finish by exploring in Sec. 5.2.3 the interplay between constraints set by leptogenesis and by $0\nu\beta\beta$ experiments.

### 5.2.1 Mapping the parameter space for leptogenesis with three RH neutrino generations

The expected signature of RH neutrinos at a broad range of experiments primarily depends on their mixing angle $U_\alpha^2$ and mass scale $\bar{M}$. It is therefore primordial to comprehensively scan the parameter space and estimate the range of mixings and masses that are compatible with leptogenesis. While such scans have already been done in the minimal case $n_s = 2$, see e.g. [169,293,331] for recent results, no comprehensive studies of this sort exist for $n_s = 3$, which was only explored in the ARS regime in [451]. For $n_s = 2$, it is well known that the upper bound on the mixing angle is highly sensitive for $\bar{M} \lesssim m_W$ to how flavour hierarchical the washout can be. For large Yukawa couplings, the 2 HNLs indeed form a pseudo-Dirac pair, and the system is quickly driven to equilibrium. In this regime, a complete washout of the lepton asymmetries can only be avoided through large flavour hierarchies, the degree of which is constrained from light neutrino oscillation data [199]. The presence of a third (decoupled) HNL may, however, relax the experimental constraints, as well as reduce the amount of flavour asymmetry required in the washout. One can therefore naively expect a sizeable increase in the viable parameter space.

In order to confirm this intuition, we solve the set of QKEs (3.35) across the experimentally accessible mass range for two sets of initial conditions: 1) vanishing initial conditions (VIC), i.e. assuming the RH neutrinos have zero initial abundance, and 2) thermal initial conditions (TIC), i.e. assuming that additional interactions have brought RH neutrinos in thermal equilibrium at high temperatures (while remaining negligible across the temperature range relevant for leptogenesis). Moreover, we further impose the following three

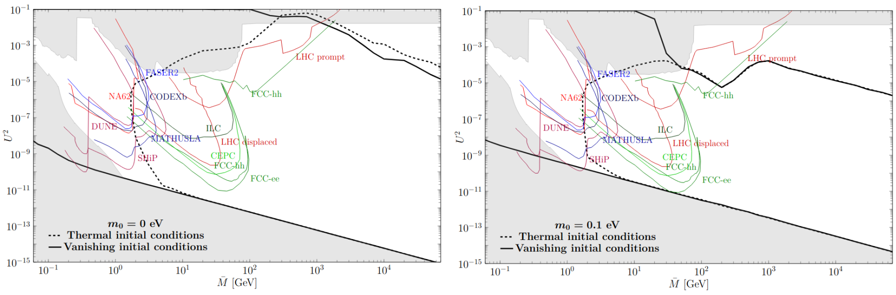


**Figure 5.8:** Allowed parameter space for leptogenesis with 3 $\nu_R$ for VIC (inside solid black line) and TIC (inside dashed black line) as well as $m_0 = 0$ eV (left panel) or $m_0 = 0.1$ eV (right panel). The gray area highlights the experimentally excluded region, while the coloured lines represent the projected sensitivities of various current and planned experiments. Further details are provided in the main text. Figure and caption slightly adapted from [1].

criteria on all parameter points to ensure the theoretical consistency of our approach. First, we ask $U^2 < 0.1$ such that the seesaw expansion (and more specifically the Casas-Ibarra parametrisation (3.21)) remains valid. Secondly, we require the vacuum HNL decay width to be smaller than half their mass such that they form well-defined quasiparticles in vacuum. Lastly, we require that the loop corrections (3.30) to the light neutrino masses remain subdominant such that using the tree-level Casas-Ibarra parametrisation is sufficient.

We display the results of this scan in the $\bar{M} - U^2$ plane, $\bar{M}$ being the averaged HNL mass, in Fig. 5.8. Given that the upper bound on $U_\mu^2$ is typically close to that on $U^2$, and that experimental searches tend to be most sensitive to scenarios with a pure muon mixing, experimental sensitivities are expressed assuming a $U_e^2 : U_\mu^2 : U_\tau^2 = 0 : 1 : 0$ mixing pattern. In gray, we display the already experimentally excluded region for this model. This region includes a broad range of different constraints. Values of $U^2$ below the naive seesaw limit (3.17) are excluded as they cannot reproduce neutrino oscillation data [236]. For masses below 1 GeV, cosmological constraints start to be relevant. Indeed, it has been long known that sufficiently long lived HNLs, i.e. HNLs with lifetime larger than $\sim 0.1$s, will spoil BBN [452–455][6] and the post-BBN history [295, 456–458], mainly because the additional contribution of HNLs to the universe's energy density increases the Hubble rate, leading to an earlier freeze-out of the $p \leftrightarrow n$ conversion, and because their decays to leptons and/or mesons will modify the rates of $p \leftrightarrow n$ conversion, e.g. by distorting the SM neutrino spectrum or due to meson-driven conver-

[6] This condition relaxes for $\bar{M} \lesssim 50$ MeV, see e.g. Fig. 6 of Ref. [454].

sions such as $\pi^- + p \to n + \pi^0$ [455]. These two constraints effectively set a lower bound on the mixing of RH neutrinos, which is stronger than the lower limit obtained from neutrino oscillation data [250] for masses below a few GeVs. Even though BBN constraints in principle depend on the mixing flavour pattern, we marginalise in this work over the mixing pattern to only display the region of the parameter space that is excluded with certainty.[7] Finally, this gray region also comprises the experimentally excluded region identified in the global scan [439]. In particular, the largest values of the sterile-active mixing angle $U^2$ are excluded by a combination of peak (cf. e.g. the searches performed at PIENU [461], E949 [462], KEK [463], and NA62 [200]) and displaced vertex (cf. e.g. the searches performed at PS-191 [464, 465], BEBC [466, 467], NuTeV [468], DELPHI [469], CHARM [470], T2K [201], ATLAS [202], and CMS [204, 471]) searches as well as electroweak precision data and constraints from CKM unitarity. The latter two provide the leading constraints for masses above $\mathcal{O}(100)$ GeV. The coloured lines indicate the estimated sensitivities of the LHC main detectors (taken from [215, 216, 472, 473]) and NA62 [199] along with that of selected planned or proposed experiments (DUNE [210], FASER2 [474], SHiP [213, 214], MATHUSLA [475], Codex-b [476]) as well as future lepton colliders [384] or proton colliders [477]. We emphasise that most of these studies assume that HNLs only couple to one unique SM flavour. While this assumption is suitable to define a set of commonly agreed benchmarks for a reasonable comparison between experiments, see e.g. [478, 479], realistic models require HNL mixings with all three SM flavours, see e.g. Fig. 5.1, and some experimental searches, in particular displaced vertex searches, can show a strong dependence on the relative mixing pattern $U_e^2 : U_\mu^2 : U_\tau^2$ [480, 481].

Comparing the left panel of this figure to e.g. figure 1 in [293], it is clear that the total active-sterile mixing angle $U^2$ consistent with the observed BAU can be orders of magnitude larger than what is possible in the $n_s = 2$ model. One reason that can explain this increase is the presence of the third HNL, which can almost decouple from the SM in the approximate $B - L$-conserving regime, see e.g. Eq. (3.20). Hence, its equilibration can be delayed up to a point where most of the baryon asymmetry is generated just before the freeze-

[7] Note that there exist also constraints on the HNL (and other feebly coupled particle species) mixing from their impact on supernova explosions, but these depend on the details of modelling the explosion (cf. e.g. [459] and references therein), and have been shown to be avoidable for axion-like particles [460]. We therefore chose to ignore these in this work.

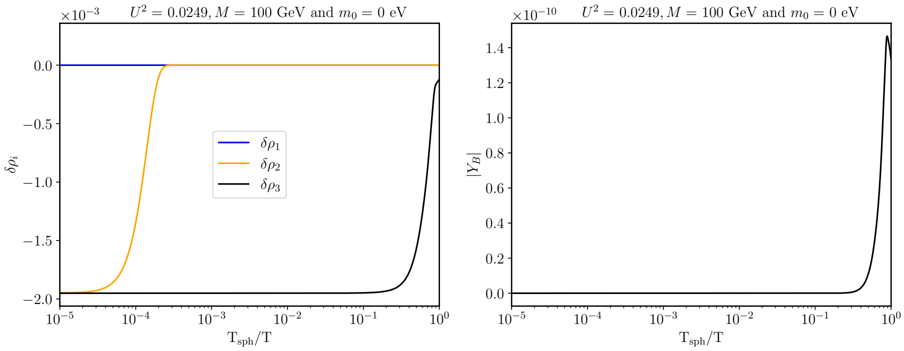


**Figure 5.9:** Evolution of the RH neutrino abundances in the flavour basis (left panel) and the total BAU (right panel) as a function of the temperature for a benchmark close to the upper bound displayed in Fig. 5.8. Figure taken from [10].

out of the sphaleron process.[8] This behaviour is illustrated for a specific choice of parameters in Fig. 5.9. While one might naively expect the upper bound on the mixing angle to scale as $1/\bar{M}$ above the TeV scale based on the scaling law derived in [169], we find that this is not the case as the constraints on the radiative corrections to the light neutrino masses spoil this simple behaviour.

For masses above the electroweak scale, it is interesting to remark that the parameter space for TIC is slightly larger than the one for VIC. This is simply a consequence of the well-known fact [262] that the asymmetry produced during the HNL approach to thermal equilibrium is of opposite sign compared to the asymmetry generated during HNL freeze-out. Hence, those partially cancel in the case of VIC, leading to a slightly smaller baryon asymmetry. In addition, we observe that leptogenesis remains feasible for masses as low as 1.7 GeV if one assumes TIC. This part of the parameter space lies within reach of various current experimental searches and could already be tested at e.g. NA62, albeit only a tiny fraction of it could be probed. While this might seem surprising given that $\bar{M} \ll T_{\text{sph}}$ in this mass range, the enhancement of the asymmetry due to resonant and flavour effects turns out to be sufficient to overcome the suppression by $(\bar{M}/T)^2$ of the deviation from equilibrium [169,293,412,482]. For VIC on the hand, the lower limit on the HNL mass set by leptogenesis is weaker than the constraints from BBN and past experimental searches.

In the right panel of Fig. 5.8, we also explore the impact of the lightest neutrino mass on the size of the parameter space. While the range of allowed

[8] This observation calls into question our approximation of treating the sphaleron freeze-out as instantaneous. However, we postpone a detailed study of the impact of a non-instantaneous sphaleron freeze-out on our upper bound to future work.

HNL mixing $U^2$ remains orders of magnitude larger than in the $n_s = 2$ case, it is noticeably reduced compared to the latter. In particular, the upper bound on $U^2$ exhibits a significant dip at $\bar{M} \approx 100$ GeV. This behaviour can be understood as the third RH neutrino generation can exactly decouple in the limit $m_0 \to 0$. For $m_0 \neq 0$, all three generations remain at least feebly coupled, which hinders the possibility of late BAU production noted in Fig. 5.9. The observed dip marks the transition between a regime where most of the BAU is produced during the HNL freeze-in to a regime where most of the baryon asymmetry is generated during their freeze-out.

Finally, at the phenomenological level, the much larger range of mixings consistent with leptogenesis not only significantly enhances the prospects for discovering HNLs at existing or near-future experiments, but also imply that a much larger number of them may be observed. For instance, the benchmarks 5.1 lie outside the experimentally excluded region and as much as $10^5$ displaced vertex events could potentially be observed at FCC-ee with these choices of parameters [6]. As highlighted in Sec. 5.1.1, this could allow the reconstruction of several model parameters. The resulting information could then be used to perform consistency checks of the hypothesis that the model (3.7) can simultaneously generate the light neutrino masses and the matter-antimatter asymmetry in the universe.

### 5.2.2 Leptogenesis with flavour symmetries

As we have seen earlier, type-I seesaw models endowed with flavour and CP symmetries feature a reduced parameter space, and the parametric dependence of the branching fraction $U_\alpha^2/U^2$ is simplified. As a consequence, one can also expect a better analytical understanding of the BAU as a function of the different model parameters. On the other hand, this reduction in parameter space may also significantly limit the feasibility of leptogenesis. In this subsection, we investigate these two aspects. We note that resonant leptogenesis assuming a type-I seesaw scenario with the same flavour and CP symmetries has also been studied in [483].

#### Analytical understanding of the baryon asymmetry

Assuming VIC and that lepton chemical potentials are initially vanishing, one can solve the set of QKEs (3.35) perturbatively in $H_N$ and $\Gamma$. At leading order, no asymmetry is generated since $\mathrm{d}\rho/\mathrm{d}t \sim \mathrm{d}\bar{\rho}/\mathrm{d}t \sim i\Gamma\rho_{\mathrm{eq}}$. At second order in these parameters, the source term is proportional to

$$\mathrm{Tr}\left[\tilde{\Gamma}_\alpha(\bar{\rho}-\rho)\right] \propto \mathrm{Tr}\left(\tilde{\Gamma}_\alpha\ [H_N,\Gamma]\right)\ . \tag{5.24}$$

A similar argument can be made for TIC. Given that both the rates and the thermal and Higgs corrections to the Hamiltonian can be decomposed according to Eq. (4.17), it is possible to understand BAU generation in terms of the following three CP-violating combinations:

$$\begin{aligned} C_{\mathrm{LFV},\alpha} &= i\,\mathrm{Tr}\Big(\left[\hat{M}_M^2, \hat{Y}^\dagger\,\hat{Y}\right]\,\hat{Y}^\dagger\,P_\alpha\,\hat{Y}\Big)\,, &(5.25)\\ C_{\mathrm{LNV},\alpha} &= i\,\mathrm{Tr}\Big(\left[\hat{M}_M^2, \hat{Y}^\dagger\,\hat{Y}\right]\,\hat{Y}^T\,P_\alpha\,\hat{Y}^*\Big)\,, &(5.26)\\ C_{\mathrm{DEG},\alpha} &= i\,\mathrm{Tr}\Big(\left[\hat{Y}^T\,\hat{Y}^*, \hat{Y}^\dagger\,\hat{Y}\right]\,\hat{Y}^T\,P_\alpha\,\hat{Y}^*\Big)\,, &(5.27)\end{aligned}$$

where $P_\alpha$ represents the projector on the SM lepton flavour $\alpha$,

$$P_e = \begin{pmatrix} 1 & 0 & 0\\ 0 & 0 & 0\\ 0 & 0 & 0\end{pmatrix}\ ,\ P_\mu = \begin{pmatrix} 0 & 0 & 0\\ 0 & 1 & 0\\ 0 & 0 & 0\end{pmatrix}\ ,\ P_\tau = \begin{pmatrix} 0 & 0 & 0\\ 0 & 0 & 0\\ 0 & 0 & 1\end{pmatrix}\ . \tag{5.28}$$

These CP-violating combinations play different roles and can dominate in different regimes of leptogenesis. In the following, we briefly summarise their main features:

- $C_{\mathrm{LFV},\alpha}$ violates lepton flavour but conserves the total lepton number, i.e. $\sum_\alpha C_{\mathrm{LFV},\alpha} = 0$. Therefore, any asymmetry generated by this term critically relies on the existence of a flavour-asymmetric washout, typically parametrised by the following *flavoured washout parameter*

$$f_\alpha = \frac{(\hat{Y}\hat{Y}^\dagger)_{\alpha\alpha}}{\mathrm{Tr}(\hat{Y}\hat{Y}^\dagger)}\ , \tag{5.29}$$

  in order to yield a non-zero total lepton number. As a consequence, the resulting BAU is of $\mathcal{O}(Y^6)$, instead of $\mathcal{O}(Y^4)$ as one would naively expect from Eq. (5.25). Nonetheless, it tends to dominate the BAU production in the low mass regime, i.e. for $M \ll 100$ GeV, as the remaining two contributions are helicity-suppressed (by $(M/T)^2$).

- On the other hand, $C_{\mathrm{LNV},\alpha}$ directly violates the total lepton number. While it is suppressed by $(M/T)^2$ in the relativistic regime, it can give sizeable contribution already for masses of $\mathcal{O}(10)$ GeV since it arises at

$\mathcal{O}(Y^4)$. For larger masses, we typically have $\gamma_+ \simeq \gamma_-$ and this contribution can be of the same order or larger than the one from $C_{\text{LFV},\alpha}$.

- Finally, the last CP invariant, $C_{\text{DEG},\alpha}$, appears due to the thermal and Higgs corrections to the Hamiltonian $H_N$, and can exist even for degenerate RH neutrinos at the Lagrangian level, i.e. for $\kappa = \lambda = 0$. Because $H_N$ and $\Gamma$ commute in both the ultra-relativistic and non-relativistic limits, i.e. the mass and flavour bases are aligned, the asymmetry generated by this invariant peaks at $M/T \sim 1$. Furthermore, since it only violates lepton flavour and not the total lepton number, it also relies on the presence of a flavour-asymmetric washout and, therefore, the BAU can only appear at $\mathcal{O}(Y^8)$.

Interestingly, one can directly relate the above CP-violating combinations to the flavoured decay asymmetries $\epsilon_{Ni\alpha}$, which — omitting a possible regulator and factor $(\hat{Y}^\dagger \hat{Y})_{ii}$, both of which generally depend on the index $i$ of the RH neutrinos — read [267]

$$\sum_j \text{Im}\left(\hat{Y}^\dagger_{i\alpha} \hat{Y}_{\alpha j}\right) \text{Re}\left((\hat{Y}^\dagger \hat{Y})_{ij}\right) (M_i^2 - M_j^2) \,. \tag{5.30}$$

On the other hand, one can develop the expressions for $C_{\text{LFV},\alpha}$ and $C_{\text{LNV},\alpha}$ found in Eqs. (5.25) and (5.26) to obtain

$$C_{\text{LFV},\alpha} = i \sum_{i,j} M_j^2 \,\{(\hat{Y}^T \hat{Y}^*)_{ij} \,(\hat{Y}^\dagger_{i\alpha} \hat{Y}_{\alpha j}) - (\hat{Y}^\dagger \hat{Y})_{ij} \,(\hat{Y}^T_{i\alpha} \hat{Y}^*_{\alpha j})\} \tag{5.31}$$

and

$$C_{\text{LNV},\alpha} = i \sum_{i,j} M_j^2 \,\{(\hat{Y}^T \hat{Y}^*)_{ij} \,(\hat{Y}^T_{i\alpha} \hat{Y}^*_{\alpha j}) - (\hat{Y}^\dagger \hat{Y})_{ij} \,(\hat{Y}^\dagger_{i\alpha} \hat{Y}_{\alpha j})\} \,. \tag{5.32}$$

In the non-relativistic regime, $\gamma_+ \simeq \gamma_-$, and the decay asymmetries are sensitive to the combinations $\frac{1}{2}(C_{\text{LFV},\alpha} - C_{\text{LNV},\alpha})$. Combining the results (5.31) and (5.32), and exchanging the indices $i$ and $j$, we obtain

$$\frac{1}{2}(C_{\text{LFV},\alpha} - C_{\text{LNV},\alpha}) = \sum_{i,j} (M_i^2 - M_j^2) \,\text{Re}\left((\hat{Y}^\dagger \hat{Y})_{ij}\right) \text{Im}\left(\hat{Y}^\dagger_{i\alpha} \hat{Y}_{\alpha j}\right) \,, \tag{5.33}$$

which is very similar to the expression in Eq. (5.30). These coefficients have been computed for the same neutrino mass model in Ref. [483], which we will use for comparison.

Lastly, in the limit of large $|\kappa| \gg |\lambda|$, oscillations between $N_1$ and $N_2, N_3$ average out and the final baryon asymmetry is suppressed, see e.g. [44] for analytical estimates. As a result, the system effectively reduces to two RH neutrinos, which are degenerate if $\lambda = 0$. Similarly to the degenerate case presented above, CP violation can only be generated in this limit through thermal and Higgs corrections to the Hamiltonian of the $N_2 - N_3$-subsystem. In this regime, the BAU production is governed by the reduced mass-degenerate CP-violating combinations

$$C^{(23)}_{\mathrm{DEG},\alpha} = i\,\mathrm{Tr}\Big( \Big[\hat{Y}^T_{(23)}\,\hat{Y}^*_{(23)}, \hat{Y}^\dagger_{(23)}\,\hat{Y}_{(23)}\Big]\;\hat{Y}^T_{(23)}\,P_\alpha\,\hat{Y}^*_{(23)}\Big)\;, \tag{5.34}$$

where $\hat{Y}_{(23)}$ is the reduced $3 \times 2$ Yukawa matrix. Explicitly,

$$(\hat{Y}_{(23)})_{\alpha i} = \hat{Y}_{\alpha i} \quad \text{for} \quad i \in \{2, 3\}\,. \tag{5.35}$$

Exactly as for $C_{\mathrm{DEG},\alpha}$, the CP-violating combinations conserve the total lepton number.

We now evaluate these CP-violating combinations for a subset of the possible cases and explicitly show how they can be used to analytically understand the dependence of the BAU with the model parameters. To keep expressions compact, it is convenient to define

$$\Delta\sigma_{12} = (3\,\kappa - \lambda)\,(2 + \kappa + \lambda) \quad \text{and} \quad \Delta\sigma_{23} = \lambda\,(1 - \kappa)\,. \tag{5.36}$$

A mass-degeneracy between the $i^{\mathrm{th}}$ and $j^{\mathrm{th}}$ RH neutrinos automatically translates into the vanishing of $\Delta\sigma_{ij}$. We also introduce the quantities

$$\Delta y^2_{ij} = y^2_i - y^2_j \tag{5.37}$$

defined for $i$ being smaller than $j$ as well as

$$\Sigma y^2 = y^2_1 + y^2_2 + y^2_3\;. \tag{5.38}$$

**Case 1)** Because the form of the Yukawa coupling depends on the parity of $s$, see Sec. 3.4.3, we need to distinguish between $s$ even and $s$ odd. For $s$ even, $C_{\mathrm{LFV},\alpha}$ reads

$$C_{\mathrm{LFV},\alpha} = \frac{4}{9}\,M^2\,y_2\,\Delta\sigma_{12}\,\Big(y_1\,\Delta y^2_{12}\,\cos\theta_{L,\alpha}\,\cos\theta_R - y_3\,\Delta y^2_{23}\,\sin\theta_{L,\alpha}\,\sin\theta_R\Big)\,\sin 3\,\varphi_s\;, \tag{5.39}$$

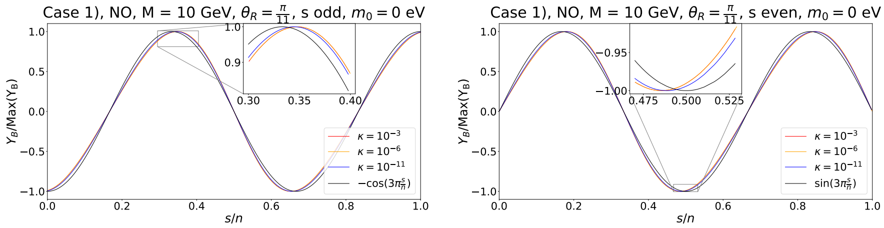


**(a)** Vanishing initial conditions. **(b)** Vanishing initial conditions.

**Figure 5.10: Case 1)** Baryonic yield $Y_B$ as function of $\frac{s}{n}$, treated as continuous parameter, for $s$ odd (left plot) and $s$ even (right plot) respectively. We set the Majorana mass to $M = 10$ GeV, $\theta_R$ to $\pi/11$, $m_0 = 0$, assume NO and choose three different benchmarks for $\kappa$, i.e. $\kappa \in \{10^{-3}, 10^{-6}, 10^{-11}\}$, which are displayed in red, orange and blue respectively. Additionally, we show the expected dependence on $\varphi_s$ ($\frac{s}{n}$) from the CP-violating combinations, compare Eqs. (5.39) and (5.40), in black. Figure taken from [2].

whereas $C_{\mathrm{LNV},\alpha}$ can be written

$$\begin{aligned} C_{\mathrm{LNV},\alpha} &= \tfrac{4}{9}\, M^2\, y_2\, \Delta\sigma_{12} \Big( y_1 \left(\Delta y_{23}^2 - \Delta y_{13}^2 \cos 2\,\theta_R\right) \cos\theta_{L,\alpha} \cos\theta_R \\ &\qquad - y_3 \left(\Delta y_{12}^2 + \Delta y_{13}^2 \cos 2\,\theta_R\right) \sin\theta_{L,\alpha} \sin\theta_R \Big) \sin 3\,\varphi_s \,. \end{aligned} \tag{5.40}$$

Moreover, we find that the mass-degenerate CP-violating combination vanishes, while its reduced equivalent $C^{(23)}_{\mathrm{DEG},\alpha}$ is non-vanishing and reads

$$\begin{aligned} C^{(23)}_{\mathrm{DEG},\alpha} = \;& \tfrac{4}{27}\, y_2\, \Delta y_{13}^2 \left(2\,\Delta y_{12}^2 - \Delta y_{13}^2 \left(1 + 2\cos 2\theta_R\right)\right) \left(y_1 \cos\theta_{L,\alpha} \sin\theta_R \right. \\ & \left. - y_3 \sin\theta_{L,\alpha} \cos\theta_R\right) \sin 2\,\theta_R\, \sin 3\,\varphi_s \,. \end{aligned} \tag{5.41}$$

The equivalent expressions for $s$ odd can be obtained by simply replacing $\sin 3\,\varphi_s$ by $-\cos 3\,\varphi_s$ in the above formulae. We checked that $C_{\mathrm{LFV},\alpha} - C_{\mathrm{LNV},\alpha}$ present the same dependence on the parameters $s$, $y_i$, $\theta_L$ and $\theta_R$ as the flavoured decay asymmetries in [483], compare equation (4.10) in this reference.

Given that all (non-vanishing) CP-violating combinations depends in the same way on $\varphi_s$ while the flavoured washout parameter (5.29) is independent of it, we expect the BAU to also scale as $\sin 3\,\varphi_s$ for $s$ even and $-\cos 3\,\varphi_s$ for $s$ odd. We verify this behaviour explicitly for NO and $M = 10$ GeV in Fig. 5.10. In particular, we verify that, for $s/n = 1/2$, the BAU vanishes exactly. We also note small deviations, increasing with $\kappa$, from the behaviour expected from the CP combinations. These deviations cannot be understood in a simple way analytically, since they result from the dynamics of the system.

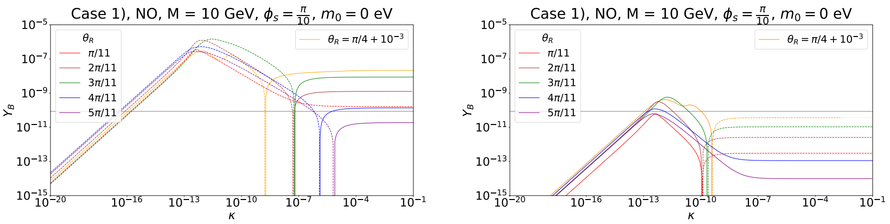


**(a)** Vanishing initial conditions. **(b)** Thermal initial conditions.

**Figure 5.11: Case 1)** We display $Y_B$ as a function of the splitting $\kappa$ for both VIC (left plots) and TIC (right plots) assuming $M = 10$ GeV, $m_0 = \lambda = 0$, $s/n = 1/10$ as well as NO. For each of these initial conditions, different choices for $\theta_R$ are displayed. Continuous (dashed) lines indicate that $Y_B$ is positive (negative). Moreover, the grey line indicates the observed value of the BAU, $Y_B \approx 8.6 \cdot 10^{-11}$. The special benchmark $\theta_R = \frac{\pi}{4} + 10^{-3}$ (shown in orange) corresponds to a value of $\theta_R$ yielding large Yukawa couplings. Faint lines indicate where the condition (3.75) is not verified. Figure taken from [2].

It is also interesting to examine the behaviour of the BAU as a function of the mass splitting $\kappa$ (assuming $\lambda = 0$). This behaviour is displayed for a specific set of benchmarks in Fig. 5.11. While the dependence of the BAU with $\kappa$ is in general complicated, some general features can be understood analytically. We start by noting that, since $C_{\mathrm{DEG},\alpha}$ vanishes exactly, the BAU also vanishes in the limit $\kappa \to 0$. For extremely small values of $\kappa$, the BAU grows linearly with $\kappa$, which is in agreement with the behaviour observed in Eqs. (5.39) and (5.40). The BAU then peaks before decreasing when the resonance condition $\Delta M^2/2E \sim \Gamma$ can no longer be satisfied. Interestingly, we also observe that the BAU does not vanish in the limit of large $\kappa$ but instead reaches a plateau. This can be understood as the reduced mass-degenerate CP-violating combination $C^{(23)}_{\mathrm{DEG},\alpha}$ is non-zero, highlighting the fact that two out of the three RH neutrinos remain almost degenerate and can provide the necessary CP violation.

Finally, we also illustrate in Fig. 5.12 the dependence on the BAU on the HNL mass splittings when both $\kappa$ and $\lambda$ are non-vanishing, see caption for details on the chosen benchmark. For $\kappa \gg \lambda$, we again observe that the BAU reaches a plateau for large $\kappa$. In contrast, large values of $\lambda$ always suppress the BAU, as expected since the HNL mass spectrum is completely non-degenerate in this case. Interestingly, leptogenesis remains nonetheless viable for relatively large mass splittings, i.e. $\lambda \sim 10^{-4}$ and $\kappa \sim 10^{-1}$. Moreover, we observe that the BAU vanishes exactly if $3\kappa = \lambda$ as expected from Eqs. (5.39) and (5.40).

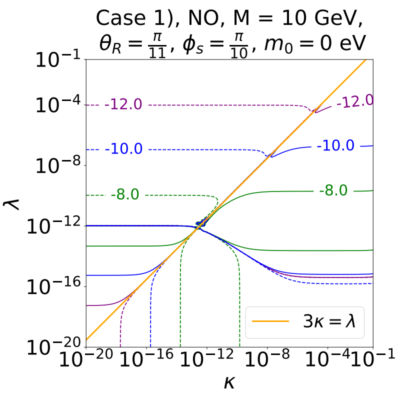


**(a)** Vanishing initial conditions.

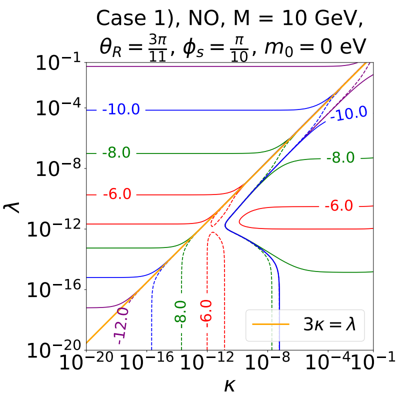


**(b)** Vanishing initial conditions.

**Figure 5.12: Case 1)** Contour plots of $\log_{10}(Y_B)$ as function of both splittings $\kappa$ and $\lambda$ for two different values of the angle $\theta_R$, $\theta_R = \frac{\pi}{11}$ (left panel) and $\theta_R = \frac{3\,\pi}{11}$ (right panel). We, furthermore, show the line corresponding to $3\,\kappa = \lambda$ in orange. In these two plots, we set $M = 10$ GeV, $m_0 = 0$, $s/n = 1/10$ and assume NO for the light neutrino mass spectrum. Figure taken from [2].

**Case 3 b.1)** Similarly to Case 1), the different CP-violating combinations depend on the parity of the group theory parameters $m$ and $s$. Moreover, expressions are in general more complex for Case 3 b.1). For the sake of brevity, we therefore only provide in this subsection a (small) subset of all possible expressions, which highlights interesting qualitative features, and refer the reader to section 6.4 and appendix G of [2] for a more comprehensive study.

In Fig. 5.13, we display the BAU as a function of the splitting $\kappa$ for $s$ even, $m$ odd and $m_0 = 0$ (left panel) and $s$ even, $m$ even and $m_0 = 0.03$ eV (right panel). More details about the chosen benchmarks are provided in the caption. These two choices exhibit qualitatively new features. For $s$ even and $m$ odd, we again observe that the BAU reaches a plateau for large values of $\kappa$. This is consistent with the fact that

$$C^{(23)}_{\mathrm{DEG},\alpha} = \frac{2}{27}\,\Delta y_{12}^2\left(2\,\Delta y_{23}^2 + \Delta y_{12}^2\,(1 + 5\,\cos 2\,\theta_R)\right)\Big(y_3(y_1\,\sin\theta_L\cos\theta_R + y_2\,\cos\theta_L\,\sin\theta_R)\,\sin\varphi_{m,\alpha} - \sqrt{2}\,y_1\,y_2\,\cos\varphi_{m,\alpha}\Big)\,\sin 2\,\theta_R\,\sin 3\,\varphi_s\,, \quad (5.42)$$

is non-zero. In contrast to Case 1) however, the BAU also reaches a plateau for $\kappa \to 0$. Indeed, in this case, we have that the mass-degenerate CP-violating combination $C_{\mathrm{DEG},\alpha}$ does not vanish, i.e.

$$C_{\mathrm{DEG},\alpha} = -\frac{\sqrt{2}}{3}\,y_1\,y_2\,(\Delta y_{12}^2)^2\,\sin 4\,\theta_R\,\cos\varphi_{m,\alpha}\,\sin 3\,\varphi_s\,. \quad (5.43)$$

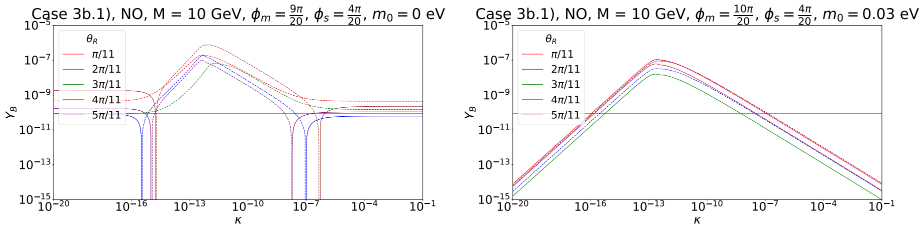


**(a)** Vanishing initial conditions. **(b)** Vanishing initial conditions.

**Figure 5.13: Case 3 b.1)** $Y_B$ as function of the splitting $\kappa$ for a Majorana mass $M = 10$ GeV and assuming NO as well as VIC. In the left (right) panel, we set the group theory parameters $\{n, m, s\}$ to $\{20, 9, 4\}$ ($\{20, 9, 4\}$) and assume $m_0 = 0$ (0.03 eV). Dashed (continuous) lines indicate where $Y_B < 0$ ($> 0$) while the grey line indicates the observed value of the BAU, $Y_B \approx 8.6 \cdot 10^{-11}$. Plots taken from [2].

On the contrary, these two CP-violating combinations vanish for $m, s$ both even, explaining why the BAU decreases as a power law for both large and small values of $\kappa$ in the right panel of Fig. 5.13. For $\lambda = 0$, we indeed have for $C_{\mathrm{LFV},\alpha}$

$$C_{\mathrm{LFV},\alpha} \;=\; \frac{2}{9}\, M^2 \left( \sqrt{2}\, y_1\, y_2\, \Delta y_{12}^2\, \Delta\sigma_{12}\, tcs_{R,-}\, tcs_{R,+}\, \cos\varphi_{m,\alpha}\, \sin 3\,\varphi_s \right) ,$$

where we have defined

$$\varphi_{m,\alpha} = \frac{\pi\, m}{n} + \rho_\alpha\, \frac{4\,\pi}{3} = \varphi_m + \rho_\alpha\, \frac{4\,\pi}{3} \quad \text{with} \quad \rho_e = 0\,,\ \rho_\mu = +1\,,\ \rho_\tau = -1\,, \tag{5.44}$$

as well as

$$tcs_{R,-} = \sqrt{2}\,\cos\theta_R - \sin\theta_R \quad \text{and} \quad tcs_{R,+} = \cos\theta_R + \sqrt{2}\,\sin\theta_R\,. \tag{5.45}$$

Since $M = 10$ GeV for this benchmark, $C_{\mathrm{LFV},\alpha}$ captures well the behaviour of the BAU for small $\kappa$, while the behaviour at large $\kappa$ is slightly less trivial but known, see e.g. [44].

### Parameter space for leptogenesis with flavour symmetries

The enhanced predictive power of type-I seesaw models endowed with flavour and CP symmetries stems from the small number of free parameters in the model. This might in turn reduce the parameter space consistent with leptogenesis and one might wonder whether this could also hurt the prospects of detecting RH neutrinos in laboratory experiments. In order to address this question, we perform in this section a complete scan of the parameter space of

| Parameter | Range of values | Prior |
|---|---|---|
| $M$ | $[50\ \text{MeV},\ 70\ \text{TeV}]$ | Log |
| $\lvert\kappa\rvert$ | $[10^{-20}, 10^{-1}]$ | Log |
| $\theta_R$ | $[0, 2\pi]$ | Log on $\lvert\theta_R - k\frac{\pi}{4}\rvert$ |
| Case 1) | | |
| $\frac{s}{n}$ | $[0, 1]$ | Linear |
| Case 3 b.1) | | Linear |
| $\frac{m}{n}$ | $[0.44, 0.56]$ | Linear |
| $\frac{s}{n}$ | $[0, 1]$ | Linear |

**Table 5.3: Range of values for the free parameters used in this analysis.** The allowed range of $\frac{m}{n}$, relevant for Case 3 b.1), slightly depends on the value of $\frac{s}{n}$ and vice versa. In this table, we only mention the maximal ranges allowed. "Prior" refers here to the measure in parameter space taken for the randomisation and is not meant to indicate a Bayesian parameter fit. Note $k$ is an integer and its actual value depends on the case. The remaining parameters are constrained as follows: $\theta_L$ is fitted in order to reproduce the measured lepton mixing angles; the splitting $\lambda$ is set to zero, if not otherwise stated; the lightest neutrino mass $m_0$ is either fixed to $m_0 = 0$ or $m_0 = 0.03\,(0.015)$ eV for NO (IO). Table slightly adapted from [8].

these scenarios, focusing again on Case 1) and 3 b.1). We refer the reader to section 5.2 of [8] for a more comprehensive overview of the parameter space of all cases. The exact ranges of values used for the different parameters involved in our scans are listed in Tab. 5.3. Note that we assume the parity of $s$ and $m$ to always be such that large values of the mixing angle $U^2$ are possible.

**Case 1)** As in the previous subsection, we start with Case 1). The range of mixing angle $U_\alpha^2$ (as a function of the averaged mass $M$) consistent with the observed BAU is displayed for both NO and IO in Fig. 5.14. We have marginalised over both the mass splitting[9] $\kappa$ as well as the group theory parameters $\varphi_s$ and the angle $\theta_R$. Similarly to Fig. 5.8, the upper grey-shaded area summarises the existing limits from electroweak precision data as well as previous experiments, which have been extracted from [84, 439]. Below, the light grey-shaded area represents the constraints set by BBN [454, 455] while the lower left part is excluded by neutrino oscillation experiments[10]. In addition, the colourful lines indicate the reach of several current or proposed experiments, i.e. DUNE [210], FASER2 [474], FCC-ee/CEPC [162], displaced

[9]While in this plot, $\lambda$ has been set to zero, we checked numerically that additionally marginalising over $\lambda$ does not visibly change the range of viable $U_\mu^2$.

[10]Note that the upper boundary of this area (slightly) depends on the light neutrino mass ordering and the lepton flavour $\alpha$ of the active-sterile mixing, i.e. $U_\alpha^2/U^2$.

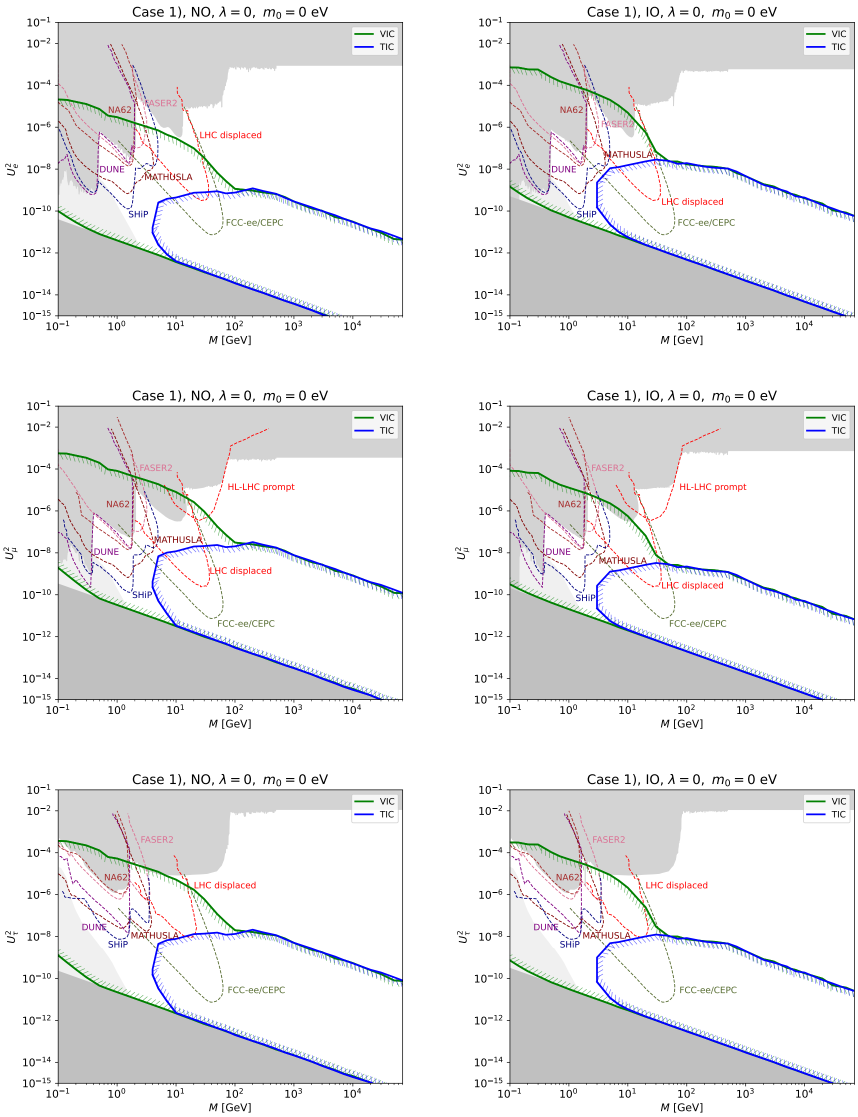


**Figure 5.14: Case 1)** Viable parameter space for leptogenesis displayed in the different planes $M - U_\alpha^2$, $\alpha = e, \mu, \tau$ (top, middle, bottom plots) assuming $m_0 = 0$ and NO (left plots) or IO (right plots). Results for both VIC and TIC are shown. Expected sensitivities of various experiments, extracted from [84, 162, 216], are represented by different coloured dashed lines, see main text for details. Figure taken from [8].

vertex [216, 472] and prompt [215, 472] searches at LHC and its upgrade HL-LHC, MATHUSLA [475, 484], NA62 [199] and SHiP [213, 214]; see [84] for a recent review of these constraints. While other proposed experiments, such as a muon collider [485, 486] or the ILC [449, 487], also constrain the HNL mix-

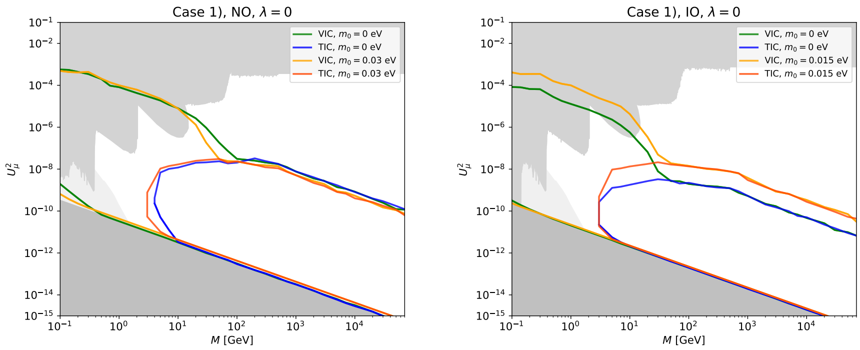


**Figure 5.15: Case 1)** Comparison of the range of mixing $U_\mu^2$ consistent with leptogenesis for vanishing lightest neutrino mass, $m_0 = 0$, and its cosmological upper limit $m_0 = 0.03\,(0.015)$ eV for NO (IO). Green and blue lines refer to $m_0 = 0$, while yellow and orange lines to non-zero $m_0$. Both, VIC and TIC, are considered. The left (right) plot assumes light neutrino masses with NO (IO). Figure taken from [8].

ing, we focus on those that provide the leading constraints on the parameter space of the scenarios under consideration.

Strikingly, Fig. 5.14 demonstrates that the parameter space is significantly reduced compared to the agnostic $n_s = 3$ scenario, compare with Fig. 5.8, although it remains larger than the minimal scenario with $n_s = 2$. Except in the case of pure $\tau$-mixing, which is not compatible with light neutrino oscillation data, the parameter space generally closes below the kaon mass.[11] We also notice that a large fraction of the remaining parameter space is expected to be probed for $M \lesssim m_Z$ by a combination of fixed-target experiments and colliders. In particular, the testability prospects are best for a pure muon coupling, which is why we will mainly explore the parameter space in $M - U_\mu^2$ plane in the rest of this section.

In Fig. 5.15, we examine the influence of the lightest neutrino mass on the shape of the parameter space. In contrast to the agnostic scenario, the impact of $m_0$ is relatively weak. Nonetheless, we notice that it exhibits the same qualitative features, i.e. the dip marking the transition between the freeze-in-dominated and freeze-out-dominated dynamics becomes more pronounced.

**Case 3 b.1)** Moving on to Case 3 b.1), we display in Fig. 5.16 the viable parameter space (in the $M - U_\mu^2$ plane) for both NO and IO and assuming $m_0 = 0$. The relative mass splitting $\kappa$ was marginalised over as well as the group

[11] A more careful analysis, which, in particular, includes more realistic HNL mixing patterns, indicates that, for $n_s = 2$, a small viable window remains near the pion mass [488].

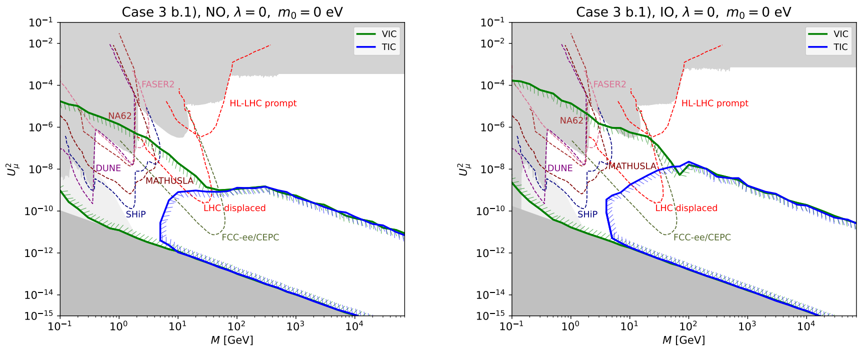


**Figure 5.16: Case 3 b.1)** Parameter space consistent with leptogenesis shown in the $M - U_\mu^2$-plane, resulting from fully marginalising over the splitting $\kappa$ and the ratios $\frac{m}{n}$ and $\frac{s}{n}$ according to the ranges in Tab. 5.3. We considered both NO (left plot) and IO (right plot) as well as both types of initial conditions, i.e. VIC and TIC. For all configurations, we assume $m_0 = 0$. The quoted experimental sensitivities are the same as in Fig. 5.14 for Case 1). Figure taken from [8].

theory parameters $m/n$ and $s/n$. Overall, the size of the viable parameter space is comparable to that in Case 1).

As was highlighted earlier, a qualitatively new feature of Case 3 b.1) is the possibility (for $m$ odd and $s$ even) of achieving leptogenesis with $\kappa = \lambda = 0$, i.e. without any mass splitting at the Lagrangian level. In the left panel of Fig. 5.17, we show the parameter space consistent with this scenario. As expected, the parameter space is much more constrained and leptogenesis can only work for relatively sizeable masses, i.e. $M \gtrsim 4$ GeV, even for VIC. Only the proposed FCC-ee could probe part of this parameter space. In the right panel of this figure, we provide a complementary slice of the parameter space, showing the range of $U^2 M$ consistent with leptogenesis as a function of $\kappa$. We observe the same two features as in the left panel of Fig. 5.13, i.e. the BAU becomes independent of $\kappa$ for both small and large values of $\kappa$. At intermediate values of the mass splitting, we observe that the parameter space is enhanced as expected since the HNL interaction width is comparable to the mass splitting in this region. As guidance for the eye, we indicate in red where the resonance condition

$$\Gamma_{\text{naive}} = \Delta M \; . \tag{5.46}$$

is fulfilled. In this equation, the quantity $\Gamma_{\text{naive}}$ denotes the HNL decay width in the symmetric phase and non-relativistic regime, i.e. $\Gamma_{\text{naive}} = \frac{M}{8\pi}(\hat{Y}^\dagger \hat{Y})_{ii}$, while $\Delta M$ is defined as the largest RH neutrino mass splitting, $3\kappa M$ in this

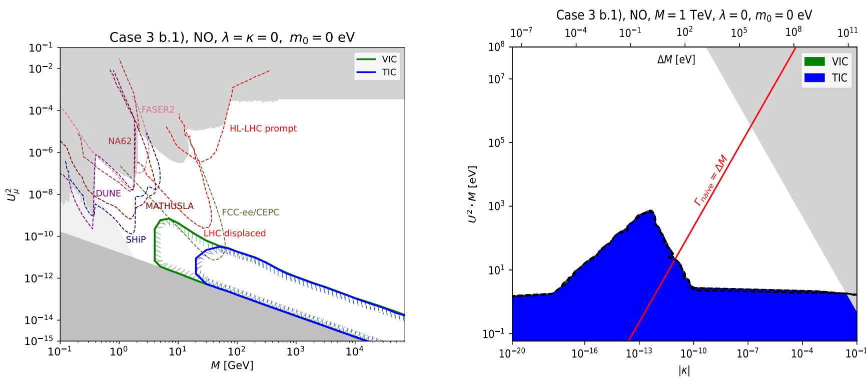


**Figure 5.17: Case 3 b.1)** Left plot: $M - U_\mu^2$-slice of the parameter space consistent with leptogenesis assuming vanishing splittings, $\kappa = 0$ and $\lambda = 0$. The different coloured dashed lines refer to various experiments, see text and Fig. 5.14 for details. Right plot: Viable parameter space for leptogenesis in the $|\kappa|(\Delta M) - U^2 \cdot M$-plane with $M = 1$ TeV. The red line indicates the resonance condition $\Gamma_{\text{naive}} = \Delta M = 3\,\kappa\,M$, see Eq. (5.46), while the upper right grey area highlights the region where the consistency condition (3.76) is not satisfied. In both panels, we display results for both types of initial conditions, VIC and TIC, and assume $m_0 = 0$ as well as light neutrino masses with NO. Figure taken from [8].

case. As is evident, the enhancement of the parameter space does not align exactly with the region where this equation is satisfied. However, we emphasise that finite-temperature and Higgs corrections to the Hamiltonian and interaction rates are not accounted for in Eq. (5.46) (but are in our numerical scan). One should therefore not expect that Eq. (5.46) precisely reproduces the region of parameter space which maximises the BAU. On a more phenomenological note, this red line also typically signals the transition between the region of parameter space where HNL decays at colliders are anticipated to violate lepton number (to the left of the red line, for $\Gamma_{\text{naive}} \ll \Delta M$) and the region where no lepton number violation is expected (to the right of the red line, for $\Gamma_{\text{naive}} \gg \Delta M$); see e.g. [489–491].

### 5.2.3 Interplay between leptogenesis and $0\nu\beta\beta$

The previous sections examined different probes of heavy neutrinos: direct and indirect searches at colliders or fixed-target experiments, light neutrino oscillation and electroweak precision data, and cosmological bounds. Beyond these, the Majorana nature of the light and heavy neutrinos and the associated lepton number violation imply the possibility of $0\nu\beta\beta$ [128], a process in which two neutrons in a nucleus are converted into two protons and two electrons without any associated neutrinos, see e.g. [492–495] for reviews. This process is forbidden in the SM and its detection would unequivocally signal the presence of new physics. While it would not constitute proof of the existence of HNLs, its observation would unambiguously indicate the Majorana nature of neutrinos and confirm the existence of light neutrino masses [496,497]. The current best lower limit on the half-life of $0\nu\beta\beta$ in $^{136}$Xe atoms at $3.8 \times 10^{26}$ years [217] lies among the most sensitive probes of the Majorana nature of neutrinos. In the near-future, next-generation experiments are expected to improve this bound by about two orders of magnitude [218–220].

The $0\nu\beta\beta$ decay lifetime depends on the nuclei properties, rendering accurate theoretical predictions of its value challenging. It is now well known that it can be parametrised as

$$\left(T^{0\nu}_{1/2}\right)^{-1} = G_{01}\, g_A^4 \frac{V_{ud}^4}{m_e^2} \left|\bar{m}_{\beta\beta}\right|^2 \mathcal{A}(0)^2 \,, \tag{5.47}$$

where $G_{01}$ is a phase-space factor (here, we use $G_{01} = 1.4 \cdot 10^{-14}$ y$^{-1}$ for $^{136}$Xe and $G_{01} = 2.2 \cdot 10^{-15}$ y$^{-1}$ for $^{76}$Ge [498]), $g_A \simeq 1.27$ is the nucleon axial coupling, $V_{ud} \simeq 0.97$ is the up-down CKM matrix element and $\bar{m}_{\beta\beta}$ is the effective neutrino Majorana mass. The latter only depends on the mixings of active and sterile neutrinos with the electron flavour and reads

$$\begin{aligned} \bar{m}_{\beta\beta} &= \frac{1}{\mathcal{A}(0)} \left( \sum_{i=1}^{3} m_i \left(U_\nu\right)^2_{ei} \mathcal{A}(m_i) + \sum_{i=1}^{n_s} M_i U_{ei}^2 \mathcal{A}(M_i) \right) \\ &\equiv m_{\beta\beta} + \sum_{i=1}^{n_s} M_i U_{ei}^2 \frac{\mathcal{A}(M_i)}{\mathcal{A}(0)} \end{aligned} \tag{5.48}$$

in the type-I seesaw model (3.7). The amplitudes $\mathcal{A}(m_i)$, $\mathcal{A}(M_i)$ encode all hadronic and nuclear physics, and for large masses $m$, i.e. $m \gtrsim 2$ GeV, they typically scale as $1/m^2$. Note that, in good approximation, we have $\mathcal{A}(m_i) \approx \mathcal{A}(0)$ for the light neutrino contribution. The first term in Eq. (5.48) captures the standard active neutrino exchange, whereas the second one encodes the additional contribution from HNLs. While the former largely dominates for high-scale seesaw models, the HNL contribution can be of comparable magnitude — or even larger — for masses around the nuclear Fermi momentum $k_F \simeq 140$ MeV, which is a typical nuclear scale characterising the average momentum transfer of the process [499].

While the direct impact of HNLs on $0\nu\beta\beta$ rates has already been investigated in e.g. [446, 499–505] and similar studies of the interplay between constraints set by $0\nu\beta\beta$ and low-scale leptogenesis were performed in [411, 506, 507], these works were based on simplified formulae for the amplitudes $\mathcal{A}(\bar{M})$, which are not accurate enough for $\bar{M} \lesssim 2$ GeV. Moreover, no comprehensive parameter space scans were performed. In this thesis, we use the recent results from Refs. [508,509], which have applied the recently developed chiral EFT framework for $0\nu\beta\beta$ computations involving light HNLs and have included several new effects not considered in more traditional approaches. Similarly to Sec. 5.2.1, we scan the parameter space of the vanilla type-I seesaw model (3.7) consistent with both light neutrino oscillation data and leptogenesis. We then analyse how $0\nu\beta\beta$ experiments further constrain this parameter space. However, contrary to the previous sections, we focus here on the case $n_s = 2$ and leave the $n_s = 3$ scenario for future work.[12]

Because neutrino mixing remains unitary when including both light and heavy neutrino contributions, we have a partial cancellation between light and heavy contribution to the $0\nu\beta\beta$ rates

$$m_1 \left(U_\nu\right)_{e1}^2 + m_2 \left(U_\nu\right)_{e2}^2 + m_3 \left(U_\nu\right)_{e3}^2 = -M_1 U_{e1}^2 - M_2 U_{e2}^2 \,, \tag{5.49}$$

which is not complete because $\mathcal{A}(M_i) \neq \mathcal{A}(0)$. Inserting Eq. (5.49) into Eq. (5.48) and expanding in the mass splitting $\mu = (M_2 - M_1)/\bar{M}$, with $\bar{M} = (M_2 + M_1)/2$ the averaged mass of the system, we obtain, at first order,

$$\bar{m}_{\beta\beta} \simeq \quad e^{i\,\arg(m_{\beta\beta})} \left( |m_{\beta\beta}| \left[ 1 - \frac{\mathcal{A}(\bar{M})}{\mathcal{A}(0)} \right] - \frac{1}{2} e^{i\lambda} \bar{M}^2 \mu \, U_e^2 \left| \frac{\mathcal{A}'(\bar{M})}{\mathcal{A}(0)} \right| \right) \,, \tag{5.50}$$

with $\mathcal{A}'(\bar{M}) \equiv \mathrm{d}\mathcal{A}(\bar{M})/\mathrm{d}\bar{M}$. Explicit expression (for both NO and IO) for the phase $\lambda \equiv 2\mathrm{Re}(\omega) + \varphi$, where $\varphi$ depends only on the Majorana phase $\eta$ and the measured light neutrino parameters, as well as $|m_{\beta\beta}|$ can be found in appendix C of [5].

From Eq. (5.50), we observe that, at leading order in $\mu$, HNLs only affect the $0\nu\beta\beta$ rate in two ways: 1) a suppression by a factor $1 - \mathcal{A}(\bar{M})/\mathcal{A}(0)$ of the active neutrino due to the unitarity of neutrino mixing, and 2) an additional (positive or negative) contribution proportional to the product of the mass splitting and electron coupling $\mu U_e^2$. However, because radiative corrections to the light neutrino masses (3.30) are sensitive to the same combination of parameters, HNL corrections to the $0\nu\beta\beta$ rates should be bounded from

[12] See [505] for a study of $0\nu\beta\beta$ constraints on the type-I seesaw model with $n_s = 3$, though the impact of leptogenesis was not investigated.

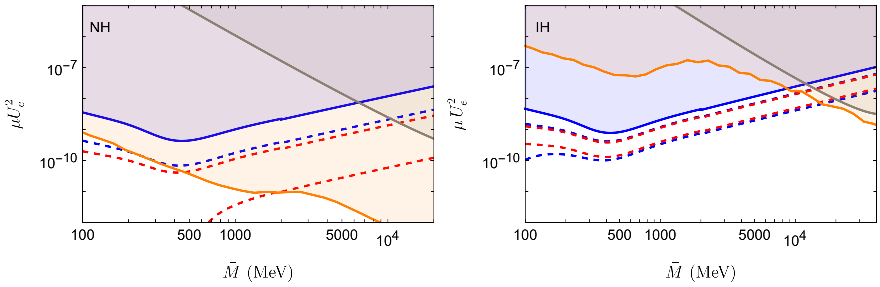


**Figure 5.18:** Bounds in the $\bar{M} - \mu U_e^2$ plane for normal (left) and inverted (right) hierarchies. The limits are shown with blue ($0\nu\beta\beta$ decay), orange (leptogenesis), and grey (radiative corrections) solid lines, and the shaded regions are excluded. We also show with dashed lines the regions that would be allowed by $0\nu\beta\beta$ with $10^2\times$ (blue) and $10^3\times$ (red) stronger limits in case no signal is observed. Figure taken from [5].

above to avoid fine-tuning issues. Requiring the absence of fine-tuning yields the constraint

$$\mu\, U_e^2 \leq \frac{v_{\rm ew}^2 |m_{\beta\beta}|}{\bar{M}^3} \frac{(4\pi)^2}{2l'(\bar{M}^2)} \,. \tag{5.51}$$

This upper bound is shown in grey in Fig. 5.18. Inserting this upper bound in Eq. (5.50), Eq. (5.51) translates into an upper bound on the mass of HNLs which can give a sizeable contribution to $0\nu\beta\beta$

$$\bar{M} \lesssim v_{\rm ew}^2 \frac{(4\pi)^2}{4l'(\bar{M}^2)} \frac{\mathcal{A}'(\bar{M})}{|\mathcal{A}(0)|} \sim 10\,\text{GeV}\,. \tag{5.52}$$

A similar bound was found in [261].

In Fig. 5.18, we display for both NO and IO the constraints set by current $0\nu\beta\beta$ experiments (in solid blue) in the $\bar{M} - \mu U_e^2$ plane, and compare them to constraints set by leptogenesis (in orange) and radiative corrections to light neutrino masses (in grey). As is clear, the constraints set by current $0\nu\beta\beta$ experiments become weaker than those imposed by the requirement of avoiding fine-tuning for $\bar{M} \gtrsim 10$ GeV. Inspired by the projections for nEXO [218] and LEGEND [219], we also display in blue (red) dashed lines the respective upper and lower bounds on the value of $\mu U_e^2$ if no signal is observed after an improvement by two (three) orders of magnitude on the current constraints.

In the case of IO, an improvement by two orders of magnitude is sufficient to completely probe the standard scenario with only three active neutrinos. The absence of any signal at next-generation experiments would therefore clearly indicate the presence of new physics. Within the type-I seesaw model (3.7)

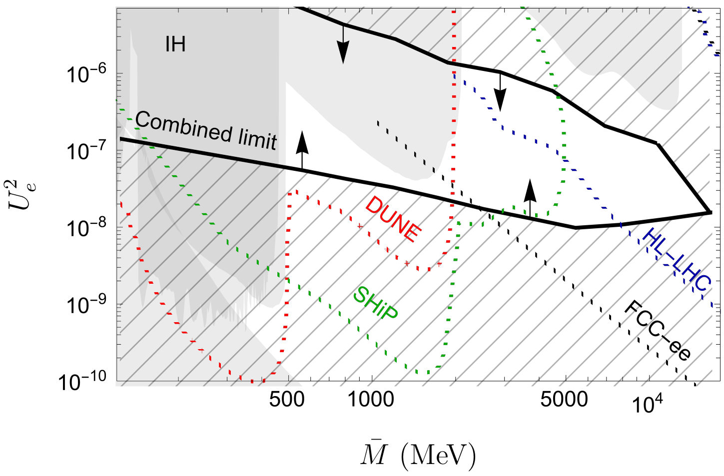


**Figure 5.19:** Future (projected) constraints on $U_e^2$ for IO marginalized over $\mu$ in absence of any observation of $0\nu\beta\beta$ at next-generation experiments. Combined limits from $T_{1/2}^{0\nu}(^{136}\mathrm{Xe}) > 3.8 \cdot 10^{28}$ y, leptogenesis, and current experimental and BBN constraints, would force the mixing angle to lie within the region bounded in black (the arrows point towards the allowed region). The dotted lines represent projected upper bounds on $U_e^2$ from DUNE, SHiP, HL-LHC, and FCC-ee, while the currently constrained regions are shaded in grey. Figure taken from [5].

with $n_s = 2$, the HNL mixings and mass splittings would be required to lie within the bands shown in the right panel of Fig. 5.18 in order to cancel the contribution from the light neutrinos. For $\bar{M} \lesssim 100$ MeV, the cancellation due to the unitarity of neutrino mixing starts to be sufficient on its own to explain the absence of signal and we note that the lower bound on $\mu U_e^2$ starts to decrease. Further improving the experimental constraints on the $0\nu\beta\beta$ lifetime would not reduce the width of this band (for $\bar{M} \gtrsim 100$ MeV), as it is dominated by the uncertainties on the values of the PMNS parameters in this regime. We also note that the constraints set by leptogenesis are subdominant for $\bar{M} \lesssim 10$ TeV.

In contrast, the standard prediction for the $0\nu\beta\beta$ lifetime for NO lies more than an order of magnitude below that for IO. As a results, improving the experimental sensitivity by a factor 100 is insufficient and only yields an upper bound on $\mu U_e^2$. At the same time, the parameter space consistent with the observed BAU is significantly more constrained, and as a result, bounds from leptogenesis currently dominate across most of the relevant parameter space. Further improving the sensitivity by an order of magnitude would yield a lower bound on $\mu U_e^2$.

One can also look at the constraints set by $0\nu\beta\beta$ on $U_e^2$ alone by marginalising over $\mu$, which we can then compare to various other experimental searches. In Fig. 5.19, we show the parameter space that remains viable if no signal is observed by the next generation of $0\nu\beta\beta$ experiments (assuming $T_{1/2}^{0\nu}(^{136}\mathrm{Xe}) > 3.8 \cdot 10^{28}$ y) and remains consistent with leptogenesis. We additionally display constraints from previous laboratory experiments[13] as well as BBN in grey whereas the dotted colourful lines represent the expected sensitivity of the future DUNE, SHiP, HL-LHC and FCC-ee experiments. As one can see, marginalising over the splitting $\mu$ renders the resulting parameter space (in the $\bar{M} - U_e^2$ plane) tightly constrained. It will be fully probed by a combination of DUNE, SHiP, HL-LHC and FCC-ee. Above $20$ GeV, the parameter space closes because the HNLs cannot contribute sizeably to the $0\nu\beta\beta$ rates. We then go back to the standard scenario with 3 active neutrinos, which is excluded for IO.

Finally, we note that the theoretical predictions for the $0\nu\beta\beta$ rates relies on the knowledge of various nuclear matrix elements and low-energy constants, which are typically plagued with various $\mathcal{O}(1)$ uncertainties. While one might wonder how these uncertainties affect our results, one can show these are subdominant compared to the uncertainties coming from the free PMNS phases. To confirm this, an explicit estimate of these uncertainties was done in [5], see figure 3 in this reference.

## 5.3 Summary and outlook

Extending the SM with RH neutrinos offers a minimal solution to several problems in particle physics and cosmology, including the origin of the neutrino masses, of the baryon asymmetry of our universe and of dark matter. Understanding their properties and how they are constrained by various cosmological and laboratory experiments is therefore of crucial importance. In particular, while the minimal type-I seesaw model with two generations of RH neutrinos has already been comprehensively studied, the next-to-minimal scenario with three near-degenerate RH neutrino generations has largely escaped attention until now. Exploring different aspects of this scenario was the main goal of this chapter. To that end, we proceeded in two steps, each aiming to answer one of the following key questions:

[13] We focus on peak searches, such as the ones performed at PIENU [461], E949 [462], KEK [463], and NA62 [200], which are less sensitive to the HNL mixing pattern, and displaced vertex searches [201, 202, 465, 467, 470, 471].

1. Assuming RH neutrinos are responsible for the origin of the light neutrino masses, how much information about the model parameters can be retrieved in the event of a discovery at laboratory experiments?

2. What additional constraints are placed on the parameter space if one assumes RH neutrinos are also responsible for the generation of the BAU through low-scale leptogenesis?

We examined both these questions, first within the vanilla type-I seesaw model, where the Yukawa couplings are only required to reproduce the light neutrino oscillation data, and then in scenarios endowed with flavour and CP symmetries.

Starting with the first question, we focus in Sec. 5.1.1 on the amount of information that can be retrieved on model parameters from measurements of the flavour ratios $U_{\alpha i}^2/U^2$ at displaced vertex searches at FCC-ee/CEPC. Our main findings are that all 13 free parameters of the $n_s = 3$ parameter space can in principle, i.e. assuming an infinite number of observed events, be extracted from measurements of these ratios provided that the Dirac phase $\delta$ has been determined independently. Interestingly, we find that information on all model parameters can already be retrieved at $\mathcal{O}(1/\sqrt{\epsilon}) \simeq \mathcal{O}\left(\sqrt{m_\nu/U^2\bar{M}}\right)$ instead of $\mathcal{O}(\epsilon^0)$ as is the case for $n_s = 2$. This key difference partially compensates for the larger dimensionality of the $n_s = 3$ parameter space. Assuming a realistic number of events of $\approx 10^5$, we find that, while some parameters can be accurately extracted, some degeneracies and correlations among others persist.

In Sec. 5.1.2, we examine how the standard predictions for the $U_\alpha^2/U^2$ are modified in presence of flavour and CP symmetries, focusing on a scenario where the flavour symmetry group is $\Delta(6n^2)$. As expected, the range of flavour ratios consistent with light neutrino oscillation data is reduced. Remarkably, assuming a similar number of events as chosen in the previous subsection, measuring these flavour ratios would allow in some cases for a precise determination of various model parameters, such as the lightest neutrino mass or the mass ordering, and differentiate between different realisations of the flavour symmetry. In addition, low-energy experiments, such as DUNE, are expected to provide valuable insights and potentially exclude some of the cases discussed by measuring the low-energy CP phases. We finished in Sec. 5.1.3 by briefly discussing the possibility to access different model parameters by measuring the lifetime distribution of HNL decays.

Moving on to the second question, we performed in Sec. 5.2.1 the first comprehensive scan of the $n_s = 3$ parameter space consistent with the observed

BAU. We found that the range of viable mixing angle is increased by several orders of magnitude compared to the $n_s = 2$ parameter space. This could be explained by the observation that the third RH neutrino generation is less constrained by neutrino oscillation data and can largely decouple, such that the BAU production is delayed until just before the sphaleron freeze-out. In view of the results of the previous two sections, this large increase in the viable parameter space opens up the possibility to not only discover HNLs but also produce sufficiently many events at colliders or fixed-target experiments to perform consistency checks of the model. In Sec. 5.2.2, we examine how this conclusion is changed in presence of flavour symmetries. We first observe that the reduced parameter space allows us to gain some analytical insight into the dependence of the BAU on the model parameters. We also numerically scanned the viable parameter space for different cases, which we found to be much smaller than in the agnostic $n_s = 3$ scenario. Nonetheless, it remains larger than in the $n_s = 2$ case, sufficiently large to be probed by a broad range of experiments.

Finally, we showed in Sec. 5.2.3 that $0\nu\beta\beta$ experiments can put interesting constraints on the leptogenesis parameter space. In particular, we find that, for inverted ordering, bounds on $\mu U_e^2$ from $0\nu\beta\beta$ experiments are stronger than bounds from leptogenesis. Moreover, the absence of a signal in the next generation of experiments would force the mixing angle to lie in a relatively small band in the $\bar{M} - \mu U_e^2$ plane, since a sizeable contribution from HNL would be required to cancel the active neutrino contribution. For NO, further experimental improvements will be necessary to reach the same conclusions. While in this subsection we focused on the $n_s = 2$ scenario, it would be interesting to see how these conclusions are modified for $n_s = 3$.

In summary, we find that the $n_s = 3$ case exhibits a rich phenomenology and, in particular, could be tested across broad range of experiments, probing the parameter space in complementary directions. In particular, producing a sufficient number of events at future colliders to measure the branching fractions into the different SM flavours could provide valuable insights into the presence of new symmetries, offer a complementary probe of light neutrino oscillation data and test leptogenesis.

Looking ahead, a more detailed study of the parameter space consistent with leptogenesis in the vanilla type-I seesaw model would be desirable. In particular, further clarifying the key physical differences between the $n_s = 2$ and $n_s = 3$ parameter spaces remains important. Moreover, characterising the upper bound on the flavoured mixing angle $U_\alpha^2$ — rather than on the total mixing angle $U^2$ — along with constraints on other parameters such as the mass splittings would significantly improve our ability to assess potential experimental signatures.

# Part III

# The decoupling of neutrinos

# Introduction

The Cosmic Microwave Background (CMB) provides some of the most stringent constraints on the content and evolution of our universe. In particular, it serves as a powerful probe amount of radiation at the recombination epoch, commonly parametrised by the so-called effective number of neutrinos $N_{\text{eff}}$. Within the SM, only photons and neutrinos remain relativistic up until recombination. At high temperatures, both are interacting strongly enough to remain in equilibrium with each other. However, as the temperature decreases below $T \sim \mathcal{O}(1)$ MeV, neutrinos progressively decouple from the rest of the plasma. The subsequent annihilation of electrons and positrons then finishes to reheat the photon bath compared to its neutrino counterpart, leading to the temperature ratio $T \simeq (11/4)^{1/3} T_\nu$, $T_\nu$ and $T$ being the temperatures of the neutrino and photon bath respectively. An illustration of the evolution of $T/T_\nu$ is displayed in the following Fig. 6.1. $N_{\text{eff}}$, defined by the relation

$$\rho_{\text{rad}} \equiv \frac{\pi^2 T^2}{15} \left(1 + \frac{7}{8}\left(\frac{4}{11}\right)^{4/3} N_{\text{eff}}\right) , \tag{6.1}$$

with $\rho_{\text{rad}}$ denoting the total energy density of relativistic particles, precisely captures this effect. Note that Eq. (6.1) has been normalised such that, in the SM, $N_{\text{eff}}$ approximately quantifies the number of neutrino generations, i.e.[1] $N_{\text{eff}} \simeq 3$. Beyond the SM however, the presence of additional radiation, in the form of e.g. GWs (see footnote 2 and references therein) or yet undiscovered light particles such as sterile neutrinos [510–513], axions [514–519] or dark photons [520–522], can severely modify the value of $N_{\text{eff}}$. Improving the experimental accuracy of $N_{\text{eff}}$ measurements as well as the robustness of our theoretical predictions is therefore essential to constrain these models.

On the experimental side, the CMB provides as previously highlighted the leading constraints on $N_{\text{eff}}$; though it should be noted that the precision measurements of various light element abundances provide compatible predictions and of only slightly weaker accuracy [523]. In a nutshell, increasing[2] $N_{\text{eff}}$ leads to an accelerated expansion rate, which in turn results in an increase in the

[1] Interestingly, this does not depend on the nature of neutrinos, i.e. Dirac or Majorana. While Dirac neutrinos possess twice as many internal degrees of freedom, only half of these gets populated by the weak interaction in the early universe.

[2] This statement is naturally dependent on how one modifies the remaining cosmological parameters. In order to keep the angular scale of the sound horizon and the redshift at matter-radiation equality fixed, the increase in $N_{\text{eff}}$ is generally accompanied with a simultaneous increase in the cold DM density and density of dark energy [524].

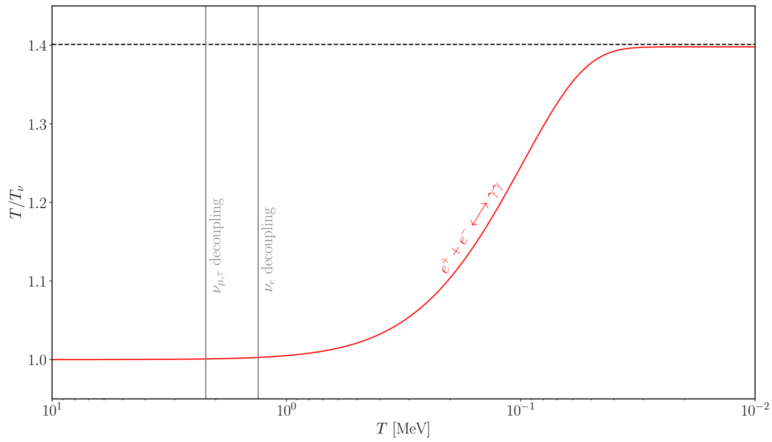


**Figure 6.1:** Evolution of the photon-to-neutrino temperature ratio. The black dashed line represents the SM naive expectation $T/T_\nu = (11/4)^{1/3}$ whereas the two gray lines display the instantaneous decoupling temperature of the electron, muon and tau neutrinos.

angular scale at which photons efficiently erase temperature anisotropies. As a consequence, the high-multipole tail of the CMB spectrum is suppressed [524], see also [104, 525, 526] for pedagogical reviews. The current best constraints on $N_{\text{eff}}$ were set by the space observatory Planck [117] (combined with baryon acoustic oscillation measurements from galaxy surveys, see e.g. [437, 438])

$$N_{\text{eff}}^{\text{obs}} = 2.99 \pm 0.17 \tag{6.2}$$

at $68\%$ C.L.. More recently, results from the South-Pole telescope (SPT-3G) [527] seem to have reduced the experimental uncertainty to $0.13$ (at $68\%$ C.L.) [528] when combined with previous data from Planck. Similar performances were achieved in March of this year by the Atacama Cosmology Telescope (ACT) [529]. In the near future, measurements from the Simons observatory [530, 531] and CMB-S4 [53] are expected to bring this uncertainty to $0.045$ and $0.027$ respectively. On the longer term,[3] CMB-HD could even bring our experimental accuracy down to $0.014$ [118].

Given the planned improvement in experimental accuracy, it is only logical for the theory to follow. Over the last three decades, intensive efforts have been deployed on the theoretical side to accurately predict the expected value for $N_{\text{eff}}$ within the SM. Indeed, even within the SM, deviations from $N_{\text{eff}} = 3$

[3] $\mathcal{O}(10-15)$ years depending on funding availabilities.

are expected for numerous reasons. First, the electron mass being of the same order of magnitude as the neutrino decoupling temperature, overlaps with the electron-positron annihilation, the neutrino sector is also heated to an extent by the $e^+e^-$ annihilation, leading to a percent-level correction to $N_{\rm eff}$ [532–542]. These works typically also include subleading [543] corrections from non-instantaneous nature of the neutrino decoupling as well as from small spectral distortions in the neutrino distribution function. Second, the Quantum Electrodynamics (QED) plasma itself is not a perfect gas and electron, positrons and photons are constantly interacting with each other, modifying the QED equation of state (EoS) and leading to an additional sub-percent correction to $N_{\rm eff}^{\rm SM}$ [544–549]. Finally, more recently, the impact of neutrino flavour oscillations has also been investigated [550–552]. A more detailed list of all possible SM corrections and their respective impact on $N_{\rm eff}^{\rm SM}$ is provided in Tab. 6.1. Accounting for all of the above, the current state-of-the-art result[4] is [543, 555, 556]

$$N_{\rm eff}^{\rm SM} = 3.0440 \pm 0.0002 \,, \tag{6.3}$$

the dependence on the values of the different SM parameters being weak [543, 557].

Even though Eq. (6.3) is the result of an already impressive theoretical endeavour, some effects nonetheless remain to be properly estimated. In particular, we focused in this work on estimating the yet unexplored impact on the benchmark (6.3) of

1. NLO finite-temperature corrections to the neutrino-electron interaction rates,

2. the formation of bound states, positronium in particular.

Note that the theoretical uncertainty in (6.3) do not account for these effects. While we nonetheless expect the correction from these effects to be smaller than the anticipated sensitivity of e.g. CMB-S4, providing an accurate theoretical prediction for $N_{\rm eff}^{\rm SM}$ at the per mille level remains highly desirable, as it allows theoretical uncertainties to be safely neglected in cosmological parameter inferences. In this chapter, we begin in Sec. 6.1 by describing how we

[4]This result assumes the neutrino field to be isotropic and the absence of lepton asymmetry. See [553] for the potential impact of inhomogeneities in the neutrino field and [540, 554] for the impact of lepton asymmetry.

| Standard-model corrections to $N_{\rm eff}^{\rm SM}$ | Leading contribution |
|---|---|
| $m_e/T_d$ correction | $+0.04$ |
| $\mathcal{O}(e^2)$ Finite-temperature correction to the QED EoS | $+0.01$ |
| Non-instantaneous decoupling+spectral distortion | $-0.006$ |
| $\mathcal{O}(e^3)$ Finite-temperature correction to the QED EoS | $-0.001$ |
| Flavour oscillations | $+0.0005$ |
| Type (a) finite-temperature corrections (thermal mass) to the weak rates | $\lesssim 10^{-4}$ |
| Type (d) finite-temperature corrections (fermion loop) to the weak rates | $\lesssim 10^{-5}$ |
| $\mathcal{O}(e^4)$ Finite-temperature correction to the QED EoS | $3 \times 10^{-6}$ |
| Electron/positron chemical decoupling | $\sim -10^{-7}$ |
| Sources of uncertainty | |
| Numerical solution by `FortEPiaNO` | $\pm 0.0001$ |
| Input solar neutrino mixing angle $\theta_{12}$ | $\pm 0.0001$ |

**Table 6.1:** Leading-digit correction to $N_{\rm eff}^{\rm SM}$ from various effects, listed in order of importance. Only the first five have been accounted for in (6.3), the rest falls below the numerical accuracy. The type (a) and (d) finite-temperature QED corrections to the weak rates refers to the diagrams in Fig. 6.3. Type-(a) was only approximately accounted for by including thermal corrections to the electron mass, thereby modifying the electron phase space. Electron/positron chemical decoupling denotes the impact of the residual entropy remaining in the electron sector from the incomplete $e^+e^-$ annihilation at $T \simeq 20$ keV [558], at which time electrons and positrons chemically decouple and do not affect the photon bath any more. Table taken from [4]; see also explanations therein. Note that it does not include the impact of positronium formation, which will be discussed in Sec. 6.3.

model the evolution of neutrinos and the QED bath across the neutrino decoupling era. Then, we examine in Sec. 6.2 the impact of NLO corrections to the neutrino-electron interaction rates on the value of $N_{\rm eff}^{\rm SM}$. Finally, in Sec. 6.3, we present an estimate of the impact of bound-state formation on $N_{\rm eff}^{\rm SM}$, considering various formation scenarios. Explicit expressions for different functions appearing in the QED EoS and in the calculation of the rates are provided in appendix D. The material presented in this part is based on Refs. [4, 7] and closely follow their structures.

Chapter 6

# The effective number of neutrinos $N_{\text{eff}}$

## 6.1 Modelling the decoupling of neutrinos

We start this section by describing how the decoupling of neutrinos in the early universe can be modelled. Essentially, one has to solve a set of coupled equations including

1. the so-called *continuity equation* to track the time evolution of the QED sector, as well as
2. a set of QKEs to capture the evolution of the neutrino sector.

### 6.1.1 Continuity equation

It is standard knowledge that the total pressure and energy density of an FLRW universe, which we write $\rho_{\text{tot}}$ and $P_{\text{tot}}$, verifies the following continuity equation

$$\frac{\mathrm{d}\rho_{\text{tot}}}{\mathrm{d}t} + 3H(\rho_{\text{tot}} + P_{\text{tot}}) = 0. \tag{6.4}$$

As in the previous chapters, $H$ denotes the standard Hubble rate. We note that, in thermal equilibrium, the continuity equation combined with the thermodynamic consistency relation (1.57c) automatically implies the conservation of entropy, i.e.

$$\frac{\mathrm{d}}{\mathrm{d}t} s a^3 = 0. \tag{6.5}$$

For practical purposes, we express the continuity equation in terms of the co-moving variables

$$x = m_e\, a, \quad y = p\, a \text{ and } z = T\, a\ , \tag{6.6}$$

with $a$ the scale factor, $p$ the physical neutrino momentum and $T$ the temperature of the photon bath. During radiation domination and before $e^+e^-$ annihilation, we have $T \propto 1/a$ and $z$ is thus constant and typically normalised to 1. Recalling that $\mathrm{d}/\mathrm{d}x = \partial/\partial x + (\mathrm{d}z/\mathrm{d}x)\partial/\partial z$, we can rewrite Eq. (6.4) in the following way

$$\frac{\mathrm{d}z}{\mathrm{d}x} = \frac{\left(\bar{\rho}_{\rm tot} - 3\bar{P}_{\rm tot}\right)/x - \partial\bar{\rho}_{\rm tot}/\partial x}{\partial\bar{\rho}_{\rm tot}/\partial z}. \tag{6.7}$$

In the equation above, we define the dimensionless variables $\bar{\rho}_{\rm tot} = a^4\rho_{\rm tot}$ and $\bar{P}_{\rm tot} = a^4 P_{\rm tot}$. At temperatures close to neutrino decoupling, i.e. $T \sim \mathcal{O}(1)$ MeV, the SM plasma is solely constituted of photons, electrons and neutrinos. The total pressure and energy densities can then be decomposed in the following way

$$\rho_{\rm tot} \equiv \rho_{\rm QED} + \rho_\nu \text{ and } P_{\rm tot} \equiv P_{\rm QED} + P_\nu\ , \tag{6.8}$$

where $\rho_{\rm QED},\ P_{\rm QED}$ are the energy and pressure densities of the QED sector and $\rho_\nu,\ P_\nu$ are their neutrino counterparts. Starting from their formal definition in equilibrium, Eq. (1.57), the former have been computed from an equilibrated QED sector up to[5] $\mathcal{O}(e^3)$ for $m_e \neq 0$ and arbitrary chemical potential $\mu_e$ [563, 564]. Using these results, one can show [548] that Eq. (6.7) takes in the SM the standard form

$$\frac{\mathrm{d}z}{\mathrm{d}x} = \frac{\tau J_+(\tau) - 1/(2z^3)\mathrm{d}\bar{\rho}_\nu/\mathrm{d}x + G_1(\tau)}{\tau^2 J_+(\tau) + Y_+(\tau) + 2\pi^2/15 + G_2(\tau)}\ , \tag{6.9}$$

where we defined $\tau \equiv x/z = m_e/T$. $J_+$ and $Y_+$ capture the contribution from $e^+e^-$ annihilation whereas the functions $G_{1,2}$ encode the non-ideal (finite-temperature) corrections to the QED EoS due to the interactions of electrons, positrons and photons. Explicit definitions for these functions can be found in appendix D.1. In Sec. 6.3.1, we will examine how Eq. (6.9) can be modified to account for the presence of bound states.

[5]These quantities are even known up to $\mathcal{O}(e^5)$ in the limit $m_e,\ \mu \to 0$ [559, 560], see also [561, 562].

### 6.1.2 Neutrino kinetic equations

The second ingredient needed to obtain $N_{\text{eff}}^{\text{SM}}$ is the time evolution of the neutrino energy density, which also directly enters the continuity equation as can be seen in Eq. (6.9). The evolution of SM neutrinos present many similarities with that of RH neutrinos in low-scale leptogenesis scenarios, discussed in the previous chapters. In particular, their evolution can effectively be described by a similar-looking set of QKEs [297] (expressed in the flavour basis)

$$\partial_t \varrho - pH\partial_p \varrho = -\mathrm{i}[H_\nu, \varrho] + \mathcal{I}_\nu[\varrho] \,, \tag{6.10}$$

where $\varrho \equiv \varrho(p, T)$ is the $3 \times 3$ matrix of neutrino momentum distributions and $H_\nu \equiv H_\nu(p, t) = H_{\nu,\text{vac}} + V_\nu$ is the effective Hamiltonian. Vacuum flavour oscillations are incorporated in $H_{\nu,\text{vac}}$, whereas $V_\nu$ captures in-medium corrections. $\mathcal{I}_\nu[\varrho]$ is the so-called collision integral and can be written as the difference between a gain $\big(\Gamma^<(p,t)\big)$ and loss term $\big(\Gamma^>(p,t)\big)$ in the following way

$$\mathcal{I}_\nu[\varrho] = \frac{1}{2}\Big((\mathbf{1} - \varrho)\Gamma^< - \varrho\Gamma^>\Big) + \text{h.c.} \tag{6.11}$$

The rates $\Gamma^{\gtrless}$ can be more explicitly written as a function of the neutrino Wightman self-energies $\Sigma_\alpha^{\gtrless}$

$$\Gamma^{\gtrless}(p) = \mp \frac{1}{2p^0} \,\text{Tr}\left[\not{p}\Sigma^{\gtrless}\right]\Big|_{p^0 = E_p} \,, \tag{6.12}$$

As highlighted in the introduction, we neglect any lepton asymmetry in this work. For this reason, it is sufficient to solve Eq. (6.10) for $\varrho = \varrho_\nu + \bar{\varrho}_\nu$, since antineutrinos evolve identically.

#### Damping approximation

The momentum and flavour dependence of the neutrinos QKEs, which one should retain for precision computations of $N_{\text{eff}}^{\text{SM}}$, makes it in general challenging to solve the system (6.10). In addition, the set of equations (6.10) is in general non-linear as $\Gamma_\alpha^{\gtrless}$ also depends on the neutrino matrix of densities $\varrho$. Though purpose-built public neutrino decoupling codes, such as `FortEPianNO` [511, 543], solving numerically Eqs. (6.9) and (6.10) without approximations do exist, it remains numerically expensive to do so. Such high precision is not necessary in order to obtain a first estimate of the *relative* impact of the various subleading corrections we examine in this work. As a first attempt, we will therefore work in a simplified framework, making the so-called *damping approximation*. This consists in assuming that all interaction partners of the neutrino entering the self-energy[6] (6.12) are in perfect thermal equilibrium with a common temperature $T$. In that case, one can use the KMS relation to simplify the collision integral to the more familiar form

$$\mathcal{I}_\nu[\varrho] = \frac{1}{2}\{\varrho - \varrho^{\rm eq}, \Gamma\} \tag{6.13}$$

with

$$\Gamma \equiv \Gamma^> + \Gamma^< = \frac{i}{2p^0}\,\mathrm{Tr}\left[\not{p}(\Sigma^< - \Sigma^>)\right]\Big|_{p^0=E_p} = \frac{i}{2p^0 f_{\rm F}(p^0)}\,\mathrm{Tr}\left[\not{p}\Sigma^<\right]\Big|_{p^0=E_p}. \tag{6.14}$$

Further neglecting the effect of the neutrino masses, which is justified since $T \gg m_\nu$, the damping rate $\Gamma$ is diagonal and we can re-express the collision term as

$$\{\mathcal{I}[\varrho(p)]\}_{\alpha\beta} \simeq -\{D(p,T)\}_{\alpha\beta}\Big[\{\varrho(p)\}_{\alpha\beta} - \delta_{\alpha\beta} f_{\rm F}(p)\Big], \tag{6.15}$$

where $\delta_{\alpha\beta}$ is a Kronecker-$\delta$, and the damping rate matrix $D(p,T)$ can be written in components

$$\{D(p,T)\}_{\alpha\beta} \equiv \frac{1}{2}\Big[\{\Gamma(p,T)\}_{\alpha\alpha} + \{\Gamma(p,T)\}_{\beta\beta}\Big]. \tag{6.16}$$

The damping approximation has the major practical advantage that it decouples the different components of $\varrho$. Since the total energy density entering the continuity equation (6.9) can be obtained by integrating the diagonal elements of the matrix of neutrino distributions, i.e.

$$\frac{\mathrm{d}\bar{\rho}_\nu}{\mathrm{d}x} = \frac{1}{\pi^2}\int \mathrm{d}y\, y^3 \sum_\alpha \frac{\mathrm{d}}{\mathrm{d}x}\varrho_{\alpha\alpha}\,, \tag{6.17}$$

it is therefore only necessary to track the diagonal elements.

If we further neglect the impact of neutrino oscillations, which is in general small (see Tab. 6.1), one can write Eq. (6.10) in terms of the comoving variables (6.6) and find the much simpler expression

$$\frac{\mathrm{d}}{\mathrm{d}x}\varrho_{\alpha\alpha} \simeq -\frac{\Gamma_\alpha}{xH}\Big[\varrho_{\alpha\alpha} - f_{\rm F}(yT/z)\Big]\,, \tag{6.18}$$

[6]This includes electrons and positrons, for which this approximation is expected to hold extremely well, but also other neutrinos for which the error is larger.

where, for the sake of brevity, we write $\Gamma_\alpha = \{D(p,T)\}_{\alpha\alpha}$. In order to accurately capture the momentum dependence of the neutrino distribution function, one can solve Eq. (6.18) for a range of momenta $y$ covering the bulk of the neutrino population (typically, a set of comoving momenta in the interval $[0.01, 30]$ is sufficient). We will call this strategy the "full-momentum" approach in the rest of this chapter.

Alternatively, a good approximation can be obtained by solving the momentum average of Eq. (6.18). For that purpose, one needs to make an ansatz for the form of the neutrino distribution functions. As neutrinos remain close to equilibrium at all times and their interaction rates are dominated by the kinematic region close to the averaged momentum $\langle p \rangle / T = 7\pi^4/180\zeta(3) \simeq 3.15$, it is reasonable to assume

$$\{\varrho(y)\}_{\alpha\alpha} = \{\varrho(\langle y \rangle)\}_{\alpha\alpha} \frac{f_{\rm F}(yT)}{f_{\rm F}(\langle y \rangle T)}, \qquad \Gamma(y) = \Gamma(\langle y \rangle) \,. \tag{6.19}$$

In this case, one can perform the momentum integral explicitly and we obtain

$$\frac{\mathrm{d}\bar{\rho}_\nu}{\mathrm{d}x} = -\frac{7\pi^2}{120 x H(x)} \left[ \sum_\alpha \Gamma_\alpha(\langle y \rangle) \left( \frac{\{\varrho(\langle y \rangle)\}_{\alpha\alpha}}{f_{\rm F}(\langle y \rangle T)} - z^3(x) \right) \right] . \tag{6.20}$$

We call this second procedure the "mean-momentum" approach.

### 6.1.3 Extracting the value of $N_{\rm eff}^{\rm SM}$

Simultaneously solving Eqs. (6.9) and (6.18) (or (6.20)), we can then extract the SM value for $N_{\rm eff}$ through the relation

$$N_{\rm eff}^{\rm SM} \equiv \frac{8}{7} \left(\frac{11}{4}\right)^{4/3} \frac{\rho_\nu}{\rho_\gamma}\bigg|_{x\to\infty} = \frac{120}{7\pi^2} \left(\frac{11}{4}\right)^{4/3} \left[\frac{z(T_{\rm ini})}{z(x)}\right]^4 \bar{\rho}_\nu(x)\bigg|_{x\to\infty} , \tag{6.21}$$

where $T_{\rm ini}$ is the photon temperature at initialisation (which is equal to the neutrino temperature at this stage). In the following, we will use $T_{\rm ini} = 10$ MeV but the final result is fairly insensitive to the choice of initial temperature (as long as $T_{\rm ini}$ is much larger the neutrino decoupling temperature).

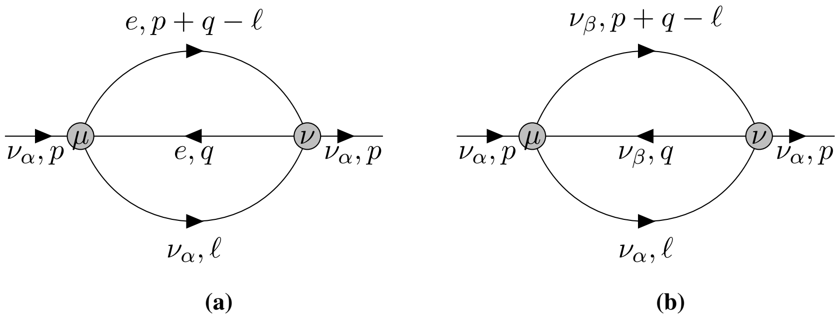


**Figure 6.2:** Tree-level neutrino self-energy. The left panel encodes the interaction with electrons whereas the right panel captures the neutrino self-interaction.

## 6.2 Impact of QED NLO corrections to the weak rates on $N_{\rm eff}^{\rm SM}$

### 6.2.1 Motivation

At temperatures close to neutrino decoupling, we have $T \ll m_W,\ m_Z$ and one can therefore integrate out $W$ and $Z$ bosons. Neutrinos then only interact through the 4-fermion interaction[7]

$$\mathcal{L}_{\rm 4F} \supset -\frac{4G_F}{\sqrt{2}}\left[\bar{\psi}_\alpha\gamma_\mu P_L\psi_\alpha\right]\left[g_L^\alpha J_L^\mu + g_R J_R^\mu + \frac{1}{4}\bar{\psi}_\beta\gamma_\mu P_L\psi_\beta\right]. \tag{6.22}$$

In the above equation, $\psi_\alpha$ ($\psi_\beta$) denotes the spinor associated with the neutrino of flavour $\alpha$ $(\beta)$ $\in \{e, \mu, \tau\}$ whereas $J^\mu_{L/R} = \bar{\psi}_e\gamma^\mu P_{L/R}\psi_e$ represent the left- and right-handed electron currents. $g_{L/R}$ are the right- and left-handed couplings, which take the respective values $g_R = \sin^2\theta_W$ and $g_L^\alpha = -\frac{1}{2} + \sin^2\theta_W + \delta^{\alpha e}$ in the SM.

At tree level, neutrino interactions are well understood and captured by the two self-energies displayed in Fig. 6.2. Their leading-order interaction rates can be obtained using the results of Chap. 4, see also appendix C, and have been included in the state-of-the-art result (6.3). The impact of (finite-temperature[8]) NLO corrections to these rates remains however to be accurately quantified. At NLO, the four diagrams, (a) to (d), displayed in Fig. 6.3 will contribute. We note in passing that NLO corrections from the Fermi inter-

[7]As discussed in Chap. 4, see footnote 7, we use the Fierz identities to unify the charged and neutral current contributions.

[8]NLO corrections to the neutrino-electron interaction rates in vacuum due to diagrams (a)–(d) in Fig. 6.3, including the non-perturbative contributions from quark, were already calculated previously in Ref. [565].

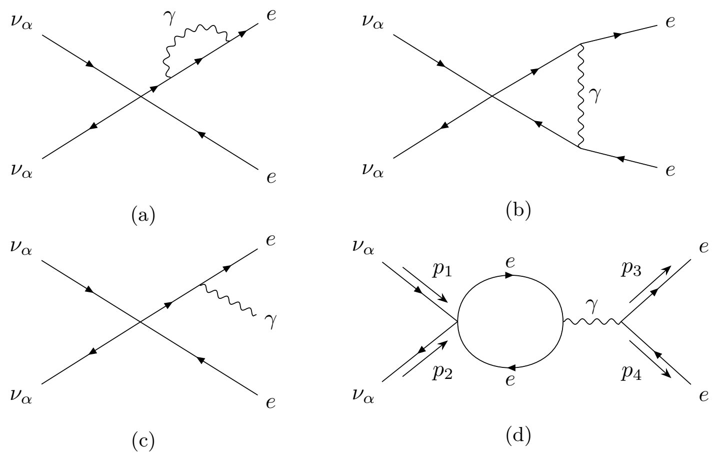


**Figure 6.3:** Diagrammatic representation of all four qualitatively different amplitudes contributing at NLO (in $\alpha_{\rm em}$) to the neutrino interaction rate. These corresponds to (a) modification of the electron dispersion relation, (b) virtual photon exchange, (c) real photon emission and absorption, and (d) corrections with a closed fermion loop. Note that, while we will focus on the case with an electron running in the loop, diagrams of type-(d) exist with any fermion running in the loop. In the above diagrams, one should sum over all time directions to account for all possible scattering channels. Figure taken from [4].

action itself can safely be neglected here, as they are expected to be further suppressed by powers of $T/m_W \ll 1$. This also implies that only neutrino-electron interaction rates are impacted and one can safely use the tree-level result for neutrino self-interactions. Though these NLO QED contributions are expected to be suppressed by the electromagnetic fine-structure constant $\alpha_{\rm em} \equiv e^2/4\pi$, there has been some debate [4, 543, 549, 566–568] about the precise impact of these NLO corrections on $N_{\rm eff}^{\rm SM}$ and, in particular, whether they can modify the last significant digit of the benchmark (6.3). The key differences between these different analyses can be summarised as follows:

- In [543, 549], only type-(a) corrections to the neutrino-electron interaction rates were investigated. In practice, this amounts to modifying the electron mass shell to include its thermal mass $\delta m_e(p, T)$, i.e. making the replacement $m_e^2 \to m_e^2 + \delta m_e^2$ in every electron propagator[9]. For the sake of simplicity, they further neglected the subleading (see e.g. Fig. 15 in [547]) correction from the momentum dependence of this thermal mass. Overall, [549] concluded in an an absolute impact on $N_{\rm eff}^{\rm SM}$

[9] Such a procedure can also be used to obtain the $\mathcal{O}(e^2)$ correction to the QED EoS, though one has to be careful to include the proper symmetry factors [545].

of approximately $-8 \times 10^{-5}$, below the current theoretical uncertainty of $\mathcal{O}(10^{-4})$.

- In [566], the impact on $N_{\rm eff}^{\rm SM}$ of type-(a) to (c) diagrams was examined, claiming a substantial effect of $\approx -7 \times 10^{-4}$. The NLO rates in this study were calculated based on early works [569, 570] in the context of stellar energy losses, essentially extending their approach from $T \sim 1$ MeV to $T \sim 20$ MeV. However, by doing so, they neglect Pauli blocking effects of final-state neutrinos, which are irrelevant in stellar environments due to the long mean free path of neutrinos. This is not necessarily justified in the context of the primordial universe. Moreover, they also neglected corrections from $\nu_\alpha e \to \nu_\alpha e$ scatterings as well as type-(d) corrections, see Fig. 6.3. In particular, the latter presents a $t$-channel enhancement and should naively dominate the NLO contribution.

- More recently, G. Jackson and M. Laine performed in [567, 568] the most complete calculation up to date. They considered all diagrams in Fig. 6.3, even including an estimate for the hadronic corrections to diagram (d) following [571]. While they worked in the imaginary time formalism, which in principle does not allow to consider out-of-equilibrium situations, they provided in their second work [568] the double-differential[10] neutrino rates that can be incorporated in non-averaged kinetic equations and comprehensively account for distortions in the neutrino distribution functions. In doing so, they found that NLO corrections to the rates are of order $0.2 - 0.3\%$. They therefore concluded that NLO effects are unlikely to impact $N_{\rm eff}^{\rm SM}$ at the per mille level, even though they did not explicitly estimate the impact of these corrections on $N_{\rm eff}^{\rm SM}$. However, we note that the authors assumed a negligible electron mass by setting $m_e = 0$, which is not always a good approximation.

In this section, we therefore intend to clarify whether or not QED corrections to the neutrino-electron interaction rate can alter the value of $N_{\rm eff}^{\rm SM}$ within the SM at the per mille level as claimed in [566]. To that end, we restrict ourselves to computing the type-(d) NLO correction, since it is expected to dominate the NLO QED corrections,[11] but make no further approximation. This in particular means retaining the finite electron mass, contrary to [567, 568],

[10] We here means the neutrino interaction rates that have been differentiated twice with respect to the energies of the two scattering neutrinos.

[11] This has been confirmed explicitly in the limit $m_e = 0$ in [567, 568].

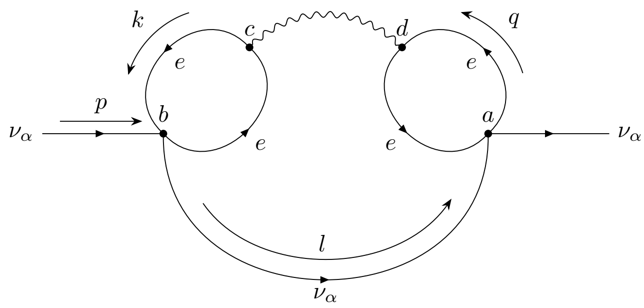


**Figure 6.4:** Self-energy corresponding to the type-(d) contribution in Fig. 6.3. We explicitly label both the external (i.e. $a$ and $b$) and the summed (i.e. $c$ and $d$) CTP indices. We also indicate the particle species ($e$ and $\nu_\alpha$) as well as the chosen convention for momenta ($k, l, p$ and $q$). Figure taken from [4].

and the effect of Pauli blocking as well as every possible scattering channels, contrary to [566]. As a side note, we perform our computation from first principles using the real-time formalism, which in thermal equilibrium is equivalent to the imaginary time formalism used in [567, 568] but can be more easily extended to nonequilibrium settings.

### 6.2.2 Estimating the type-(d) NLO correction to the weak rates

The neutrino self-energy, displayed for a generic choice of CTP indices in Fig. 6.4, constitutes the crucial ingredient needed to obtain the neutrino-electron interaction rates. It reads

$$
\begin{aligned}
\mathrm{Tr}\left[\not{p}\Sigma^{ba,cd}\right] &= -\mathrm{sgn}(abcd)(ie)^2\left(\frac{i4G_F}{\sqrt{2}}\right)^2 \times \qquad (6.23)\\
&\times \int_{l,q,k} \mathrm{Tr}\left[iS_e^{ad}(q)\gamma_\rho(P_L g_L^\alpha + P_R g_R) iS_e^{da}(q+p-l)\gamma^\mu\right] iD_{\mu\nu}^{cd}(p-l)\\
&\times \mathrm{Tr}\left[\not{p}\gamma^\rho P_L iS_{\nu_\alpha}^{ba}(l)\gamma^\sigma P_L\right]\mathrm{Tr}\left[iS_e^{cb}(k)\gamma^\nu iS_e^{bc}(k+p-l)\gamma_\sigma(P_L g_L^\alpha + P_R g_R)\right].
\end{aligned}
$$

To keep the preceding expression compact, we abbreviated $\int_p \equiv \int \mathrm{d}^4p/(2\pi)^4$. Note also that the propagators' subscripts ("$e$" or "$\nu_\alpha$") indicate the specific particle they are associated with. From Eq. (6.14), we know that it is only necessary to compute the rates for $b = +$ and $a = -$. Out of the four possibles combinations of indices $c$ and $d$, one can show that only $\Sigma^{+-,++}$ and $\Sigma^{+-,--}$ are non-vanishing. The remaining two cuts put the intermediate photon in Fig. 6.4 on-shell, leading to processes that are kinematically forbidden at tree level. From the structure of the thermal propagators (1.51), it follows that $\mathrm{Tr}\left[\not{p}\Sigma^{+-,++}\right] = \mathrm{Tr}\left[\not{p}\Sigma^{+-,--}\right]^*$ and, hence, the type-(d) contribution is solely determined by $\Sigma^{+-,++}$

$$\mathrm{Tr}\left[\not{p}\Sigma^{+-}_{\rm NLO}\right] = 2\mathrm{Re}\,\mathrm{Tr}\left[\not{p}\Sigma^{+-,++}\right]. \tag{6.24}$$

Using Eq. (6.23), the self-energy (6.24) can be brought into the explicit form

$$\mathrm{Tr}\left[\not{p}\Sigma^{+-}_{\rm NLO}\right] = (2\pi)^3 \int_{q,l} \delta(p_2^2)\delta(p_3^2 - m_e^2)\delta(p_4^2 - m_e^2)\mathcal{F}(p_2^0, p_3^0, p_4^0)\mathcal{T}_{\rm NLO}. \tag{6.25}$$

For the sake of brevity, we identified different combinations of the 4-momenta $p, l, q$ in Fig. 6.4 with the momenta $p_1, p_2, p_3, p_4$ of the external neutrinos and electrons of the underlying $2 \to 2$ process represented by diagram (d) of Fig. 6.3. Specifically, we have

$$p_1 = p, \qquad p_2 = -l, \qquad p_3 = q + p - l, \qquad p_4 = -q. \tag{6.26}$$

In Eq. (6.25), we also defined the population factor

$$\mathcal{F}(p_2^0, p_3^0, p_4^0) = \left[\mathrm{sgn}(p_2^0)(1 - f_{\rm F}(p_2^0))\right]\left[\mathrm{sgn}(p_3^0) f_{\rm F}(p_3^0)\right]\left[\mathrm{sgn}(p_4^0) f_{\rm F}(p_4^0)\right] \tag{6.27}$$

as well as the quantity $\mathcal{T}_{\rm NLO}$

$$\begin{aligned}\mathcal{T}_{\rm NLO} = -16 G_F^2 g_V^\alpha \mathrm{Re}\Big\{&\mathrm{Tr}\left[(\not{p}_3 + m_e)\gamma^\mu\,(m_e - \not{p}_4)\gamma^\rho\,(g_L^\alpha P_L + g_R P_R)\right] \\ &\times \mathrm{Tr}\left[\not{p}_1\gamma_\rho P_L \not{p}_2 \gamma_\sigma P_L\right] D^{11}_{\mu\nu}(P)\Pi^{\nu\sigma}_{11}(P)\Big\}. \end{aligned} \tag{6.28}$$

The latter can be seen as the equivalent S-matrix element entering the collision integral in standard Boltzmann equations, see e.g. [45]. It captures the entire difference between the NLO and LO rates; that is, the LO rates can be recovered by replacing

$$\mathcal{T}_{\rm NLO} \to \mathcal{T}_{\rm LO} = 2^7 G_F^2\left[(g_L^\alpha)^2\,(p_1\cdot p_4)^2 + g_R^2\,(p_2\cdot p_4)^2 + g_L^\alpha g_R m_e^2\,(p_1\cdot p_2)\right]. \tag{6.29}$$

In Eq. (6.28), we introduced the notation $P = p_1 + p_2$ for the photon momentum and $g^\alpha_{V,A} = \frac{1}{2}(g_L^\alpha \pm g_R)$ for the vector and axial couplings, which arise because of the vector-like nature of QED. Moreover, $\Pi^{\mu\nu}_{ab}$ denotes the one-loop photon self-energy, which is computed in details in appendix D.3.1.

By decomposing each propagator, one can in general split $\mathcal{T}_{\rm NLO}$ into 'vacuum' and 'thermal' contributions:

$$\mathcal{T}_{\rm NLO} = \mathcal{T}_{\rm vac} + \mathcal{T}_{\rm th} \,, \tag{6.30}$$

such that $\mathcal{T}_{\rm vac}$ does not depend directly on the temperature[12] while $\mathcal{T}_{\rm th} \to 0$ as $T \to 0$. The former can be expressed in terms of the 1-loop vacuum photon self-energy $\Pi_2$ as

$$\mathcal{T}_{\rm vac} = -2^{10} G_F^2\, \alpha_{\rm em}\, [(g_V^\alpha)^2/(4\pi)] \left[m_e^2 (p_1 \cdot p_2) + 2(p_1 \cdot p_4)^2\right] \mathrm{Re}\,\Pi_2(P^2). \tag{6.31}$$

Note that, in order to make the expression (6.31) more compact, we made use of the symmetry of the integrand under the exchange $p_3 \leftrightarrow p_4$. Combined with the conservation of 4-momenta, this symmetry also ensures the absence of any antisymmetric term containing Levi-Civita symbols arising from traces of $\gamma^5$ with four or more $\gamma$-matrices. The decomposition (6.30) has the advantage that the photon self-energy $\Pi_2$ was already computed in vacuum in Ref. [565], whose result we used in this work.

The thermal matrix element $\mathcal{T}_{\rm th}$ possesses a more complicated structure. Its temperature dependence arises directly from the finite-temperature part of $S_e^{++}$, which effectively puts one of the electron on-shell and is therefore proportional to its distribution function. Interestingly, putting both 'internal'[13] electrons on-shell yields a purely imaginary contribution, which cancels when summing over the possible CTP indices $c = d = +$ and $c = d = -$. Therefore, only the two combinations that puts either internal electron on-shell survive. They are proportional to $f_{\rm F}(|k^0|)$ and $f_{\rm F}(|k^0 + P^0|)$, respectively, see Fig. 6.4 for the momentum convention.

A distinctive feature of this thermal contribution to the NLO QED correction is the emergence of a $t$-channel (logarithmic) divergence in the limit of soft momentum exchange. This singularity can be easily understood by looking at the scaling of the 1-loop photon self-energy. In the Hard Thermal Loop (HTL) limit, i.e. assuming the photon to be soft[14] $|P_0| < |\mathbf{P}| \ll \pi T$ and neglecting the electron mass, the finite-temperature photon self-energy scales as

[12] The interaction rates will however depend on the temperature because of the temperature dependence of the population factor (6.27).

[13] By internal, we mean electrons that have not been cut through, i.e. for which the propagator is $S_e^{++}$.

[14] For t-channel processes, one always has $P^2 \leq 0$. Moreover, $P^2 = 0$ can only be reached for $P_0, |\mathbf{P}|$ both vanishing.

$T^2$ instead of $P^2$ like it does in vacuum. Therefore, it cannot compensate any more for the $1/P^2$ behaviour of the photon propagator. In addition, the divergence is worsened by the Bose-enhancement of soft photons. It can however be regulated by replacing the tree-level photon propagator $D^{cd}_{\mu\nu}$ in Eq. (6.28) with its 1PI-resummed equivalent $\bar{D}^{ab}_{\mu\nu}$. At finite temperature, the longitudinal ("$L$") and transverse ("$T$") photon degrees of freedom behave differently. Consequently, it is necessary to decompose the thermal matrix element $\mathcal{T}_{\text{th}}$ accordingly, i.e. $\mathcal{T}_{\text{th}} = \mathcal{T}^L_{\text{th}} + \mathcal{T}^T_{\text{th}}$ with

$$\begin{aligned}\mathcal{T}^{L/T}_{\text{th}} = -2^8 G_F^2 (g_V^\alpha)^2 \text{Re}\, \bar{D}^{L/T}_R(P) \text{Re}\, \Pi^{L/T}_{R,T\neq 0}(P) \Big[ 2(p_1 \cdot p_4) P^{1,4}_{L/T} \\ + (p_1 \cdot p_2)(a_{L/T}(p_1 \cdot p_2) + P^{2,2}_{L/T} + P^{4,4}_{L/T}) \Big] . \quad (6.32)\end{aligned}$$

In the previous equation, $\bar{D}^{L/T}_R$ denotes the longitudinal/transverse component of the retarded resummed photon propagator whereas $\Pi^{L/T}_{R,T\neq 0}$ is the longitudinal/transverse component of the retarded thermal photon self-energy, which contains the $f_{\text{F}}(|k^0|)$ and $f_{\text{F}}(|k^0 + P^0|)$ terms described earlier. To keep the formula compact, we introduced the shorthand notation $P^{i,j}_{L/T} = P^{\mu\nu}_{L/T} p_{i,\mu} p_{j,\nu}$. Additionally, the coefficient $a_{L/T} = (3 \mp 1)/4$ further distinguishes between the longitudinal and transverse contributions. Complete expressions for $\text{Re}\,\Pi^{L/T}_{++,T\neq 0}$ and $\text{Re}\,\bar{D}^{L/T}_{++}$ are provided in Eqs. (D.27), (D.29) and (D.55). One can in turn easily map these to $\text{Re}\,\Pi^{L/T}_{R,T\neq 0}$ and $\text{Re}\,\bar{D}_R$, which enters Eq. (6.32) more directly, through the trivial relations

$$\text{Re}\,\bar{D}^{L/T}_R = \text{Re}\,\bar{D}^{L/T}_{++} , \qquad \text{Re}\,\Pi^{L/T}_R = \text{Re}\,\Pi^{L/T}_{++} . \quad (6.33)$$

More details on the derivation of these results along with explicit expressions for the relevant integrals can be found in appendices D.2 and D.3.

Before moving on to the numerical evaluation of the rates, we would like to comment on a few technical aspects. First, we note that it is in principle necessary for consistency reasons to replace the tree-level photon propagator by its resummed equivalent also in the vacuum contribution (6.31). However, this is not needed in practice because the vacuum photon self-energy does not exhibit any IR divergence and is therefore not dominated by small photon momenta. We numerically checked that the choice of propagator does not impact the final result in any visible way. For the same reasons, we can safely set $\bar{D}_R \to D_R$, where $D_R$ is the tree-level counterpart of $\bar{D}_R$, in the $s$-channel. Second, the resummation of the photon propagator introduces an imaginary part in $\bar{D}^{L/T}_{++}$. Therefore, the argument given below Eq. (6.23) for neglecting contributions such as $\Sigma^{+-,+-}$ no longer holds, as the so-called plasmon process $\gamma \to \nu\bar{\nu}$ become kinematically possible. However, such processes are formally of higher-order in $\alpha_{\rm em}$, contributing at $\mathcal{O}(\alpha_{\rm em}^2)$ (see appendix C in [572]), while we are only interested in this work in the leading $\mathcal{O}(\alpha_{\rm em})$ correction.

### Numerical results

We now numerically evaluate the NLO QED correction to the neutrino damping rate (6.14) by integrating over the two remaining momenta $l$ and $q$ in Eq.(6.25), making use of the phase-space parametrisation detailed in appendix B. The SM constants listed below are fixed to their best-fit experimental values as reported by the Particle Data Group [573].

- Fermi constant: $G_F = 1.166\,378\,8(6)\,\text{MeV}^{-2}$,
- Electron mass: $m_e = 0.510\,998\,950\,00(15)\,\text{MeV}$,
- Electromagnetic fine-structure constant: $\alpha_{\rm em}^{-1}(0) = 137.035\,999\,180(10)$, and
- Weinberg angle: $\sin^2\theta_W(0)_{\overline{\rm MS}} = 0.238\,63(5)$.

The vacuum correction (6.31) is also sensitive (through the photon self-energy) to the choice of renormalisation scale $\mu_R$, which we identify with the electron mass, i.e. $\mu_R = m_e$. Note also that we neglect the running of the different SM constants, which is small in the temperature range of interest; see e.g. [574,575].

Our results for the NLO QED corrections to the neutrino damping rates relative to the LO result are shown in Fig. 6.5 for $0.1$ MeV $< T < 3$ MeV, which covers the relevant dynamics for $N_{\rm eff}^{\rm SM}$. We display these rates evaluated at the mean momentum $p = 3.15T$ both for the $\nu_e - e$ interaction rate (top panel) and $\nu_{\mu,\tau} - e$ interaction rate (bottom panel). We find this relative correction to fall in the range $-0.2 \to +0.1\%$ and $-0.0005 \to +0.0002\%$, for $\nu_e$ and $\nu_{\mu,\tau}$ respectively, for temperatures between $1$ and $3$ MeV. We also make the following observations:

1. Close to neutrino decoupling, for $T \sim 2\,\text{MeV}$, [566] concluded that finite-temperature corrections were subdominant to the vacuum correction (and bremsstrahlung process). In contrast, we instead observe that

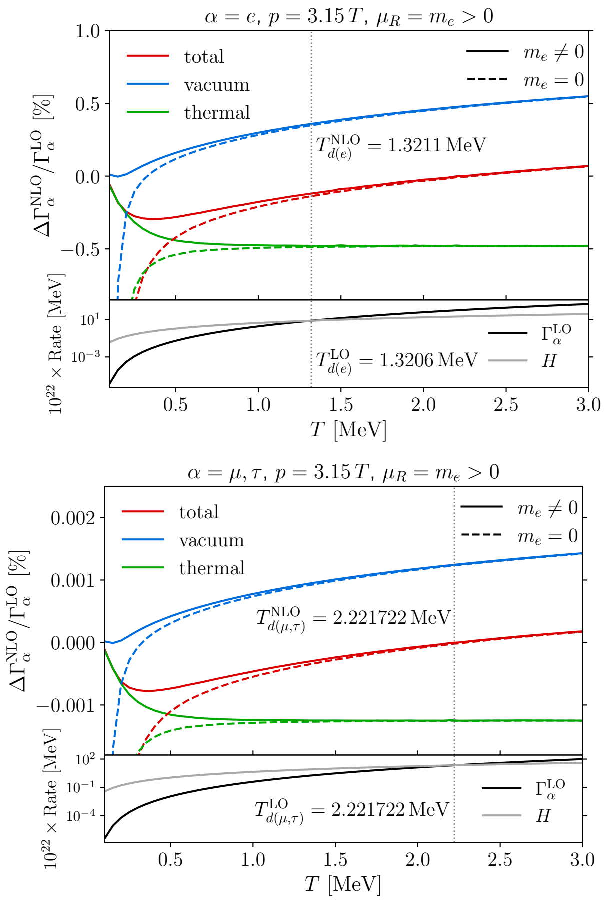


**Figure 6.5:** *Top*: Temperature dependence of the type-(d) NLO contributions to the $\nu_e$ interaction rate for the mean neutrino momentum $p = 3.15T$, normalised to the LO result. We do this comparison for both a finite (solid lines) and a vanishing (dashed lines) electron mass, the LO result being always evaluated with $m_e \neq 0$ to ensure a common normalisation. We further split the total rate correction (red) into the vacuum (blue) and the thermal contribution (green), see main text for details. In the lower panel, we compare the LO $\nu - e$ interaction rate to the Hubble rate defined via $\Gamma_\alpha(T_{d(e)}) = H(T_{d(e)})$, $T_d$ indicating the decoupling temperature. *Bottom*: Same as top, but for $\nu_{\mu,\tau}$. Figure taken from [4].

thermal (see (6.32)) and vacuum (see (6.31)) contributions to the correction are roughly equal in magnitude and opposite in signs (green vs blue lines in figure 6.5).

2. Similarly, Ref. [566] also reported the absence of flavour dependence of the damping rates, i.e. $|\Gamma_e/\Gamma_{\mu,\tau} - 1| \lesssim 1\%$ at neutrino decoupling. On the other hand, we observe a strong flavour dependence of our rates,

exceeding two orders of magnitude as can be seen by comparing the top and bottom panel of Fig. 6.5. This flavour dependence was also noted in [567] and can be traced back to the hierarchy between the vector couplings $g_V^e \sim 0.49$ and $g_V^{\mu,\tau} \sim -0.012$, very roughly two orders of magnitude apart from one another. Ultimately, this hierarchy arises from the fact that electron neutrinos experience both neutral and charged current interactions with the $e^{\pm}$ thermal bath whereas the muon- and tau-flavoured neutrinos interact only via the neutral current.

3. In order to assess the validity of the $m_e = 0$ approximation performed in [567], we have computed the rates both retaining the full dependence on the electron mass (solid lines in Fig. 6.5) and in the massless limit $m_e \to 0$ (dashed lines in Fig. 6.5), using the HTL approximation for the photon self-energy and propagator.

   As expected, the error from neglecting $m_e$ can be safely ignored at temperatures close to neutrino decoupling $T \gtrsim 3m_e$, but becomes sizeable at low temperatures. In particular, the ratio $\Gamma_\alpha^{\rm NLO}/\Gamma_\alpha^{\rm LO}$ vanishes in the limit $T \to 0$ for $m_e > 0$ whereas it diverges if $m_e = 0$ because of the additional Boltzmann suppression of the LO rates. Although the impact of NLO corrections on the neutrino decoupling temperature is relatively minor, the evolution of neutrinos in general needs to be tracked down to much lower temperatures to accurately estimate $N_{\rm eff}^{\rm SM}$ [543, 556]. The impact of retaining the electron mass may therefore be non-negligible, see Sec. 6.2.3 for more details.

4. In the relativistic regime $T \gg m_e$, the thermal component of the NLO correction exhibits the same temperature dependence as the LO rate, since $T$ is the only relevant scale. In contrast, the vacuum correction retains a (mild) residual temperature dependence arising from the choice of renormalisation scale $\mu_R = m_e$.

Regarding the first two points, we note however that [566] only considered type-(a) to (c) NLO corrections while we restricted ourselves to the corrections of type-(d) such that a direct comparison is not possible.

We also examine in more detail the impact of different possible resummation schemes — see appendix D.3 — in Fig. 6.6, focusing on the (enhanced) $t$-channel, which is more sensitive on the choice of scheme. In this figure, we compare four different approximations i The complete one-loop result, i.e. using the 1PI-resummed photon propagator, including a finite $m_e$ everywhere,

ii The complete one-loop result in the limit $m_e \to 0$,

iii Using instead the HTL-resummed photon propagator (which does not depend on the electron mass) while retaining the finite electron mass everywhere else,[15]

iv Using the HTL-resummed photon propagator and setting $m_e = 0$ everywhere.

As expected, in the limit $m_e \to 0$, using the HTL-resummed propagator reproduces in very good accuracy the complete one-loop result. In contrast, this approximation is expected to deteriorate in the non-relativistic regime. This is illustrated by the lower panel of Fig. 6.6, which displays the ratio of (i) to (iv), revealing $\mathcal{O}(1)$ errors for $T \lesssim m_e$.

### 6.2.3 Impact on $N_{\text{eff}}^{\text{SM}}$

Now that we have computed the type-(d) correction to the $\nu - e$ interaction rate, we are in a position to estimate its effect on $N_{\text{eff}}^{\text{SM}}$. Since a complete numerical evaluation of $N_{\text{eff}}^{\text{SM}}$ is computationally expensive, we will limit ourselves in this work to two different approximations in order to assess whether these corrections are likely to induce a significant change in $N_{\text{eff}}^{\text{SM}}$.

1. As already highlighted in Tab. 6.1, the leading correction to $N_{\text{eff}}^{\text{SM}}$ arises from the fact that electrons and positrons are only mildly relativistic at neutrino decoupling, i.e. $m_e/T_d \neq 0$. It seems therefore reasonable to expect that NLO corrections will also be dominated by the change in $T_d$. Hence, we will first assume that neutrinos decouple instantaneously. In this case, $\delta N_{\text{eff}} \equiv N_{\text{eff}}^{\text{NLO}} - N_{\text{eff}}^{\text{LO}}$ can be estimated from entropy conservation argument.

2. As a slightly more precise estimate, we may also compute in a second time $\delta N_{\text{eff}}$ by solving directly the continuity equation (6.9) along with the QKEs (6.10), with and without averaging over the momenta. For simplicity, we will also make use of the damping approximation (6.15) and neglect neutrino oscillations.

[15] Although physically inconsistent, keeping $m_e$ in the electron propagator but not in the photon propagator remains helpful for extracting the dependence of the neutrino damping rate on the resummation scheme.

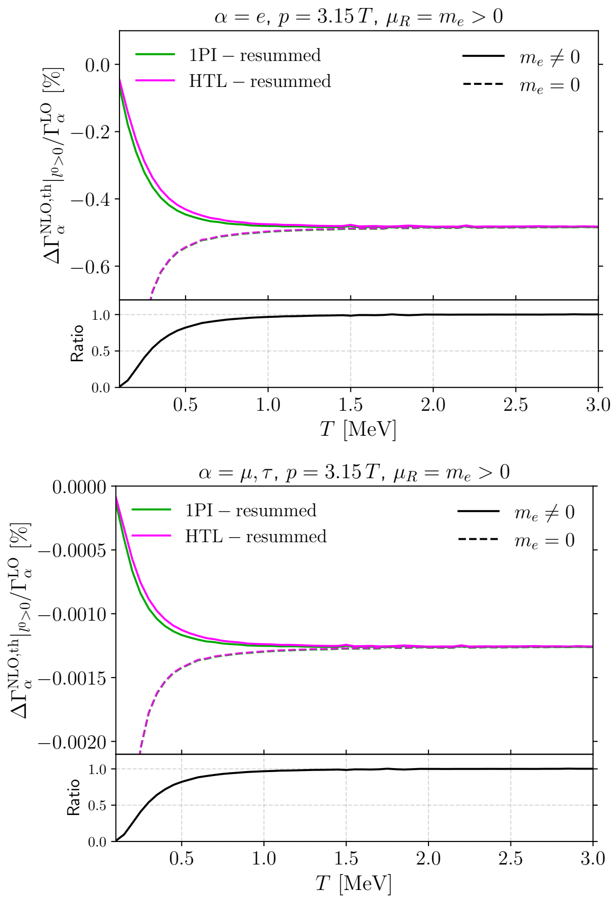


**Figure 6.6:** *Top:* The $t$-channel contribution ($l^0 > 0$) to the NLO $\nu_e - e$ interaction rate normalised to the LO result, both evaluated at the average momentum $p = 3.15T$. We compare different approximations for the photon propagator, i.e. the 1PI-resummed form (in green) and the HTL-resummed form (in magenta). Each is shown for both $m_e \neq 0$ (solid lines) and $m_e = 0$ (dashed lines), the LO result being always computed for $m_e \neq 0$ to ensure a common normalisation. The lower panel displays the temperature dependence of the ratio of the 1PI result with $m_e \neq 0$ to the HTL result with $m_e = 0$. *Bottom*: Same as top, but for $\alpha \in \{\mu, \tau\}$. Figure taken from [4].

## Entropy argument

For systems close to equilibrium and evolving adiabatically as is the case here, the total entropy density is expected to remain conserved. Similarly, long after the decoupling of neutrinos, one would expect the entropy density to be separately conserved in the QED and neutrino sectors. Writing $a_{d+}$ the scale factor immediately before neutrino decoupling, we can write these conservation rules as

$$
\begin{aligned}
s_{\text{eq}}(a_{d+})a_{d+}^3 &= s_{\text{eq}}(a_f)a_f^3, \\
s_{\nu_\alpha}(a_{d+})a_{d+}^3 &= s_{\nu_\alpha}(a_f)a_f^3,
\end{aligned}
\tag{6.34}
$$

where $a_f$ is the scale factor chosen at a later time, which is chosen to be long after electron/positron annihilation. $s_{\nu_\alpha}$ is the entropy density stored in neutrinos of flavour $\alpha$, while $s_{\text{eq}} \equiv s_\gamma + s_e + \sum_{\beta\neq\alpha} s_{\nu_\beta} + \cdots$ denotes the entropy stored in the QED plasma plus any neutrino species $\nu_\beta$ that may still be in equilibrium with it. At $a = a_{d+}$, we note that the temperature in the neutrino and QED sector are the same, i.e. $T_\nu(a = a_{d+}) = T_d$.

If the decoupling is instantaneous, the neutrinos will maintain in excellent approximation an equilibrium distribution. Therefore, their entropy density will continue to scale as $s_{\nu_\alpha}(a) \propto T_{\nu_\alpha}^3(a)$ and their temperature as the inverse scale factor, i.e. $T_{\nu_\alpha}(a_f) = (a_{d+}/a_f)T_{\nu_\alpha}(a_{d+}) = (a_{d+}/a_f)T_d$. Similarly, the entropy density of the part of the plasma that remains in equilibrium can be parametrised in the following way

$$
s_{\text{eq}}(a) = \frac{2\pi^2}{45}\tilde{g}_s(a)T^3(a) \ , \tag{6.35}
$$

where the effective number of entropic degrees of freedom $\tilde{g}_s$ reads

$$
\tilde{g}_s(a) \equiv g_\gamma + \frac{45}{4\pi^4}\frac{g_e}{T^4(a)}\int_0^\infty \mathrm{d}p\, p^2 \left(E_e + \frac{p^2}{3E_e}\right) f_{\text{F}}(E_e, T(a)) + \frac{7}{8}\sum_{\beta\neq\alpha} g_{\nu_\beta} \tag{6.36}
$$

in the ideal gas limit. In the above equation, we have $g_\gamma = 2$, $g_e = 4$, and $g_{\nu_\beta} = 2$. Though in general deviations from the ideal gas limit are not negligible at $T = T_d$ (see [549] for details), we are here only interested in the relative change in $N_{\text{eff}}^{\text{SM}}$ due to NLO QED corrections such that this approximation should not significantly impact our conclusions.

Inserting Eqs. (6.35) and (6.36) into the conservation relation (6.34), we can derive the late-time photon-to-neutrino temperature ratio

$$
\frac{T(a_f)}{T_{\nu_\alpha}(a_f)} = \left[\frac{\tilde{g}_s(a_{d+})}{\tilde{g}_s(a_f)}\right]^{1/3} , \tag{6.37}
$$

which one can then relate to $\delta N_{\text{eff}}$. Eq. (6.37) highlights that an accurate determination of $T_d$ is crucial in order to precisely infer $\delta N_{\text{eff}}$. Therefore, we first estimate the change in the decoupling temperature caused by the type-(d) NLO corrections.

**Changes in the neutrino decoupling temperature:** The decoupling temperature of neutrinos is defined by the solution to $\Gamma = H$, where the Hubble rate $H$ verifies $H^2(T) = (\rho_{\rm QED} + \rho_\nu)/(3m_{\rm Pl}^2)$ in the temperature range of interest, $\rho_\nu = 3g_\nu(7/8)(\pi^2/30)T^4$ is the energy density stored in the three neutrino families (each with $g_\nu = 2$) and

$$\rho_{\rm QED} = g_\gamma \frac{\pi^2}{30} T^4 + \frac{g_e}{2\pi^2} \int_0^\infty {\rm d}p\, p^2 E_e f_{\rm F}(E_e) \tag{6.38}$$

the energy density stored in the QED plasma (in the ideal gas limit). At tree level, solving the equation $\Gamma_\alpha^{\rm LO}(T_{d(\alpha)}) = H(T_{d(\alpha)})$ leads to the (flavour-dependent) LO decoupling temperature[16] $T_{d(\alpha)}$

$$\begin{aligned} T_{d(e)}^{\rm LO} &\simeq 1.320\,58\,{\rm MeV}, \\ T_{d(\mu,\tau)}^{\rm LO} &\simeq 2.221\,722\,09\,{\rm MeV}. \end{aligned} \tag{6.39}$$

These results are illustrated in the lower panels of the two plots in Fig. 6.5, which compare the LO $\nu_e$ and $\nu_{\mu,\tau}$ interaction rates with the Hubble expansion rate. Including now the type-(d) corrections to the rates, we find instead the decoupling temperatures

$$\begin{aligned} T_{d(e)}^{\rm NLO} &\simeq 1.321\,10\,{\rm MeV}\ , \\ T_{d(\mu,\tau)}^{\rm NLO} &\simeq 2.221\,722\,11\,{\rm MeV}\ , \end{aligned} \tag{6.40}$$

corresponding to a relative increase of $\sim 0.04\,\%$ for $\nu_e$ and of $\sim 8\times 10^{-7}\,\%$ for $\nu_{\mu,\tau}$. The smallness of the correction to the muon/tau neutrino decoupling temperature can be attributed not only to the suppression of their interaction rates by a factor of $\mathcal{O}(10^{-2})$ (compared to electron neutrinos) but also to an approximate cancellation between the vacuum and thermal NLO contributions near $T_{d(\mu,\tau)}^{\rm LO}$, see Fig. 6.5.

Finally, for comparison with [567], it is also useful to compute the shift in the decoupling temperature using the rates in the limit $m_e = 0$. We find in this case

$$\begin{aligned} T_{d(e)}^{{\rm NLO},m_e=0} &\simeq 1.321\,18\,{\rm MeV}, \\ T_{d(\mu,\tau)}^{{\rm NLO},m_e=0} &\simeq 2.221\,722\,23\,{\rm MeV}\ , \end{aligned} \tag{6.41}$$

[16]These results slightly differ from the earlier estimates of [549], which might be traced to different choices for the Weinberg angle.

i.e. a $0.05\%$ and $6 \times 10^{-6}\%$ relative shift for the $\nu_e$ and $\nu_{\mu,\tau}$ decoupling temperature. We can now move on to estimating $\delta N_{\text{eff}}$.

**Common decoupling temperature:** We begin by working under the approximation that all neutrino species decouple at the same temperature, i.e. at $T = T_{d(e)}$. This can be justified by the observation that neutrino oscillations become relevant already at temperatures of order $10 - 20$ MeV, see e.g. [550,576,577]. Since at late times all electrons and positrons have annihilated, i.e. $\tilde{g}_s(a_f) = g_\gamma = 2$, combining Eq. (6.37) with Eq. (6.21) leads to the simple estimate

$$N_{\text{eff}} = 3 \times \left[\frac{11}{4}\frac{2}{\tilde{g}_s(a_{d+})}\right]^{4/3} . \tag{6.42}$$

Inserting in the above equation the LO and NLO electron neutrino decoupling temperatures (Eqs. (6.39) and (6.40) respectively), we obtain a relative shift in $N_{\text{eff}}^{\text{SM}}$ of

$$\delta N_{\text{eff}}/N_{\text{eff}}^{\text{LO}} \simeq -1.1 \times 10^{-5} \tag{6.43}$$

due to the NLO type-(d) corrections. Using instead the $m_e = 0$ NLO decoupling temperatures (6.41), the relative shift in $N_{\text{eff}}^{\text{SM}}$ would have been

$$\delta N_{\text{eff}}/N_{\text{eff}}^{\text{LO}} \simeq -1.2 \times 10^{-5} . \tag{6.44}$$

This confirms that setting $m_e = 0$ works reasonably well at the neutrino decoupling temperature. These results are summarised in the first line of Tab. 6.2.

**Flavour-dependent decoupling:** Alternatively, one can also work in the opposite limit and neglect neutrino oscillations altogether. In this case, one needs to adapt the reasoning developed at the beginning of this subsection to consider three different epochs: i) before $\nu_{\mu/\tau}$-decoupling ($a < a^+_{d(\mu,\tau)}$), ii) between $\nu_{\mu,\tau}$-decoupling and $\nu_e$-decoupling ($a^-_{d(\mu,\tau)} < a < a^+_{d(e)}$) and iii) after $\nu_e$-decoupling $a > a^-_{d(e)}$). The corresponding numbers of degrees of freedom (in equilibrium with photons) are

$$
\begin{aligned}
\tilde{g}_s(a^+_{d(\mu,\tau)}) &= 2 + \frac{45}{\pi^4 T^4_{d(\mu,\tau)}} \int_0^\infty \mathrm{d}p\, p^2 \left(E_e + \frac{p^2}{3E_e}\right) f_{\rm F}(E_e, T_{d(\mu,\tau)}) + \frac{7}{8} g_{\nu_e}, \\
\tilde{g}_s(a^-_{d(e)}) &= 2 + \frac{45}{\pi^4 T^4_{d(e)}} \int_0^\infty \mathrm{d}p\, p^2 \left(E_e + \frac{p^2}{3E_e}\right) f_{\rm F}(E_e, T_{d(e)}) + \frac{7}{8} g_{\nu_e}, \\
\tilde{g}_s(a^+_{d(e)}) &= 2 + \frac{45}{\pi^4 T^4_{d(e)}} \int_0^\infty \mathrm{d}p\, p^2 \left(E_e + \frac{p^2}{3E_e}\right) f_{\rm F}(E_e, T_{d(e)}), \\
\tilde{g}_s(a_f) &= 2.
\end{aligned}
\tag{6.45}
$$

From there, we can estimate the $\nu_e$-to-photon and $\nu_{\mu,\tau}$-to-photon energy density ratio long after neutrino decoupling, at $a = a_f$,

$$
\frac{\rho_{\nu_e}(a_f)}{\rho_\gamma(a_f)} = \frac{7}{8}\left[\frac{\tilde{g}_s(a_f)}{\tilde{g}_s(a^+_{d(e)})}\right]^{4/3} = \frac{7}{8}\left[\frac{2}{\tilde{g}_s(a^+_{d(e)})}\right]^{4/3}, \tag{6.46a}
$$

$$
\frac{\rho_{\nu_{\mu,\tau}}(a_f)}{\rho_\gamma(a_f)} = \frac{7}{8}\left[\frac{2}{\tilde{g}_s(a^+_{d(e)})}\frac{\tilde{g}_s(a^-_{d(e)})}{\tilde{g}_s(a^+_{d(\mu,\tau)})}\right]^{4/3}. \tag{6.46b}
$$

Combining these results, we find

$$
N_{\rm eff} = \left(\frac{11}{4}\frac{2}{\tilde{g}_s(a^+_{d(e)})}\right)^{4/3}\left[1 + 2\times\left(\frac{\tilde{g}_s(a^-_{d(e)})}{\tilde{g}_s(a^+_{d(\mu,\tau)})}\right)^{4/3}\right]. \tag{6.47}
$$

Similarly to the common decoupling estimate, we evaluate (6.47) using the LO and NLO decoupling temperatures (6.39), (6.40) (retaining the finite electron mass) and (6.41) (for $m_e = 0$). We then find the following relative shift in $N_{\rm eff}^{\rm SM}$

$$
\delta N_{\rm eff}/N_{\rm eff}^{\rm LO} \simeq -5.4\times 10^{-5}\,, \tag{6.48}
$$

$$
\delta N_{\rm eff}^{m_e=0}/N_{\rm eff}^{\rm LO} \simeq -6.1\times 10^{-5}\,. \tag{6.49}
$$

These results are summarised in the second line of Tab. 6.2. We note that the flavour-dependent decoupling estimates of $\delta N_{\rm eff}/N_{\rm eff}^{\rm LO}$ are suppressed by a factor of $\mathcal{O}(2)$ compared to the common decoupling estimate. This is expected since the NLO corrections to the $\nu_{\mu,\tau} - e$ interaction rate are extremely suppressed compared to the corrections to the $\nu_e - e$ interaction rate. Nevertheless,

| Method | $\delta N_{\rm eff}/N_{\rm eff}^{\rm LO}$ | $\delta N_{\rm eff}^{m_e=0}/N_{\rm eff}^{\rm LO}$ |
|---|---|---|
| Entropy conservation (common decoupling) | $-1.1 \times 10^{-5}$ | $-1.2 \times 10^{-5}$ |
| Entropy conservation (flavour-dependent decoupling) | $-5.4 \times 10^{-6}$ | $-6.1 \times 10^{-6}$ |
| Boltzmann damping approximation (mean momentum) | $-7.8 \times 10^{-6}$ | $-1.6 \times 10^{-5}$ |
| Boltzmann damping approximation (full momentum) | $-7.9 \times 10^{-6}$ | $-2.6 \times 10^{-5}$ |

**Table 6.2:** Relative correction to $N_{\rm eff}^{\rm SM}$ due to type-(d) NLO corrections to the $\nu_\alpha - e$ interaction rates, as measured by the different approaches described in Sec. 6.2.3. Table adapted from [4].

it should be emphasised that both estimates are crude approximations and the true shift in $N_{\rm eff}^{\rm SM}$ will likely fall somewhere in-between.

### Solving the continuity and neutrino kinetic equations

As a more precise estimate, we solve the continuity equation (6.9) together with the momentum-dependent neutrino QKEs (6.18), applying the damping approximation. We also compare this full-momentum treatment to the mean-momentum approach (6.20). Results from both methods, obtained with or without the inclusion of the electron mass in the NLO correction to the rates, are summarised in Tab. 6.2.

Tab. 6.2 highlights several interesting aspects. First, in the case $m_e \neq 0$, both the full- and mean-momentum approaches yield a similar relative shift in $N_{\rm eff}^{\rm SM}$ of $\delta N_{\rm eff}/N_{\rm eff}^{\rm LO} \simeq (-7.8 \to -7.9) \times 10^{-6}$, which is broadly consistent with the entropy argument detailed earlier. The equivalent estimates for a vanishing electron mass, on the other hand, differ by $\sim 50\%$ between the full- ($\delta N_{\rm eff}^{m_e=0}/N_{\rm eff}^{\rm LO} \simeq -2.6 \times 10^{-5}$) and mean-momentum ($\delta N_{\rm eff}^{m_e=0}/N_{\rm eff}^{\rm LO} \simeq -1.6 \times 10^{-5}$) approaches. The full-momentum approach, especially, is larger by a factor of $\sim 4$ compared to the entropy argument. This difference is nonetheless consistent with the expectation that neutrino decoupling is not an instantaneous process and, in particular, is not fully completed by the time electrons and positrons start to annihilate at $T \simeq m_e$. As a result, $N_{\rm eff}^{\rm SM}$ is expected to be sensitive to some extent to the neutrino-electron interaction rates at low temperatures $T \lesssim m_e$, an effect that is not captured by the entropy argument. Given that the NLO rates for $m_e = 0$, displayed in Figs. 6.5 and 6.6, diverge relative to the Boltzmann-suppressed LO rates in the limit of low temperatures while their $m_e \neq 0$ counterparts vanish in the same limit, we therefore expect a larger impact in $N_{\rm eff}^{\rm SM}$ if one takes the limit $m_e \to 0$ in these

| Property | Expression at $T = 0$ | Numerical value |
|---|---|---|
| Binding energy of energy level $n$ | $\Delta E_n = m_e \alpha_{\rm em}^2/(4n^2)$ | $6.8/n^2$ eV |
| Mass | $m_{\rm Ps} = 2m_e - \Delta E_1$ | 1.022 MeV |
| Bohr radius | $a_0 = 2/(m_e \alpha_{\rm em})$ | 536 MeV$^{-1}$ |
| Lifetime (for $n = 1$): | | |
| • Para-positronium ($s = 0$) | $\tau_0 = 2/(m_e \alpha_{\rm em}^5)$ | 0.1244 ns |
| • Ortho-positronium ($s = 1$) | $\tau_1 = 9\pi/[2(\pi^2 - 9) m_e \alpha_{\rm em}^6]$ | 138.7 ns |

**Table 6.3:** Physical properties of the positronium at $T = 0$ (see e.g. [578]). Table taken from [7].

NLO corrections. Thus, although the overall effect of the NLO rate corrections on $N_{\rm eff}^{\rm SM}$ is small, we conclude that neglecting $m_e$ in their computations is not justified in the context of high-precision determinations of $N_{\rm eff}^{\rm SM}$.

To conclude this section, our results suggest that, contrary to the claim of Ref. [566] and in agreement with [567, 568], the change in $N_{\rm eff}^{\rm SM}$ from NLO QED corrections to the neutrino-electron interaction rates are smaller than the numerical and experimental uncertainties listed in [4], both of $\mathcal{O}(10^{-4})$, and should therefore not affect the theoretical benchmark (6.3).

## 6.3 Impact of bound-state formation on $N_{\rm eff}^{\rm SM}$

In the previous section, we investigated the impact of QED corrections to the weak rates on $N_{\rm eff}^{\rm SM}$. Beyond affecting neutrino damping, QED effects can also modify the early universe plasma through the formation of electron-positron bound states, i.e. positronia (Ps). These bound states, whose properties in vacuum are summarised in Tab. 6.3, may begin to form once the electron-positron bath becomes sufficiently non-relativistic, i.e. at $T \lesssim m_e$. Even though positronium is intrinsically unstable and is in addition rapidly ionised by the photon bath in the relevant temperature range, a transient population of positronia in dynamical equilibrium with the rest of the QED bath at $\mathcal{O}(10)$ keV $\lesssim T \lesssim m_e$ could nonetheless alter the universe's dynamics sufficiently to affect $N_{\rm eff}^{\rm SM}$. An estimate of the magnitude of this effect has been lacking until now, and it is the goal of this work to fill that gap. More specifically, we expect that the presence of positronium will predominantly affect $N_{\rm eff}^{\rm SM}$ by modifying the QED EoS, whereas its direct impact on the neutrino sector is likely negligible. Therefore, we focus in this section on assessing the conditions under which positronia can form and how the continuity equation (6.9) can be modified to capture their formation.

Because a complete first-principles study of positronium formation is currently out of reach, we explore in this section different phenomenological models for the formation and equilibration of these bound states. These differ primarily in their treatment of entropy evolution. First, in Sec. 6.3.1, we assess the expected change in $N_{\rm eff}^{\rm SM}$ assuming positronium is produced out of equilibrium at a temperature $T_{\rm Ps}^{\rm eq}$, considering both the case of an instantaneous equilibration and that of a more gradual thermalisation. In the next section, we estimate $T_{\rm Ps}^{\rm eq}$ by examining the conditions under which positronium can form and how quickly it equilibrates once produced. Lastly, in Sec. 6.3.3, we consider the opposite limit, where positronium production proceeds adiabatically and the QED sector remains in thermodynamic equilibrium at all times after neutrino decoupling.

Before delving into technical details, we would like to comment on the qualitative differences compared to the intuition gained from more familiar processes, such as recombination or BBN. In these cases, the observed effect crucially relies on the presence of a frozen-out population of particles (neutral hydrogen in the first case, nuclei in the second) free from ionisation and photodissociation. This is neither required nor verified in our case. As long as the positronium formation rate is large enough to maintain a dynamical equilibrium with the rest of the bath, its mere presence could noticeably affect $N_{\rm eff}^{\rm SM}$.[17] Closer to our system is the formation of positronium-like dark matter metastable bound states prior to dark matter freeze-out (see e.g. [579–581]), although the primary focus in these studies was the enhancement of the DM annihilation cross-section and subsequent depletion of the DM relic density due to the existence of these bound states.

### 6.3.1 Modelling out-of-equilibrium positronium formation and its impact on $N_{\rm eff}^{\rm SM}$

In this section, we begin by considering an out-of-equilibrium production of positronium, first assuming it occurs instantaneously, before later relaxing this assumption.

[17]This observation also applies to any bound states, including hydrogen and atomic nuclei. However, since these are significantly heavier, their number densities are typically too suppressed to have any impact on $N_{\rm eff}^{\rm SM}$.

### Instantaneous positronium production

Assuming an instantaneous production, we can adapt the entropy argument developed in Sec. 6.2.3. Essentially, one needs to consider three different epochs, which we label by their scale factors, $a_1$, $a_2$, and $a_3$, corresponding respectively to:

1. The time of instantaneous neutrino decoupling, $T = T_\nu = T_{d(e)} \simeq$ 1.3 MeV; see the previous section for details.
2. The moment of instantaneous positronium production. We assume that both $n = 1$ singlet and triplet states, also called para- and ortho-positronium respectively, are populated at their equilibrium number densities at the same time.
3. A later time at which electrons, positrons and positronium have all completely annihilated.

Importantly, we assume the production of positronium to happen after neutrino decoupling, which is justified as bound states tend to form only in the non-relativistic regime. Moreover, we assume that kinetic and chemical equilibrium hold at all times and for all particle species, except at positronium formation. Then, using a similar argument as in the previous section, we can relate the entropy in the QED sector $s_{\rm eq}$ between the different epochs, i.e.

$$\begin{aligned} s_1 a_1^3 &= s_{2-} a_2^3, \\ s_{2+} a_2^3 &= s_3 a_3^3. \end{aligned} \tag{6.50}$$

We define $s_i \equiv s_{\rm eq}(a = a_i)$ whereas the subscripts $-$ and $+$ indicate whether the entropy is computed before or after positronium formation (occurring at $a = a_2$). Then, defining $\delta s \equiv s_{2+} - s_{2-}$ the absolute change in entropy at $a = a_2$ and using the fact that $T_\nu \propto a^{-1}$ after neutrino decoupling, Eq. (6.50) yields

$$\frac{s_1}{T_{\nu,1}^3}\left(1 + \frac{\delta s}{s_{2-}}\right) = \frac{s_3}{T_{\nu,3}^3} \,. \tag{6.51}$$

As a result, the neutrino-to-photon temperature ratio reads

$$\frac{T_{\nu,3}}{T_3} = \left[\frac{\tilde{g}_{s1}}{\tilde{g}_{s3}}\left(1 + \frac{\delta s}{s_{2-}}\right)\right]^{-1/3} = \left(\frac{4}{11}\right)^{1/3}\left(1 + \frac{\delta s}{s_{2-}}\right)^{-1/3} , \tag{6.52}$$

where $\tilde{g}_{si}$, defined in Eq. (6.36), is the effective number of entropic degrees of freedom in equilibrium with photons at $a = a_i$. Right after neutrino decoupling, we have[18] $\tilde{g}_{s1} = 11/2$ while $\tilde{g}_{s3} = 2$ well below $e^+e^-$ annihilation. The neutrino and photon energy densities after $e^+e^-$ annihilation (at $a = a_3$) can then be related via

$$\rho_{\nu,3} = 3 \times \frac{7}{8}\left(\frac{4}{11}\right)^{4/3}\left(1 + \frac{\delta s}{s_{2-}}\right)^{-4/3}\rho_{\gamma,3}. \tag{6.53}$$

Inserting this result into the definition (6.21), we finally obtain[19]

$$\Delta N_{\rm eff} = N_{\rm eff}^{\rm SM} - 3 = 3\left[\left(1 + \frac{\delta s}{s_{2-}}\right)^{-4/3} - 1\right] \simeq -4\frac{\delta s}{s_{2-}} \tag{6.54}$$

for the change in $N_{\rm eff}^{\rm SM}$ due to instantaneous positronium production.

As can be seen, the crucial ingredient is the change in entropy at positronium formation $\delta s$. This quantity can be determined by assuming that energy is conserved during the production, which implies the following conservation equation

$$\rho_e(a_2, T_2) + \rho_\gamma(a_2, T_2) = \rho_e(a_2, T_{2,\rm new}) + \rho_\gamma(a_2, T_{2,\rm new}) + \rho_{\rm Ps}(a_2, T_{2,\rm new})\,. \tag{6.55}$$

$T_{2,\rm new}$ is the new temperature the system relaxes to following the instantaneous production of positronium. In the remainder of this work, we numerically solve Eq. (6.55) to obtain $T_{2,\rm new}$, and thus fully determine $\delta s$. Nonetheless, it is useful to first develop an analytical understanding of $\delta s$. Since positronium can only form for $T \lesssim m_e$, we expect that $\rho_{\rm Ps} \ll \rho_\gamma$ and, therefore, $|\delta T = T_{2,\rm new} - T_2| \ll T_2$. We can thus expand Eq. (6.55) in $\delta T$ to find

$$\delta T \simeq -\left.\frac{\rho_{\rm Ps}}{\frac{\partial}{\partial T}\left(\rho_e + \rho_\gamma + \rho_{\rm Ps}\right)}\right|_{T=T_2}\,. \tag{6.56}$$

[18] $\tilde{g}_{s1}$ actually slightly deviates from $11/2$ due to the finite electron mass as well as finite-temperature corrections to the QED EoS. However, since we are only interested in the relative change in $N_{\rm eff}^{\rm SM}$ generated by the formation of positronium, neglecting this effect should not visibly impact our result.

[19] Note that we denote the change in $N_{\rm eff}^{\rm SM}$ as $\Delta N_{\rm eff}$, and not $\delta N_{\rm eff}$, to clearly distinguish it from the correction derived in the previous section.

As a result, the change in entropy reads

$$\begin{aligned}\delta s &\simeq s_{\text{Ps}}(T_2) + \frac{\partial}{\partial T}\left(s_e + s_\gamma + s_{\text{Ps}}\right)\Big|_{T=T_2} \delta T \\ &= s_{\text{Ps}}(T_2) - \frac{\frac{\partial}{\partial T}\left(s_e + s_\gamma + s_{\text{Ps}}\right)}{\frac{\partial}{\partial T}\left(\rho_e + \rho_\gamma + \rho_{\text{Ps}}\right)}\Bigg|_{T=T_2} \rho_{\text{PS}}(T_2).\end{aligned} \tag{6.57}$$

Since $s_\gamma \gg s_e, s_{\text{Ps}}$ and $\rho_\gamma \gg \rho_e, \rho_{\text{Ps}}$ in the non-relativistic regime $T \ll m_e$, we can further approximate

$$\delta s \simeq s_{\text{Ps}}(T_2) - \frac{\rho_{\text{Ps}}(T_2)}{T_2} = \frac{P_{\text{Ps}}(T_2)}{T_2}\,. \tag{6.58}$$

In this equation, we used $s_\gamma \propto (4/3)\,T^3$ and $\rho_\gamma \propto T^4$. Finally, inserting this result into Eq. (6.54), we obtain the absolute change in $N_{\text{eff}}^{\text{SM}}$

$$\Delta N_{\text{eff}} \simeq -4 \times \frac{P_{\text{Ps}}(T_2)/T_2}{s_\gamma(T_2) + s_e(T_2)} \simeq -\frac{45}{\pi^2}\frac{P_{\text{Ps}}(T_2)}{T_2^4}. \tag{6.59}$$

As is evident from this equation, $\Delta N_{\text{eff}}$ is always negative. This aligns with our expectation that positronium primarily impacts the QED bath by slowing down its redshifting, thereby increasing the photon temperature relative to that of neutrinos.

In Fig. 6.7, we display in blue the expected change in $N_{\text{eff}}^{\text{SM}}$ as a function of the positronium equilibration temperature, considering only the $n = 1$ bound states and assuming that both ortho- and parapositronium reach equilibrium instantaneously at the same temperature. Interestingly, we find that, within this approximation, positronium needs to equilibrate at $T \approx 97$ keV in order to yield an effect on $N_{\text{eff}}^{\text{SM}}$ of the size of the current theoretical uncertainty, i.e. $|\Delta N_{\text{eff}}| \approx 10^{-3}$. This is to be contrasted with the impact of bound states on the DM relic abundance. As highlighted earlier, the primary effect of bound states in this context is an enhancement of the DM annihilation cross-section and, therefore, to delay the freeze-out of DM. Translated to our system, this would imply a delay in the electron-positron freeze-out. This would only shift $N_{\text{eff}}^{\text{SM}}$ by at most $\mathcal{O}(10^{-7})$, see Tab. 6.1 and further details in the caption, and is therefore negligible compared to the effect discussed in this section. We will detail the remaining features of this plot in the next subsection.

Before concluding this subsection, we would also like to reiterate that the high temperature relative to the positronium binding energy $T \gg \Delta E_1$, see Tab. 6.3 for numerical values, does not prevent the existence of a dynamically

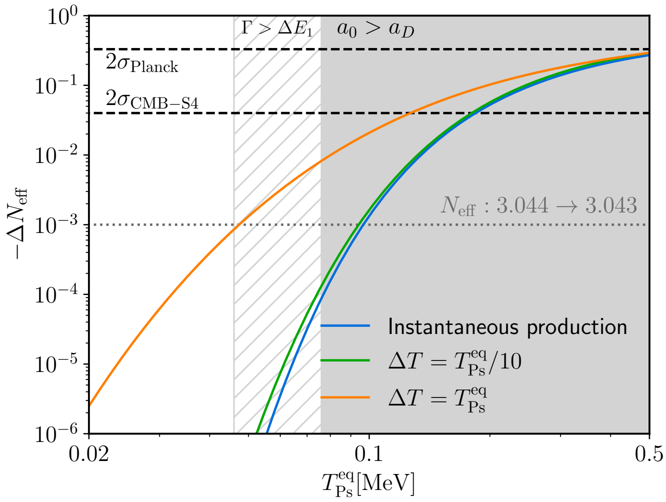


**Figure 6.7:** We display the (negative) shift in $N_{\rm eff}^{\rm SM}$, $-\Delta N_{\rm eff}$, as a function of the temperature $T_{\rm Ps}^{\rm eq}$ at which both $n=1$ positronium states reach equilibrium. We use two different approximations to compute $\Delta N_{\rm eff}$: The blue line represents the estimate derived from the entropy argument of Sec. 6.3.1 assuming instantaneous positronium equilibration. The green and orange lines denote $\Delta N_{\rm eff}$ expected from a non-instantaneous production scenario, modelled with the parametrisation (6.66) for the choices of $\Delta T/T_{\rm Ps}^{\rm eq} \in \{0.1, 1\}$, respectively. Positronium formation is prevented by Debye screening in the grey-shaded region. In the hatched region, we expect scatterings with the plasma to prevent the formation of stable bound states, but more detailed computations are required to quantify its exact impact. The three horizontal lines represent, from top to bottom, the current sensitivity of Planck at 95% C.L. [117], the planned sensitivity of CMB-S4 [53] at 95% C.L., and the last but one significant digit of the SM benchmark value $N_{\rm eff}^{\rm SM}$ [511, 543, 555, 556]. Figure and caption taken from [7].

sustained population provided that the formation rate are sufficiently large to overcome the rapid decays and ionisations.[20] In fact, our approach is fully consistent with the commonly used Saha equation (see e.g. [582]) which predicts that only a residual fraction of electrons are bound in the non-relativistic regime, with $n_e/n_{\rm Ps} \sim e^{m_e/T} \gg 1$. This further supports our assumption that the electron-positron bath remains in thermodynamic equilibrium at all times, even if positronium is formed out of equilibrium.

### Non-instantaneous positronium production

To capture scenarios where the positronium equilibration rates are not sufficiently fast, it is useful to relax the assumption of instantaneous equilibra-

[20]We verify explicitly in Sec. 6.3.2 that this is indeed the case.

tion and consider a more gradual production, symmetric around $T_{\rm Ps}^{\rm eq}$. Because positronia effectively start to populate the QED bath at higher temperatures in this scenario, we expect an increase in the entropy production, which in turn leads to a larger shift in $N_{\rm eff}^{\rm SM}$. To capture this effect, we need to incorporate the impact of positronium formation in the continuity equation (6.9). In general, the impact of a particle $X$ (with energy density $\rho_X$ and pressure density $P_X$) on the continuity equation can be incorporated by making the replacement

$$\begin{aligned} &G_1 \to G_1 - (\tau^3/2m_e^4)\left(3(\rho_X + P_X) - (m_e/\tau)\partial_T \rho_X\right) \ , \\ &G_2 \to G_2 + (\tau/m_e)^3 \partial_T \rho_X/2 \ . \end{aligned} \tag{6.60}$$

In practice, we need to phenomenologically model the time evolution of positronium. Assuming that it retains at all times a thermal distribution with the same temperature as the photon bath, one can perform a similar ansatz to Eq. (6.20) and parametrise the positronium distribution function through a smooth transfer function $\sigma$ rescaling the positronium distribution function

$$f_{\rm Ps} = \sigma(\tau) f_{\rm Ps}^{\rm eq} \ . \tag{6.61}$$

As a result, its (dimensionless) energy density scales in the following way

$$\bar\rho_{\rm Ps}(x,y,z) = \sigma(\tau)\bar\rho_{\rm Ps}^{\rm eq}(x,y,z) = \sigma(\tau)\frac{g_{\rm Ps}}{2\pi^2}\int {\rm d}y\, y^2 \ \frac{\sqrt{y^2+x_{\rm Ps}^2}}{\exp(\sqrt{y^2+x_{\rm Ps}^2}/z)-1} \ , \tag{6.62}$$

with $x_{\rm Ps} = (m_{\rm Ps}/m_e)x \simeq 2x$ and $g_{\rm Ps} = 4$ is the number of degrees of freedom of the $n = 1$ positronium state. A similar expression holds for the pressure density[21] $\bar P_{\rm Ps}$. Then, we find

$$\begin{aligned} \frac{1}{2z^3}\left(\frac{\bar\rho_{\rm Ps} - 3\bar P_{\rm Ps}}{x} - \frac{\partial\bar\rho_{\rm Ps}}{\partial x}\right) =& \frac{g_{\rm Ps}}{4}\sigma(\tau)\times \\ &\times\left[\tau\left(\frac{m_{\rm Ps}}{m_e}\right)^2 J_-\left(\frac{m_{\rm Ps}}{m_e}\tau\right) - zW_-\left(\frac{m_{\rm Ps}}{m_e}\tau\right)\partial_x\right] , \end{aligned} \tag{6.63}$$

and

$$\frac{1}{2z^3}\frac{\partial\bar\rho_{\rm Ps}}{\partial z} = \frac{g_{\rm Ps}}{4}\sigma(\tau)\times \tag{6.64}$$

[21] Note that this ansatz does not verify the thermodynamic consistency relation $\rho = -p + T\partial_T p$, see Eq. (1.57). This is however expected as, although we assume the positronium distribution function to retain a thermal shape, we postulate in this section that the production of positronium happens out of equilibrium.

$$\times\left[\tau^2\left(\frac{m_{\rm Ps}}{m_e}\right)^2 J_-\left(\frac{m_{\rm Ps}}{m_e}\tau\right)+\frac{m_{\rm Ps}}{m_e}Y_-\left(\frac{m_{\rm Ps}}{m_e}\tau\right)+zW_-\left(\frac{m_{\rm Ps}}{m_e}\tau\right)\partial_z\right],$$

where $J_-$ and $Y_-$ are the Bose-Einstein equivalents of $J_+$ and $Y_+$, whereas $W_-(\tau)$ is a genuinely new function. Explicit expressions for all of these functions can be found in appendix D.1. Inserting these two results in the continuity equation and setting $m_{\rm Ps}\simeq 2m_e$ and $g_{\rm Ps}=4$, we find that the continuity equation in the presence of positronium reads

$$\frac{\mathrm{d}z}{\mathrm{d}x}=\frac{\tau[J_+(\tau)+4\sigma(\tau)J_-(2\tau)]-z\partial_x\sigma(\tau)W_-(2\tau)}{\tau^2\left[J_+(\tau)+4\sigma(\tau)J_-(2\tau)\right]+Y_+(\tau)+Y_-(2\tau)-x\partial_x\sigma(\tau)W_-(2\tau)+2\pi^2/15},\tag{6.65}$$

where we have also used the property $\partial_z\sigma=-(x/z)\partial_x\sigma=-\tau\partial_x\sigma$. To keep this expression compact, note that we have dropped the terms proportional to $G_{1,2}$ and to the neutrino abundance $\rho_\nu$.[22] Regarding the form of the transfer function $\sigma(\tau)$, we adopt the following ansatz

$$\sigma(T)=\frac{1}{2}\left[1+\tanh\left(\frac{T_{\rm Ps}^{\rm eq}-T}{\Delta T}\right)\right],\tag{6.66}$$

which is motivated by our expectation that the energy density of a species far from equilibrium should scale as $\rho\propto 1-e^{-\int\Gamma_{\rm prod}/(Hx)\mathrm{d}x}$, with $\Gamma_{\rm prod}$ being the positronium production rate. In the above equation, the width $\Delta T$ parametrises the effective positronium equilibration timescale. The green and orange lines in Fig. 6.7 correspond to the expected shift in $N_{\rm eff}^{\rm SM}$ for two different choices $\Delta T=T_{\rm Ps}^{\rm eq}/10$ and $\Delta T=T_{\rm Ps}^{\rm eq}$, which serves as benchmarks for fast and slow positronium equilibration, respectively. We confirm our previous expectation that the faster the equilibration, the smaller the change in $N_{\rm eff}^{\rm SM}$. Moreover, in the limit $\Delta T\to 0$, we recover exactly the estimates obtained in the previous subsection using entropy conservation arguments. We also checked that different functional forms for $\sigma$ yield broadly similar results as long as the formation model contains an exponential dependence on $(T_{\rm Ps}^{\rm eq}-T)/\Delta T$.

### 6.3.2 When does positronium form?

As is clear from Fig. 6.7, $N_{\rm eff}^{\rm SM}$ is exponentially sensitive to the equilibration temperature of positronium $T_{\rm Ps}^{\rm eq}$. It is therefore crucial to accurately assess its

[22]We have explicitly checked that this has a negligible impact on our estimate of $\Delta N_{\rm eff}$.

value, but also how quickly positronium can equilibrate once it is allowed to form.

Ideally, one would extract this information by calculating the full time evolution of $n$-point correlation functions in the QED plasma using the CTP formalism developed in Chap. 1. However, while steps in this direction have been taken in the non-relativistic regime in [583], applying this formalism to the system at hand proves to be both technically and computationally challenging. Therefore, before undertaking this non-trivial task, we first rely on various physical arguments to evaluate whether the anticipated impact on $N_{\rm eff}^{\rm SM}$ justifies such an effort.

In the relevant temperature range, the QED bath remains close to thermal equilibrium and the electrons/positrons that compose it are predominantly non-relativistic. Hence, the formation of positronium can in good approximation be understood in terms of a finite-temperature effective static potential $V(r)$. In the HTL limit, the latter takes the form [583, 584][23]

$$V(r) = -\alpha_{\rm em} m_D - \frac{\alpha_{\rm em}}{r} e^{-m_D r} - \mathrm{i}\alpha_{\rm em} T \varphi(m_D r), \tag{6.67}$$

with

$$\varphi(y) = 2\int_0^{+\infty} \mathrm{d}u \frac{u}{(u^2+1)^2}\left(1 - \frac{\sin(uy)}{uy}\right), \tag{6.68}$$

where the Debye mass $m_D$, defined in Eq. (D.32), is responsible for the screening of the potential. The first contribution in Eq. (6.67) is commonly known as the Salpeter term. We will discuss in more detail the origin of the different contributions to this potential in the next subsection. This approach was initially developed in the context of hot QCD to understand the formation of heavy quark-antiquark pairs. In this case, the natural hierarchy between the electron and the quark masses ensures the validity of the HTL approximation. In our case, the HTL approximation requires $T \gg m_e$ and therefore cannot accommodate the requirement to remain in the non-relativistic regime (where $T \lesssim m_e$). Nonetheless, we will work in the following with the potential (6.67) but substituting the HTL Debye mass $m_D^{\rm HTL} = eT/\sqrt{3}$ with a value extracted from the full one-loop photon self-energy derived in appendix D.3.1, see Eq. (D.32).

[23]The exact shape of this potential depends on the theory (QCD, QED, etc.), the temperature range under consideration, the hierarchy between the different scales, etc. and has been the subject of intensive studies over the last years, see e.g. [583–592].

As long as the imaginary part of the potential (6.67) remains small, the standard quasiparticle picture on which we based Sec. 6.3 holds. In this regime, the real part of the potential $\mathrm{Re}[V(r)]$ captures the energy of the bound states whereas their thermal width is instead encoded in the imaginary part $\mathrm{Im}[V(r)]$. Based on this understanding, we can break down the problem of positronium formation into two different aspects:

(i) At which temperatures can positronium exist as a quasiparticle in the early universe plasma?

(ii) Once positronium formation becomes possible, how fast does it equilibrate?

The next two subsections will be dedicated to each of these questions.

### Existence of positronium

Bound states are in general quite sensitive to in-medium effects. In particular, it is well known that they cease to exist at sufficiently high temperatures and/or densities, a phenomenon commonly referred to as *bound state melting*, due to the following medium-induced effects:

(i) Debye screening of the mediator, and

(ii) Scatterings between the mediator and particles in the plasma.

In the quasiparticle limit, the first effect can be associated with the real part of the potential (6.67) whereas its imaginary part captures the second effect. Precisely calculating the melting temperature from theoretical considerations is generally intricate [584, 591]. For this reason, we restrict ourselves in this work to obtaining a first estimate of its value for positronium, based on the two simple physical arguments outlined below.

**Debye screening:** At finite temperature, photons develop a thermal mass from forward scatterings with the rest of the plasma. This results in a screening of the electrostatic potential

$$V(r) \sim \frac{e^{-r/a_D}}{r} \,, \tag{6.69}$$

quickly suppressing the electromagnetic interaction at distances larger than the Debye screening length $r \gtrsim a_D$, which is related to the Debye mass defined in

Eq. (D.32) through

$$a_D \equiv \frac{1}{m_D} = \frac{1}{\sqrt{-\operatorname{Re}\Pi^R_{L,00}\left(q_0=0,|\mathbf{q}|\to 0\right)}}\,. \tag{6.70}$$

In the HTL limit, we have $a_D^{\rm HTL} = \sqrt{3}/(eT)$. To provide a first estimate of the positronium melting temperature, it seems reasonable to follow the approach of [591, 593] and assume that positronium can only form as long as the Debye screening length is larger than the most likely positronium radius $a_D \gtrsim r_\ell \approx a_0 n^2$, where $a_0$ is the positronium's Bohr radius defined as

$$a_0 = \frac{1}{m_{\rm r}\alpha_{\rm em}} = \frac{8\pi}{m_e e^2} \simeq 536\ \text{MeV}^{-1}. \tag{6.71}$$

In the above equation, $m_r = m_e/2$ is the reduced mass associated with the electron-positron system. We note, however, that $r_\ell$ captures the most likely positronium radius only as long as the electrostatic potential remains Coulombian. Once Debye screening becomes effective, numerically solving the Schrödinger equation is necessary to obtain a more precise estimate. Early numerical analyses [593–595] of eigenstates of the Schrödinger equation for a pure Yukawa potential suggest a slightly more constraining condition, i.e. $a_D \gtrsim a_0/0.84$ for $n = 1$. This would however only modify the predicted melting temperature by $\mathcal{O}(5\%)$, which we neglect for this first estimate. Moreover, the complex momentum-dependence of the 1PI-resummed photon propagator may render this numerical estimate unreliable, as it relies on a momentum-independent thermal correction to the photon propagator.

Neglecting any chemical potential in the electron sector,[24] we display in Fig. 6.8 the Debye screening length $a_D$, extracted from the 1PI-resummed photon self-energy [4], as a function of temperature. For completeness, we also compare to the screening length obtained with the HTL approximation $a_D^{\rm HTL}$. The criterion $a_D > r_\ell$ then implies that the formation of positronium ground states ($n = 1$) can only occur at temperatures

$$T \lesssim T_D \simeq 75.6\ \text{keV}\,. \tag{6.72}$$

As a comparison, the melting temperature for $n = 2$ positronium is approximately 55 keV. Based on Eq. (6.72), we shade the region where positronium formation is forbidden in gray in Fig. 6.7. We directly see that, assuming in-

[24] Charge conservation implies that, across the relevant temperature range, the electron asymmetry can be at most as large as the baryon asymmetry, thereby justifying our approximation.

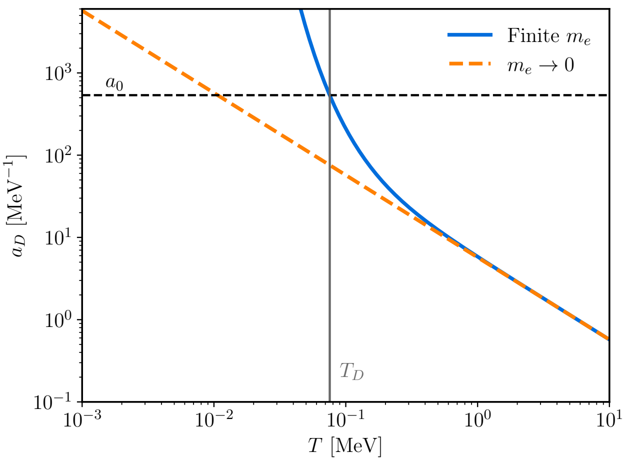


**Figure 6.8:** Debye screening length as a function of the temperature computed from the 1PI-resummed photon propagator (blue) and the HTL approximation (orange dashed). Observe that while the two estimates coincide at $T \gtrsim m_e$, the former is significantly larger at $T \lesssim m_e$. We compare $a_D$ to the Bohr radius $a_0$ of the positronium state in vacuum (black dashed horizontal line). The vertical line represents $T_D$, the temperature at which $a_0 = a_D$ and above which Debye screening becomes effective. Figure and caption taken from [7].

stantaneous equilibration, the largest value of $|\Delta N_{\text{eff}}|$ consistent with the constraint (6.72) is $\approx 10^{-4}$. Non-instantaneous equilibration generally leads to larger changes in $N_{\text{eff}}^{\text{SM}}$. For illustration, one can mimic a gradual positronium formation around $T_D$ by adopting the kernel $\sigma(T) = 1 - \exp[(a_D/a_0)^k]$, with $k \in \mathbb{N}$. This yields $\Delta N_{\text{eff}} = -2.25 \times 10^{-3}, -2.61 \times 10^{-4}$ for $k = 2, 4$, respectively. As a side remark, we note that using the HTL result $a_D^{\text{HTL}} = \sqrt{3}/(eT)$, which overestimates the amount of screening at such low temperature, would have led to a much lower melting temperature $T_D \approx 10.7$ keV, too low to impact $N_{\text{eff}}^{\text{SM}}$ in any measurable way.

**Dissociation from scatterings:** In addition to the Debye screening of the electric field, positronium can also dissociate because of Landau damping [584, 585, 591], i.e. the real scatterings of the photons with the rest of the early universe bath. This mechanism has actually been shown to constitute the dominant cause of melting in the case of heavy quarkonia [586–588]. This effect is generally captured by the imaginary part of the potential (6.67) and can be understood in the following way. Bound states remain well-defined propagating states only as long as their contributions to the spectral function can be separated from the continuum. However, as the temperature increases, the thermal width of the positronium also increases until it becomes much larger than the positronium's binding energy, at which point the positronium is expected to dissociate into an electron-positron pair. This thermal width $\Gamma$ is in general challenging to compute exactly. In this work, we use the results from Ref. [584] and approximate

$$\Gamma = \alpha_{\rm em} T \int {\rm d}^3\mathbf{r}\ \varphi(r/a_D) |\Psi_{1s}^{\rm Ps}(\mathbf{r})|^2 \,, \tag{6.73}$$

with $r = |\mathbf{r}|$. In the above equation, we write $\Psi_{1s}^{\rm Ps}$ the wavefunction associated to the ground state of positronium whereas the function $\varphi$ has been defined earlier in Eq. (6.68). These results have strictly speaking only been derived in the HTL approximation. Similarly to the Debye screening argument, we nonetheless assume that this form holds within the temperature range of interest, up to the substitution of the HTL expression for $a_D$ by the complete one-loop result. Adopting this functional shape for $\Gamma$, we can then, based on the previous discussion, apply the simple criterion that bound states dissociate as soon as their width equals their binding energy, defining the so-called dissociation temperature $T_{\rm dis}$

$$\Gamma(T_{\rm dis}) = \Delta E_n = \frac{m_e \alpha_{\rm em}^2}{4n^2} \,. \tag{6.74}$$

The constraint from Eq. (6.74) is typically stronger than the one from Debye screening. Therefore, $a_D \gg a_0$ close to dissociation, and it is a reasonable approximation to assume that the positronium wavefunction takes its zero-temperature form. We then find, by evaluating Eq. (6.73), that

$$T_{\rm dis} \simeq 45.8 \ {\rm keV} \tag{6.75}$$

for the $n = 1$ state.[25] As anticipated, this threshold lies well below the melting temperature $T_D \simeq 75.6$ keV obtained from the Debye screening argument. As a sanity check, we also calculated the dissociation temperatures of the hydrogen and the muonic hydrogen, which were already computed using a similar approach (but with a slightly different ansatz for the photon propagator) in [589,590]. We found good agreement with these references, within 10% for both systems.

[25] Again, we will not consider here excited states as their production is delayed. For instance, we find $T_{\rm dis} \simeq 40.5$ keV for $n = 2$.

The hatched region in Fig. 6.7 indicates the temperature range for which positronium is expected to be dissociated by real scatterings. Assuming an instantaneous production, the low formation temperature (6.75) would yield a negligible change in $N_{\rm eff}^{\rm SM}$, i.e. $\Delta N_{\rm eff} \simeq -3 \times 10^{-8}$. However, there remains at this stage various uncertainties that could modify this conclusion. In particular, dissociation from scatterings is expected to be a continuous process, resulting from the gradual broadening of the spectral function peak associated to positronium. This is to be contrasted with the melting from Debye screening, where the photon thermal mass sets the scale above which positronium cannot exist. Therefore, even though the standard quasiparticle picture does not hold in the intermediate regime $T_{\rm dis} < T < T_D$ and one cannot as a result write a set of on-shell Boltzmann equations to directly evaluate the positronium equilibration temperature and rate, it is reasonable to expect some non-zero contributions from the melted peaks to the energy and pressure density of the QED bath. This effect may be captured to an extent by a transfer function of the form (6.66) with a non-zero value of $\Delta T/T_{\rm Ps}^{\rm eq}$,[26] leading to a larger value of $\Delta N_{\rm eff}$. Accurately modelling this effect remains however challenging, as it would require a detailed analysis of the complete finite-temperature two- and four-point correlation functions in QED, see e.g. [583], which lies beyond the scope of the present work.

### Positronium equilibration

Now that we have established upper bounds on the positronium formation temperature, we can turn to the question of whether this formation can occur fast enough to produce a sizeable effect on $N_{\rm eff}^{\rm SM}$. Throughout this subsection, we will assume that (momentum-averaged) Boltzmann equations provide a valid description of positronium production.

Properties of positronium in vacuum have been under scrutiny for decades, see e.g. [596] and references therein. Moreover, positronium-like DM bound states have also been the subject of intensive study due to their potential impact on DM freeze-out and relic abundance as well as on indirect DM searches, see e.g. [580, 597–599]. As a result, the set of Boltzmann equations describing the evolution of positronium as well as their production rate in a non-relativistic plasma are very well known, see e.g. [580, 581]. In the situation under consideration, electrons, positrons and photons all remain in kinetic equilibrium

[26] Though one should note that, because the standard Boltzmann picture does not apply in this intermediate regime, it is challenging to directly relate $\Delta T$ to any microphysical interaction rate.

throughout the relevant epoch. The Boltzmann equation governing the evolution of the positronium number density $n_{\rm Ps}$ then takes the form

$$\frac{\mathrm{d}}{\mathrm{d}x}(n_{\rm Ps}x^3) = -\frac{1}{Hx}\left[\Gamma^{\rm dec} + \Gamma^{\rm ion}(T)\right]\left(n_{\rm Ps}x^3 - n_{\rm Ps}^{\rm eq}x^3\right) \,, \tag{6.76}$$

with $n_{\rm Ps}^{\rm eq}$ the equilibrium positronium number density. In the non-relativistic regime, the decay rate $\Gamma^{\rm dec}$ and the ionisation rate $\Gamma^{\rm ion}$ are given for $n = 1$ by [581]

$$\Gamma^{\rm dec} = \begin{cases} m_{\rm r}\alpha_{\rm em}^5, & \text{for } s = 0, \\ \frac{4(\pi^2-9)}{9\pi} m_{\rm r}\alpha_{\rm em}^6, & \text{for } s = 1, \end{cases} \tag{6.77a}$$

$$\Gamma^{\rm ion}(T) = \frac{m_{\rm r}\alpha_{\rm em}^5}{8\pi}\int_0^{+\infty}\frac{\mathrm{d}\xi\;\xi^{-4}}{\exp\left[\left(\frac{1}{n^2}+\frac{1}{\xi^2}\right)\frac{m_e\alpha_{\rm em}^2}{4T}\right]-1}S^{\rm BSF}(\xi), \tag{6.77b}$$

where $s$ distinguishes between the singlet ($s = 0$) and triplet ($s = 1$) positronium states. Moreover, the bound-state factor $S^{\rm BSF}$ is defined (for $n = 1$) as

$$S^{\rm BSF}(\xi) = \frac{2^9}{3}\frac{\xi^4 e^{-4\xi\cot^{-1}(1/\xi)}}{(\xi^2+1)^2}\frac{2\pi\xi}{1-e^{-2\pi\xi}}. \tag{6.78}$$

We recognise the standard $s$-wave Sommerfeld factor $2\pi\xi/(1-e^{-2\pi\xi})$, where $\xi \equiv \alpha_{\rm em}/v_{\rm rel}$ ($v_{\rm rel}$ being the electron-positron relative velocity), which captures the cross-section enhancement at low velocities due to the long-range nature of the electromagnetic interaction.

In order to track the evolution of the positronium abundance, it is in general necessary to solve the Boltzmann equation (6.76) for both singlet and triplet states using the rates (6.77). However, we know from the previous subsections that positronium can only form for $T \lesssim T_D$. Thus, since

$$\left.\frac{\Gamma^{\rm dec}+\Gamma^{\rm ion}}{H}\right|_{T\leq T_D} \gtrsim 10^{16} \gg 1 \,, \tag{6.79}$$

one can directly conclude that, *in the absence of the melting effects* discussed earlier, the equilibration of positronium would be instantaneous. As a side note, we remark that the decay contribution $\Gamma^{\rm dec}$ can be safely neglected in the relevant temperature range 20 keV $\lesssim T \lesssim T_D$.

Strictly speaking, the rates (6.77) only apply to non-relativistic particles. While this should be a good approximation at $T \lesssim 80$ keV, one may nonetheless wonder if this approach overestimates the contribution from the relativistic tail of the electron/positron distribution. In order to clarify this aspect, we also consider a worst-case scenario estimate for the positronium rates by selecting only electron momenta corresponding to kinetic energies smaller than the positronium binding energy, i.e.

$$\begin{aligned}\Gamma_{\rm extr} &= \Gamma^{\rm ion}\left(\frac{n_e^{\rm eq}(p<p_{\rm lim})}{n_e^{\rm eq}}\right)^2\\ &= \Gamma^{\rm ion}\left(\frac{\int_0^{p_{\rm lim}} p^2 f_{\rm FD}(p/T, m_e/T){\rm d}p}{\int_0^{+\infty} p^2 f_{\rm FD}(p/T, m_e/T){\rm d}p}\right)^2 ,\end{aligned} \tag{6.80}$$

where $p_{\rm lim}$ is the largest momentum for which $v_{\rm rel}$ satisfies $v_{\rm rel} < \alpha_{\rm em}$. Using this extremely conservative estimate, we nonetheless still find

$$\left.\frac{\Gamma_{\rm extr}}{H}\right|_{T=T_D} \simeq 290\ . \tag{6.81}$$

This again indicates a rapid approach to equilibrium as soon as formation is allowed, strengthening our previous claim. We therefore conclude that positronium formation is not limited by the production rates, but rather by the system's spectral features between $T_{\rm dis}$ and $T_D$. Given that the overall change in $N_{\rm eff}^{\rm SM}$ in this temperature range is exponentially sensitive to the positronium equilibration temperature, a more comprehensive investigation will be needed to reliably assess the ultimate impact of positronium formation on $N_{\rm eff}^{\rm SM}$.

### 6.3.3 Positronium as non-ideal gas correction

In the previous subsection, we have focused on scenarios where the production of positronium is accompanied by the simultaneous generation of entropy. This is particularly obvious in the instantaneous production model where the entropy density presents a discontinuity at $T = T_{\rm Ps}^{\rm eq}$, see Eq. (6.58), but even parametrising the positronium distribution function with the ansatz (6.61), which captures a more progressive equilibration, does not satisfy the thermodynamic relation (1.57c). The change in $N_{\rm eff}^{\rm SM}$ is then directly connected to the amount of entropy generated during positronium formation, see e.g. Eq. (6.54). In this subsection, we instead consider the opposite limit in which the creation of positronium does not generate entropy overall and the QED bath remains in complete thermal equilibrium (with itself) at all times.

In this limit, the entropy argument presented in Sec. 6.2.3 applies[27] and the change in $N_{\rm eff}^{\rm SM}$ will solely depends on the contribution of bound states to the total entropy at $T = T_d$. Since the screening of the electric field and scatterings with the QED plasma prevent any bound-state formation at such early times, one might naively conclude that their impact on $N_{\rm eff}^{\rm SM}$ is negligible in this limit. This simple reasoning would however be misleading. For the total entropy to be conserved (and all thermodynamic quantities to remain continuous), one also needs to properly include the non-ideal contribution from scattering states ($e^\pm e^\pm$ or $e^+e^-$), which is non-vanishing even at temperatures $T \gg T_D$.

In this subsection, we start by estimating the temperature dependence of the thermodynamic pressure within this scenario, including non-ideal (and non-perturbative) contributions from both bound and scattering states. We then use this estimate to compute the expected change in $N_{\rm eff}^{\rm SM}$.

### Extracting thermodynamic quantities from the Beth-Uhlenbeck formula

Due to the non-perturbative nature of the problem, it is in general impossible to obtain explicit formulae for the entropy and other thermodynamic quantities in terms of the microphysics of the system. In the non-relativistic and dilute limit however, i.e. $T \ll m_e, m_e - \mu_e$, these can be extracted from the so-called *Beth-Uhlenbeck formula* [600],

$$\beta(P - P^{(0)}) = 4\left(\frac{2m_eT}{2\pi}\right)^{3/2} e^{-\beta 2m_e}\sum_{\ell=0}^{\infty}(2\ell+1)b_\ell\,, \tag{6.82}$$

which consistently includes the contributions from both bound and interacting scattering states in the non-ideal pressure. In this equation, $P^{(0)}$ represents the ideal pressure density corresponding to a non-interacting plasma, $\beta \equiv 1/T$ is the inverse temperature and the coefficients $b_\ell$ are defined as

$$\begin{aligned} b_\ell = &\sum_{n\geq \ell+1} e^{-\beta E_{n\ell}} \\ &+ \frac{1}{\pi}\int_0^\infty \mathrm{d}E e^{-\beta E}\frac{\mathrm{d}}{\mathrm{d}E}\left\{\delta_\ell^{e^+e^-} + \left(\frac{1}{2} - \frac{(-1)^\ell}{4}\right)\left(\delta_\ell^{e^+e^+} + \delta_\ell^{e^-e^-}\right)\right\}\,. \end{aligned} \tag{6.83}$$

In the following, we will take this equation for granted and refer the reader to [583, 601, 602] for a more pedagogical introduction on its derivation. In

[27] This statement assumes the entire neutrino sector, which is not the focus of this subsection, to decouple instantaneously at $T_d = T_{d(e)} \simeq 1.3$ MeV. We will lift this assumption at the end of this subsection.

Eq. (6.83), the first term captures the bound-state contribution, with $E_{n\ell}$ being the binding energy of the positronium with principal quantum number $n$ and orbital angular momentum $\ell$. The second term on the other hand encodes the contribution from scattering states, with $\delta_\ell$ representing the phase shift of the attractive ($\delta_\ell^{e^+e^-}$) and repulsive ($\delta_\ell^{e^+e^+} = \delta_\ell^{e^-e^-}$) scattering states. Knowing the pressure, the energy and entropy densities can then be extracted from the consistency relations (1.57).

Explicit expressions for the binding energies and phase shifts do not exist for the Yukawa potential (6.69). For this reason, we approximate the Yukawa potential by the so-called *Hulthén potential*

$$V_H(r) = -\frac{\alpha_{\rm em}\kappa m_D e^{-\kappa m_D r}}{1-e^{-\kappa m_D r}} \,, \tag{6.84}$$

which has been shown to reproduce well the formation of the $n = 1, \ell = 0$ bound state of the Yukawa potential if one sets $\kappa = \pi^2/6$ [603]. Explicit results for the the binding energies and phase shifts exist for the $s$-wave ($\ell = 0$), see e.g. [604, 605]:

$$\delta_{\ell=0} = \mathrm{Arg}\frac{\mathrm{i}\Gamma(\lambda_+ + \lambda_- - 2)}{\Gamma(\lambda_+)\Gamma(\lambda_-)} \,, \tag{6.85}$$

$$E_{n,\ell=0} = -\frac{\alpha_{\rm em}^2 m_e}{4n^2}\left(1-\kappa\epsilon_\varphi n^2\right)^2 \,, \quad \text{for } m_D \le \frac{\alpha_{\rm em} m_e}{\kappa n^2} \,, \tag{6.86}$$

where $\Gamma$ is the standard Gamma function,

$$\lambda_\pm = \begin{cases} 1 + \mathrm{i}\frac{\epsilon_v}{\kappa\epsilon_\varphi} \pm \frac{\sqrt{\kappa\epsilon_\varphi - \epsilon_v^2}}{\kappa\epsilon_\varphi}, & \text{for } e^+e^- \\ 1 + \mathrm{i}\frac{\epsilon_v}{\kappa\epsilon_\varphi} \pm \mathrm{i}\frac{\sqrt{\kappa\epsilon_\varphi + \epsilon_v^2}}{\kappa\epsilon_\varphi}, & \text{for } e^+e^+, e^-e^- \end{cases} \,, \tag{6.87}$$

and we defined the following dimensionless quantities

$$\epsilon_v^2 = \frac{E}{\alpha_{\rm em}^2 m_e} \,, \quad \epsilon_\varphi = \frac{m_D}{\alpha_{\rm em} m_e} \,. \tag{6.88}$$

Equivalent approximations do exist for higher partial waves but are rather inaccurate due to the existence of quasibound states [606]. In the following, we will therefore limit ourselves to the $s$-wave contribution.

To illustrate the impact of the scattering-state contribution, we display in Fig. 6.9 the value of the coefficient $b_0$ as a function of the temperature in the non-relativistic regime $T \lesssim m_e$, distinguishing between the different contributions appearing in Eq. (6.83).

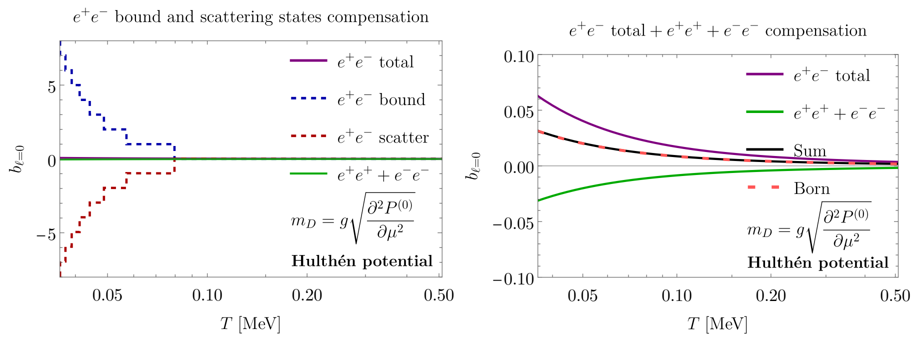


**Figure 6.9:** Temperature dependence of the different contributions to the coefficient $b_0$ in (6.83). The right panel shows a zoomed-in view of the left panel. Figure taken from [7].

One observes several interesting features. First, the appearance of bound states is signalled by discontinuities in $b_0$ (and, as a consequence, also in the entropy density), the first of which appears at $T = T_D$ as expected from the Debye screening argument discussed in the previous subsection, see Eq. (6.72). As the temperature decreases, the number of bound states then quickly increases due to the Boltzmann suppression of $m_D$. However, we notice that the contribution from attractive scattering states also present discontinuities at the same temperatures but of opposite signs, thereby partially cancelling the bound-state contribution and ensuring that all thermodynamic quantities remain continuous. Mathematically, the origin of this cancellation can be understood in a simple manner by taking the limit $\beta \to 0$. The Levinson theorem indeed ensures that the number of bound states $n_\ell$ can be directly related to the phase shift in that limit, i.e.

$$\lim_{\beta\to 0} b_\ell = n_\ell + \frac{1}{\pi}\left[\delta_\ell^{e^+e^-}(E=\infty) - \delta_\ell^{e^+e^-}(E=0)\right] = 0. \tag{6.89}$$

Second, the right panel of Fig. 6.9 indicates that a second compensation, this time between the attractive and repulsive scattering states, takes place. The remaining contribution (shown as a continuous black line) corresponds to a good approximation to the well-known [564] $\mathcal{O}(e^2)$ Born contribution

$$\left(P - P^{(0)}\right)\big|_{\rm Born} = \frac{e^2 m_e^2 T^2}{8\pi^3} e^{-2m_e/T}\,. \tag{6.90}$$

This result suggests that non-perturbative contributions to the pressure exactly cancel, or, at the very least, are largely subdominant, and that the perturbative approach chosen in [549] works well. A more formal proof of this observation

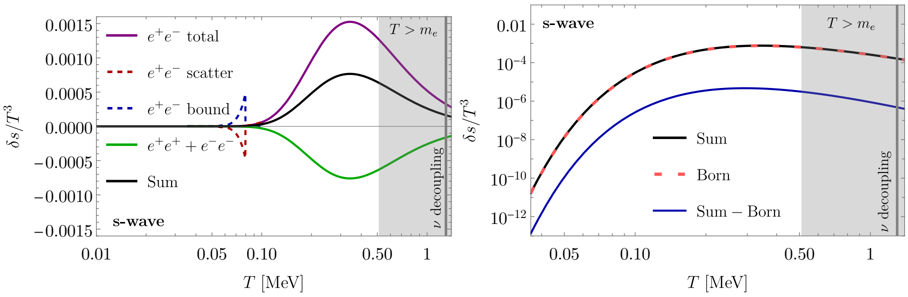


**Figure 6.10:** (Left panel) Temperature dependence of the change in entropy due to different (perturbative and non-perturbative) contributions. (Right panel) Equivalent figure on a logarithmic scale, focusing on the comparison between the total change in the pressure with the Born approximation (6.90). The difference between the two, shown in blue, remains small, suggesting that perturbation theory remains under control. Figure taken from [7].

is provided in [7]. Since the perturbative computation is well understood even in the relativistic regime, this observation enables us to extrapolate the Beth-Uhlenbeck formula to the relativistic regime and compute the resulting change in $N_{\text{eff}}^{\text{SM}}$.

### Impact on $N_{\text{eff}}^{\text{SM}}$

Now that we have the tools to evaluate all thermodynamic quantities, let us turn to the question of the overall impact of bound-state formation on $N_{\text{eff}}^{\text{SM}}$. Using a similar argument as in Sec. 6.2.3, one obtains the following estimates for $\Delta N_{\text{eff}}$:

$$\Delta N_{\text{eff}} \simeq -4 \left.\frac{\delta s}{s_{\text{eq}}}\right|_{T=T_d} \simeq -\frac{180}{11\pi^2} \left.\frac{\delta s}{T^3}\right|_{T=T_d} , \tag{6.91}$$

with

$$\delta s = \partial_T (P - P^{(0)}) \, . \tag{6.92}$$

In the above equation, we have approximated the entropy at positronium formation as $s_{\text{eq}} \simeq (11\pi^2/45)T^3$, effectively neglecting the electron mass.

Using the Hulthén potential and restricting ourselves to the $s$-wave contribution, we display the expected change in entropy in Fig. 6.10. In the left panel, we show again the cancellation between the attractive and repulsive scattering states, as measured by $\delta s$, while the right panel focuses on their total contribution. As expected, the perturbative $\mathcal{O}(e^2)$ Born contribution, which was already included in [549], dominate the total contribution to $\delta s$. Removing this contribution from the pressure, we display in blue the remaining correction to $\delta s$. Its impact on $N_{\text{eff}}^{\text{SM}}$ is of the same order as the $\mathcal{O}(e^4)$ relativistic correction computed in [549], i.e. $|\Delta N_{\text{eff}}| \sim \mathcal{O}(10^{-6})$. In order to verify if the change is completely perturbative, one should in principle also remove this $\mathcal{O}(e^4)$ correction from this blue line and confirm that the remaining $\Delta N_{\text{eff}}$ is suppressed by an additional factor of $\mathcal{O}(e^2)$.[28] This however goes beyond the scope of this work since non-relativistic limits need to be derived and compared consistently. Moreover, the corresponding change in $N_{\text{eff}}^{\text{SM}}$ is already tiny, well below the current uncertainty on the state-of-the-art theoretical benchmark derived in [543, 555, 556], which reduces the necessity to perform this analysis.

Beyond the entropy estimate (6.92), we also implemented this non-ideal correction (where we removed the Born contribution) into the continuity equation (6.9). Using the momentum-independent (momentum-dependent) neutrino QKEs, we observed an absolute impact on $N_{\text{eff}}^{\text{SM}}$ of approximately $-5.9\times 10^{-7}$ ($-2.7\times 10^{-7}$), consistent with the previous estimate. These results therefore indicates that bound states likely do not impact $N_{\text{eff}}^{\text{SM}}$ in a visible manner if no deviation from equilibrium is provided. Before concluding, we would however like to caution again that we only used the $s$-wave estimate in Fig. 6.10 and a proper estimate of the impact of higher partial waves remains to be done.[29] Moreover, the approach developed in this section completely neglected the Salpeter contribution to the electrostatic potential, its thermal width as well as deviations from the HTL form (6.67).

## 6.4 Conclusion and outlook

The effective number of neutrinos $N_{\text{eff}}$ serves as a crucial probe of the $\Lambda$CDM model and of physics beyond it. In view of the future cosmological experimental program, intensive theoretical efforts have been directed towards refining the theoretical prediction for its value within the SM and have converged towards the state-of-the-art result $N_{\text{eff}}^{\text{SM}} = 3.0440 \pm 0.0002$. In this work, we have considered the impact on this theoretical prediction of two previously unexplored effects:

---

[28] We note that the sign of the $\mathcal{O}(e^4)$-correction estimated in [549] is however positive, contrary to the $\mathcal{O}(e^4)$-correction in Fig. 6.10.

[29] In the Born case, higher partial waves contribute to the entropy by up to an order of magnitude.

1. NLO QED corrections to the weak neutrino-electron interaction rates, and

2. positronium formation.

Starting with the first aspect, we focused more specifically on the impact of the diagram of type (d), displayed in Fig. 6.4, which is expected to be $t$-channel enhanced and therefore dominate the NLO corrections. While similar NLO QED corrections were also investigated in [566–568], their results differ significantly. Specifically, [566] reported sizeable NLO corrections to the rates, sufficient to shift $N_{\text{eff}}^{\text{SM}}$ from 3.044 to 3.043, whereas Ref. [567] found much more moderate NLO corrections.

Contrary to [566], our first-principles calculations suggest that NLO QED corrections are modest. In the temperature range $T \sim 1 \to 3$ MeV, we find that corrections to the electron neutrino interaction rate range from $-0.2$ to $+0.1\%$ relative to the LO rate. These results are qualitatively consistent with those reported by Ref. [567], despite differences between the formalisms (imaginary versus real-time) and some approximations (vanishing versus finite $m_e$) used. Moreover, we also observe, in agreement with [567], a strong flavour dependence of these rates as the muon and tau neutrinos interaction rates are severely suppressed, ranging from $-0.0005$ to $+0.0002\%$ in the same temperature range.

Using these rates, we then proceeded to estimate the induced change in $N_{\text{eff}}^{\text{SM}}$. Employing different approximations (instantaneous decoupling versus solving momentum-(in)dependent Boltzmann equations in the damping approximation for the neutrino sector), we find that the resulting relative shift in $N_{\text{eff}}^{\text{SM}}$ ranges from $-1.1$ to $-0.5 \times 10^{-5}$, an order of magnitude below the uncertainty of the current benchmark. Therefore, even though we confirm the sign of the correction observed in [566], the relative change in $N_{\text{eff}}^{\text{SM}}$ we observe is a factor $\mathcal{O}(30)$ smaller than claimed in [566] and indicate that NLO corrections are unlikely to impact $N_{\text{eff}}^{\text{SM}}$ in any sizeable way. Interestingly, we also find that, because neutrino decoupling is not instantaneous, $N_{\text{eff}}^{\text{SM}}$ remains sensitive to some extent to the neutrino dynamics at $T \lesssim T_d$ and neglecting the finite electron mass in the NLO rates can lead to an enhancement of up to a factor of $2-3$ in the prediction for $\delta N_{\text{eff}}$.

Regarding the second aspect, we for the first time investigated the impact of positronium formation on $N_{\text{eff}}^{\text{SM}}$. Although a first-principles analysis of positronium properties and its impact on $N_{\text{eff}}^{\text{SM}}$ rooted in the CTP formalism would be desirable, it is at the moment extremely challenging. To assess whether such an effort is warranted, we restricted ourselves in this work to estimating $\Delta N_{\text{eff}}$ based on simple physical arguments, which mainly differ in their assumptions about the equilibrium nature of positronium formation as well as the rapidity with which it equilibrates. In order to systematically compare these different assumptions, we first adopt a simplified model of the QED bath, assuming it can effectively be described by a Yukawa potential that captures the screening of the electrostatic interaction due to the photon's thermal mass. In this approximation, positronium states have no width and can be treated as on-shell particles, for which it is possible to write a set of Boltzmann equations tracking their evolution.

We began by considering a scenario where positronium formation proceeds out of equilibrium, accompanied by a simultaneous generation of entropy. In this case, the impact of positronium on $N_{\text{eff}}^{\text{SM}}$ is primarily determined by its equilibration temperature $T_{\text{Ps}}^{\text{eq}}$. Assuming that positronium equilibrates instantaneously and that the total energy density is conserved during its formation, the expected change in $N_{\text{eff}}^{\text{SM}}$, $\Delta N_{\text{eff}}$, is displayed in blue as a function of $T_{\text{Ps}}^{\text{eq}}$ in Fig. 6.7. Identifying this equilibration temperature with the highest temperature at which the considered Yukawa potential can support bound states, i.e. $T_{\text{Ps}}^{\text{eq}} = T_D \simeq 75.6$ keV, would lead us to conclude that $|\Delta N_{\text{eff}}| \lesssim 10^{-4}$, a value smaller than the uncertainties in current precision calculations of $N_{\text{eff}}^{\text{SM}}$. It is however conceivable that positronium equilibration proceeds more gradually, e.g. because of its finite width. We mimic the resulting effect on $\Delta N_{\text{eff}}$ by adopting the ansatz (6.66), assuming that equilibration takes place symmetrically around $T_{\text{Ps}}^{\text{eq}}$ over a finite temperature range $\Delta T$. Because, in this parametrisation, a small positronium population is effectively present in the plasma at temperatures $T > T_{\text{Ps}}^{\text{eq}}$, a large transition parameter $\Delta T$ tends to drive up entropy production and, as a result, $\Delta N_{\text{eff}}$, compare e.g. the orange and blue lines in Fig. 6.7.

Alternatively, we also considered the possibility that positronium forms while the QED bath overall remains in complete thermodynamic equilibrium. In this limit, the change in $N_{\text{eff}}^{\text{SM}}$ is governed by the change in entropy at neutrino decoupling. Using the Beth-Uhlenbeck formula — a non-relativistic, non-perturbative expression for the pressure that consistently accounts for bound- and scattering-state contributions — we find, see Fig. 6.10, that the non-perturbative contribution from positronium formation is cancelled by that from resonant $e^+e^-$ scatterings. In particular, we found good agreement with the previously computed $O(e^2)$ thermodynamics quantities, even close to the bound-state formation threshold, indicating that perturbation theory remains reliable across the relevant temperature range. Given that the first unaccounted-for[30] contribution appears only at $\mathcal{O}(e^4)$, we concluded that, in the equilibrium scenario, the change in $N_{\text{eff}}^{\text{SM}}$ from the $s$-wave contribution should be limited to $|\Delta N_{\text{eff}}| \lesssim 10^{-6}$.

Because it only considers a real Yukawa potential, the discussion above does not account for modifications of positronium properties arising from real scatterings of photons with plasma constituents. In the static limit, this effect manifests as an imaginary component in the potential (6.67). In the out-of-equilibrium formation model, the evolution of positronium states cannot be described by Boltzmann equations in the regime where this imaginary contribution is important. We therefore assumed, as a first approximation, that the sole effect of this contribution is to lower the bound-state formation threshold. Under this assumption, the instantaneous equilibration scenario suggests $|\Delta N_{\text{eff}}| \simeq 3 \times 10^{-8}$, well below the hard Debye cut-off estimate, $|\Delta N_{\text{eff}}| \simeq 10^{-4}$. In the equilibrium case, however, no analogue of the Beth-Uhlenbeck formula exists for complex potentials. Hence, it is currently not possible to determine whether a similar cancellation between bound- and scattering-state contributions still occurs.

In conclusion, our results suggest that the SM benchmark value (6.3) remains correct within the quoted uncertainties. While numerically solving the momentum-dependent QKEs with a dedicated neutrino decoupling code — such as `FortEPiaNO` [511] — including all NLO contributions from diagrams (a) to (d) to the weak rates would be highly desirable to definitively conclude this discussion, we consider it unlikely that a more detailed investigation of NLO effects on the neutrino interaction rate would yield a deviation from the existing SM benchmark $N_{\text{eff}}^{\text{SM}}$ that is large enough to be of any relevance for cosmological observations in the foreseeable future, barring any new and previously unaccounted-for effects. Likewise, while many uncertainties remain on the modelling of positronium production, our current estimates suggest that the change in $N_{\text{eff}}^{\text{SM}}$ stemming from the formation of positronium is likely to be $10^{-4}$ or smaller, below other theoretical uncertainties and an order of magnitude smaller than the expected sensitivity of next-generation experiments such as CMB-S4.

[30] $\mathcal{O}(e^4)$ contributions have only been estimated in the $m_e \to 0$ limit in [549].

Chapter 7

# General conclusions and perspectives

Understanding the early universe and its evolutions requires a detailed understanding of its constituents. Particles indeed behave very differently in the hot, dense plasma of the early universe than they do in vacuum, and simulating their evolution requires dedicated tools such as the CTP formalism. The latter, in particular, can be used to describe a broad range of processes throughout the universe's history. It was the primary goal of this thesis to refine theoretical predictions for various cosmological processes using the CTP formalism, and subsequently examine the expected phenomenology – both in the early universe and at colliders – of a broad range of models. Specifically, we focused on three different processes, spanning epochs from the Planck scale down to the MeV scale:

1. Cosmological GW backgrounds emitted by feebly interacting hidden sectors in thermal equilibrium.
2. The generation of a matter-antimatter asymmetry by RH neutrinos through low-scale leptogenesis.
3. The decoupling of SM neutrinos from the QED plasma.

Starting in Chap. 2 with the first process, we investigated thermal GW backgrounds emitted by generic hidden sectors, which are expected to be enhanced for $f \ll 10^{11}$ Hz if these hidden sectors are feebly coupled. Using the CTP formalism, we derived analytical formulae for the expected strength of these GWBs, which allowed us to establish model-independent upper bounds on their magnitude. These bounds turned out to be highly constraining, severely limiting the prospects for detection. We also applied our results to two well-motivated benchmarks, right-handed neutrinos and axion-like particles. Although challenging in practice, we generally found that a potential measurements of thermal GW backgrounds would allow us to extract valuable information about the underlying particle physics model, such as the operator dimension, cut-off scale, or particle mass.

Next, in the second part of this thesis, we focused on RH neutrinos as a possible explanation for both neutrino masses and the observed baryon asymmetry of the universe.

On the theoretical side, in Chap. 4, we computed from first principles the interaction rates of generic fermions in Fermi-like theories. We then applied these results to the $\nu$MSM, where they are crucial for accurate predictions of the DM abundance, and to the mLRSM, where they are needed to predict the BAU through low-scale leptogenesis.

On the phenomenological side, we examined in Chap. 5 the testability of the type-I seesaw model with three generations of RH neutrinos. We focused on two distinct cases: 1) the vanilla type-I seesaw model, and 2) a type-I seesaw model endowed with flavour and CP symmetries. In the vanilla case, we showed that, despite the high dimensionality of the associated parameter space, future colliders could potentially produce a sufficient number of events to access some of the underlying model parameters, including low-energy quantities such as the lightest SM neutrino mass $m_0$. Moreover, we found that the parameter space consistent with the observed BAU is enhanced by orders of magnitude compared to the minimal scenario with 2 RH neutrino generations. We also demonstrated, though only for the $n_s = 2$ case, that next-generation $0\nu\beta\beta$ experiments will be able to place meaningful constraints on the leptogenesis parameter space. Taken together, these observations suggest that laboratory experiments may, in optimistic cases, observe enough events to test the hypothesis that RH neutrinos provide a common origin for neutrino masses and the matter-antimatter asymmetry of our universe. If the theory is further endowed with flavour and CP symmetries, its predictivity is significantly enhanced, while, at the same time, the parameter space consistent with leptogenesis is reduced. In such scenarios, measuring the HNL branching ratios into each flavour could be sufficient to distinguish between different incarnations of these flavour symmetries, or to access low-energy parameters such as $m_0$, the neutrino mass ordering or the CP phases.

Finally, in Chap. 6, we examined two finite-temperature effects that impact the SM prediction for the effective number of neutrinos, $N_{\text{eff}}^{\text{SM}}$. First, using the real-time formalism, we performed a partial computation of the NLO corrections to the neutrino-electron interaction rates. We concluded that the impact of these NLO corrections on $N_{\text{eff}}^{\text{SM}}$ is most likely smaller than the current theoretical uncertainty, and much smaller than existing experimental ones. We also investigated the expected corrections due to positronium formation, considering different phenomenological models to describe the process. While the magnitude of the expected $\Delta N_{\text{eff}}$ greatly varies between these models, our results suggest that the effect of positronium is likely subdominant compared to other theoretical uncertainties.

Looking forward, it would be desirable to expand these different research directions in several ways. Regarding the first part of this thesis, extending our results to scenarios beyond equilibrium or cosmologies beyond radiation domination would be extremely valuable. In particular, GW production could be largely enhanced during (p)reheating or in the case of e.g. early matter domination, thereby improving detection prospects. Regarding the second part, a more comprehensive analysis of the $n_s = 3$ leptogenesis parameter space would be highly beneficial. At the level of the formalism, it is also expected that the set of quantum kinetic equations should be modified in the presence of HNL self-interactions. Deriving these corrections from first principles would be particularly helpful to properly describe the phenomenology of models such as the mLRSM. Finally, a complete estimate of the impact on $N_{\text{eff}}^{\text{SM}}$ from NLO QED corrections to the rates, consistently including the contributions of all diagrams, is still lacking. Moreover, the CTP formalism would also be ideally suited to extend our computations to various BSM models, such as light and feebly interacting DM candidates.

THE END.

PIPPIN: *I didn't think it would end this way.*

GANDALF: *End? No, the journey doesn't end here.* ~~*Death*~~ *The PhD thesis is just another path, one that we all must take. The grey rain-curtain of this world rolls back, and all turns to silver glass, and then you see it.*

PIPPIN: *What? Gandalf? See what?*

GANDALF: *White shores, and beyond, a far green country under a swift sunrise.*

PIPPIN: *Well, that isn't so bad.*

GANDALF: *No. No, it isn't.*

(Slightly) adapted from J.R.R. Tolkien, *The Lord of the Rings*

Appendix A

# Collection of results regarding gravitational wave backgrounds from hidden sectors

In this appendix, we collect different useful results concerning Chap. 2. We first discuss the general form of spectral functions at finite temperature in Sec. A.1 before displaying in Sec. A.2 additional formulae for the expected GW background from non-renormalisable interactions.

## A.1 Finite-temperature spectral function

In thermodynamic equilibrium, one can show, see e.g. [607], that the spectral function of a massive Dirac or Majorana fermion $\psi$ is exactly given by

$$S_p^{\mathcal{A}} \equiv \frac{i}{2}\left(S_p^R - S_p^A\right) = \frac{i}{2}\left(\frac{1}{\not{p} - m - \Sigma_p^H + i\Sigma_p^{\mathcal{A}}} - \frac{1}{\not{p} - m - \Sigma_p^H - i\Sigma_p^{\mathcal{A}}}\right) , \tag{A.1}$$

where, as defined in Chap. 1, $S_p^R$ and $S_p^A$ are the retarded and advanced propagators of $\psi$ and $\Sigma_p^H$ and $\Sigma_p^{\mathcal{A}}$ are its (anti-)hermitian self-energies. These self-energies only depend on the momentum $p$ as well as the plasma 4-velocity $u$ $(= (1, \mathbf{0})$ in its rest frame). Given that the set of 16 $4 \times 4$ matrices $\{\mathbb{1}, \gamma^5, \gamma^\mu, \gamma^\mu\gamma^5, \frac{i}{2}[\gamma^\mu, \gamma^\nu]\}$ forms a basis, $\Sigma_p^H$ and $\Sigma_p^{\mathcal{A}}$ can in full generality be decomposed in the plasma 4-velocity rest frame as

$$\Sigma_p^{\mathcal{X}} = \frac{\left(\sigma_1^{\mathcal{X}}\,\not{p} + \tilde{\sigma}_1^{\mathcal{X}}\,\not{\tilde{p}}\right)\mathbb{1} + \left(\sigma_5^{\mathcal{X}}\,\not{p} + \tilde{\sigma}_5^{\mathcal{X}}\,\not{\tilde{p}}\right)\gamma_5}{p^2} + \delta_1^{\mathcal{X}}\,\mathbb{1} + \delta_5^{\mathcal{X}}\gamma_5 \ , \quad \tilde{p}^\mu = (|\boldsymbol{p}|, p_0\frac{\boldsymbol{p}}{|\boldsymbol{p}|}) \ , \tag{A.2}$$

where $\mathcal{X} \in \{\mathcal{A}, H\}$ and $\tilde{p}^\mu$ is defined[1] such that $\tilde{p}^2 = -p^2$ and $\tilde{p}p = 0$. One can verify that $p^\mu$ and $\tilde{p}^\mu$ are linearly independent and span the space of four-vectors with spatial

[1]Instead of $\{p, \tilde{p}\}$, another common choice, which we will use in the later chapters of this thesis, is to decompose the self-energy using the set of vectors $\{p, u\}$.

part parallel to $\boldsymbol{p}$. The scalar coefficients appearing in Eq. (A.2) can straightforwardly be extracted from the traces

$$\sigma_i^{\mathcal{X}} = \frac{1}{4}\,\mathrm{Tr}\left[P_i \not{p}\,\Sigma_p^{\mathcal{X}}\right],\ \tilde{\sigma}_i^{\mathcal{X}} = -\frac{1}{4}\,\mathrm{Tr}\left[P_i \tilde{\not{p}}\,\Sigma_p^{\mathcal{X}}\right],\ \delta_i^{\mathcal{X}} = \frac{1}{4}\,\mathrm{Tr}\left[P_i \Sigma_p^{\mathcal{X}}\right], \tag{A.3}$$

with

$$P_5 = \gamma_5\,, \qquad\qquad P_1 = \mathbb{1}. \tag{A.4}$$

Using the decomposition (A.2), we can recast the advanced and retarded propagators as

$$S_p^{A,R} = \left(\not{p} + m - \overline{\Sigma}_p^{\mathcal{H}} \mp i\overline{\Sigma}_p^{\mathcal{A}}\right)\frac{1}{\Omega_p \mp i\Gamma_p}\,, \qquad \overline{\Sigma}_p^{\mathcal{X}} = \Sigma_p^{\mathcal{X}} - 2\delta_1^{\mathcal{X}}\mathbb{1}. \tag{A.5}$$

The functions $\Omega_p$ and $\Gamma_p$ are defined as

$$\begin{aligned} p^2\Omega_p \equiv{}& (p^2 - \sigma_1^H)^2 - \sigma_1^{\mathcal{A}\,2} - \tilde{\sigma}_1^{H\,2} + \tilde{\sigma}_1^{\mathcal{A}\,2} - \sigma_5^{H\,2} + \sigma_5^{\mathcal{A}\,2} + \tilde{\sigma}_5^{H\,2} - \tilde{\sigma}_5^{\mathcal{A}\,2} \\ & - p^2[(m + \delta_1^H)^2 - \delta_1^{\mathcal{A}\,,2} - \delta_5^{H\,2} + \delta_5^{\mathcal{A}\,2}]\,, \end{aligned} \tag{A.6a}$$

$$p^2\Gamma_p \equiv 2\left[(p^2 - \sigma_1^{\mathcal{H}})\sigma_1^{\mathcal{A}} + \tilde{\sigma}_1^{\mathcal{H}}\tilde{\sigma}_1^{\mathcal{A}} + \sigma_5^{\mathcal{H}}\sigma_5^{\mathcal{A}} - \tilde{\sigma}_5^{\mathcal{H}}\tilde{\sigma}_5^{\mathcal{A}}\right] + 2p^2[\delta_1^{\mathcal{A}}(m + \delta_1^{\mathcal{H}}) - \delta_5^{\mathcal{H}}\delta_5^{\mathcal{A}}]\,. \tag{A.6b}$$

Hence, plugging Eq. (A.2) into the spectral function (A.1), the latter becomes

$$S_p^{\mathcal{A}} = \left(\not{p} + m - \overline{\Sigma}_p^{\mathcal{H}}\right)\Delta_p - \overline{\Sigma}_p^{\mathcal{A}}\Pi_p\,, \tag{A.7}$$

where

$$\Delta_p = \frac{\Gamma_p}{\Omega_p^2 + \Gamma_p^2}\,, \qquad\qquad \Pi_p = \frac{\Omega_p}{\Omega_p^2 + \Gamma_p^2}\,. \tag{A.8}$$

The location of the particle mass shell can be determined by solving $\Omega_p = 0$, whereas the parameter $\Gamma_p = \mathrm{Tr}\left[(\not{p} + m)\Sigma_p^{\mathcal{A}}\right]/4$ is proportional to the finite-temperature width $\Upsilon_{\mathrm{p}}$ of the particle. In the absence of interactions, $\Gamma_p \to 0$, and one recovers the expected behaviour

$$\Delta_p \to \pi\delta(\Omega_p)\,, \qquad\qquad \Pi_p \to \mathcal{P}\left(\frac{1}{\Omega_p}\right)\,, \tag{A.9}$$

where $\mathcal{P}\,(\cdot)$ denotes the Cauchy principal value. Eq. (A.9) highlights the well-known fact that the term $\propto \Delta_p$ encodes the propagation of single-particle excitations, including both quasiparticle and hole modes. On the other hand, $\Pi_p$ encodes the effect of scatterings mediated by these modes. Given that we focus in this work on the case of feebly interacting particles, we can approximate $S_p^{\mathcal{A}}$ as

$$S_p^{\mathcal{A}} = (\not{p} + m)\Delta_p + \mathcal{O}(\Sigma^2)\,. \tag{A.10}$$

Similarly, it is justified in this limit to retain only the leading order, in the (feeble) coupling, contributions to $\Omega_p$ and $\Gamma_p$

$$\Omega_p = p^2 - m^2 \,, \qquad\qquad \Gamma_p = 2\left(\sigma_1^{\mathcal{A}} + m\,\delta_1^{\mathcal{A}}\right) + \mathcal{O}(\Sigma^2)\,, \tag{A.11}$$

thereby recovering the result of Eq (2.34). Effectively, Eq. (A.11) neglects the contribution from hole modes. This approximation is however justified since the integral (2.31) is dominated by hard momenta $|\boldsymbol{p}| \sim \pi T$, where the residues associated with hole-modes are exponentially suppressed [28]. In addition, we note that, for large enough temperature, quasiparticles develop a thermal mass $\propto gT$ that can significantly exceed the tree-level mass $m$ and is not captured by the expression (A.11). However, this thermal mass always remains much smaller than the typical hard momenta $|\boldsymbol{p}| \sim \pi T$, and we therefore do not expect it to visibly affect our results. As a side remark, we also note the similarity between Eq. (A.7) and the $++$-component of the resummed photon propagator derived exactly in Sec. D.3.2, see Eq. (D.55).

## A.2 Supplementary formulae for GW backgrounds from non-renormalisable interactions

In this appendix, we derive in more detail the present-day GWB from hidden particles whose width is dominated by non-renormalisable interactions. To keep the results simple, we approximate the production rate (2.50) as

$$\Pi(k) \overset{m \lll T}{\simeq} g_X \frac{16\pi^2}{225} T^5 \begin{cases} 1/2\Upsilon_{\text{av}} & T > T_c \\ 5\Upsilon_{\text{av}}/k^2 & T < T_c \end{cases} . \tag{A.12}$$

Since the GW production in the non-renormalisable case is typically dominated by temperatures $T \simeq T_c$, we expect this approximation to lead to at most an $\mathcal{O}(1)$ error on the final result. We then compute the high-temperature background by inserting the approximation (A.12) along with the expression (2.64) (assuming $d > 4$) for the width into the integral (2.21) and setting $T_{\text{min}} \to m$. The hydrodynamic contribution takes the form

$$h^2\Omega_{\text{GW}}^{T>m}(f) \overset{\text{Hydro}}{\simeq} g_d^- \left(\frac{f}{\text{Hz}}\right)^2 \left[\min\left(\frac{f\,m}{f_{\text{hyd}}\,m_{\text{Pl}}}, \frac{T_c}{m_{\text{Pl}}}\right) - \min\left(\frac{f\,T_{\text{max}}}{f_{\text{max}}\,m_{\text{Pl}}}, \frac{T_c}{m_{\text{Pl}}}\right)\right] , \tag{A.13}$$

whereas the Boltzmann contribution reads

$$h^2\Omega_{\text{GW}}^{T>m}(f) \overset{\text{Boltz.}}{\simeq} g_d^+ \left(\frac{f}{\text{Hz}}\right)^2 \left[\min\left(\frac{f_{\text{max}}\,T_{\text{max}}}{f\,m_{\text{Pl}}}, \frac{T_c}{m_{\text{Pl}}}\right) - \min\left(\frac{f_{\text{hyd}}\,m}{f\,m_{\text{Pl}}}, \frac{T_c}{m_{\text{Pl}}}\right)\right] . \tag{A.14}$$

In the above equations, we defined

$$g_d^{\pm} = \frac{5.3\, g_X \times 10^{-29}}{2(d-4) \pm 1} \ , \quad T_{\max} = \max\left(m, \min\left(T_{\text{entry}}, T_\star\right)\right) \ , \quad f_{\max} = f_c \left(\frac{T_{\max}}{\Lambda}\right)^{2(d-4)} \ . \tag{A.15}$$

The complete GWB is then obtained by summing these two contributions

$$h^2\Omega_{\text{GW}}^{T>m}(f) \simeq g_d^+ \left(\frac{f}{\text{Hz}}\right)^2 \begin{cases} \frac{g_d^-}{g_d^+}\left(\frac{f\, m}{f_{\text{hyd}} m_{\text{Pl}}} - \frac{f\, T_{\max}}{f_{\max}\, m_{\text{Pl}}}\right) & f_{\text{hyd}} > f \\ \left(\frac{T_c}{m_{\text{Pl}}} - \frac{f_{\text{hyd}}\, m}{f\, m_{\text{Pl}}}\right) + \frac{g_d^-}{g_d^+}\left(\frac{T_c}{m_{\text{Pl}}} - \frac{f\, T_{\max}}{f_{\max}\, m_{\text{Pl}}}\right) & f_{\text{hyd}} < f < f_{\max} \\ \left(\frac{f_{\max}\, T_{\max}}{f\, m_{\text{Pl}}} - \frac{f_{\text{hyd}}\, m}{f\, m_{\text{Pl}}}\right) & f_{\max} < f \end{cases} \ . \tag{A.16}$$

In many realistic scenarios, hierarchies exist between the different problem scales, e.g. $m \ll T_{\max}$ or, equivalently, $f_{\text{hyd}} \ll f_{\max}$. In the following, we will hence focus on such cases. Retaining only the leading terms for each regime, we can then further simplify Eq. (A.16) into

$$h^2\Omega_{\text{GW}}^{T>m}(f) \simeq g_d^+ \left(\frac{f}{\text{Hz}}\right)^2 \begin{cases} \frac{g_d^-}{g_d^+}\frac{f\, m}{f_{\text{hyd}} m_{\text{Pl}}} & f_{\text{hyd}} > f \\ \left(1 + \frac{g_d^-}{g_d^+}\right)\frac{T_c}{m_{\text{Pl}}} & f_{\text{hyd}} < f < f_{\max} \\ \frac{f_{\max}\, T_{\max}}{f\, m_{\text{Pl}}} & f_{\max} < f \end{cases} \ . \tag{A.17}$$

From (A.15), it follows

$$f_{\max} = \begin{cases} f_{\text{hyd}} & f < f_{\text{nr}} \\ f_{\text{int}} & f_{\text{nr}} < f < f_\star \\ f_{\text{bol}} & f_\star < f \end{cases} \ , \tag{A.18}$$

with the crossing frequency $f_x$ defined in (2.72) and

$$f_{\text{int}} \equiv f_x \left(\frac{f}{f_x}\right)^{2(d-4)} = \frac{f}{f_c}\left(\frac{\pi m_0}{f_{\text{peak}}\Lambda}\right)^{2(d-4)} \ . \tag{A.19}$$

One can also easily verify the following properties

$$f_{\text{hyd}} < f_{\max} < f_{\text{bol}} \ , \quad f_{\text{hyd}} = f_x \left(\frac{f_{\text{nr}}}{f_x}\right)^{2(d-4)} \ , \quad f_{\text{bol}} = f_x \left(\frac{f_\star}{f_x}\right)^{2(d-4)} \ . \tag{A.20}$$

We note that the high-temperature contribution to the thermal GWB vanishes for $f < f_{\text{nr}}$ since the temperature at horizon entry lies below the hidden particle's mass. Therefore, we will solely focus on frequencies larger than $f_{\text{nr}}$. One can distinguish four separate cases:

**Case 1:** This case is defined by the hierarchy $f_{\rm hyd} < f_{\rm nr}, f_{\rm bol} < f_\star$. The GW spectrum takes the form

$$h^2\Omega_{\rm GW}^{T\geq m}(f) \simeq g_d^+ \left(\frac{f}{\rm Hz}\right)^2 \begin{cases} \left(\frac{f_{\rm int}\, T_{\rm entry}}{f\, m_{\rm Pl}} - \frac{f_{\rm hyd}\, m}{f\, m_{\rm Pl}}\right) & f_{\rm nr} < f < f_\star \\ \left(\frac{f_{\rm bol}\, T_\star}{f\, m_{\rm Pl}} - \frac{f_{\rm hyd}\, m}{f\, m_{\rm Pl}}\right) & f_\star < f \end{cases} . \tag{A.21}$$

Keeping only the leading terms, one has

$$h^2\Omega_{\rm GW}^{T\geq m}(f) \simeq g_d^+ \left(\frac{f}{\rm Hz}\right)^2 \begin{cases} \frac{f_{\rm int}\, T_{\rm entry}}{f\, m_{\rm Pl}} & f_{\rm nr} < f < f_\star \\ \frac{f_{\rm bol}\, T_\star}{f\, m_{\rm Pl}} & f_\star < f \end{cases} . \tag{A.22}$$

Using the definition (A.19) of $f_{\rm int}$ and expressing $T_{\rm entry}$, $T_\star$ in terms of $f_\star$, one can then recover Eq. (2.75). Similar reasoning applies to the remaining cases.

**Case 2:** This case is defined by the hierarchy $f_{\rm hyd} < f_{\rm nr} < f_\star < f_{\rm bol}$. The GW spectrum takes the form

$$h^2\Omega_{\rm GW}^{T\geq m}(f) \simeq g_d^+ \left(\frac{f}{\rm Hz}\right)^2 \begin{cases} \left(\frac{f_{\rm int}\, T_{\rm entry}}{f\, m_{\rm Pl}} - \frac{f_{\rm hyd}\, m}{f\, m_{\rm Pl}}\right) & f_{\rm nr} < f < f_x \\ \left(\frac{T_c}{m_{\rm Pl}} - \frac{f_{\rm hyd}\, m}{f\, m_{\rm Pl}}\right) + \frac{g_d^-}{g_d^+}\left(\frac{T_c}{m_{\rm Pl}} - \frac{f\, T_{\rm entry}}{f_{\rm int}\, m_{\rm Pl}}\right) & f_x < f < f_\star \\ \left(\frac{T_c}{m_{\rm Pl}} - \frac{f_{\rm hyd}\, m}{f\, m_{\rm Pl}}\right) + \frac{g_d^-}{g_d^+}\left(\frac{T_c}{m_{\rm Pl}} - \frac{f\, T_\star}{f_{\rm bol}\, m_{\rm Pl}}\right) & f_\star < f < f_{\rm bol} \\ \left(\frac{f_{\rm bol}\, T_\star}{f\, m_{\rm Pl}} - \frac{f_{\rm hyd}\, m}{f\, m_{\rm Pl}}\right) & f_{\rm bol} < f \end{cases} . \tag{A.23}$$

Keeping only the leading terms, one has

$$h^2\Omega_{\rm GW}^{T\geq m}(f) \simeq g_d^+ \left(\frac{f}{\rm Hz}\right)^2 \begin{cases} \frac{f_{\rm int}\, T_{\rm entry}}{f\, m_{\rm Pl}} & f_{\rm nr} < f < f_x \\ \left(1 + \frac{g_d^-}{g_d^+}\right)\frac{T_c}{m_{\rm Pl}} & f_x < f < f_{\rm bol} \\ \frac{f_{\rm bol}\, T_\star}{f\, m_{\rm Pl}} & f_{\rm bol} < f \end{cases} . \tag{A.24}$$

**Case 3:** This case is defined by the hierarchy $f_{\rm nr} < f_{\rm hyd} < f_\star < f_{\rm bol}$. The GW spectrum takes the form

$$h^2\Omega_{\rm GW}^{T\geq m}(f) \simeq g_d^+ \left(\frac{f}{\rm Hz}\right)^2 \begin{cases} \frac{g_d^-}{g_d^+}\left(\frac{f\, m}{f_{\rm hyd} m_{\rm Pl}} - \frac{f\, T_{\rm entry}}{f_{\rm int}\, m_{\rm Pl}}\right) & f_{\rm nr} < f < f_{\rm hyd} \\ \left(\frac{T_c}{m_{\rm Pl}} - \frac{f_{\rm hyd}\, m}{f\, m_{\rm Pl}}\right) + \frac{g_d^-}{g_d^+}\left(\frac{T_c}{m_{\rm Pl}} - \frac{f\, T_{\rm entry}}{f_{\rm int}\, m_{\rm Pl}}\right) & f_{\rm hyd} < f < f_\star \\ \left(\frac{T_c}{m_{\rm Pl}} - \frac{f_{\rm hyd}\, m}{f\, m_{\rm Pl}}\right) + \frac{g_d^-}{g_d^+}\left(\frac{T_c}{m_{\rm Pl}} - \frac{f\, T_\star}{f_{\rm bol}\, m_{\rm Pl}}\right) & f_\star < f < f_{\rm bol} \\ \left(\frac{f_{\rm bol}\, T_\star}{f\, m_{\rm Pl}} - \frac{f_{\rm hyd}\, m}{f\, m_{\rm Pl}}\right) & f_{\rm bol} < f \end{cases} . \tag{A.25}$$

Keeping only the leading terms, one has

$$h^2\Omega_{\rm GW}^{T>m}(f) \simeq g_d^+ \left(\frac{f}{\rm Hz}\right)^2 \begin{cases} \frac{g_d^-}{g_d^+}\frac{f\,m}{f_{\rm hyd}m_{\rm Pl}} & f_{\rm nr} < f < f_{\rm hyd} \\ \left(1+\frac{g_d^-}{g_d^+}\right)\frac{T_c}{m_{\rm Pl}} & f_{\rm hyd} < f < f_{\rm bol} \\ \frac{f_{\rm bol}\,T_\star}{f\,m_{\rm Pl}} & f_{\rm bol} < f \end{cases} . \tag{A.26}$$

**Case 4:** This case is defined by the hierarchy $f_{\rm nr} < f_\star < f_{\rm hyd} < f_{\rm bol}$. The GW spectrum takes the form

$$h^2\Omega_{\rm GW}^{T>m}(f) \simeq g_d^+ \left(\frac{f}{\rm Hz}\right)^2 \begin{cases} \frac{g_d^-}{g_d^+}\left(\frac{f\,m}{f_{\rm hyd}m_{\rm Pl}} - \frac{f\,T_{\rm entry}}{f_{\rm int}\,m_{\rm Pl}}\right) & f_{\rm nr} < f < f_\star \\ \frac{g_d^-}{g_d^+}\left(\frac{f\,m}{f_{\rm hyd}m_{\rm Pl}} - \frac{f\,T_\star}{f_{\rm bol}\,m_{\rm Pl}}\right) & f_\star < f < f_{\rm hyd} \\ \left(\frac{T_c}{m_{\rm Pl}} - \frac{f_{\rm hyd}\,m}{f\,m_{\rm Pl}}\right) + \frac{g_d^-}{g_d^+}\left(\frac{T_c}{m_{\rm Pl}} - \frac{f\,T_\star}{f_{\rm bol}\,m_{\rm Pl}}\right) & f_{\rm hyd} < f < f_{\rm bol} \\ \left(\frac{f_{\rm bol}\,T_\star}{f\,m_{\rm Pl}} - \frac{f_{\rm hyd}\,m}{f\,m_{\rm Pl}}\right) & f_{\rm bol} < f \end{cases} . \tag{A.27}$$

Keeping only the leading terms, one has

$$h^2\Omega_{\rm GW}^{T>m}(f) \simeq g_d^+ \left(\frac{f}{\rm Hz}\right)^2 \begin{cases} \frac{g_d^-}{g_d^+}\frac{f\,m}{f_{\rm hyd}m_{\rm Pl}} & f_{\rm nr} < f < f_{\rm hyd} \\ \left(1+\frac{g_d^-}{g_d^+}\right)\frac{T_c}{m_{\rm Pl}} & f_{\rm hyd} < f < f_{\rm bol} \\ \frac{f_{\rm bol}\,T_\star}{f\,m_{\rm Pl}} & f_{\rm bol} < f \end{cases} . \tag{A.28}$$

Notice that this expression is the same as Eq. (A.26).

Considering the limit of a massless hidden particle, where $f_{\rm hyd}, f_{\rm nr} \to 0$, only two cases survive:

**Case 1:** In this limit, the GW spectrum simplifies to

$$h^2\Omega_{\rm GW}^{T>m}(f) \simeq g_d^+ \left(\frac{f}{\rm Hz}\right)^2 \begin{cases} \frac{f_{\rm int}\,T_{\rm entry}}{f\,m_{\rm Pl}} & f < f_\star \\ \frac{f_{\rm bol}\,T_\star}{f\,m_{\rm Pl}} & f_\star < f \end{cases} . \tag{A.29}$$

**Case 2:** In this limit, the GW spectrum can be written

$$h^2\Omega_{\rm GW}^{T>m}(f) \simeq g_d^+ \left(\frac{f}{\rm Hz}\right)^2 \begin{cases} \frac{f_{\rm int}\,T_{\rm entry}}{f\,m_{\rm Pl}} & f < f_x \\ \frac{T_c}{m_{\rm Pl}} + \frac{g_d^-}{g_d^+}\left(\frac{T_c}{m_{\rm Pl}} - \frac{f\,T_{\rm entry}}{f_{\rm int}\,m_{\rm Pl}}\right) & f_x < f < f_\star \\ \frac{T_c}{m_{\rm Pl}} + \frac{g_d^-}{g_d^+}\left(\frac{T_c}{m_{\rm Pl}} - \frac{f\,T_\star}{f_{\rm bol}\,m_{\rm Pl}}\right) & f_\star < f < f_{\rm bol} \\ \frac{f_{\rm bol}\,T_\star}{f\,m_{\rm Pl}} & f_{\rm bol} < f \end{cases} . \tag{A.30}$$

Appendix B

# Three-particle phase space integration

In this appendix, we detail the parametrisation used in part II and III of this thesis to compute various 4-fermion interaction rates. This parametrisation is particularly useful to reduce the original 9-dimensional integral to only three dimensions and was used to compute the rates in Chaps. 4 and 6.2.2. It was already developed in appendices A and B of [401], which we will here closely follow.

In order to compute interaction rates arising from 4-fermion contact interactions, one generically needs to evaluate terms of the form

$$\int \frac{\mathrm{d}^3\boldsymbol{p}_1 \mathrm{d}^3\boldsymbol{p}_2 \mathrm{d}^3\boldsymbol{p}_3}{(2\pi)^9} \frac{(2\pi)^4 \delta^{(4)}(q - p_1 - p_2 - p_3)}{8E_1 E_2 E_3} \mathcal{F}\left[u, p_1, p_2, p_3, q\right] \,, \tag{B.1}$$

where $\mathcal{F}\left[u, p_1, p_2, p_3, q\right]$ consists of a Lorentz-invariant trace $\mathcal{T}\left[p_1, p_2, p_3, q\right]$, see Eq. (4.9) for an example, and a product of distribution functions $f_i$, e.g.

$$\mathcal{F}\left[u, p_1, p_2, p_3, q\right] \supset \mathcal{T}\left[p_1, p_2, p_3, q\right] f_1(E_1) f_2(E_2) f_3(E_3). \tag{B.2}$$

In the above equations, $q$ is the momentum of the particle whose interaction rate we are computing and $u$ is the plasma 4-velocity. $E_i \equiv p_i \cdot u$ is the energy associated with particle $i$ and reduces to $\sqrt{\boldsymbol{p}_i^2 + m_i^2}$ in the plasma rest frame. However, if we instead keep the frame general, the expression (B.1) is completely Lorentz-invariant. In that case, one can therefore boost every momentum in the rest frame of $p_3 - q$, i.e. the frame for which $\hat{\boldsymbol{p}}_3 - \hat{\boldsymbol{q}} = \Lambda_{p_3 - q}(\boldsymbol{p}_3 - \boldsymbol{q}) = 0$. We will denote quantities in this frame with a hat $\hat{p} = \Lambda_{p_3 - q} p$ for any $p$. Performing this Lorentz boost on the Lorentz-invariant subpart of the integral (B.1) containing $p_1$ and $p_2$ allows us to rewrite it as

$$\int \mathrm{d}^3\boldsymbol{p}_3 \int \frac{\mathrm{d}^3\hat{\boldsymbol{p}}_1 \mathrm{d}^3\hat{\boldsymbol{p}}_2}{(2\pi)^9} \frac{(2\pi)^4 \delta^{(3)}(\hat{\boldsymbol{p}}_1 + \hat{\boldsymbol{p}}_2) \delta(\hat{E}_q - \hat{E}_1 - \hat{E}_2 - \hat{E}_3)}{8\hat{E}_1 \hat{E}_2 \hat{E}_3} \mathcal{F}\left[\hat{u}, \hat{p}_1, \hat{p}_2, \hat{p}_3, \hat{q}\right] . \tag{B.3}$$

It is now straightforward to perform the integral over $\hat{\boldsymbol{p}}_2$

$$\int \frac{\mathrm{d}^3\boldsymbol{p}_3}{(2\pi)^3 2E_3} \int \frac{\mathrm{d}^3\hat{\boldsymbol{p}}_1}{(2\pi)^2} \frac{\delta(\hat{E}_q - \sqrt{\hat{p}_1^2 + m_1^2} - \sqrt{\hat{p}_1^2 + m_2^2} - \hat{E}_3)}{4\sqrt{\hat{p}_1^2 + m_1^2}\sqrt{\hat{p}_1^2 + m_2^2}} \times \\ \times \mathcal{F}\left[\hat{u}, \hat{p}_1, (\sqrt{\hat{p}_1^2 + m_2^2}, -\hat{p}_1), \hat{p}_3, \hat{q}\right]. \quad \text{(B.4)}$$

We will then use the last $\delta$ distribution to perform the integration over $|\hat{\boldsymbol{p}}_1|$. We start by observing that $\sqrt{x^2 + m_1^2} + \sqrt{x^2 + m_2^2} = E$ for

$$|\hat{\boldsymbol{p}}_1| = \lambda_{12}(E) \equiv \frac{1}{2E}\sqrt{E^4 - 2E^2(m_1^2 + m_2^2) + (m_1^2 - m_2^2)^2} \quad \text{(B.5)}$$

as long as $E > m_1 + m_2$. This implies

$$\int \mathrm{d}x \frac{x^2 h(x)}{\sqrt{x^2 + m_1^2}\sqrt{x^2 + m_2^2}} \delta(\sqrt{x^2 + m_1^2} + \sqrt{x^2 + m_2^2} - E) \\ = \Theta(E - m_1 - m_2) \frac{\lambda_{12}(E) h(\lambda_{12}(E))}{E}. \quad \text{(B.6)}$$

Identifying $E = \hat{E}_q - \hat{E}_3$, we can then simplify Eq. (B.4) as

$$\int \frac{\mathrm{d}^3\boldsymbol{p}_3}{(2\pi)^3 2E_3} \int \frac{\mathrm{d}\cos\hat{\theta}_1 \mathrm{d}\varphi_1}{(4\pi)^2} \frac{\lambda_{12}(\hat{E}_q - \hat{E}_3)}{\hat{E}_q - \hat{E}_3} \Theta(\hat{E}_q - \hat{E}_3 - m_1 - m_2) \times \\ \times \mathcal{F}\left[\hat{u}, \hat{p}_1, (\sqrt{\hat{p}_1^2 + m_2^2}, -\hat{p}_1), \hat{p}_3, \hat{q}\right]. \quad \text{(B.7)}$$

In $\mathcal{F}$, we set $|\hat{\boldsymbol{p}}_1| = \lambda_{12}(\hat{E}_q - \hat{E}_3)$ (but do not write it explicitly to keep expressions compact). To further simplify this result, we can then analytically perform the integration over the angular part of $\mathrm{d}^3\boldsymbol{p}_3 = \boldsymbol{p}_3^2 \mathrm{d}|\boldsymbol{p}_3| \mathrm{d}\cos\theta_3 \mathrm{d}\varphi_3$. Given that our universe is isotropic, one can choose $\boldsymbol{q}$ to be aligned with the z-axis and $\boldsymbol{p}_3$ to lie in the $x - z$ plane, i.e. $\boldsymbol{q} = |\boldsymbol{q}|(0, 0, 1)$ and $\boldsymbol{p}_3 = |\boldsymbol{p}_3|(\sin\theta_3, 0, \cos\theta_3)$. As it is independent of $\varphi_3$, this integration leads to an overall factor $2\pi$. Moreover, since $\mathcal{F}$ depends (at tree level) at best quadratically on $p_1$, one can show that it can be parametrised as

$$\mathcal{F}\left[\hat{u}, \hat{p}_1, (\sqrt{\hat{p}_1^2 + m_2^2}, -\hat{p}_1), \hat{p}_3, \hat{q}\right] = \alpha + \beta\cos\varphi_1 + \gamma\cos\varphi_1^2. \quad \text{(B.8)}$$

This in turns implies that

$$\int_0^{2\pi} \mathrm{d}\varphi_1 \mathcal{F}\left[\hat{u}, \hat{p}_1, (\sqrt{\hat{p}_1^2 + m_2^2}, -\hat{p}_1), \hat{p}_3, \hat{q}\right] = \pi\left[\mathcal{F}(\varphi_1 = \pi/4) + \mathcal{F}(\varphi_1 = 3\pi/4)\right]. \quad \text{(B.9)}$$

Combining these results, we finally obtain that

$$\int \frac{\mathrm{d}|\boldsymbol{p}_3|\mathrm{d}\cos\theta_3\mathrm{d}\cos\hat{\theta}_1}{128\pi^3 E_3} \frac{\lambda_{12}(\hat{E}_q - \hat{E}_3)}{\hat{E}_q - \hat{E}_3} \Theta(\hat{E}_q - \hat{E}_3 - m_1 - m_2) \times \\ \times \left[\mathcal{F}(\varphi_1 = \pi/4) + \mathcal{F}(\varphi_1 = 3\pi/4)\right]. \quad \text{(B.10)}$$

Two comments are now in order regarding the validity of Eq. (B.10). First, though Eq. (B.1) strictly only applies to the case of $1 \to 3$ decays, it is straightforward to adapt this parametrisation to different kinematic situations by boosting to a different rest frame, e.g. the rest frame of $p_3 + q$, and replacing $E = \hat{E}_q - \hat{E}_3$ accordingly. Second, the property (B.8) only holds at tree level. If one includes loop corrections as studied in Chap. 6, the dependence on $\varphi_1$ can be different and one needs to perform the integral numerically.

Appendix C

# Explicit formulae for the adimensional functions $\mathcal{I}_{\pm}$, $\mathcal{J}_{\pm}, \mathcal{K}, \mathcal{L}$ and the heavy fermion interaction rates

In this appendix, we provide explicit expression for the functions $\mathcal{I}_{\pm}$, $\mathcal{J}_{\pm}$, $\mathcal{K}$ and $\mathcal{L}$ used as building blocks for the self-energies (4.12a), (4.12b), (4.14) and (4.15). The first 2 functions, $\mathcal{I}_{\pm}$ and $\mathcal{J}_{\pm}$, can be expressed as

$$\begin{aligned}
\mathcal{I}_{\pm}(m_1, m_2, m_3) = &\frac{1}{T^5} 32\pi^4 f_{\rm F}^{-1}(-q_0) \int \frac{\mathrm{d}^3\mathbf{p}_1}{(2\pi)^3 2E_1} \int \frac{\mathrm{d}^3\mathbf{p}_2}{(2\pi)^3 2E_2} \int \frac{\mathrm{d}^3\mathbf{p}_3}{(2\pi)^3 2E_3} \times \\
&\times \Big[\delta^{(4)}(p_1+p_2+p_3-q)\,(1-f_{\rm F}(E_1))\,(1-f_{\rm F}(E_2))\,(1-f_{\rm F}(E_3)) \\
&\qquad + \delta^{(4)}(p_1+p_2-p_3-q)\,(1-f_{\rm F}(E_1))\,(1-f_{\rm F}(E_2))\,f_{\rm F}(E_3) \\
&+ \delta^{(4)}(p_1+p_3-p_2-q)\,(1-f_{\rm F}(E_1))\,f_{\rm F}(E_2)\,(1-f_{\rm F}(E_3)) \\
&\qquad + \delta^{(4)}(p_2+p_3-p_1-q) f_{\rm F}(E_1)\,(1-f_{\rm F}(E_2))\,(1-f_{\rm F}(E_3)) \\
&+ \delta^{(4)}(p_3-p_1-p_2-q) f_{\rm F}(E_1) f_{\rm F}(E_2)\,(1-f_{\rm F}(E_3)) \\
&+ \delta^{(4)}(p_2-p_1-p_3-q) f_{\rm F}(E_1)\,(1-f_{\rm F}(E_2))\,f_{\rm F}(E_3) + \delta^{(4)}(p_1-p_2-p_3-q) \times \\
&\times (1-f_{\rm F}(E_1))\,f_{\rm F}(E_2) f_{\rm F}(E_3)\Big] \frac{p_2\cdot p_3}{4} \left((1 \pm \frac{q_0}{|\mathbf{q}|})(p_1\cdot u) \mp \frac{p_1\cdot q}{|\mathbf{q}|}\right)
\end{aligned} \tag{C.1}$$

and

$$\begin{aligned}
\mathcal{J}_{\pm}(m_1, m_2, m_3) = &\frac{1}{T^5} 32\pi^4 f_{\rm F}^{-1}(-q_0) \int \frac{\mathrm{d}^3\mathbf{p}_1}{(2\pi)^3 2E_1} \int \frac{\mathrm{d}^3\mathbf{p}_2}{(2\pi)^3 2E_2} \int \frac{\mathrm{d}^3\mathbf{p}_3}{(2\pi)^3 2E_3} \times \\
&\times \Big[ -\delta^{(4)}(p_1+p_2+p_3-q)\,(1-f_{\rm F}(E_1))\,(1-f_{\rm F}(E_2))\,(1-f_{\rm F}(E_3)) \\
&\qquad + \delta^{(4)}(p_1+p_2-p_3-q)\,(1-f_{\rm F}(E_1))\,(1-f_{\rm F}(E_2))\,f_{\rm F}(E_3) \\
&+ \delta^{(4)}(p_1+p_3-p_2-q)\,(1-f_{\rm F}(E_1))\,f_{\rm F}(E_2)\,(1-f_{\rm F}(E_3))
\end{aligned}$$

$$
\begin{aligned}
&\quad - \delta^{(4)}(p_2+p_3-p_1-q) f_{\mathrm{F}}(E_1)\,(1-f_{\mathrm{F}}(E_2))\,(1-f_{\mathrm{F}}(E_3)) \\
&+ \delta^{(4)}(p_3-p_1-p_2-q) f_{\mathrm{F}}(E_1) f_{\mathrm{F}}(E_2)\,(1-f_{\mathrm{F}}(E_3)) \\
&+ \delta^{(4)}(p_2-p_1-p_3-q) f_{\mathrm{F}}(E_1)\,(1-f_{\mathrm{F}}(E_2))\, f_{\mathrm{F}}(E_3) - \delta^{(4)}(p_1-p_2-p_3-q)\times \\
&\times (1-f_{\mathrm{F}}(E_1))\, f_{\mathrm{F}}(E_2) f_{\mathrm{F}}(E_3)\Big] \frac{m_2 m_3}{4}\left((1 \pm \frac{q_0}{|\mathbf{q}|})(p_1\cdot u) \mp \frac{p_1\cdot q}{|\mathbf{q}|}\right), \qquad \text{(C.2)}
\end{aligned}
$$

where, as a reminder, we have defined $E_i = \sqrt{\mathbf{p}_i^2 + m_i^2}$. In addition, one can write $\Gamma$ and $\bar{\Gamma}$, the interaction rates of positive and negative helicity $N$ respectively, under the form

$$
\Gamma(q) = \Gamma_1(q) + \Gamma_2(q), \;\; \bar{\Gamma}(q) = \bar{\Gamma}_1(q) + \bar{\Gamma}_2(q) \qquad \text{(C.3)}
$$

where $\Gamma_1, \bar{\Gamma}_1$ and $\Gamma_2, \bar{\Gamma}_2$ are rates associated with the type-1 and type-2 (if the latter is present in the theory) self-energies respectively. The former can in turn be expressed in terms of the functions $\mathcal{I}_\pm$ and $\mathcal{J}_\pm$ as

$$
\begin{aligned}
\Gamma_1(q) = \frac{128\mathcal{G}^2T^5}{|q_0|}\mathcal{C}_{\mathcal{J}_L}\Bigg[&(|a_L|^2+|b_L|^2)q_-\left[\mathcal{I}_+(m_1,m_2,m_3)+\mathcal{I}_+(m_2,m_1,m_3)\right] \\
&+ (|b_L|^2-|a_L|^2)q_-\mathcal{J}_+(m_3,m_2,m_1)\Bigg] \\
+ \frac{128\mathcal{G}^2T^5}{|q_0|}\mathcal{C}_{\mathcal{J}_R}\Bigg[&(|a_R|^2+|b_R|^2)q_+\left[\mathcal{I}_-(m_1,m_2,m_3)+\mathcal{I}_-(m_2,m_1,m_3)\right] \\
&+ (|b_R|^2-|a_R|^2)q_+\mathcal{J}_-(m_3,m_2,m_1)\Bigg], \qquad \text{(C.4a)}
\end{aligned}
$$

$$
\begin{aligned}
\bar{\Gamma}_1(q) = \frac{128\mathcal{G}^2T^5}{|q_0|}\mathcal{C}_{\mathcal{J}_L}\Bigg[&(|a_L|^2+|b_L|^2)q_+\left[\mathcal{I}_-(m_1,m_2,m_3)+\mathcal{I}_-(m_2,m_1,m_3)\right] \\
&+ (|b_L|^2-|a_L|^2)q_+\mathcal{J}_-(m_3,m_2,m_1)\Bigg] \\
+ \frac{128\mathcal{G}^2T^5}{|q_0|}\mathcal{C}_{\mathcal{J}_R}\Bigg[&(|a_R|^2+|b_R|^2)q_-\left[\mathcal{I}_+(m_1,m_2,m_3)+\mathcal{I}_+(m_2,m_1,m_3)\right] \\
&+ (|b_R|^2-|a_R|^2)q_-\mathcal{J}_+(m_3,m_2,m_1)\Bigg]. \qquad \text{(C.4b)}
\end{aligned}
$$

Similarly, $\Gamma_2$ and $\bar{\Gamma}_2$ can be written

$$
\Gamma_2(q) = -\frac{64\mathcal{G}^2T^5}{|q_0|}\mathcal{C}_{\mathcal{J}_L}\Bigg[ -2(a_L-b_L)(c_L-d_L)q_-\mathcal{I}_+(m_2,m_1,m_3)
$$

$$+ (a_L + b_L)(c_L + d_L) q_- \mathcal{J}_+(m_2, m_1, m_3) + (a_L - b_L)(c_L + d_L) q_- \mathcal{J}_+(m_3, m_2, m_1) \\ + (a_L + b_L)(c_L - d_L) q_- \mathcal{J}_+(m_1, m_2, m_3) \Big]$$

$$- \frac{64\mathcal{G}^2 T^5}{|q_0|} \mathcal{C}_{\mathcal{J}_R} \Big[ -2(a_R + b_R)(c_R + d_R) q_+ \mathcal{I}_-(m_2, m_1, m_3) \\ + (a_R - b_R)(c_R - d_R) q_+ \mathcal{J}_-(m_2, m_1, m_3) + (a_R + b_R)(c_R - d_R) q_+ \mathcal{J}_-(m_3, m_2, m_1) \\ + (a_R - b_R)(c_R + d_R) q_+ \mathcal{J}_-(m_1, m_2, m_3) \Big], \quad \text{(C.5a)}$$

$$\bar{\Gamma}_2(q) = - \frac{64\mathcal{G}^2 T^5}{|q_0|} \mathcal{C}_{\mathcal{J}_L} \Big[ -2(a_L - b_L)(c_L - d_L) q_+ \mathcal{I}_-(m_2, m_1, m_3) \\ + (a_L + b_L)(c_L + d_L) q_+ \mathcal{J}_-(m_2, m_1, m_3) + (a_L - b_L)(c_L + d_L) q_+ \mathcal{J}_-(m_3, m_2, m_1) \\ + (a_L + b_L)(c_L - d_L) q_+ \mathcal{J}_-(m_1, m_2, m_3) \Big]$$

$$- \frac{64\mathcal{G}^2 T^5}{|q_0|} \mathcal{C}_{\mathcal{J}_R} \Big[ -2(a_R + b_R)(c_R + d_R) q_- \mathcal{I}_+(m_2, m_1, m_3) \\ + (a_R - b_R)(c_R - d_R) q_- \mathcal{J}_+(m_2, m_1, m_3) + (a_R + b_R)(c_R - d_R) q_- \mathcal{J}_+(m_3, m_2, m_1) \\ + (a_R - b_R)(c_R + d_R) q_- \mathcal{J}_+(m_1, m_2, m_3) \Big]. \quad \text{(C.5b)}$$

For a Majorana particle, $\mathcal{C}_{\mathcal{J}_L} = \mathcal{C}_{\mathcal{J}_R}$ and $a_L = a_R,\ b_L = b_R,\ c_L = c_R,\ d_L = d_R$ such that $\Gamma = \bar{\Gamma}$ as expected.

Concerning the scalar contribution, the equivalent functions are defined as

$$\mathcal{K}(m_1, m_2, m_3) = \frac{1}{T^5} 32\pi^4 f_{\mathrm{F}}^{-1}(-q_0) \int \frac{\mathrm{d}^3\mathbf{p}_1}{(2\pi)^3 2E_1} \int \frac{\mathrm{d}^3\mathbf{p}_2}{(2\pi)^3 2E_2} \int \frac{\mathrm{d}^3\mathbf{p}_3}{(2\pi)^3 2E_3} \times \\ \times \Big[ \delta^{(4)}(p_1 + p_2 + p_3 - q)\,(1 - f_{\mathrm{F}}(E_1))\,(1 - f_{\mathrm{F}}(E_2))\,(1 - f_{\mathrm{F}}(E_3)) \\ - \delta^{(4)}(p_1 + p_2 - p_3 - q)\,(1 - f_{\mathrm{F}}(E_1))\,(1 - f_{\mathrm{F}}(E_2))\, f_{\mathrm{F}}(E_3) \\ + \delta^{(4)}(p_1 + p_3 - p_2 - q)\,(1 - f_{\mathrm{F}}(E_1))\, f_{\mathrm{F}}(E_2)\,(1 - f_{\mathrm{F}}(E_3)) \\ + \delta^{(4)}(p_2 + p_3 - p_1 - q) f_{\mathrm{F}}(E_1)\,(1 - f_{\mathrm{F}}(E_2))\,(1 - f_{\mathrm{F}}(E_3)) \\ + \delta^{(4)}(p_3 - p_1 - p_2 - q) f_{\mathrm{F}}(E_1) f_{\mathrm{F}}(E_2)\,(1 - f_{\mathrm{F}}(E_3)) \\ - \delta^{(4)}(p_2 - p_1 - p_3 - q) f_{\mathrm{F}}(E_1)\,(1 - f_{\mathrm{F}}(E_2))\, f_{\mathrm{F}}(E_3) \\ - \delta^{(4)}(p_1 - p_2 - p_3 - q)\,(1 - f_{\mathrm{F}}(E_1))\, f_{\mathrm{F}}(E_2) f_{\mathrm{F}}(E_3) \Big] m_3 \frac{p_1 \cdot p_2}{4} \quad \text{(C.6)}$$

and

$$\mathcal{L}(m_1, m_2, m_3) = \frac{1}{T^5} 32\pi^4 f_{\mathrm{F}}^{-1}(-q_0) \int \frac{\mathrm{d}^3\mathbf{p}_1}{(2\pi)^3 2E_1} \int \frac{\mathrm{d}^3\mathbf{p}_2}{(2\pi)^3 2E_2} \int \frac{\mathrm{d}^3\mathbf{p}_3}{(2\pi)^3 2E_3} \times$$

$$\begin{aligned}
\times\Big[ &-\delta^{(4)}(p_1+p_2+p_3-q)\,(1-f_{\rm F}(E_1))\,(1-f_{\rm F}(E_2))\,(1-f_{\rm F}(E_3)) \\
&\qquad + \delta^{(4)}(p_1+p_2-p_3-q)\,(1-f_{\rm F}(E_1))\,(1-f_{\rm F}(E_2))\,f_{\rm F}(E_3) \\
&+\delta^{(4)}(p_1+p_3-p_2-q)\,(1-f_{\rm F}(E_1))\,f_{\rm F}(E_2)\,(1-f_{\rm F}(E_3)) \\
&\qquad + \delta^{(4)}(p_2+p_3-p_1-q) f_{\rm F}(E_1)\,(1-f_{\rm F}(E_2))\,(1-f_{\rm F}(E_3)) \\
&-\delta^{(4)}(p_3-p_1-p_2-q) f_{\rm F}(E_1) f_{\rm F}(E_2)\,(1-f_{\rm F}(E_3)) \\
&\qquad - \delta^{(4)}(p_2-p_1-p_3-q) f_{\rm F}(E_1)\,(1-f_{\rm F}(E_2))\,f_{\rm F}(E_3) \\
&-\delta^{(4)}(p_1-p_2-p_3-q)\,(1-f_{\rm F}(E_1))\,f_{\rm F}(E_2) f_{\rm F}(E_3)\Big]\frac{m_1 m_2 m_3}{4}. \qquad \text{(C.7)}
\end{aligned}$$

The rates $\Gamma^S = \bar{\Gamma}^S$ arising from the scalar contribution to the self-energy (independently of the helicity of $N$) takes the form

$$\Gamma^S = \bar{\Gamma}^S = \mathcal{C}^S_{\mathcal{J}_R}\frac{\operatorname{Im}\hat{\Sigma}^S_R}{|q_0|}M + \mathcal{C}^S_{\mathcal{J}_L}\frac{\operatorname{Im}\hat{\Sigma}^S_L}{|q_0|}M^* \qquad \text{(C.8)}$$

In general, $\mathcal{C}^S_{\mathcal{J}_R}\operatorname{Im}\hat{\Sigma}^S_R = \left(\mathcal{C}^S_{\mathcal{J}_L}\operatorname{Im}\hat{\Sigma}^S_L\right)^*$ such that the full result is still real. Note that, in the mass basis, $M = M^*$, and, hence,

$$\Gamma^S = \bar{\Gamma}^S = 2\mathcal{C}^S_{\mathcal{J}_R}\frac{\operatorname{Im}\hat{\Sigma}^S_R}{|q_0|}M. \qquad \text{(C.9)}$$

One can write these rates as $\Gamma^S = \Gamma^{S,1} + \Gamma^{S,2}$, where $\Gamma^{S,i}$ are associated with the self-energy of type-i. These in turn can be expressed in terms of the dimensionless functions $\mathcal{K}, \mathcal{L}$ in the following manner.

$$\begin{aligned}
\Gamma^{S,1}(q) &= -2\mathcal{C}^S_{\mathcal{J}_R}\frac{128\mathcal{G}^2T^5}{|q_0|}M\times \qquad \text{(C.10)} \\
&\times\left[(a_L a_R^* + b_L b_R^*)\mathcal{K}(m_1,m_2,m_3) + 2(b_L b_R^* - a_L a_R^*)\mathcal{L}(m_1,m_2,m_3)\right], \\
\Gamma^{S,2}(q) &= -2\mathcal{C}^S_{\mathcal{J}_R}\frac{64\mathcal{G}^2T^5}{|q_0|}M\big[-2(a_L-b_L)(c_R+d_R)\mathcal{L}(m_1,m_2,m_3) \\
&+(a_L+b_L)(c_R+d_R)\mathcal{K}(m_3,m_2,m_1) + (a_L+b_L)(c_R-d_R)\mathcal{K}(m_1,m_3,m_2) \\
&\qquad + (a_L-b_L)(c_R-d_R)\mathcal{K}(m_1,m_2,m_3)\big]. \qquad \text{(C.11)}
\end{aligned}$$

As an example, we can apply the above formulae for the case of neutrino-neutrino scatterings within the SM. Assuming the light neutrinos are in thermal equilibrium, the neutrino (of flavour $\alpha$) interaction rates write

$$\Gamma(q) + \bar{\Gamma}(q) = \frac{128G_F^2T^5}{|q_0|}\left(q_-\mathcal{I}_+(0,0,0) + q_+\mathcal{I}_-(0,0,0)\right) \qquad \text{(C.12)}$$

$$
\begin{aligned}
&= \frac{2048\pi^4 G_F^2}{|q_0| f_{\mathrm{F}}(-q_0)} \int \frac{\mathrm{d}^3\mathbf{p}_1}{(2\pi)^3 2E_1} \int \frac{\mathrm{d}^3\mathbf{p}_2}{(2\pi)^3 2E_2} \int \frac{\mathrm{d}^3\mathbf{p}_3}{(2\pi)^3 2E_3} \times \\
&\times \Big[ \delta^{(4)}(p_1 + p_2 + p_3 - q)\,(1 - f_{\mathrm{F}}(E_1))\,(1 - f_{\mathrm{F}}(E_2))\,(1 - f_{\mathrm{F}}(E_3)) \\
&\qquad + \delta^{(4)}(p_1 + p_2 - p_3 - q)\,(1 - f_{\mathrm{F}}(E_1))\,(1 - f_{\mathrm{F}}(E_2))\,f_{\mathrm{F}}(E_3) \\
&+ \delta^{(4)}(p_1 + p_3 - p_2 - q)\,(1 - f_{\mathrm{F}}(E_1))\,f_{\mathrm{F}}(E_2)\,(1 - f_{\mathrm{F}}(E_3)) \\
&\qquad + \delta^{(4)}(p_2 + p_3 - p_1 - q) f_{\mathrm{F}}(E_1)\,(1 - f_{\mathrm{F}}(E_2))\,(1 - f_{\mathrm{F}}(E_3)) \\
&+ \delta^{(4)}(p_3 - p_1 - p_2 - q) f_{\mathrm{F}}(E_1) f_{\mathrm{F}}(E_2)\,(1 - f_{\mathrm{F}}(E_3)) \\
&\qquad + \delta^{(4)}(p_2 - p_1 - p_3 - q) f_{\mathrm{F}}(E_1)\,(1 - f_{\mathrm{F}}(E_2))\,f_{\mathrm{F}}(E_3) \\
&+ \delta^{(4)}(p_1 - p_2 - p_3 - q)\,(1 - f_{\mathrm{F}}(E_1))\,f_{\mathrm{F}}(E_2) f_{\mathrm{F}}(E_3) \Big] (p_1 \cdot p_3)(p_2 \cdot q)
\end{aligned}
$$

since they are massless and purely left-handed. One recognizes the usual neutrino scattering matrix elements, compare, e.g., to table 1 in [608].

Appendix D

# Collection of results regarding $N_{\text{eff}}$

In this appendix, we provide various useful results concerning Chap. 6.

## D.1 Functions in the continuity equation

We start by defining the functions $K, J_\pm, Y_\pm, W_\pm$, and $G_{1,2}$ entering the continuity equation (6.9), which we express in terms of the dimensionless variables $x, y, z$. Their explicit forms are given by [7, 548]:

$$K(\tau) = \frac{1}{\pi^2}\int \mathrm{d}\omega \, \frac{\omega^2}{\sqrt{\omega^2+\tau^2}} \frac{1}{\exp\left(\sqrt{\tau^2+\omega^2}\right)+1}, \tag{D.1}$$

$$J_\pm(\tau) = \frac{1}{\pi^2}\int \mathrm{d}\omega \, \omega^2 \frac{\exp\left(\sqrt{\tau^2+\omega^2}\right)}{\left[\exp\left(\sqrt{\tau^2+\omega^2}\right)\pm 1\right]^2}, \tag{D.2}$$

$$Y_\pm(\tau) = \frac{1}{\pi^2}\int \mathrm{d}\omega \, \omega^4 \frac{\exp\left(\sqrt{\tau^2+\omega^2}\right)}{\left[\exp\left(\sqrt{\tau^2+\omega^2}\right)\pm 1\right]^2}, \tag{D.3}$$

$$W_\pm(\tau) = \frac{1}{\pi^2}\int_0^\infty \mathrm{d}\omega \, \omega^2 \frac{\sqrt{\omega^2+\tau^2}}{\exp(\sqrt{\omega^2+\tau^2})\pm 1}, \tag{D.4}$$

$$\begin{aligned} G_1(\tau) = 2\pi\alpha\Bigg[&\frac{1}{\tau}\left(\frac{K(\tau)}{3}+2K^2(\tau)-\frac{J(\tau)}{6}-K(\tau)J(\tau)\right) \\ &+\left(\frac{K'(\tau)}{6}-K(\tau)K'(\tau)+\frac{J'(\tau)}{6}+J'(\tau)K(\tau)+J(\tau)K'(\tau)\right)\Bigg], \end{aligned} \tag{D.5}$$

$$\begin{aligned} G_2(\tau) = &-8\pi\alpha\left(\frac{K(\tau)}{6}+\frac{J(\tau)}{6}-\frac{1}{2}K^2(\tau)+K(\tau)J(\tau)\right) \\ &+2\pi\alpha\left(\frac{K'(\tau)}{6}-K(\tau)K'(\tau)+\frac{J'(\tau)}{6}+J'(\tau)K(\tau)+J(\tau)K'(\tau)\right), \end{aligned} \tag{D.6}$$

where the symbol $'$ denotes the partial derivative $\partial/\partial\tau$, and the $+$ sign ($-$ sign) highlights the fermionic (bosonic) nature of the contribution. Regarding $G_1$ and $G_2$, we only provide here the $\mathcal{O}(e^2)$-result.[1] Explicit expressions for $G_{1,2}(\tau)$ at the next order, $\mathcal{O}(e^3)$, have been obtained in [549].

## D.2 Thermal integrals

The calculation of the 1PI photon self-energy and resummed propagator (in the plasma rest frame) rely on the following two thermal integrals

$$\begin{aligned} K^\mu(P) &= 2e^2 \int \frac{\mathrm{d}^4 k}{(2\pi)^3} k^\mu \frac{\delta(k^2 - m_e^2) f_{\mathrm{F}}(|k^0|)}{(P+k)^2 - m_e^2 + i\epsilon}, \\ K^{\mu\nu}(P) &= 2e^2 \int \frac{\mathrm{d}^4 k}{(2\pi)^3} k^\mu k^\nu \frac{\delta(k^2 - m_e^2) f_{\mathrm{F}}(|k^0|)}{(P+k)^2 - m_e^2 + i\epsilon}. \end{aligned} \tag{D.7}$$

We can define two unit vectors $\mathbf{e}_1$ and $\mathbf{e}_2$ perpendicular to the photon momentum (of corresponding unit vector $\hat{\mathbf{P}} \equiv \mathbf{P}/|\mathbf{P}|$) such that the set $\{\hat{\mathbf{P}}, \mathbf{e}_1, \mathbf{e}_2\}$ forms a complete orthogonal basis. The spatial part of the integration variable can then be parametrised in the following way:

$$\mathbf{k} = |\boldsymbol{k}|(\cos\vartheta \hat{\mathbf{P}} + \cos\varphi \sin\vartheta \mathbf{e}_1 + \sin\varphi \sin\vartheta \mathbf{e}_2). \tag{D.8}$$

Starting with $K^\mu$, we can easily show that the contributions proportional to $\mathbf{e}_1$ and $\mathbf{e}_2$ vanish after the azimuthal integration. Hence, the spatial part of $K^\mu$ simply reads

$$\mathbf{K} = \frac{\mathbf{P}}{|\boldsymbol{P}|^3} \frac{\alpha_{\mathrm{em}}}{4\pi} \int_{m_e}^{\infty} \mathrm{d}\omega \left[ P^2 \ell_1(\omega, P) + 2\omega P_0 \ell_2(\omega, P) - 8|\boldsymbol{k}||\boldsymbol{P}| \right] f_{\mathrm{F}}(\omega), \tag{D.9}$$

where $\omega = |k^0| = \sqrt{|\boldsymbol{k}|^2 + m_e^2}$ is the on-shell electron energy, and the two functions

$$\begin{aligned} \ell_1(\omega, P) &= \ln \left| \frac{(P^2 + 2|\boldsymbol{k}||\boldsymbol{P}|)^2 - 4P_0^2\omega^2}{(P^2 - 2|\boldsymbol{k}||\boldsymbol{P}|)^2 - 4P_0^2\omega^2} \right|, \\ \ell_2(\omega, P) &= \ln \left| \frac{P^4 - 4(P_0\omega + |\boldsymbol{P}||\boldsymbol{k}|)^2}{P^4 - 4(P_0\omega - |\boldsymbol{P}||\boldsymbol{k}|)^2} \right| \end{aligned} \tag{D.10}$$

stem from the integration over $\cos\vartheta$. Correspondingly, the temporal component of $K^\mu$ reads

$$K^0 = \frac{\alpha_{\mathrm{em}}}{2\pi|\boldsymbol{P}|} \int_{m_e}^{\infty} \mathrm{d}\omega\omega\, \ell_2(\omega, P) f_{\mathrm{F}}(\omega). \tag{D.11}$$

The tensor integral $K^{\mu\nu}$ can be computed using a similar approach. Starting with the spatial components $K^{ij}$, one can show that, after the azimuthal integral, only terms proportional to $\hat{P}^i \hat{P}^j$ and $\sum_{k=1,2} e_k^i e_k^j$ will remain. One can then make use of

[1] Note that, in principle, additional logarithmic contributions also appear at $\mathcal{O}(e^2)$. These have however been shown to be negligible [549] and are therefore not included here.

the completeness relation

$$\delta^{ij} = \hat{P}^i \hat{P}^j + \sum_{k=1,2} e_k^i e_k^j \tag{D.12}$$

to obtain

$$K^{ij} = \hat{P}^i \hat{P}^j I_1 + (\delta^{ij} - \hat{P}^i \hat{P}^j)(I_2 - I_1/2)\,. \tag{D.13}$$

In the previous equation, we have introduced the two auxiliary functions

$$\begin{aligned}
I_1 &= \frac{\alpha_{\mathrm{em}}}{8\pi|\boldsymbol{P}|^3}\int_{m_e}^{\infty} \mathrm{d}\omega\, \left[(P^4 + 4P_0^2\omega^2)\ell_1(\omega,P) + 4P^2 P_0\,\omega\,\ell_2(\omega,P) - 8|\boldsymbol{P}||\mathbf{k}|P^2\right] f_{\mathrm{F}}(\omega),\\
I_2 &= \frac{\alpha_{\mathrm{em}}}{4\pi|\boldsymbol{P}|}\int_{m_e}^{\infty} \mathrm{d}\omega |\boldsymbol{k}|^2 \ell_1(\omega,P) f_{\mathrm{F}}(\omega).
\end{aligned} \tag{D.14}$$

The remaining components of $K^{\mu\nu}$ can be extracted in a similar manner

$$\begin{aligned}
K^{00}(P) &= \frac{\alpha_{\mathrm{em}}}{2\pi|\boldsymbol{P}|}\int_{m_e}^{\infty} \mathrm{d}\omega\omega^2\, \ell_1(\omega,P) f_{\mathrm{F}}(\omega),\\
K^{0i} &= \frac{\alpha_{\mathrm{em}}\hat{P}^i}{4\pi|\boldsymbol{P}|^2}\int_{m_e}^{\infty} \mathrm{d}\omega\omega\, \left[2P_0\omega\ell_1(\omega,P) + P^2\ell_2(\omega,P)\right] f_{\mathrm{F}}(\omega).
\end{aligned} \tag{D.15}$$

The remaining one-dimensional integrals (D.9), (D.11), (D.14) and (D.15) can be very efficiently evaluated numerically.

## D.3 1PI-resumming the photon propagator

As highlighted in Sec. 6.2.2, the NLO rates exhibit an IR divergence, which can be regulated by resumming the photon propagator. In this appendix, we start by presenting an exact derivation of the (finite-temperature) photon self-energy at the one-loop level, using the CTP formalism and assuming electrons in thermal equilibrium with vanishing chemical potentials. We then extract in Sec. D.3.2 the 1PI-resummed Feynman propagator. Exact explicit expressions for the photon self-energy and resummed propagators already exist, either in the HTL approximation [28, 609] or in the simplified scenarios wherein $T \ll m_e$ [610] or $m_e = 0$ [611], see also [612] for analytic approximations for off-shell photons. In this appendix, we lift these assumptions and derive a propagator valid for all values of the electron mass $m_e$ and photon 4-momentum $P$, at the cost of losing a closed-form expression. We note in passing that Ref. [572] also examined the photon propagator without making the HTL approximation, and retaining as well the finite electron chemical potential, but did not provide explicit formulae.

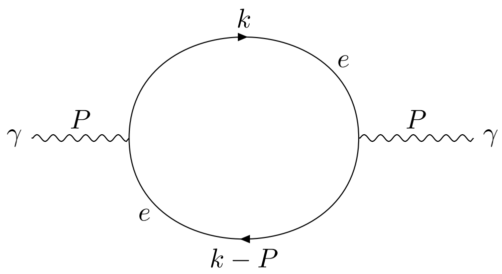


**Figure D.1:** One-loop contribution to the photon self-energy. Taken from [4].

### D.3.1 1-loop photon self-energy

Since, in the temperature range relevant for $N_{\text{eff}}$, the abundance of any fermion heavier than the electron is strongly Boltzmann suppressed, photons effectively only interact with electrons and its thermal self-energy, displayed in Fig. D.1, reads at the one-loop level

$$\Pi^{\mu\nu}_{ab}(P) = \text{sgn}(ab) i e^2 \int \frac{\mathrm{d}^4 k}{(2\pi)^4} \text{Tr}\left[ i S^{ab}_e(k) \gamma^\mu i S^{ba}_e(k-P) \gamma^\nu \right] \tag{D.16}$$

for general CTP indices $a, b \in \{+, -\}$. Given that electrons are in thermal equilibrium at the relevant temperature range,[2] it is sufficient to compute $\Pi_{++}$ and $\Pi_{+-}$ and obtain the remaining two self-energies via the bosonic KMS relation, i.e.

$$\Pi^{\mu\nu}_{-+}(P) = e^{P_0/T} \Pi^{\mu\nu}_{+-}(P) \tag{D.17}$$

and

$$\Pi^{\mu\nu}_{--}(P) = -\Pi^{\mu\nu;*}_{++}(P) \tag{D.18}$$

for a general four-vector $P$. In addition, it is useful to note that both $\Pi^{\mu\nu}_{+-}$ and $\Pi^{\mu\nu}_{-+}$ are purely imaginary and verify the following relation

$$\text{Im}\, \Pi^{\mu\nu}_{++} = \frac{i}{2}(\Pi^{\mu\nu}_{+-} + \Pi^{\mu\nu}_{-+}) = \frac{i}{2}\left(1 + e^{P_0/T}\right) \Pi^{\mu\nu}_{+-}. \tag{D.19}$$

As in the main text, we will split the self-energy into a vacuum and finite-temperature contribution $\Pi^{\mu\nu}_{ab, T\neq 0}$. Starting with the vacuum contribution, the $++$ self-energy can

[2] The freeze-out of electron-positron annihilation only happen around 16 keV at which moment $N_{\text{eff}}$ is expected to be modified by at most $10^{-7}$ [558].

be written

$$\Pi_2^{\mu\nu} = ie^2 \int_k \frac{i}{k^2 - m_e^2 + i\epsilon} \frac{i}{(k+P)^2 - m_e^2 + i\epsilon} \mathrm{Tr}\left[(\not{k} + m_e)\gamma^\mu(\not{k} + \not{P} + m_e)\gamma^\nu\right] \tag{D.20}$$

while the $+-$ self-energy vanishes since processes of the form $e \leftrightarrow e + \gamma$ are forbidden in vacuum. The renormalised vacuum part $\Pi_2^{\mu\nu}(P) = (\alpha_{\rm em}/\pi)(P^2 g^{\mu\nu} - P^\nu P^\mu)\Pi_2(P^2)$ is textbook material and, in the $\overline{\rm MS}$-scheme, reads

$$\begin{aligned} \Pi_2(P^2) &= \frac{2}{3}\ln\left(\frac{\mu}{m_e}\right) + \frac{5}{9} + \frac{\tau}{3} + \frac{1}{3}\left(1 + \frac{\tau}{2}\right)\sqrt{1-\tau}\ln\left(\frac{\sqrt{1-\tau}-1}{\sqrt{1-\tau}+1}\right) \\ &\longrightarrow \frac{1}{3}\ln\left(\frac{\mu^2}{-P^2}\right) + \frac{5}{9} \quad \text{for } m_e \to 0, \end{aligned} \tag{D.21}$$

with $\tau = 4m_e^2/P^2$ (see, e.g., appendix A of [613] for the derivation). In practice, we note that the vacuum contribution to the photon self-energy is numerically irrelevant when resumming the photon propagator, as it vanishes in the soft photon exchange limit for which $P^2 = 0$. We can therefore safely neglect it in the resummed propagator.

Moving on the finite-temperature contribution, it is common to decompose $\Pi^{\mu\nu}$ into a longitudinal and a transverse part,

$$\Pi_{ab}^{\mu\nu} = \Pi_{ab}^L P_L^{\mu\nu} + \Pi_{ab}^T P_T^{\mu\nu}\,, \tag{D.22}$$

where we define the corresponding projectors [24, 614]

$$\begin{aligned} &P_T^{00} = P_T^{0i} = P_T^{i0} = 0, \quad P_T^{ij} = -\delta^{ij} + \hat{P}^i\hat{P}^j, \\ &P_L^{\mu\nu} = g^{\mu\nu} - \frac{P^\mu P^\nu}{P^2} - P_T^{\mu\nu}. \end{aligned} \tag{D.23}$$

From their definition (D.23), it is straightforward to verify that $P_\mu P_{L/T}^{\mu\nu} = 0$ and, therefore, the photon self-energy fulfils the Ward-Takahashi identity $P_\mu \Pi_{ab}^{\mu\nu} = 0$. Though it is not obvious from its definition, we note in passing that the longitudinal projector can alternatively be expressed in a Lorentz-invariant manner as

$$P_L^{\mu\nu} = \tilde{u}^\mu \tilde{u}^\nu / \tilde{u}^2\,, \tag{D.24}$$

with $\tilde{u}^\mu = P^2 u^\mu - (u\cdot P)P^\mu$ a function of the heat bath four-velocity $u^\mu$ ($= \delta_0^\mu$ in its rest frame).

Let us now start by computing the real part of $\Pi_{++}^{\mu\nu}$. It can be written in terms of the integrals $K^\mu$ and $K^{\mu\nu}$, computed in appendix D.2, as

$$\mathrm{Re}\,\Pi_{++,T\neq0}^{\mu\nu} = -\mathrm{Re}\,\Pi_{--,T\neq0}^{\mu\nu} = 4(-g^{\mu\nu} K\cdot P + 2K^{\mu\nu} + K^\mu P^\nu + K^\nu P^\mu). \tag{D.25}$$

Using the explicit results (D.9), (D.11), (D.13) and (D.15) for these integrals, we can then decompose the self-energy according to Eq. (D.22). For the longitudinal component, we find

$$\mathrm{Re}\,\Pi^L_{++,T\neq 0} = \frac{\alpha_{\rm em}P^2}{\pi|\boldsymbol{P}|^3}\int_{m_e}^{\infty}\mathrm{d}\omega\,\left[8|\boldsymbol{k}||\boldsymbol{P}| - \ell_1(\omega,P)(P^2+4\omega^2) - 4\ell_2(\omega,P)P_0\omega\right] f_{\rm F}(\omega) \tag{D.26}$$

$$\stackrel{\rm HTL}{\approx} -3\omega_p^2\left(1-\frac{P_0^2}{|\boldsymbol{P}|^2}\right)\left[1-\frac{P_0}{2|\boldsymbol{P}|}\ln\left|\frac{P_0+|\boldsymbol{P}|}{P_0-|\boldsymbol{P}|}\right|\right] \longrightarrow -3\omega_p^2 \text{ for } P_0=0, \tag{D.27}$$

whereas we obtain for the transverse one

$$\begin{aligned}\mathrm{Re}\,\Pi^T_{++,T\neq 0} &= \frac{\alpha_{\rm em}}{\pi|\boldsymbol{P}|^3}\int_{m_e}^{\infty}\mathrm{d}\omega\,\Big[2\ell_2(\omega,P)P_0P^2\omega - 4|\boldsymbol{k}||\boldsymbol{P}|(P_0^2+|\boldsymbol{P}|^2) \\ &\quad + \ell_1(\omega,P)(|\boldsymbol{P}|^2P^2 + 2P_0^2\omega^2 - 2|\boldsymbol{k}|^2|\boldsymbol{P}|^2 + \frac{1}{2}P^4)\Big] f_{\rm F}(\omega)\end{aligned} \tag{D.28}$$

$$\stackrel{\rm HTL}{\approx} -\frac{3}{2}\omega_p^2\frac{P_0^2}{|\boldsymbol{P}|^2}\left[1-\left(1-\frac{|\boldsymbol{P}|^2}{P_0^2}\right)\frac{P_0}{2|\boldsymbol{P}|}\ln\left|\frac{P_0+|\boldsymbol{P}|}{P_0-|\boldsymbol{P}|}\right|\right] \longrightarrow 0 \text{ for } P_0=0, \tag{D.29}$$

with the plasma frequency $\omega_p$ being simply given by $eT/3$ in the HTL limit. In both equations, the symbol $\stackrel{\rm HTL}{\approx}$ indicates that the result was obtained in the HTL approximation [615]. In this regime, the photon momentum is soft and one can expand in $P/k$. To be more precise, we have first expanded the fully momentum- and mass-dependent self-energy (D.26) and (D.28) in $P_0/|\mathbf{k}|$ and then in $P_0/|\mathbf{P}|$ in a second time, using that

$$\ell_1(\omega,P) \stackrel{\rm HTL}{\approx} -2\frac{|\boldsymbol{P}|}{|\boldsymbol{k}|},\quad \ell_2(\omega,P) \stackrel{\rm HTL}{\approx} 2\ln\left|\frac{P_0+|\boldsymbol{P}|}{P_0-|\boldsymbol{P}|}\right| \tag{D.30}$$

in this limit. Furthermore, we have also neglected the electron mass such that $|\mathbf{k}| = \omega$. Noticing that

$$\int_0^{\infty}\mathrm{d}kk\, f_{\rm F}(k) = \pi^2T^2/12\,, \tag{D.31}$$

the integral over $\omega$ can be performed analytically, yielding the well-known HTL result (D.27) (or (D.29)). It is interesting to observe that, in the limit $P_0 \to 0$, the longitudinal photon degrees of freedom[3] possess a mass while the transverse excitations do not. Ultimately, this feature is related to the absence of magnetic monopoles and the impossibility to screen (static) magnetic fields. The so-called *Debye mass* $m_D$, sometimes also known as the *electric mass*, characterising the screening of elec-

[3] Sometimes referred to as “plasmons” in the literature.

tric fields in a charged medium, can be extracted from the longitudinal self-energy through the standard relation

$$m_D = \sqrt{-\operatorname{Re}\Pi^L_{++}\left(q_0 = 0, |\mathbf{q}| \to 0\right)}. \tag{D.32}$$

Equivalently, $m_D$ can be obtained from the QED EoS via the relation (see, e.g., [28, 564])

$$\operatorname{Re}\Pi^L_{++}(q_0 = 0, |\mathbf{q}| \to 0) = -e^2 \frac{\partial^2 P(\mu, T)}{\partial \mu^2}, \tag{D.33}$$

where $P(\mu, T)$ is the pressure of the $e^+e^-\gamma$ system with chemical potential $\mu$, given in the ideal gas limit by

$$P^{(0)}(\mu, T) = \frac{T}{\pi^2} \int_0^\infty \mathrm{d}pp^2 \log\left[\frac{(1 + e^{-(E_e-\mu)/T})^2}{1 + e^{-p/T}}\right], \tag{D.34}$$

with $E_e = \sqrt{p^2 + m_e^2}$. Therefore,

$$m_D^2 = \frac{2e^2}{\pi^2 T} \int_0^\infty \mathrm{d}pp^2 f_{\mathrm{F}}(E)\left(1 - f_{\mathrm{F}}(E)\right). \tag{D.35}$$

One can then evaluate (D.35) in the limit $m_e \to 0$ by observing that

$$\int_0^\infty \mathrm{d}kk^2 f_{\mathrm{F}}(k)\left[1 - f_{\mathrm{F}}(k)\right] = \pi^2 T^3/6\,, \tag{D.36}$$

which yields the well-known HTL result $m_D^2 = 3\omega_p^2 = e^2T^2/3$ [28].

Moving on to the off-diagonal component $\Pi^{\mu\nu}_{+-}$, it takes the form

$$\begin{aligned}\Pi^{\mu\nu}_{+-} = i(ie)^2 \int \frac{\mathrm{d}^4k}{(2\pi)^4} 16\pi^2 \delta\left(k^2 - m_e^2\right)\left(f_{\mathrm{F}}(|k^0|) - \Theta(k^0)\right)\delta\left((k+P)^2 - m_e^2\right) \times \\ \times \left(f_{\mathrm{F}}(|k^0 + P^0|) - \Theta(-k^0 - P^0)\right) T^{\mu\nu}\,,\end{aligned} \tag{D.37}$$

where we defined

$$T^{\mu\nu} = -g^{\mu\nu} k \cdot P + 2k^\mu k^\nu + k^\nu P^\mu + k^\mu P^\nu. \tag{D.38}$$

We note that, in Eq. (D.37), the minus sign associated with the fermionic loop cancels against the one resulting from the different CTP vertices. In order to calculate this integral, we will follow a similar approach as in Sec. D.2 to obtain the thermal integrals. Decomposing $\boldsymbol{k}$ as in Eq. (D.8), we can use the two $\delta$-functions in Eq. (D.38) to fix $k^0 = \pm\sqrt{|\mathbf{k}|^2 + m_e^2}$ as well as the polar angle $\theta$

$$\cos\theta^*_\pm = \frac{P^2 \pm 2\omega P_0}{2|\boldsymbol{k}||\boldsymbol{P}|}. \tag{D.39}$$

Decomposing $T^{\mu\nu}$ into a longitudinal and transverse piece

$$T^L_\pm = \frac{P^2}{2} - \frac{P^2}{2|\boldsymbol{P}|^2}(P_0 \pm 2\omega)^2 \,, \tag{D.40a}$$

$$T^T_\pm = \frac{P^2}{2} - |\boldsymbol{k}|^2 \sin^2\theta^*_\pm \,, \tag{D.40b}$$

we get

$$\Pi^{L/T}_{+-} = -i\frac{2\alpha_{\rm em}}{|\boldsymbol{P}|}\times \tag{D.41}$$
$$\times \int_{m_e}^{\infty} {\rm d}\omega \sum_\pm \Theta(1-|\cos\theta^*_\pm|)(f_{\rm F}(\omega) - \Theta(k^0))(f_{\rm F}(|k^0+P^0|) - \Theta(-k^0-P^0))T^{L/T}_\pm ,$$

where the sum runs over positive and negative values of $k^0$. Making use of Eq. (D.36), we find that $\Pi^{L/T}_{+-}$ becomes in the HTL limit

$$\Pi^L_{+-} \overset{\rm HTL}{\approx} -i\frac{\pi e^2 P^2 T^3}{3|\boldsymbol{P}|^3}\Theta(|\boldsymbol{P}| - |P^0|), \tag{D.42}$$

$$\Pi^T_{+-} \overset{\rm HTL}{\approx} i\frac{\pi e^2 P^2 T^3}{6|\boldsymbol{P}|^3}\Theta(|\boldsymbol{P}| - |P^0|), \tag{D.43}$$

Using the relation (D.19), the imaginary part of $\Pi^{\mu\nu}_{++}$ can then be easily extracted from Eq. (D.41). We note in passing that the $+-$ self-energy vanishes for $P^2 \geq 0$ as naively expected from a simple kinematic analysis.

As will be explained in the next section, it is more convenient to resum the retarded and advanced propagators first. Using Eq. (D.19) and assuming thermal equilibrium, the associated self-energies read

$$\begin{aligned}\Pi^{T/L}_{R/A} = \Pi^{T/L}_{++} + \Pi^{T/L}_{+-/-+} &= {\rm Re}\,\Pi^{T/L}_{++} \pm \frac{1}{2}\left(\Pi^{T/L}_{+-} - \Pi^{T/L}_{-+}\right) \\ &= {\rm Re}\,\Pi^{T/L}_{++} \pm \frac{1}{2}\left(1 - e^{P_0/T}\right)\Pi^{T/L}_{+-} \,.\end{aligned} \tag{D.44}$$

The above equation makes evident that ${\rm Re}\,\Pi^R = {\rm Re}\,\Pi^A$ while ${\rm Im}\,\Pi^R = -{\rm Im}\,\Pi^A$.

As a cross-check, we can compare our results to previous works, [609] in particular. Since $\Pi^{L/T}_{R/A} \overset{\rm HTL}{\approx} {\rm Re}\,\Pi^{L/T}_{11} \mp \frac{P^0}{2T}\Pi^{L/T}_{12}$ in the HTL limit, our transverse self-energy agrees with [609]. While our longitudinal self-energy differs from [609, 611][4] by a term $P_0^2/|\boldsymbol{P}|^2$, it is however consistent with the more recent Ref. [28]. We also note that, at sufficiently high temperature $T \gtrsim 2\sqrt{3}m_e/e$, Eq. (D.41) would allow for photon decays into two electrons. This is unphysical [572] as the electron also pick up a sizeable thermal mass at such high temperatures. This could be resolved by additionally resumming the photon propagator. Such resummation is however not

[4] This different factor is responsible for the discrepancy between Fig. D.3 and figure 4 in [611].

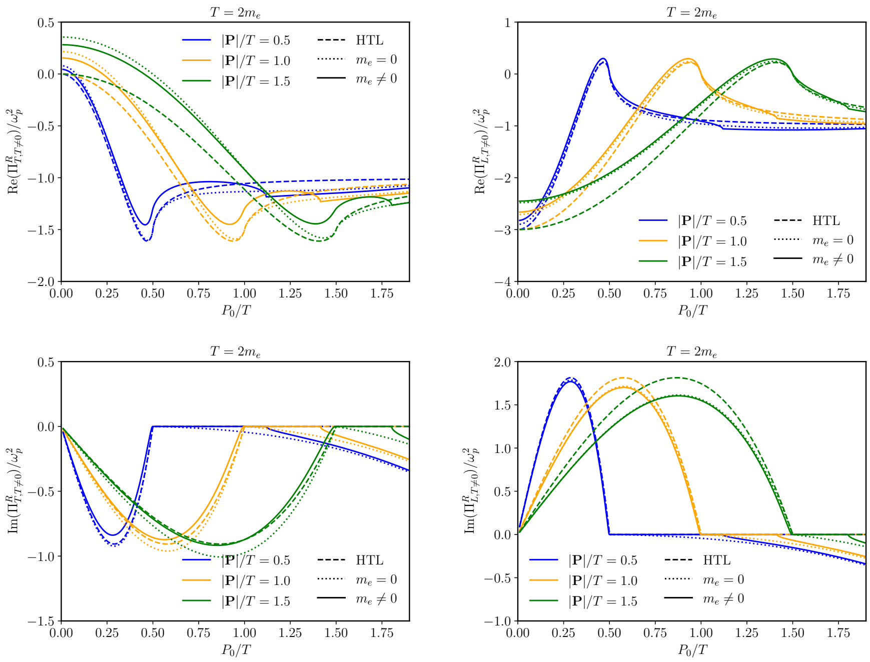

**Figure D.2:** Finite-temperature part of the retarded longitudinal and transverse photon self-energy normalised to the plasma frequency $\omega_p^2$. We compare for various choices of $|\boldsymbol{P}|/T$ the complete one-loop result (continuous lines) to its equivalent in the vanishing electron mass limit (dotted lines) and in the HTL approximation (dashed lines). For all subfigures, we set at $T = 2m_e$. Figure adapted from [4].

necessary for our purposes since the relevant dynamics for neutrino decoupling occur at lower temperatures.

We illustrate the energy, momentum and temperature dependence of these various self-energies in Figs. D.2 and D.3. In Fig. D.2, we display the dependence with $P_0/T$ of the real and the imaginary parts of the retarded transverse and longitudinal propagators for various choices of $|\boldsymbol{P}|/T$, setting the temperature to $T = 2m_e$ in all cases. We compare the full one-loop self-energy (in continuous) normalised to the plasma frequency $\omega_p^2$ to the corresponding result i) in the limit $m_e \to 0$ (in dotted) and ii) in the HTL limit (in dashed). We perform a similar analysis in Fig. D.3, fixing instead the ratio $|\boldsymbol{P}|/T = 0.5$ and choosing different benchmarks for the temperature. Interestingly, we observe that the finite electron mass has a visible impact on the self-energy even for temperatures close to neutrino decoupling, i.e. $T/m_e \sim 2$.

As highlighted in Sec. 2.2.1 (in the context of GW production), a useful approximation for weakly coupled theories is to replace the full 1PI-resummed propagator by a Breit-Wigner distribution peaking at $P_0 = w(|\mathbf{P}|)$, where $P_0 = w(|\mathbf{P}|)$ is a solution to the equation $P^2 + \mathrm{Re}\,\Pi_{11}^{T/L}(P) = 0$ and defines the dispersion relation of the different degrees of freedom of the photon. This dispersion relation is displayed

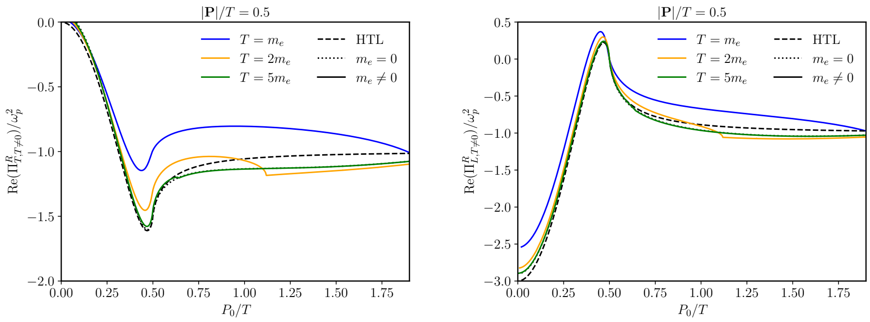


**Figure D.3:** Equivalent figure to Fig. D.2 but for fixed $|\boldsymbol{P}|/T = 0.5$ and different temperatures $T \in \{m_e, 2m_e, 5m_e\}$ instead. Figure adapted from [4].

for the benchmark $T = 2m_e$ case in Fig. D.4. While we do not make such approximation in this work, it might be useful for the interested reader to specify the residue of the transverse and longitudinal photon propagators, which are needed to make this approximation. These are in general quantified by

$$Z^{T/L} = \lim_{P_0 \to w(|\mathbf{P}|)} \left[ 1 + \frac{\partial \mathrm{Re}\, \Pi_{11}^{T/L}}{\partial P_0^2} \right]^{-1} . \tag{D.45}$$

and take the explicit form

$$\begin{aligned} Z^L = \Bigg[ 1 - \frac{\alpha_{\rm em}}{\pi |\mathbf{P}|^3} \int_{m_e}^{\infty} \mathrm{d}\omega f_{\rm F}(\omega) \Big[ \ell_2'(\omega, P) \left(4\omega P_0 P^2\right) + \ell_2(\omega, P) \times \\ \times \left(2\omega(3P_0 - |\mathbf{P}|^2/P_0)\right) + \ell_1'(\omega, P) \left(P^4 + 4\omega^2 P^2\right) \\ + \ell_1(\omega, P) \left(2P^2 + 4\omega^2\right) - 8|\boldsymbol{k}||\mathbf{P}| \Big]_{|P_0 = w(|\mathbf{P}|)} \Bigg]^{-1} , \end{aligned} \tag{D.46a}$$

$$\begin{aligned} Z^T = \Bigg[ 1 + \frac{\alpha_{\rm em}}{2\pi |\mathbf{P}|^3} \int_{m_e}^{\infty} \mathrm{d}\omega f_{\rm F}(\omega) \Big[ \ell_2'(\omega, P) \left(4\omega P_0 P^2\right) + \ell_2(\omega, P) \times \\ \times \left(2\omega(3P_0 - |\mathbf{P}|^2/P_0)\right) + \ell_1'(\omega, P) \left(P^4 + 4\omega^2 P_0^2 - 4|\boldsymbol{k}|^2|\mathbf{P}|^2 + 2P^2|\mathbf{P}|^2\right) \\ + \ell_1(\omega, P) \left(4\omega^2 + 2P_0^2\right) - 8|\boldsymbol{k}||\mathbf{P}| \Big]_{|P_0 = w(|\mathbf{P}|)} \Bigg]^{-1} . \end{aligned} \tag{D.46b}$$

In the above equations, we have defined the following derivatives

$$\ell_1'(\omega, P) \equiv \frac{\partial \ell_1}{\partial P_0^2} = \frac{2(P^2 + 2|\boldsymbol{k}||\mathbf{P}|) - 4\omega^2}{(P^2 + 2|\boldsymbol{k}||\mathbf{P}|)^2 - 4P_0^2\omega^2} - \frac{2(P^2 - 2|\boldsymbol{k}||\mathbf{P}|) - 4\omega^2}{(P^2 - 2|\boldsymbol{k}||\mathbf{P}|)^2 - 4P_0^2\omega^2}, \tag{D.47a}$$

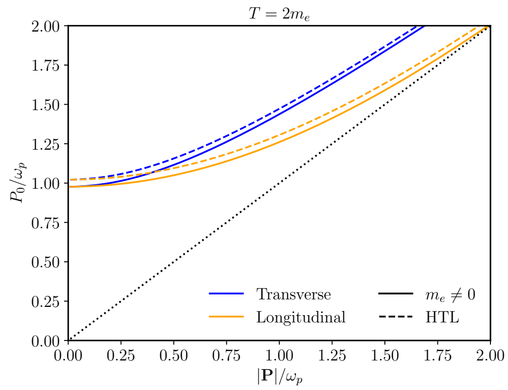


**Figure D.4:** Dispersion relation for transverse (blue lines) and longitudinal (orange lines) photons at the one-loop level with (continuous lines) and without (dashed lines) the HTL approximation at $T = 2m_e$. The black dotted line indicates the dispersion relation at zero temperature, i.e., $P_0^2 = |\mathbf{P}|^2$. Figure and caption adapted from [4].

$$\ell_2'(\omega, P) \equiv \frac{\partial \ell_2}{\partial P_0^2} = \frac{2P^2 - 4\omega(P_0\omega + |\mathbf{P}|\boldsymbol{k}|)/P_0}{P^4 - 4(P_0\omega + |\mathbf{P}||\boldsymbol{k}|)^2} - \frac{2P^2 - 4\omega(P_0\omega - |\mathbf{P}||\boldsymbol{k}|)/P_0}{P^4 - 4(P_0\omega - |\mathbf{P}||\boldsymbol{k}|)^2}, \tag{D.47b}$$

of the logarithmic functions $\ell_1(\omega, P)$ and $\ell_2(\omega, P)$ of Eq. (D.10).

## D.3.2 The resummed photon propagator

The 1PI-resummed photon propogator can be directly obtained from the Dyson-Schwinger equation

$$\bar{D}^{ab}_{\mu\nu} = D^{ab}_{\mu\nu} - \sum_{c,d} D^{ac}_{\mu\alpha}(\Pi^{\alpha\beta})^{cd}\bar{D}^{db}_{\beta\nu}. \tag{D.48}$$

In practice, the sum over the CTP indices $c$ and $d$ can be tedious. Fortunately, it can be avoided by working in the so-called R/A basis [30], i.e. by re-expressing Eq. (D.48) in terms of the retarded and advanced propagators. These are defined in momentum space in a similar fashion to the retarded/advanced self-energies (D.44), i.e.

$$D^R = D_{++} - D_{+-} = D_{-+} - D_{--}, \tag{D.49a}$$
$$D^A = D_{++} - D_{-+} = D_{+-} - D_{--}\,, \tag{D.49b}$$

where we dropped the Lorentz indices for simplicity. The results (D.49) can be derived exactly from Eq. (1.29) using the space-time translation invariance of systems in thermal equilibrium. Inserting Eq. (D.49) into the Dyson-Schwinger equation (D.48), one finds the simple explicit expression for the resummed propagator

$$\bar{D}^{R/A}_{\mu\nu} = D^{R/A}_{\mu\nu} - D^{R/A}_{\mu\alpha}(\Pi^{\alpha\beta})^{R/A}\bar{D}^{R/A}_{\beta\nu}. \tag{D.50}$$

Essentially, causality implies that there cannot be any closed loop constituted of retarded or advanced propagators only, which greatly simplifies the expression (D.48). As for the self-energies, one should decompose these resummed propagators into their transverse and longitudinal components

$$\bar{D}^{ab}_{\mu\nu} = d_{\mu\nu}\bar{D}^{ab} = -\bar{D}^{ab}_L P^L_{\mu\nu} - \bar{D}^{ab}_T P^T_{\mu\nu} - \xi\Delta^{ab}\frac{P_\mu P_\nu}{P^2} \ . \tag{D.51}$$

Using Eq. (D.50), one easily shows that $\bar{D}^{R/A}_{L/T}$ take the form

$$\bar{D}^{R/A}_{L/T} = \frac{1}{(\Delta^{R/A})^{-1} + \Pi^{R/A}_{L/T}}. \tag{D.52}$$

*In fine*, we are more directly interested in the $++$-component of the resummed propagator. Combining the definitions (1.23), (1.26) and (1.29), it is straightforward to show that

$$\bar{D}_{++} = \frac{1}{2}(\bar{D}^A + \bar{D}^R + 2\bar{D}^+) \ . \tag{D.53}$$

Moreover, in thermal equilibrium, the resummed statistical photon propagator[5] $\bar{D}^+_{\mu\nu}$ can itself be obtained from the retarded and advanced propagators through the relation [609]

$$\bar{D}^+_{\mu\nu}(P) = \frac{1}{2}[1 + 2f_B(|P^0|)]\text{sgn}(P^0)\left[\bar{D}^R_{\mu\nu} - \bar{D}^A_{\mu\nu}\right] \ . \tag{D.54}$$

Combining these results, one can therefore show that

$$\bar{D}^{L/T}_{++} = \frac{\Omega_{L/T}}{\Omega^2_{L/T} + \Gamma^2_{L/T}} - i[1 + 2f_{\text{B}}(|P^0|)]\text{sgn}(P^0)\frac{\Gamma_{L/T}}{\Omega^2_{L/T} + \Gamma^2_{L/T}} \ . \tag{D.55}$$

In the above equation, we defined

$$\Omega_{L/T} = P^2 + \text{Re}\,\Pi^R_{L/T}, \tag{D.56}$$

$$\Gamma_{L/T} = \text{Im}\,\Pi^R_{L/T} = -\frac{1}{2f_{\text{B}}(P^0)}\text{Im}\Pi^{L/T}_{+-}. \tag{D.57}$$

[5] See Eq. (1.26) for a definition in terms of the Wightman functions.

# Bibliography


[1] Marco Drewes, Yannis Georis, and Juraj Klarić, "Mapping the Viable Parameter Space for Testable Leptogenesis", *Phys. Rev. Lett.*, vol. 128, no. 5, pp. 051801, 2022.

[2] Marco Drewes, Yannis Georis, Claudia Hagedorn, and Juraj Klarić, "Low-scale leptogenesis with flavour and CP symmetries", *JHEP*, vol. 12, pp. 044, 2022.

[3] Marco Drewes, Yannis Georis, Juraj Klaric, and Philipp Klose, "Upper bound on thermal gravitational wave backgrounds from hidden sectors", *JCAP*, vol. 06, pp. 073, 2024.

[4] Marco Drewes, Yannis Georis, Michael Klasen, Luca Paolo Wiggering, and Yvonne Y. Y. Wong, "Towards a precision calculation of N $_{eff}$ in the Standard Model. Part III. Improved estimate of NLO contributions to the collision integral", *JCAP*, vol. 06, pp. 032, 2024.

[5] J. de Vries, M. Drewes, Y. Georis, J. Klarić, and V. Plakkot, "Confronting the low-scale seesaw and leptogenesis with neutrinoless double beta decay", *JHEP*, vol. 05, pp. 090, 2025.

[6] Marco Drewes, Yannis Georis, Juraj Klarić, and Antony Wendels, "On the collider-testability of the type-I seesaw model with 3 right-handed neutrinos", *JHEP*, vol. 03, pp. 176, 2025.

[7] Tobias Binder, Marco Drewes, Yannis Georis, Michael Klasen, Giovanni Pierobon, and Yvonne Y. Y. Wong, "Towards a precision calculation of $N_{\rm eff}$ in the Standard Model IV: Impact of positronium formation", 11 2024.

[8] Marco Drewes, Yannis Georis, Claudia Hagedorn, and Juraj Klaric, "Low-scale seesaw with flavour and CP symmetries – from colliders to leptogenesis", 12 2024.

[9] Marco Drewes, Yannis Georis, Juraj Klarić, and Inar Timiryasov, "Heavy Fermion Interaction Rates at Finite Temperature in Fermi Theory", To appear.

[10] Yannis Georis, "Parameter space for testable leptogenesis", in *57th Rencontres de Moriond on Electroweak Interactions and Unified Theories*, 5 2023.

[11] Yannis Georis, "Recent Developments in Testable Leptogenesis", *Acta Phys. Polon. Supp.*, vol. 17, no. 2, pp. 2–A22, 2024.

[12] M. A. Luty, "Baryogenesis via leptogenesis", *Phys. Rev. D*, vol. 45, pp. 455–465, 1992.

[13] Takeo Matsubara, "A New approach to quantum statistical mechanics", *Prog. Theor. Phys.*, vol. 14, pp. 351–378, 1955.

[14] Julian S. Schwinger, "Brownian motion of a quantum oscillator", *J. Math. Phys.*, vol. 2, pp. 407–432, 1961.

[15] L. V. Keldysh, "Diagram technique for nonequilibrium processes", *Zh. Eksp. Teor. Fiz.*, vol. 47, pp. 1515–1527, 1964.

[16] Pradip M. Bakshi and Kalyana T. Mahanthappa, "Expectation value formalism in quantum field theory. 1.", *J. Math. Phys.*, vol. 4, pp. 1–11, 1963.

[17] Pradip M. Bakshi and Kalyana T. Mahanthappa, "Expectation value formalism in quantum field theory. 2.", *J. Math. Phys.*, vol. 4, pp. 12–16, 1963.

[18] Yasushi Takahasi and Hiroomi Umezawa, "Thermo field dynamics", *Collect. Phenom.*, vol. 2, pp. 55–80, 1975.

[19] Y. Takahashi and H. Umezawa, "Thermo field dynamics", *Int. J. Mod. Phys. B*, vol. 10, pp. 1755–1805, 1996.

[20] Juan Martin Maldacena, "Non-Gaussian features of primordial fluctuations in single field inflationary models", *JHEP*, vol. 05, pp. 013, 2003.

[21] Steven Weinberg, "Quantum contributions to cosmological correlations", *Phys. Rev. D*, vol. 72, pp. 043514, 2005.

[22] Kuang-chao Chou, Zhao-bin Su, Bai-lin Hao, and Lu Yu, "Equilibrium and Nonequilibrium Formalisms Made Unified", *Phys. Rept.*, vol. 118, pp. 1–131, 1985.

[23] E. Calzetta and B. L. Hu, "Nonequilibrium Quantum Fields: Closed Time Path Effective Action, Wigner Function and Boltzmann Equation", *Phys. Rev. D*, vol. 37, pp. 2878, 1988.

[24] N. P. Landsman and C. G. van Weert, "Real and Imaginary Time Field Theory at Finite Temperature and Density", *Phys. Rept.*, vol. 145, pp. 141, 1987.

[25] Juergen Berges, "Introduction to nonequilibrium quantum field theory", *AIP Conf. Proc.*, vol. 739, no. 1, pp. 3–62, 2004.

[26] Jorgen Rammer, *Quantum field theory of non-equilibrium states*, 2007.

[27] Esteban A. Calzetta and Bei-Lok B. Hu, *Nonequilibrium Quantum Field Theory*, Oxford University Press, 2009.

[28] Michel Le Bellac, *Thermal Field Theory*, Cambridge Monographs on Mathematical Physics. Cambridge University Press, 3 2011.

[29] Torbjörn Lundberg and Roman Pasechnik, “Thermal Field Theory in real-time formalism: concepts and applications for particle decays”, *Eur. Phys. J. A*, vol. 57, no. 2, pp. 71, 2021.

[30] Jacopo Ghiglieri, Aleksi Kurkela, Michael Strickland, and Aleksi Vuorinen, “Perturbative Thermal QCD: Formalism and Applications”, *Phys. Rept.*, vol. 880, pp. 1–73, 2020.

[31] Michael E. Peskin and Daniel V. Schroeder, *An Introduction to quantum field theory*, Addison-Wesley, Reading, USA, 1995.

[32] Bjorn Garbrecht and Mathias Garny, “Finite Width in out-of-Equilibrium Propagators and Kinetic Theory”, *Annals Phys.*, vol. 327, pp. 914–934, 2012.

[33] AA Abrikosov, LP Gorkov, and IE Dzyaloshinskii, “On the application of quantum-field-theory methods to problems of quantum statistics at finite temperatures”, *Sov. Phys. JETP*, vol. 9, no. 3, pp. 636–641, 1959.

[34] ES Fradkin, “The green’s function method in quantum statistics”, *Nuclear Physics*, vol. 12, no. 5, pp. 465–484, 1959.

[35] Paul C Martin and Julian Schwinger, “Theory of many-particle systems. i”, *Physical Review*, vol. 115, no. 6, pp. 1342, 1959.

[36] Claude W. Bernard, “Feynman Rules for Gauge Theories at Finite Temperature”, *Phys. Rev. D*, vol. 9, pp. 3312, 1974.

[37] L. Dolan and R. Jackiw, “Symmetry Behavior at Finite Temperature”, *Phys. Rev. D*, vol. 9, pp. 3320–3341, 1974.

[38] Steven Weinberg, “Gauge and Global Symmetries at High Temperature”, *Phys. Rev. D*, vol. 9, pp. 3357–3378, 1974.

[39] Mathias Garny and Markus Michael Muller, “Kadanoff-Baym Equations with Non-Gaussian Initial Conditions: The Equilibrium Limit”, *Phys. Rev. D*, vol. 80, pp. 085011, 2009.

[40] John M. Cornwall, R. Jackiw, and E. Tomboulis, “Effective Action for Composite Operators”, *Phys. Rev. D*, vol. 10, pp. 2428–2445, 1974.

[41] R Wezeman, *Weyl quantization and Wigner distributions on phase space*, PhD thesis, Faculty of Science and Engineering, 2014.

[42] A. Hohenegger, A. Kartavtsev, and M. Lindner, “Deriving Boltzmann Equations from Kadanoff-Baym Equations in Curved Space-Time”, *Phys. Rev. D*, vol. 78, pp. 085027, 2008.

[43] Martin Beneke, Bjorn Garbrecht, Matti Herranen, and Pedro Schwaller, “Finite Number Density Corrections to Leptogenesis”, *Nucl. Phys. B*, vol. 838, pp. 1–27, 2010.

[44] Marco Drewes, Bjorn Garbrecht, Dario Gueter, and Juraj Klaric, "Leptogenesis from Oscillations of Heavy Neutrinos with Large Mixing Angles", *JHEP*, vol. 12, pp. 150, 2016.

[45] Edward W. Kolb and Michael S. Turner, *The Early Universe*, vol. 69, Taylor and Francis, 5 2019.

[46] B. P. Abbott et al., "Observation of Gravitational Waves from a Binary Black Hole Merger", *Phys. Rev. Lett.*, vol. 116, no. 6, pp. 061102, 2016.

[47] Gabriella Agazie et al., "The NANOGrav 15 yr Data Set: Evidence for a Gravitational-wave Background", *Astrophys. J. Lett.*, vol. 951, no. 1, pp. L8, 2023.

[48] Adeela Afzal et al., "The NANOGrav 15 yr Data Set: Search for Signals from New Physics", *Astrophys. J. Lett.*, vol. 951, no. 1, pp. L11, 2023, [Erratum: Astrophys.J.Lett. 971, L27 (2024), Erratum: Astrophys.J. 971, L27 (2024)].

[49] J. Antoniadis et al., "The second data release from the European Pulsar Timing Array - III. Search for gravitational wave signals", *Astron. Astrophys.*, vol. 678, pp. A50, 2023.

[50] Daniel J. Reardon et al., "Search for an Isotropic Gravitational-wave Background with the Parkes Pulsar Timing Array", *Astrophys. J. Lett.*, vol. 951, no. 1, pp. L6, 2023.

[51] Heng Xu et al., "Searching for the Nano-Hertz Stochastic Gravitational Wave Background with the Chinese Pulsar Timing Array Data Release I", *Res. Astron. Astrophys.*, vol. 23, no. 7, pp. 075024, 2023.

[52] Chiara Caprini and Daniel G. Figueroa, "Cosmological Backgrounds of Gravitational Waves", *Class. Quant. Grav.*, vol. 35, no. 16, pp. 163001, 2018.

[53] Kevork N. Abazajian et al., "CMB-S4 Science Book, First Edition", 10 2016.

[54] M. Punturo et al., "The Einstein Telescope: A third-generation gravitational wave observatory", *Class. Quant. Grav.*, vol. 27, pp. 194002, 2010.

[55] Michele Maggiore et al., "Science Case for the Einstein Telescope", *JCAP*, vol. 03, pp. 050, 2020.

[56] Adrian Abac et al., "The Science of the Einstein Telescope", 3 2025.

[57] David Reitze et al., "Cosmic Explorer: The U.S. Contribution to Gravitational-Wave Astronomy beyond LIGO", *Bull. Am. Astron. Soc.*, vol. 51, no. 7, pp. 035, 2019.

[58] Wen-Rui Hu and Yue-Liang Wu, "The Taiji Program in Space for gravitational wave physics and the nature of gravity", *Natl. Sci. Rev.*, vol. 4, no. 5, pp. 685–686, 2017.

[59] Jun Luo et al., “TianQin: a space-borne gravitational wave detector”, *Class. Quant. Grav.*, vol. 33, no. 3, pp. 035010, 2016.

[60] Pau Amaro-Seoane et al., “Laser Interferometer Space Antenna”, 2 2017.

[61] Seiji Kawamura et al., “The Japanese space gravitational wave antenna: DECIGO”, *Class. Quant. Grav.*, vol. 28, pp. 094011, 2011.

[62] Shuichi Sato et al., “The status of DECIGO”, *J. Phys. Conf. Ser.*, vol. 840, no. 1, pp. 012010, 2017.

[63] Vincent Corbin and Neil J. Cornish, “Detecting the cosmic gravitational wave background with the big bang observer”, *Class. Quant. Grav.*, vol. 23, pp. 2435–2446, 2006.

[64] Jeff Crowder and Neil J. Cornish, “Beyond LISA: Exploring future gravitational wave missions”, *Phys. Rev. D*, vol. 72, pp. 083005, 2005.

[65] G. M. Harry, P. Fritschel, D. A. Shaddock, W. Folkner, and E. S. Phinney, “Laser interferometry for the big bang observer”, *Class. Quant. Grav.*, vol. 23, pp. 4887–4894, 2006, [Erratum: Class.Quant.Grav. 23, 7361 (2006)].

[66] Naoki Seto, Seiji Kawamura, and Takashi Nakamura, “Possibility of direct measurement of the acceleration of the universe using 0.1-Hz band laser interferometer gravitational wave antenna in space”, *Phys. Rev. Lett.*, vol. 87, pp. 221103, 2001.

[67] Hideaki Kudoh, Atsushi Taruya, Takashi Hiramatsu, and Yoshiaki Himemoto, “Detecting a gravitational-wave background with next-generation space interferometers”, *Phys. Rev. D*, vol. 73, pp. 064006, 2006.

[68] Nancy Aggarwal et al., “Challenges and opportunities of gravitational-wave searches at MHz to GHz frequencies”, *Living Rev. Rel.*, vol. 24, no. 1, pp. 4, 2021.

[69] Nancy Aggarwal et al., “Challenges and Opportunities of Gravitational Wave Searches above 10 kHz”, 1 2025.

[70] Gian F. Giudice, Matthew McCullough, and Alfredo Urbano, “Hunting for Dark Particles with Gravitational Waves”, *JCAP*, vol. 10, pp. 001, 2016.

[71] Pierre Auclair et al., “Cosmology with the Laser Interferometer Space Antenna”, *Living Rev. Rel.*, vol. 26, no. 1, pp. 5, 2023.

[72] Rishav Roshan and Graham White, “Using gravitational waves to see the first second of the Universe”, *Rev. Mod. Phys.*, vol. 97, no. 1, pp. 015001, 2025.

[73] J. Ghiglieri and M. Laine, “Gravitational wave background from Standard Model physics: Qualitative features”, *JCAP*, vol. 07, pp. 022, 2015.

[74] J. Ghiglieri, G. Jackson, M. Laine, and Y. Zhu, “Gravitational wave background from Standard Model physics: Complete leading order”, *JHEP*, vol. 07, pp. 092, 2020.

[75] Andreas Ringwald, Jan Schütte-Engel, and Carlos Tamarit, “Gravitational Waves as a Big Bang Thermometer”, *JCAP*, vol. 03, pp. 054, 2021.

[76] K. Kajantie, M. Laine, K. Rummukainen, and Mikhail E. Shaposhnikov, “Is there a hot electroweak phase transition at $m_H \gtrsim m_W$?”, *Phys. Rev. Lett.*, vol. 77, pp. 2887–2890, 1996.

[77] Jerome Martin, Christophe Ringeval, and Vincent Vennin, “Encyclopædia Inflationaris: Opiparous Edition”, *Phys. Dark Univ.*, vol. 5-6, pp. 75–235, 2014.

[78] Jacopo Ghiglieri, Jan Schütte-Engel, and Enrico Speranza, “Freezing-in gravitational waves”, *Phys. Rev. D*, vol. 109, no. 2, pp. 023538, 2024.

[79] J. Ghiglieri, M. Laine, J. Schütte-Engel, and E. Speranza, “Double-graviton production from Standard Model plasma”, *JCAP*, vol. 04, pp. 062, 2024.

[80] Akio Hosoya, Masa-aki Sakagami, and Masaru Takao, “Nonequilibrium Thermodynamics in Field Theory: Transport Coefficients”, *Annals Phys.*, vol. 154, pp. 229, 1984.

[81] Sangyong Jeon, “Hydrodynamic transport coefficients in relativistic scalar field theory”, *Phys. Rev. D*, vol. 52, pp. 3591–3642, 1995.

[82] Sangyong Jeon and Laurence G. Yaffe, “From quantum field theory to hydrodynamics: Transport coefficients and effective kinetic theory”, *Phys. Rev. D*, vol. 53, pp. 5799–5809, 1996.

[83] Prateek Agrawal et al., “Feebly-interacting particles: FIPs 2020 workshop report”, *Eur. Phys. J. C*, vol. 81, no. 11, pp. 1015, 2021.

[84] C. Antel et al., “Feebly-interacting particles: FIPs 2022 Workshop Report”, *Eur. Phys. J. C*, vol. 83, no. 12, pp. 1122, 2023.

[85] Ryusuke Jinno, Bibhushan Shakya, and Jorinde van de Vis, “Gravitational Waves from Feebly Interacting Particles in a First Order Phase Transition”, 11 2022.

[86] P. Klose, M. Laine, and S. Procacci, “Gravitational wave background from non-Abelian reheating after axion-like inflation”, *JCAP*, vol. 05, pp. 021, 2022.

[87] P. Klose, M. Laine, and S. Procacci, “Gravitational wave background from vacuum and thermal fluctuations during axion-like inflation”, *JCAP*, vol. 12, pp. 020, 2022.

[88] G. Jackson and M. Laine, “Hydrodynamic fluctuations from a weakly coupled scalar field”, *Eur. Phys. J. C*, vol. 78, no. 4, pp. 304, 2018.

[89] Steven Weinberg, *Cosmology*, 2008.

[90] Lev Davidovich Landau, Evgenii Mikhailovich Lifshitz, and LP Pitaevskii, *Statistical physics: theory of the condensed state*, vol. 9, Butterworth-Heinemann, 1980.

[91] J. I. Kapusta, B. Muller, and M. Stephanov, "Relativistic Theory of Hydrodynamic Fluctuations with Applications to Heavy Ion Collisions", *Phys. Rev. C*, vol. 85, pp. 054906, 2012.

[92] Ryogo Kubo, "Statistical mechanical theory of irreversible processes. 1. General theory and simple applications in magnetic and conduction problems", *J. Phys. Soc. Jap.*, vol. 12, pp. 570–586, 1957.

[93] Leo P. Kadanoff and Paul C. Martin, "Hydrodynamic equations and correlation functions", *Annals Phys.*, vol. 24, pp. 419–469, 1963.

[94] H. Nyquist, "Thermal Agitation of Electric Charge in Conductors", *Phys. Rev.*, vol. 32, pp. 110–113, 1928.

[95] Herbert B. Callen and Theodore A. Welton, "Irreversibility and generalized noise", *Phys. Rev.*, vol. 83, pp. 34–40, 1951.

[96] G. Baym, H. Monien, C. J. Pethick, and D. G. Ravenhall, "Transverse Interactions and Transport in Relativistic Quark - Gluon and Electromagnetic Plasmas", *Phys. Rev. Lett.*, vol. 64, pp. 1867–1870, 1990.

[97] Peter Brockway Arnold, Guy D. Moore, and Laurence G. Yaffe, "Transport coefficients in high temperature gauge theories. 1. Leading log results", *JHEP*, vol. 11, pp. 001, 2000.

[98] Peter Brockway Arnold, Guy D. Moore, and Laurence G. Yaffe, "Effective kinetic theory for high temperature gauge theories", *JHEP*, vol. 01, pp. 030, 2003.

[99] Peter Brockway Arnold, Guy D Moore, and Laurence G. Yaffe, "Transport coefficients in high temperature gauge theories. 2. Beyond leading log", *JHEP*, vol. 05, pp. 051, 2003.

[100] D. J. Fixsen, "The Temperature of the Cosmic Microwave Background", *Astrophys. J.*, vol. 707, pp. 916–920, 2009.

[101] Gian Francesco Giudice, Edward W. Kolb, and Antonio Riotto, "Largest temperature of the radiation era and its cosmological implications", *Phys. Rev. D*, vol. 64, pp. 023508, 2001.

[102] Kyohei Mukaida and Masaki Yamada, "Thermalization Process after Inflation and Effective Potential of Scalar Field", *JCAP*, vol. 02, pp. 003, 2016.

[103] Ken'ichi Saikawa and Satoshi Shirai, "Primordial gravitational waves, precisely: The role of thermodynamics in the Standard Model", *JCAP*, vol. 05, pp. 035, 2018.

[104] S. Navas et al., "Review of particle physics", *Phys. Rev. D*, vol. 110, no. 3, pp. 030001, 2024.

[105] Massimo Giovannini, "Gravitational waves constraints on postinflationary phases stiffer than radiation", *Phys. Rev. D*, vol. 58, pp. 083504, 1998.

[106] Moritz Breitbach, Joachim Kopp, Eric Madge, Toby Opferkuch, and Pedro Schwaller, "Dark, Cold, and Noisy: Constraining Secluded Hidden Sectors with Gravitational Waves", *JCAP*, vol. 07, pp. 007, 2019.

[107] Katherine Freese and Martin Wolfgang Winkler, "Dark matter and gravitational waves from a dark big bang", *Phys. Rev. D*, vol. 107, no. 8, pp. 083522, 2023.

[108] Fatemeh Elahi, Christopher Kolda, and James Unwin, "UltraViolet Freeze-in", *JHEP*, vol. 03, pp. 048, 2015.

[109] Lev Kofman, Andrei D. Linde, and Alexei A. Starobinsky, "Reheating after inflation", *Phys. Rev. Lett.*, vol. 73, pp. 3195–3198, 1994.

[110] Lev Kofman, Andrei D. Linde, and Alexei A. Starobinsky, "Towards the theory of reheating after inflation", *Phys. Rev. D*, vol. 56, pp. 3258–3295, 1997.

[111] Marco Drewes and Jin U Kang, "The Kinematics of Cosmic Reheating", *Nucl. Phys. B*, vol. 875, pp. 315–350, 2013, [Erratum: Nucl.Phys.B 888, 284–286 (2014)].

[112] Yeuk-Kwan E. Cheung, Marco Drewes, Jin U Kang, and Jong Chol Kim, "Effective Action for Cosmological Scalar Fields at Finite Temperature", *JHEP*, vol. 08, pp. 059, 2015.

[113] Kai Schmitz, "New Sensitivity Curves for Gravitational-Wave Signals from Cosmological Phase Transitions", *JHEP*, vol. 01, pp. 097, 2021.

[114] Andreas Ringwald, Ken'ichi Saikawa, and Carlos Tamarit, "Primordial gravitational waves in a minimal model of particle physics and cosmology", *JCAP*, vol. 02, pp. 046, 2021.

[115] Eric Thrane and Joseph D. Romano, "Sensitivity curves for searches for gravitational-wave backgrounds", *Phys. Rev. D*, vol. 88, no. 12, pp. 124032, 2013.

[116] R. Abbott et al., "Upper limits on the isotropic gravitational-wave background from Advanced LIGO and Advanced Virgo's third observing run", *Phys. Rev. D*, vol. 104, no. 2, pp. 022004, 2021.

[117] N. Aghanim et al., "Planck 2018 results. VI. Cosmological parameters", *Astron. Astrophys.*, vol. 641, pp. A6, 2020, [Erratum: Astron.Astrophys. 652, C4 (2021)].

[118] Simone Aiola et al., "Snowmass2021 CMB-HD White Paper", 3 2022.

[119] Nicolas Herman, Léonard Lehoucq, and André Fúzfa, "Electromagnetic antennas for the resonant detection of the stochastic gravitational wave background", *Phys. Rev. D*, vol. 108, no. 12, pp. 124009, 2023.

[120] Pablo Navarro, Benito Gimeno, Juan Monzó-Cabrera, Alejandro Díaz-Morcillo, and Diego Blas, "Study of a cubic cavity resonator for gravitational waves detection in the microwave frequency range", *Phys. Rev. D*, vol. 109, no. 10, pp. 104048, 2024.

[121] Takehiko Asaka and Mikhail Shaposhnikov, "The $\nu$MSM, dark matter and baryon asymmetry of the universe", *Phys. Lett. B*, vol. 620, pp. 17–26, 2005.

[122] Guillermo Ballesteros, Javier Redondo, Andreas Ringwald, and Carlos Tamarit, "Standard Model—axion—seesaw—Higgs portal inflation. Five problems of particle physics and cosmology solved in one stroke", *JCAP*, vol. 08, pp. 001, 2017.

[123] Peter Minkowski, "$\mu \to e\gamma$ at a Rate of One Out of $10^9$ Muon Decays?", *Phys. Lett. B*, vol. 67, pp. 421–428, 1977.

[124] Murray Gell-Mann, Pierre Ramond, and Richard Slansky, "Complex Spinors and Unified Theories", *Conf. Proc. C*, vol. 790927, pp. 315–321, 1979.

[125] Rabindra N. Mohapatra and Goran Senjanovic, "Neutrino Mass and Spontaneous Parity Nonconservation", *Phys. Rev. Lett.*, vol. 44, pp. 912, 1980.

[126] Tsutomu Yanagida, "Horizontal Symmetry and Masses of Neutrinos", *Prog. Theor. Phys.*, vol. 64, pp. 1103, 1980.

[127] J. Schechter and J. W. F. Valle, "Neutrino Masses in SU(2) x U(1) Theories", *Phys. Rev. D*, vol. 22, pp. 2227, 1980.

[128] J. Schechter and J. W. F. Valle, "Neutrino Decay and Spontaneous Violation of Lepton Number", *Phys. Rev. D*, vol. 25, pp. 774, 1982.

[129] M. Fukugita and T. Yanagida, "Baryogenesis Without Grand Unification", *Phys. Lett. B*, vol. 174, pp. 45–47, 1986.

[130] Scott Dodelson and Lawrence M. Widrow, "Sterile-neutrinos as dark matter", *Phys. Rev. Lett.*, vol. 72, pp. 17–20, 1994.

[131] Xiang-Dong Shi and George M. Fuller, "A New dark matter candidate: Nonthermal sterile neutrinos", *Phys. Rev. Lett.*, vol. 82, pp. 2832–2835, 1999.

[132] Alexey Boyarsky, Oleg Ruchayskiy, and Mikhail Shaposhnikov, "The Role of sterile neutrinos in cosmology and astrophysics", *Ann. Rev. Nucl. Part. Sci.*, vol. 59, pp. 191–214, 2009.

[133] Marco Drewes, "The Phenomenology of Right Handed Neutrinos", *Int. J. Mod. Phys. E*, vol. 22, pp. 1330019, 2013.

[134] Asli M. Abdullahi et al., "The present and future status of heavy neutral leptons", *J. Phys. G*, vol. 50, no. 2, pp. 020501, 2023.

[135] Simone Biondini et al., "Status of rates and rate equations for thermal leptogenesis", *Int. J. Mod. Phys. A*, vol. 33, no. 05n06, pp. 1842004, 2018.

[136] Björn Garbrecht, Philipp Klose, and Carlos Tamarit, "Relativistic and spectator effects in leptogenesis with heavy sterile neutrinos", *JHEP*, vol. 02, pp. 117, 2020.

[137] G. F. Giudice, M. Peloso, A. Riotto, and I. Tkachev, "Production of massive fermions at preheating and leptogenesis", *JHEP*, vol. 08, pp. 014, 1999.

[138] Mikhail Shaposhnikov and Igor Tkachev, "The nuMSM, inflation, and dark matter", *Phys. Lett. B*, vol. 639, pp. 414–417, 2006.

[139] Raffaele Tito D'Agnolo and Sebastian A. R. Ellis, "Classical (and Quantum) Heuristics for Gravitational Wave Detection", 12 2024.

[140] Xinyao Guo, Haixing Miao, Zhi-Wei Wang, Huan Yang, and Ye-Ling Zhou, "There is Room at the Top: Fundamental Quantum Limits for Detecting Ultra-high Frequency Gravitational Waves", 1 2025.

[141] Asimina Arvanitaki and Andrew A. Geraci, "Detecting high-frequency gravitational waves with optically-levitated sensors", *Phys. Rev. Lett.*, vol. 110, no. 7, pp. 071105, 2013.

[142] Maxim Goryachev and Michael E. Tobar, "Gravitational Wave Detection with High Frequency Phonon Trapping Acoustic Cavities", *Phys. Rev. D*, vol. 90, no. 10, pp. 102005, 2014, [Erratum: Phys.Rev.D 108, 129901 (2023)].

[143] Nancy Aggarwal, George P. Winstone, Mae Teo, Masha Baryakhtar, Shane L. Larson, Vicky Kalogera, and Andrew A. Geraci, "Searching for New Physics with a Levitated-Sensor-Based Gravitational-Wave Detector", *Phys. Rev. Lett.*, vol. 128, no. 11, pp. 111101, 2022.

[144] Valerie Domcke and Camilo Garcia-Cely, "Potential of radio telescopes as high-frequency gravitational wave detectors", *Phys. Rev. Lett.*, vol. 126, no. 2, pp. 021104, 2021.

[145] Asher Berlin, Diego Blas, Raffaele Tito D'Agnolo, Sebastian A. R. Ellis, Roni Harnik, Yonatan Kahn, and Jan Schütte-Engel, "Detecting high-frequency gravitational waves with microwave cavities", *Phys. Rev. D*, vol. 105, no. 11, pp. 116011, 2022.

[146] Valerie Domcke, Camilo Garcia-Cely, and Nicholas L. Rodd, "Novel Search for High-Frequency Gravitational Waves with Low-Mass Axion Haloscopes", *Phys. Rev. Lett.*, vol. 129, no. 4, pp. 041101, 2022.

[147] Asher Berlin, Diego Blas, Raffaele Tito D'Agnolo, Sebastian A. R. Ellis, Roni Harnik, Yonatan Kahn, Jan Schütte-Engel, and Michael Wentzel, "Electromagnetic cavities as mechanical bars for gravitational waves", *Phys. Rev. D*, vol. 108, no. 8, pp. 084058, 2023.

[148] Roberto D. Peccei and Helen R. Quinn, "CP Conservation in the Presence of Instantons", *Phys. Rev. Lett.*, vol. 38, pp. 1440–1443, 1977.

[149] Roberto D. Peccei and Helen R. Quinn, "Constraints Imposed by CP Conservation in the Presence of Instantons", *Phys. Rev. D*, vol. 16, pp. 1791–1797, 1977.

[150] Frank Wilczek, "Problem of Strong P and T Invariance in the Presence of Instantons", *Phys. Rev. Lett.*, vol. 40, pp. 279–282, 1978.

[151] Steven Weinberg, "A New Light Boson?", *Phys. Rev. Lett.*, vol. 40, pp. 223–226, 1978.

[152] Luca Di Luzio, Maurizio Giannotti, Enrico Nardi, and Luca Visinelli, "The landscape of QCD axion models", *Phys. Rept.*, vol. 870, pp. 1–117, 2020.

[153] John Preskill, Mark B. Wise, and Frank Wilczek, "Cosmology of the Invisible Axion", *Phys. Lett. B*, vol. 120, pp. 127–132, 1983.

[154] Michael Dine and Willy Fischler, "The Not So Harmless Axion", *Phys. Lett. B*, vol. 120, pp. 137–141, 1983.

[155] L. F. Abbott and P. Sikivie, "A Cosmological Bound on the Invisible Axion", *Phys. Lett. B*, vol. 120, pp. 133–136, 1983.

[156] Matthew R. Adams et al., "Axion Dark Matter", *arXiv preprint*, 2022.

[157] Katherine Freese, Joshua A. Frieman, and Angela V. Olinto, "Natural inflation with pseudo Nambu-Goldstone bosons", *Phys. Rev. Lett.*, vol. 65, pp. 3233–3236, 1990.

[158] Kim Berghaus, Taniya Karwal, and Marc Kamionkowski, "Thermal Friction as a Solution to the Hubble Tension", *Phys. Rev. D*, vol. 99, pp. 083520, 2019.

[159] M. Laine, M. Meyer, and G. Nardini, "Thermal phase transition with full 2-loop effective potential", *JCAP*, vol. 10, pp. 014, 2021.

[160] Peter W. Graham, Igor G. Irastorza, Steven K. Lamoreaux, Axel Lindner, and Karl A. van Bibber, "Experimental Searches for the Axion and Axion-Like Particles", *Ann. Rev. Nucl. Part. Sci.*, vol. 65, pp. 485–514, 2015.

[161] Pierre Sikivie, "Invisible Axion Search Methods", *Rev. Mod. Phys.*, vol. 93, no. 1, pp. 015004, 2021.

[162] A. Blondel et al., "Searches for long-lived particles at the future FCC-ee", *Front. in Phys.*, vol. 10, pp. 967881, 2022.

[163] Georg G. Raffelt, "Astrophysical axion bounds", *Lect. Notes Phys.*, vol. 741, pp. 51–71, 2008.

[164] M. Laine, L. Niemi, S. Procacci, and K. Rummukainen, "Shape of the hot topological charge density spectral function", *JHEP*, vol. 11, pp. 126, 2022.

[165] Stephen F. King, Silvia Pascoli, Jessica Turner, and Ye-Ling Zhou, "Confronting SO(10) GUTs with proton decay and gravitational waves", *JHEP*, vol. 10, pp. 225, 2021.

[166] Bowen Fu, Stephen F. King, Luca Marsili, Silvia Pascoli, Jessica Turner, and Ye-Ling Zhou, "Testing realistic SO(10) SUSY GUTs with proton decay and gravitational waves", *Phys. Rev. D*, vol. 109, no. 5, pp. 055025, 2024.

[167] Lawrence J. Hall, Karsten Jedamzik, John March-Russell, and Stephen M. West, "Freeze-In Production of FIMP Dark Matter", *JHEP*, vol. 03, pp. 080, 2010.

[168] Evgeny K. Akhmedov, V. A. Rubakov, and A. Yu. Smirnov, "Baryogenesis via neutrino oscillations", *Phys. Rev. Lett.*, vol. 81, pp. 1359–1362, 1998.

[169] Juraj Klarić, Mikhail Shaposhnikov, and Inar Timiryasov, "Reconciling resonant leptogenesis and baryogenesis via neutrino oscillations", *Phys. Rev. D*, vol. 104, no. 5, pp. 055010, 2021.

[170] Shinya Kanemura and Kunio Kaneta, "Gravitational waves from particle decays during reheating", *Phys. Lett. B*, vol. 855, pp. 138807, 2024.

[171] Basabendu Barman, Nicolás Bernal, Yong Xu, and Óscar Zapata, "Bremsstrahlung-induced gravitational waves in monomial potentials during reheating", *Phys. Rev. D*, vol. 108, no. 8, pp. 083524, 2023.

[172] Basabendu Barman, Nicolás Bernal, Yong Xu, and Óscar Zapata, "Gravitational wave from graviton Bremsstrahlung during reheating", *JCAP*, vol. 05, pp. 019, 2023.

[173] Nicolás Bernal, Simon Cléry, Yann Mambrini, and Yong Xu, "Probing reheating with graviton bremsstrahlung", *JCAP*, vol. 01, pp. 065, 2024.

[174] Nicolás Bernal and Yong Xu, "Thermal gravitational waves during reheating", *JHEP*, vol. 01, pp. 137, 2025.

[175] Brian D. Fields, Keith A. Olive, Tsung-Han Yeh, and Charles Young, "Big-Bang Nucleosynthesis after Planck", *JCAP*, vol. 03, pp. 010, 2020, [Erratum: JCAP 11, E02 (2020)].

[176] Tsung-Han Yeh, Jessie Shelton, Keith A. Olive, and Brian D. Fields, "Probing physics beyond the standard model: limits from BBN and the CMB independently and combined", *JCAP*, vol. 10, pp. 046, 2022.

[177] A. D. Sakharov, "Violation of CP Invariance, C asymmetry, and baryon asymmetry of the universe", *Pisma Zh. Eksp. Teor. Fiz.*, vol. 5, pp. 32–35, 1967.

[178] C. S. Wu, E. Ambler, R. W. Hayward, D. D. Hoppes, and R. P. Hudson, "Experimental Test of Parity Conservation in $\beta$ Decay", *Phys. Rev.*, vol. 105, pp. 1413–1414, 1957.

[179] M. Goldhaber, L. Grodzins, and A. W. Sunyar, "Helicity of Neutrinos", *Phys. Rev.*, vol. 109, pp. 1015–1017, 1958.

[180] J. H. Christenson, J. W. Cronin, V. L. Fitch, and R. Turlay, "Evidence for the $2\pi$ Decay of the $K_2^0$ Meson", *Phys. Rev. Lett.*, vol. 13, pp. 138–140, 1964.

[181] Savas Dimopoulos and Leonard Susskind, "On the Baryon Number of the Universe", *Phys. Rev. D*, vol. 18, pp. 4500–4509, 1978.

[182] N. S. Manton, "Topology in the Weinberg-Salam Theory", *Phys. Rev. D*, vol. 28, pp. 2019, 1983.

[183] Frans R. Klinkhamer and N. S. Manton, "A Saddle Point Solution in the Weinberg-Salam Theory", *Phys. Rev. D*, vol. 30, pp. 2212, 1984.

[184] V. A. Kuzmin, V. A. Rubakov, and M. E. Shaposhnikov, "On the Anomalous Electroweak Baryon Number Nonconservation in the Early Universe", *Phys. Lett. B*, vol. 155, pp. 36, 1985.

[185] D. Toussaint, S. B. Treiman, Frank Wilczek, and A. Zee, "Matter - Antimatter Accounting, Thermodynamics, and Black Hole Radiation", *Phys. Rev. D*, vol. 19, pp. 1036–1045, 1979.

[186] Steven Weinberg, "Cosmological Production of Baryons", *Phys. Rev. Lett.*, vol. 42, pp. 850–853, 1979.

[187] M. E. Shaposhnikov, "Baryon Asymmetry of the Universe in Standard Electroweak Theory", *Nucl. Phys. B*, vol. 287, pp. 757–775, 1987.

[188] Glennys R. Farrar and M. E. Shaposhnikov, "Baryon asymmetry of the universe in the standard electroweak theory", *Phys. Rev. D*, vol. 50, pp. 774, 1994.

[189] M. B. Gavela, P. Hernandez, J. Orloff, and O. Pene, "Standard model CP violation and baryon asymmetry", *Mod. Phys. Lett. A*, vol. 9, pp. 795–810, 1994.

[190] M. B. Gavela, M. Lozano, J. Orloff, and O. Pene, "Standard model CP violation and baryon asymmetry. Part 1: Zero temperature", *Nucl. Phys. B*, vol. 430, pp. 345–381, 1994.

[191] M. B. Gavela, P. Hernandez, J. Orloff, O. Pene, and C. Quimbay, "Standard model CP violation and baryon asymmetry. Part 2: Finite temperature", *Nucl. Phys. B*, vol. 430, pp. 382–426, 1994.

[192] Patrick Huet and Eric Sather, "Electroweak baryogenesis and standard model CP violation", *Phys. Rev. D*, vol. 51, pp. 379–394, 1995.

[193] Motohiko Yoshimura, "Unified Gauge Theories and the Baryon Number of the Universe", *Phys. Rev. Lett.*, vol. 41, pp. 281–284, 1978.

[194] Motohiko Yoshimura, "Origin of Cosmological Baryon Asymmetry", *Phys. Lett. B*, vol. 88, pp. 294–298, 1979.

[195] Ian Affleck and Michael Dine, "A New Mechanism for Baryogenesis", *Nucl. Phys. B*, vol. 249, pp. 361–380, 1985.

[196] Andrew G. Cohen, D. B. Kaplan, and A. E. Nelson, "Progress in electroweak baryogenesis", *Ann. Rev. Nucl. Part. Sci.*, vol. 43, pp. 27–70, 1993.

[197] V. A. Rubakov and M. E. Shaposhnikov, "Electroweak baryon number nonconservation in the early universe and in high-energy collisions", *Usp. Fiz. Nauk*, vol. 166, pp. 493–537, 1996.

[198] David E. Morrissey and Michael J. Ramsey-Musolf, "Electroweak baryogenesis", *New J. Phys.*, vol. 14, pp. 125003, 2012.

[199] Marco Drewes, Jan Hajer, Juraj Klaric, and Gaia Lanfranchi, "NA62 sensitivity to heavy neutral leptons in the low scale seesaw model", *JHEP*, vol. 07, pp. 105, 2018.

[200] Eduardo Cortina Gil et al., "Search for heavy neutral lepton production in $K^+$ decays to positrons", *Phys. Lett. B*, vol. 807, pp. 135599, 2020.

[201] K. Abe et al., "Search for heavy neutrinos with the T2K near detector ND280", *Phys. Rev. D*, vol. 100, no. 5, pp. 052006, 2019.

[202] Georges Aad et al., "Search for Heavy Neutral Leptons in Decays of W Bosons Using a Dilepton Displaced Vertex in $\sqrt{s} = 13$ TeV pp Collisions with the ATLAS Detector", *Phys. Rev. Lett.*, vol. 131, no. 6, pp. 061803, 2023.

[203] M. Nayak et al., "Search for a heavy neutral lepton that mixes predominantly with the tau neutrino", *Phys. Rev. D*, vol. 109, no. 11, pp. L111102, 2024.

[204] Aram Hayrapetyan et al., "Search for long-lived heavy neutral leptons with lepton flavour conserving or violating decays to a jet and a charged lepton", *JHEP*, vol. 03, pp. 105, 2024.

[205] Aram Hayrapetyan et al., "Search for long-lived heavy neutrinos in the decays of B mesons produced in proton-proton collisions at $\sqrt{s}$ = 13 TeV", *JHEP*, vol. 06, pp. 183, 2024.

[206] Aram Hayrapetyan et al., "Search for heavy neutral leptons in final states with electrons, muons, and hadronically decaying tau leptons in proton-proton collisions at $\sqrt{s}$ = 13 TeV", *JHEP*, vol. 06, pp. 123, 2024.

[207] Aram Hayrapetyan et al., "Search for long-lived heavy neutral leptons decaying in the CMS muon detectors in proton-proton collisions at $\sqrt{s} = 13$ TeV", *Phys. Rev. D*, vol. 110, pp. 012004, 2024.

[208] Aram Hayrapetyan et al., "Search for long-lived heavy neutral leptons in proton-proton collision events with a lepton-jet pair associated with a secondary vertex at $\sqrt{s}$ = 13 TeV", *JHEP*, vol. 02, pp. 036, 2025.

[209] Igor Krasnov, "DUNE prospects in the search for sterile neutrinos", *Phys. Rev. D*, vol. 100, no. 7, pp. 075023, 2019.

[210] Peter Ballett, Tommaso Boschi, and Silvia Pascoli, "Heavy Neutral Leptons from low-scale seesaws at the DUNE Near Detector", *JHEP*, vol. 03, pp. 111, 2020.

[211] Julian Y. Günther, Jordy de Vries, Herbi K. Dreiner, Zeren Simon Wang, and Guanghui Zhou, "Long-lived neutral fermions at the DUNE near detector", *JHEP*, vol. 01, pp. 108, 2024.

[212] Sergey Alekhin et al., "A facility to Search for Hidden Particles at the CERN SPS: the SHiP physics case", *Rept. Prog. Phys.*, vol. 79, no. 12, pp. 124201, 2016.

[213] C. Ahdida et al., "Sensitivity of the SHiP experiment to Heavy Neutral Leptons", *JHEP*, vol. 04, pp. 077, 2019.

[214] Dmitry Gorbunov, Igor Krasnov, Yury Kudenko, and Sergey Suvorov, "Heavy Neutral Leptons from kaon decays in the SHiP experiment", *Phys. Lett. B*, vol. 810, pp. 135817, 2020.

[215] Silvia Pascoli, Richard Ruiz, and Cedric Weiland, "Heavy neutrinos with dynamic jet vetoes: multilepton searches at $\sqrt{s} = 14$ , 27, and 100 TeV", *JHEP*, vol. 06, pp. 049, 2019.

[216] Marco Drewes and Jan Hajer, "Heavy Neutrinos in displaced vertex searches at the LHC and HL-LHC", *JHEP*, vol. 02, pp. 070, 2020.

[217] S. Abe et al., "Search for Majorana Neutrinos with the Complete KamLAND-Zen Dataset", 6 2024.

[218] J. B. Albert et al., "Sensitivity and Discovery Potential of nEXO to Neutrinoless Double Beta Decay", *Phys. Rev. C*, vol. 97, no. 6, pp. 065503, 2018.

[219] N. Abgrall et al., "The Large Enriched Germanium Experiment for Neutrinoless Double Beta Decay (LEGEND)", *AIP Conf. Proc.*, vol. 1894, no. 1, pp. 020027, 2017.

[220] J. Aalbers et al., "Neutrinoless double beta decay sensitivity of the XLZD rare event observatory", *J. Phys. G*, vol. 52, no. 4, pp. 045102, 2025.

[221] R. J. Barlow, "The PRISM/PRIME project", *Nucl. Phys. B Proc. Suppl.*, vol. 218, pp. 44–49, 2011.

[222] L. Bartoszek et al., "Mu2e Technical Design Report", 10 2014.

[223] Yoshitaka Kuno, "*Charged lepton flavour violation*", Plenary talk at the 31st International Symposium on Lepton Photon Interactions at High Energies, Melbourne, Australia, July 2023.

[224] R. Abramishvili et al., "COMET Phase-I Technical Design Report", *PTEP*, vol. 2020, no. 3, pp. 033C01, 2020.

[225] A. M. Baldini et al., "The design of the MEG II experiment", *Eur. Phys. J. C*, vol. 78, no. 5, pp. 380, 2018.

[226] K. Arndt et al., "Technical design of the phase I Mu3e experiment", *Nucl. Instrum. Meth. A*, vol. 1014, pp. 165679, 2021.

[227] Alessandro M. Baldini et al., "The Search for $\mu$+ $\rightarrow$ e+$\gamma$ with 10–14 Sensitivity: The Upgrade of the MEG Experiment", *Symmetry*, vol. 13, no. 9, pp. 1591, 2021.

[228] K. Afanaciev et al., "A search for $\mu^+ \rightarrow e^+\gamma$ with the first dataset of the MEG II experiment", *Eur. Phys. J. C*, vol. 84, no. 3, pp. 216, 2024, [Erratum: Eur.Phys.J.C 84, 1042 (2024)].

[229] K. Afanaciev et al., "New limit on the $\mu$+->e+$\gamma$ decay with the MEG II experiment", 4 2025.

[230] W. Pauli, "Dear radioactive ladies and gentlemen", *Phys. Today*, vol. 31N9, pp. 27, 1978.

[231] C. L. Cowan, F. Reines, F. B. Harrison, H. W. Kruse, and A. D. McGuire, "Detection of the free neutrino: A Confirmation", *Science*, vol. 124, pp. 103–104, 1956.

[232] Raymond Davis, Jr., Don S. Harmer, and Kenneth C. Hoffman, "Search for neutrinos from the sun", *Phys. Rev. Lett.*, vol. 20, pp. 1205–1209, 1968.

[233] Y. Fukuda et al., "Evidence for oscillation of atmospheric neutrinos", *Phys. Rev. Lett.*, vol. 81, pp. 1562–1567, 1998.

[234] Q. R. Ahmad et al., "Measurement of the rate of $\nu_e + d \rightarrow p + p + e^-$ interactions produced by $^8$B solar neutrinos at the Sudbury Neutrino Observatory", *Phys. Rev. Lett.*, vol. 87, pp. 071301, 2001.

[235] Q. R. Ahmad et al., "Direct evidence for neutrino flavor transformation from neutral current interactions in the Sudbury Neutrino Observatory", *Phys. Rev. Lett.*, vol. 89, pp. 011301, 2002.

[236] Ivan Esteban, M. C. Gonzalez-Garcia, Michele Maltoni, Ivan Martinez-Soler, João Paulo Pinheiro, and Thomas Schwetz, "NuFit-6.0: updated global analysis of three-flavor neutrino oscillations", *JHEP*, vol. 12, pp. 216, 2024.

[237] F. Maltoni, J. M. Niczyporuk, and S. Willenbrock, "Upper bound on the scale of Majorana neutrino mass generation", *Phys. Rev. Lett.*, vol. 86, pp. 212–215, 2001.

[238] Francesco Vissani, "Do experiments suggest a hierarchy problem?", *Phys. Rev. D*, vol. 57, pp. 7027–7030, 1998.

[239] Jackson D. Clarke, Robert Foot, and Raymond R. Volkas, "Electroweak naturalness in the three-flavor type I seesaw model and implications for leptogenesis", *Phys. Rev. D*, vol. 91, no. 7, pp. 073009, 2015.

[240] Werner Rodejohann and He Zhang, "Impact of massive neutrinos on the Higgs self-coupling and electroweak vacuum stability", *JHEP*, vol. 06, pp. 022, 2012.

[241] Subrata Khan, Srubabati Goswami, and Sourov Roy, "Vacuum Stability constraints on the minimal singlet TeV Seesaw Model", *Phys. Rev. D*, vol. 89, no. 7, pp. 073021, 2014.

[242] Luigi Delle Rose, Carlo Marzo, and Alfredo Urbano, "On the stability of the electroweak vacuum in the presence of low-scale seesaw models", *JHEP*, vol. 12, pp. 050, 2015.

[243] Gulab Bambhaniya, P. S. Bhupal Dev, Srubabati Goswami, Subrata Khan, and Werner Rodejohann, "Naturalness, Vacuum Stability and Leptogenesis in the Minimal Seesaw Model", *Phys. Rev. D*, vol. 95, no. 9, pp. 095016, 2017.

[244] Seyda Ipek, Alexis D. Plascencia, and Jessica Turner, "Assessing Perturbativity and Vacuum Stability in High-Scale Leptogenesis", *JHEP*, vol. 12, pp. 111, 2018.

[245] Sanjoy Mandal, Rahul Srivastava, and José W. F. Valle, "Consistency of the dynamical high-scale type-I seesaw mechanism", *Phys. Rev. D*, vol. 101, no. 11, pp. 115030, 2020.

[246] Garv Chauhan and Thomas Steingasser, "Gravity-improved metastability bounds for the Type-I seesaw mechanism", *JHEP*, vol. 09, pp. 151, 2023.

[247] Mikhail Shaposhnikov, "A Possible symmetry of the nuMSM", *Nucl. Phys. B*, vol. 763, pp. 49–59, 2007.

[248] Jörn Kersten and Alexei Yu. Smirnov, "Right-Handed Neutrinos at CERN LHC and the Mechanism of Neutrino Mass Generation", *Phys. Rev. D*, vol. 76, pp. 073005, 2007.

[249] K. Moffat, S. Pascoli, and C. Weiland, "Equivalence between massless neutrinos and lepton number conservation in fermionic singlet extensions of the Standard Model", 12 2017.

[250] Marco Drewes, "On the Minimal Mixing of Heavy Neutrinos", 4 2019.

[251] R. N. Mohapatra, "Mechanism for Understanding Small Neutrino Mass in Superstring Theories", *Phys. Rev. Lett.*, vol. 56, pp. 561–563, 1986.

[252] R. N. Mohapatra and J. W. F. Valle, "Neutrino Mass and Baryon Number Nonconservation in Superstring Models", *Phys. Rev. D*, vol. 34, pp. 1642, 1986.

[253] J. Bernabeu, A. Santamaria, J. Vidal, A. Mendez, and J. W. F. Valle, "Lepton Flavor Nonconservation at High-Energies in a Superstring Inspired Standard Model", *Phys. Lett. B*, vol. 187, pp. 303–308, 1987.

[254] Evgeny K. Akhmedov, Manfred Lindner, Erhard Schnapka, and J. W. F. Valle, "Left-right symmetry breaking in NJL approach", *Phys. Lett. B*, vol. 368, pp. 270–280, 1996.

[255] Evgeny K. Akhmedov, Manfred Lindner, Erhard Schnapka, and J. W. F. Valle, "Dynamical left-right symmetry breaking", *Phys. Rev. D*, vol. 53, pp. 2752–2780, 1996.

[256] J. A. Casas and A. Ibarra, "Oscillating neutrinos and $\mu \to e, \gamma$", *Nucl. Phys. B*, vol. 618, pp. 171–204, 2001.

[257] Mattias Blennow and Enrique Fernandez-Martinez, "Parametrization of Seesaw Models and Light Sterile Neutrinos", *Phys. Lett. B*, vol. 704, pp. 223–229, 2011.

[258] A. Donini, P. Hernandez, J. Lopez-Pavon, M. Maltoni, and T. Schwetz, "The minimal 3+2 neutrino model versus oscillation anomalies", *JHEP*, vol. 07, pp. 161, 2012.

[259] Marco Drewes, Bjorn Garbrecht, Dario Gueter, and Juraj Klaric, "Testing the low scale seesaw and leptogenesis", *JHEP*, vol. 08, pp. 018, 2017.

[260] Apostolos Pilaftsis, "Radiatively induced neutrino masses and large Higgs neutrino couplings in the standard model with Majorana fields", *Z. Phys. C*, vol. 55, pp. 275–282, 1992.

[261] J. Lopez-Pavon, E. Molinaro, and S. T. Petcov, "Radiative Corrections to Light Neutrino Masses in Low Scale Type I Seesaw Scenarios and Neutrinoless Double Beta Decay", *JHEP*, vol. 11, pp. 030, 2015.

[262] W. Buchmuller, P. Di Bari, and M. Plumacher, "Leptogenesis for pedestrians", *Annals Phys.*, vol. 315, pp. 305–351, 2005.

[263] W. Buchmuller, R. D. Peccei, and T. Yanagida, "Leptogenesis as the origin of matter", *Ann. Rev. Nucl. Part. Sci.*, vol. 55, pp. 311–355, 2005.

[264] Sacha Davidson, Enrico Nardi, and Yosef Nir, "Leptogenesis", *Phys. Rept.*, vol. 466, pp. 105–177, 2008.

[265] M. Drewes, B. Garbrecht, P. Hernandez, M. Kekic, J. Lopez-Pavon, J. Racker, N. Rius, J. Salvado, and D. Teresi, "ARS Leptogenesis", *Int. J. Mod. Phys. A*, vol. 33, no. 05n06, pp. 1842002, 2018.

[266] Bhupal Dev, Mathias Garny, Juraj Klaric, Peter Millington, and Daniele Teresi, "Resonant enhancement in leptogenesis", *Int. J. Mod. Phys. A*, vol. 33, pp. 1842003, 2018.

[267] P. S. Bhupal Dev, Pasquale Di Bari, Bjorn Garbrecht, Stéphane Lavignac, Peter Millington, and Daniele Teresi, "Flavor effects in leptogenesis", *Int. J. Mod. Phys. A*, vol. 33, pp. 1842001, 2018.

[268] E. J. Chun et al., "Probing Leptogenesis", *Int. J. Mod. Phys. A*, vol. 33, no. 05n06, pp. 1842005, 2018.

[269] Björn Garbrecht, "Why is there more matter than antimatter? Calculational methods for leptogenesis and electroweak baryogenesis", *Prog. Part. Nucl. Phys.*, vol. 110, pp. 103727, 2020.

[270] Dietrich Bodeker and Wilfried Buchmuller, "Baryogenesis from the weak scale to the grand unification scale", *Rev. Mod. Phys.*, vol. 93, no. 3, pp. 035004, 2021.

[271] Gerard 't Hooft, "Symmetry Breaking Through Bell-Jackiw Anomalies", *Phys. Rev. Lett.*, vol. 37, pp. 8–11, 1976.

[272] Gerard 't Hooft, "Computation of the Quantum Effects Due to a Four-Dimensional Pseudoparticle", *Phys. Rev. D*, vol. 14, pp. 3432–3450, 1976, [Erratum: Phys.Rev.D 18, 2199 (1978)].

[273] Peter Brockway Arnold and Larry D. McLerran, "Sphalerons, Small Fluctuations and Baryon Number Violation in Electroweak Theory", *Phys. Rev. D*, vol. 36, pp. 581, 1987.

[274] Peter Brockway Arnold and Larry D. McLerran, "The Sphaleron Strikes Back", *Phys. Rev. D*, vol. 37, pp. 1020, 1988.

[275] S. Yu. Khlebnikov and M. E. Shaposhnikov, "The Statistical Theory of Anomalous Fermion Number Nonconservation", *Nucl. Phys. B*, vol. 308, pp. 885–912, 1988.

[276] Jan Ambjorn, T. Askgaard, H. Porter, and M. E. Shaposhnikov, "Sphaleron transitions and baryon asymmetry: A Numerical real time analysis", *Nucl. Phys. B*, vol. 353, pp. 346–378, 1991.

[277] Michela D'Onofrio, Kari Rummukainen, and Anders Tranberg, "Sphaleron Rate in the Minimal Standard Model", *Phys. Rev. Lett.*, vol. 113, no. 14, pp. 141602, 2014.

[278] Wilfried Buchmuller and Michael Plumacher, "Matter antimatter asymmetry and neutrino properties", *Phys. Rept.*, vol. 320, pp. 329–339, 1999.

[279] Sacha Davidson and Alejandro Ibarra, “A Lower bound on the right-handed neutrino mass from leptogenesis”, *Phys. Lett. B*, vol. 535, pp. 25–32, 2002.

[280] W. Buchmuller, P. Di Bari, and M. Plumacher, “A Bound on neutrino masses from baryogenesis”, *Phys. Lett. B*, vol. 547, pp. 128–132, 2002.

[281] W. Buchmuller, P. Di Bari, and M. Plumacher, “The Neutrino mass window for baryogenesis”, *Nucl. Phys. B*, vol. 665, pp. 445–468, 2003.

[282] Björn Garbrecht and Edward Wang, “The neutrino mass bound from leptogenesis revisited”, *JHEP*, vol. 03, pp. 008, 2025.

[283] J. Racker, Manuel Pena, and Nuria Rius, “Leptogenesis with small violation of B-L”, *JCAP*, vol. 07, pp. 030, 2012.

[284] K. Moffat, S. Pascoli, S. T. Petcov, H. Schulz, and J. Turner, “Three-flavored nonresonant leptogenesis at intermediate scales”, *Phys. Rev. D*, vol. 98, no. 1, pp. 015036, 2018.

[285] Jiang Liu and Gino Segre, “Reexamination of generation of baryon and lepton number asymmetries by heavy particle decay”, *Phys. Rev. D*, vol. 48, pp. 4609–4612, 1993.

[286] Marion Flanz, Emmanuel A. Paschos, and Utpal Sarkar, “Baryogenesis from a lepton asymmetric universe”, *Phys. Lett. B*, vol. 345, pp. 248–252, 1995, [Erratum: Phys.Lett.B 384, 487–487 (1996), Erratum: Phys.Lett.B 382, 447–447 (1996)].

[287] Marion Flanz, Emmanuel A. Paschos, Utpal Sarkar, and Jan Weiss, “Baryogenesis through mixing of heavy Majorana neutrinos”, *Phys. Lett. B*, vol. 389, pp. 693–699, 1996.

[288] Laura Covi, Esteban Roulet, and Francesco Vissani, “CP violating decays in leptogenesis scenarios”, *Phys. Lett. B*, vol. 384, pp. 169–174, 1996.

[289] Apostolos Pilaftsis, “CP violation and baryogenesis due to heavy Majorana neutrinos”, *Phys. Rev. D*, vol. 56, pp. 5431–5451, 1997.

[290] Apostolos Pilaftsis and Thomas E. J. Underwood, “Resonant leptogenesis”, *Nucl. Phys. B*, vol. 692, pp. 303–345, 2004.

[291] Apostolos Pilaftsis, “Resonant tau-leptogenesis with observable lepton number violation”, *Phys. Rev. Lett.*, vol. 95, pp. 081602, 2005.

[292] Apostolos Pilaftsis and Thomas E. J. Underwood, “Electroweak-scale resonant leptogenesis”, *Phys. Rev. D*, vol. 72, pp. 113001, 2005.

[293] Juraj Klarić, Mikhail Shaposhnikov, and Inar Timiryasov, “Uniting Low-Scale Leptogenesis Mechanisms”, *Phys. Rev. Lett.*, vol. 127, no. 11, pp. 111802, 2021.

[294] Marco Drewes and Björn Garbrecht, "Leptogenesis from a GeV Seesaw without Mass Degeneracy", *JHEP*, vol. 03, pp. 096, 2013.

[295] Valerie Domcke, Marco Drewes, Marco Hufnagel, and Michele Lucente, "MeV-scale Seesaw and Leptogenesis", *JHEP*, vol. 01, pp. 200, 2021.

[296] Bjorn Garbrecht and Matti Herranen, "Effective Theory of Resonant Leptogenesis in the Closed-Time-Path Approach", *Nucl. Phys. B*, vol. 861, pp. 17–52, 2012.

[297] G. Sigl and G. Raffelt, "General kinetic description of relativistic mixed neutrinos", *Nucl. Phys. B*, vol. 406, pp. 423–451, 1993.

[298] Wilfried Buchmuller and Stefan Fredenhagen, "Quantum mechanics of baryogenesis", *Phys. Lett. B*, vol. 483, pp. 217–224, 2000.

[299] D. Boyanovsky, K. Davey, and Chiu Man Ho, "Particle abundance in a thermal plasma: Quantum kinetics vs. Boltzmann equation", *Phys. Rev. D*, vol. 71, pp. 023523, 2005.

[300] Andrea De Simone and Antonio Riotto, "Quantum Boltzmann Equations and Leptogenesis", *JCAP*, vol. 08, pp. 002, 2007.

[301] M. Garny, A. Hohenegger, A. Kartavtsev, and M. Lindner, "Systematic approach to leptogenesis in nonequilibrium QFT: Vertex contribution to the CP-violating parameter", *Phys. Rev. D*, vol. 80, pp. 125027, 2009.

[302] M. Garny, A. Hohenegger, A. Kartavtsev, and M. Lindner, "Systematic approach to leptogenesis in nonequilibrium QFT: Self-energy contribution to the CP-violating parameter", *Phys. Rev. D*, vol. 81, pp. 085027, 2010.

[303] M. Garny, A. Hohenegger, and A. Kartavtsev, "Medium corrections to the CP-violating parameter in leptogenesis", *Phys. Rev. D*, vol. 81, pp. 085028, 2010.

[304] Alexey Anisimov, Wilfried Buchmüller, Marco Drewes, and Sebastián Mendizabal, "Leptogenesis from Quantum Interference in a Thermal Bath", *Phys. Rev. Lett.*, vol. 104, pp. 121102, 2010.

[305] Martin Beneke, Bjorn Garbrecht, Christian Fidler, Matti Herranen, and Pedro Schwaller, "Flavoured Leptogenesis in the CTP Formalism", *Nucl. Phys. B*, vol. 843, pp. 177–212, 2011.

[306] Jean-Sebastien Gagnon and Mikhail Shaposhnikov, "Baryon Asymmetry of the Universe without Boltzmann or Kadanoff-Baym equations", *Phys. Rev. D*, vol. 83, pp. 065021, 2011.

[307] A. Anisimov, W. Buchmüller, M. Drewes, and S. Mendizabal, "Quantum Leptogenesis I", *Annals Phys.*, vol. 326, pp. 1998–2038, 2011, [Erratum: Annals Phys. 338, 376–377 (2011)].

[308] Mathias Garny, Alexander Kartavtsev, and Andreas Hohenegger, "Leptogenesis from first principles in the resonant regime", *Annals Phys.*, vol. 328, pp. 26–63, 2013.

[309] P. S. Bhupal Dev, Peter Millington, Apostolos Pilaftsis, and Daniele Teresi, "Flavour Covariant Transport Equations: an Application to Resonant Leptogenesis", *Nucl. Phys. B*, vol. 886, pp. 569–664, 2014.

[310] P. S. Bhupal Dev, Peter Millington, Apostolos Pilaftsis, and Daniele Teresi, "Kadanoff–Baym approach to flavour mixing and oscillations in resonant leptogenesis", *Nucl. Phys. B*, vol. 891, pp. 128–158, 2015.

[311] J. Ghiglieri and M. Laine, "GeV-scale hot sterile neutrino oscillations: a derivation of evolution equations", *JHEP*, vol. 05, pp. 132, 2017.

[312] J. Ghiglieri and M. Laine, "Precision study of GeV-scale resonant leptogenesis", *JHEP*, vol. 02, pp. 014, 2019.

[313] Henri Jukkala, Kimmo Kainulainen, and Pyry M. Rahkila, "Flavour mixing transport theory and resonant leptogenesis", *JHEP*, vol. 09, pp. 119, 2021.

[314] Steve Blanchet, Pasquale Di Bari, David A. Jones, and Luca Marzola, "Leptogenesis with heavy neutrino flavours: from density matrix to Boltzmann equations", *JCAP*, vol. 01, pp. 041, 2013.

[315] Riccardo Barbieri, Paolo Creminelli, Alessandro Strumia, and Nikolaos Tetradis, "Baryogenesis through leptogenesis", *Nucl. Phys. B*, vol. 575, pp. 61–77, 2000.

[316] W. Buchmuller and M. Plumacher, "Spectator processes and baryogenesis", *Phys. Lett. B*, vol. 511, pp. 74–76, 2001.

[317] J. Ghiglieri and M. Laine, "Neutrino dynamics below the electroweak crossover", *JCAP*, vol. 07, pp. 015, 2016.

[318] S. Eijima, M. Shaposhnikov, and I. Timiryasov, "Freeze-out of baryon number in low-scale leptogenesis", *JCAP*, vol. 11, pp. 030, 2017.

[319] Björn Garbrecht and Pedro Schwaller, "Spectator Effects during Leptogenesis in the Strong Washout Regime", *JCAP*, vol. 10, pp. 012, 2014.

[320] M. Laine, "Sterile neutrino rates for general M, T, $\mu$, k: Review of a theoretical framework", *Annals Phys.*, vol. 444, pp. 169022, 2022.

[321] Takehiko Asaka, Shintaro Eijima, and Hiroyuki Ishida, "Kinetic Equations for Baryogenesis via Sterile Neutrino Oscillation", *JCAP*, vol. 02, pp. 021, 2012.

[322] Alexander Merle and Maximilian Totzauer, "keV Sterile Neutrino Dark Matter from Singlet Scalar Decays: Basic Concepts and Subtle Features", *JCAP*, vol. 06, pp. 011, 2015.

[323] Johannes König, Alexander Merle, and Maximilian Totzauer, "keV Sterile Neutrino Dark Matter from Singlet Scalar Decays: The Most General Case", *JCAP*, vol. 11, pp. 038, 2016.

[324] J. Ghiglieri and M. Laine, "GeV-scale hot sterile neutrino oscillations: a numerical solution", *JHEP*, vol. 02, pp. 078, 2018.

[325] Mikko Laine and York Schroder, "Quark mass thresholds in QCD thermodynamics", *Phys. Rev. D*, vol. 73, pp. 085009, 2006.

[326] M. Laine and M. Meyer, "Standard Model thermodynamics across the electroweak crossover", *JCAP*, vol. 07, pp. 035, 2015.

[327] Dimitrios Karamitros, Thomas McKelvey, and Apostolos Pilaftsis, "Varying entropy degrees of freedom effects in low-scale leptogenesis", *Phys. Rev. D*, vol. 109, no. 5, pp. 055007, 2024.

[328] Laurent Canetti, Marco Drewes, Tibor Frossard, and Mikhail Shaposhnikov, "Dark Matter, Baryogenesis and Neutrino Oscillations from Right Handed Neutrinos", *Phys. Rev. D*, vol. 87, pp. 093006, 2013.

[329] Laurent Canetti, Marco Drewes, and Mikhail Shaposhnikov, "Sterile Neutrinos as the Origin of Dark and Baryonic Matter", *Phys. Rev. Lett.*, vol. 110, no. 6, pp. 061801, 2013.

[330] Laurent Canetti, Marco Drewes, and Mikhail Shaposhnikov, "Matter and Antimatter in the Universe", *New J. Phys.*, vol. 14, pp. 095012, 2012.

[331] Pilar Hernandez, Jacobo Lopez-Pavon, Nuria Rius, and Stefan Sandner, "Bounds on right-handed neutrino parameters from observable leptogenesis", *JHEP*, vol. 12, pp. 012, 2022.

[332] Takehiko Asaka, Steve Blanchet, and Mikhail Shaposhnikov, "The nuMSM, dark matter and neutrino masses", *Phys. Lett. B*, vol. 631, pp. 151–156, 2005.

[333] Esra Bulbul, Maxim Markevitch, Adam Foster, Randall K. Smith, Michael Loewenstein, and Scott W. Randall, "Detection of An Unidentified Emission Line in the Stacked X-ray spectrum of Galaxy Clusters", *Astrophys. J.*, vol. 789, pp. 13, 2014.

[334] Alexey Boyarsky, Oleg Ruchayskiy, Dmytro Iakubovskyi, and Jeroen Franse, "Unidentified Line in X-Ray Spectra of the Andromeda Galaxy and Perseus Galaxy Cluster", *Phys. Rev. Lett.*, vol. 113, pp. 251301, 2014.

[335] Christopher Dessert, Joshua W. Foster, Yujin Park, and Benjamin R. Safdi, "Was There a 3.5 keV Line?", *Astrophys. J.*, vol. 964, no. 2, pp. 185, 2024.

[336] M. Laine and M. Shaposhnikov, "Sterile neutrino dark matter as a consequence of nuMSM-induced lepton asymmetry", *JCAP*, vol. 06, pp. 031, 2008.

[337] J. Ghiglieri and M. Laine, "Sterile neutrino dark matter via coinciding resonances", *JCAP*, vol. 07, pp. 012, 2020.

[338] K. N. Abazajian et al., "Light Sterile Neutrinos: A White Paper", 4 2012.

[339] M. Drewes et al., "A White Paper on keV Sterile Neutrino Dark Matter", *JCAP*, vol. 01, pp. 025, 2017.

[340] A. Boyarsky, M. Drewes, T. Lasserre, S. Mertens, and O. Ruchayskiy, "Sterile neutrino Dark Matter", *Prog. Part. Nucl. Phys.*, vol. 104, pp. 1–45, 2019.

[341] Lawrence J. Hall, Hitoshi Murayama, and Neal Weiner, "Neutrino mass anarchy", *Phys. Rev. Lett.*, vol. 84, pp. 2572–2575, 2000.

[342] Naoyuki Haba and Hitoshi Murayama, "Anarchy and hierarchy", *Phys. Rev. D*, vol. 63, pp. 053010, 2001.

[343] Andre de Gouvea and Hitoshi Murayama, "Statistical Test of Anarchy", *Phys. Lett. B*, vol. 573, pp. 94–100, 2003.

[344] Andre de Gouvea and Hitoshi Murayama, "Neutrino Mixing Anarchy: Alive and Kicking", *Phys. Lett. B*, vol. 747, pp. 479–483, 2015.

[345] P. F. Harrison, D. H. Perkins, and W. G. Scott, "Tri-bimaximal mixing and the neutrino oscillation data", *Phys. Lett. B*, vol. 530, pp. 167, 2002.

[346] Y. Abe et al., "Indication of Reactor $\bar{\nu}_e$ Disappearance in the Double Chooz Experiment", *Phys. Rev. Lett.*, vol. 108, pp. 131801, 2012.

[347] P. Adamson et al., "Improved search for muon-neutrino to electron-neutrino oscillations in MINOS", *Phys. Rev. Lett.*, vol. 107, pp. 181802, 2011.

[348] F. P. An et al., "Observation of electron-antineutrino disappearance at Daya Bay", *Phys. Rev. Lett.*, vol. 108, pp. 171803, 2012.

[349] J. K. Ahn et al., "Observation of Reactor Electron Antineutrino Disappearance in the RENO Experiment", *Phys. Rev. Lett.*, vol. 108, pp. 191802, 2012.

[350] K. Abe et al., "Observation of Electron Neutrino Appearance in a Muon Neutrino Beam", *Phys. Rev. Lett.*, vol. 112, pp. 061802, 2014.

[351] Guido Altarelli and Ferruccio Feruglio, "Discrete Flavor Symmetries and Models of Neutrino Mixing", *Rev. Mod. Phys.*, vol. 82, pp. 2701–2729, 2010.

[352] Hajime Ishimori, Tatsuo Kobayashi, Hiroshi Ohki, Yusuke Shimizu, Hiroshi Okada, and Morimitsu Tanimoto, "Non-Abelian Discrete Symmetries in Particle Physics", *Prog. Theor. Phys. Suppl.*, vol. 183, pp. 1–163, 2010.

[353] Walter Grimus and Patrick Otto Ludl, "Finite flavour groups of fermions", *J. Phys. A*, vol. 45, pp. 233001, 2012.

[354] Stephen F. King and Christoph Luhn, "Neutrino Mass and Mixing with Discrete Symmetry", *Rept. Prog. Phys.*, vol. 76, pp. 056201, 2013.

[355] Ferruccio Feruglio and Andrea Romanino, "Lepton flavor symmetries", *Rev. Mod. Phys.*, vol. 93, no. 1, pp. 015007, 2021.

[356] Zhi-zhong Xing, "Flavor structures of charged fermions and massive neutrinos", *Phys. Rept.*, vol. 854, pp. 1–147, 2020.

[357] Garv Chauhan, P. S. Bhupal Dev, Bartosz Dziewit, Wojciech Flieger, Janusz Gluza, Krzysztof Grzanka, Biswajit Karmakar, Joris Vergeest, and Szymon Zieba, "Discrete Flavor Symmetries and Lepton Masses and Mixings", in *Snowmass 2021*, 3 2022.

[358] Garv Chauhan, P. S. Bhupal Dev, Ievgen Dubovyk, Bartosz Dziewit, Wojciech Flieger, Krzysztof Grzanka, Janusz Gluza, Biswajit Karmakar, and Szymon Zięba, "Phenomenology of lepton masses and mixing with discrete flavor symmetries", *Prog. Part. Nucl. Phys.*, vol. 138, pp. 104126, 2024.

[359] Walter Grimus, Anjan S. Joshipura, Luis Lavoura, and Morimitsu Tanimoto, "Symmetry realization of texture zeros", *Eur. Phys. J. C*, vol. 36, pp. 227–232, 2004.

[360] Catherine I. Low, "Abelian family symmetries and the simplest models that give $\theta_{13} = 0$ in the neutrino mixing matrix", *Phys. Rev. D*, vol. 71, pp. 073007, 2005.

[361] C. D. Froggatt and Holger Bech Nielsen, "Hierarchy of Quark Masses, Cabibbo Angles and CP Violation", *Nucl. Phys. B*, vol. 147, pp. 277–298, 1979.

[362] G. Ecker, W. Grimus, and H. Neufeld, "Spontaneous CP Violation in Left-right Symmetric Gauge Theories", *Nucl. Phys. B*, vol. 247, pp. 70–82, 1984.

[363] G. Ecker, W. Grimus, and H. Neufeld, "A Standard Form for Generalized CP Transformations", *J. Phys. A*, vol. 20, pp. L807, 1987.

[364] H. Neufeld, W. Grimus, and G. Ecker, "Generalized CP Invariance, Neutral Flavor Conservation and the Structure of the Mixing Matrix", *Int. J. Mod. Phys. A*, vol. 3, pp. 603–616, 1988.

[365] W. Grimus and M. N. Rebelo, "Automorphisms in gauge theories and the definition of CP and P", *Phys. Rept.*, vol. 281, pp. 239–308, 1997.

[366] P. F. Harrison and W. G. Scott, "Symmetries and generalizations of tri-bimaximal neutrino mixing", *Phys. Lett. B*, vol. 535, pp. 163–169, 2002.

[367] Walter Grimus and Luis Lavoura, "A Nonstandard CP transformation leading to maximal atmospheric neutrino mixing", *Phys. Lett. B*, vol. 579, pp. 113–122, 2004.

[368] Ferruccio Feruglio, Claudia Hagedorn, and Robert Ziegler, "Lepton Mixing Parameters from Discrete and CP Symmetries", *JHEP*, vol. 07, pp. 027, 2013.

[369] Martin Holthausen, Manfred Lindner, and Michael A. Schmidt, "CP and Discrete Flavour Symmetries", *JHEP*, vol. 04, pp. 122, 2013.

[370] Mu-Chun Chen, Maximilian Fallbacher, K. T. Mahanthappa, Michael Ratz, and Andreas Trautner, "CP Violation from Finite Groups", *Nucl. Phys. B*, vol. 883, pp. 267–305, 2014.

[371] J. A. Escobar and Christoph Luhn, "The Flavor Group Delta(6n**2)", *J. Math. Phys.*, vol. 50, pp. 013524, 2009.

[372] Claudia Hagedorn, Aurora Meroni, and Emiliano Molinaro, "Lepton mixing from $\Delta(3n^2)$ and $\Delta(6n^2)$ and CP", *Nucl. Phys. B*, vol. 891, pp. 499–557, 2015.

[373] Stephen F. King, Thomas Neder, and Alexander J. Stuart, "Lepton mixing predictions from $\Delta(6n^2)$ family Symmetry", *Phys. Lett. B*, vol. 726, pp. 312–315, 2013.

[374] J. Kubo, A. Mondragon, M. Mondragon, and E. Rodriguez-Jauregui, "The Flavor symmetry", *Prog. Theor. Phys.*, vol. 109, pp. 795–807, 2003, [Erratum: Prog.Theor.Phys. 114, 287–287 (2005)].

[375] Francesco Caravaglios and Stefano Morisi, "Neutrino masses and mixings with an S(3) family permutation symmetry", 3 2005.

[376] C. Hagedorn, M. Lindner, and R. N. Mohapatra, "S(4) flavor symmetry and fermion masses: Towards a grand unified theory of flavor", *JHEP*, vol. 06, pp. 042, 2006.

[377] Yoshio Koide, "S(4) flavor symmetry embedded into SU(3) and lepton masses and mixing", *JHEP*, vol. 08, pp. 086, 2007.

[378] Guido Altarelli and Ferruccio Feruglio, "Tri-bimaximal neutrino mixing, A(4) and the modular symmetry", *Nucl. Phys. B*, vol. 741, pp. 215–235, 2006.

[379] Guido Altarelli and Davide Meloni, "A Simplest A4 Model for Tri-Bimaximal Neutrino Mixing", *J. Phys. G*, vol. 36, pp. 085005, 2009.

[380] C. Hagedorn, E. Molinaro, and S. T. Petcov, "Majorana Phases and Leptogenesis in See-Saw Models with A(4) Symmetry", *JHEP*, vol. 09, pp. 115, 2009.

[381] Claudia Hagedorn and Emiliano Molinaro, "Flavor and CP symmetries for leptogenesis and 0 $\nu\beta\beta$ decay", *Nucl. Phys. B*, vol. 919, pp. 404–469, 2017.

[382] Guido Altarelli and Ferruccio Feruglio, "Tri-bimaximal neutrino mixing from discrete symmetry in extra dimensions", *Nucl. Phys. B*, vol. 720, pp. 64–88, 2005.

[383] I. de Medeiros Varzielas, S. F. King, and G. G. Ross, "Tri-bimaximal neutrino mixing from discrete subgroups of SU(3) and SO(3) family symmetry", *Phys. Lett. B*, vol. 644, pp. 153–157, 2007.

[384] Stefan Antusch, Eros Cazzato, Marco Drewes, Oliver Fischer, Bjorn Garbrecht, Dario Gueter, and Juraj Klaric, "Probing Leptogenesis at Future Colliders", *JHEP*, vol. 09, pp. 124, 2018.

[385] S. Sandner, P. Hernandez, J. Lopez-Pavon, and N. Rius, "Predicting the baryon asymmetry with degenerate right-handed neutrinos", *JHEP*, vol. 11, pp. 153, 2023.

[386] Fedor Bezrukov, Mikhail Yu. Kalmykov, Bernd A. Kniehl, and Mikhail Shaposhnikov, "Higgs Boson Mass and New Physics", *JHEP*, vol. 10, pp. 140, 2012.

[387] R. N. Mohapatra and Jogesh C. Pati, "A Natural Left-Right Symmetry", *Phys. Rev. D*, vol. 11, pp. 2558, 1975.

[388] G. Senjanovic and Rabindra N. Mohapatra, "Exact Left-Right Symmetry and Spontaneous Violation of Parity", *Phys. Rev. D*, vol. 12, pp. 1502, 1975.

[389] D. Chang, R. N. Mohapatra, and M. K. Parida, "Decoupling Parity and SU(2)-R Breaking Scales: A New Approach to Left-Right Symmetric Models", *Phys. Rev. Lett.*, vol. 52, pp. 1072, 1984.

[390] Paul Langacker, "The Physics of Heavy $Z'$ Gauge Bosons", *Rev. Mod. Phys.*, vol. 81, pp. 1199–1228, 2009.

[391] Rabindra N. Mohapatra, "Left-right Symmetric Models of Weak Interactions: A Review", *NATO Sci. Ser. B*, vol. 122, pp. 219, 1985.

[392] Rabindra N. Mohapatra and R. E. Marshak, "Local B-L Symmetry of Electroweak Interactions, Majorana Neutrinos and Neutron Oscillations", *Phys. Rev. Lett.*, vol. 44, pp. 1316–1319, 1980, [Erratum: Phys.Rev.Lett. 44, 1643 (1980)].

[393] C. Wetterich, "Neutrino Masses and the Scale of B-L Violation", *Nucl. Phys. B*, vol. 187, pp. 343–375, 1981.

[394] W. Buchmuller, C. Greub, and P. Minkowski, "Neutrino masses, neutral vector bosons and the scale of B-L breaking", *Phys. Lett. B*, vol. 267, pp. 395–399, 1991.

[395] W. Buchmuller and T. Yanagida, "Baryogenesis and the scale of B-L breaking", *Phys. Lett. B*, vol. 302, pp. 240–244, 1993.

[396] Harald Fritzsch and Peter Minkowski, "Unified Interactions of Leptons and Hadrons", *Annals Phys.*, vol. 93, pp. 193–266, 1975.

[397] Howard Georgi, "The State of the Art—Gauge Theories", *AIP Conf. Proc.*, vol. 23, pp. 575–582, 1975.

[398] Jogesh C. Pati and Abdus Salam, "Lepton Number as the Fourth Color", *Phys. Rev. D*, vol. 10, pp. 275–289, 1974, [Erratum: Phys.Rev.D 11, 703–703 (1975)].

[399] Francisco del Aguila, Shaouly Bar-Shalom, Amarjit Soni, and Jose Wudka, "Heavy Majorana Neutrinos in the Effective Lagrangian Description: Application to Hadron Colliders", *Phys. Lett. B*, vol. 670, pp. 399–402, 2009.

[400] Marco Drewes and Jin U Kang, "Sterile neutrino Dark Matter production from scalar decay in a thermal bath", *JHEP*, vol. 05, pp. 051, 2016.

[401] Takehiko Asaka, Mikko Laine, and Mikhail Shaposhnikov, "Lightest sterile neutrino abundance within the nuMSM", *JHEP*, vol. 01, pp. 091, 2007, [Erratum: JHEP 02, 028 (2015)].

[402] J. Ghiglieri and M. Laine, "Sterile neutrino dark matter via GeV-scale leptogenesis?", *JHEP*, vol. 07, pp. 078, 2019.

[403] Jean-Marie Frere, Thomas Hambye, and Gilles Vertongen, "Is leptogenesis falsifiable at LHC?", *JHEP*, vol. 01, pp. 051, 2009.

[404] P. S. Bhupal Dev, Chang-Hun Lee, and R. N. Mohapatra, "Leptogenesis Constraints on the Mass of Right-handed Gauge Bosons", *Phys. Rev. D*, vol. 90, no. 9, pp. 095012, 2014.

[405] H. Arthur Weldon, "Simple Rules for Discontinuities in Finite Temperature Field Theory", *Phys. Rev. D*, vol. 28, pp. 2007, 1983.

[406] Ashok K. Das, *Finite Temperature Field Theory*, World Scientific, New York, 1997.

[407] M. Fierz, "Force-free particles with any spin", *Helv. Phys. Acta*, vol. 12, pp. 3–37, 1939.

[408] Takehiko Asaka, Mikko Laine, and Mikhail Shaposhnikov, "On the hadronic contribution to sterile neutrino production", *JHEP*, vol. 06, pp. 053, 2006.

[409] Alexey Anisimov, Denis Besak, and Dietrich Bodeker, "Thermal production of relativistic Majorana neutrinos: Strong enhancement by multiple soft scattering", *JCAP*, vol. 03, pp. 042, 2011.

[410] I. Ghisoiu and M. Laine, "Right-handed neutrino production rate at T $>$ 160 GeV", *JCAP*, vol. 12, pp. 032, 2014.

[411] P. Hernández, M. Kekic, J. López-Pavón, J. Racker, and J. Salvado, "Testable Baryogenesis in Seesaw Models", *JHEP*, vol. 08, pp. 157, 2016.

[412] Thomas Hambye and Daniele Teresi, "Higgs doublet decay as the origin of the baryon asymmetry", *Phys. Rev. Lett.*, vol. 117, no. 9, pp. 091801, 2016.

[413] Thomas Hambye and Daniele Teresi, "Baryogenesis from L-violating Higgs-doublet decay in the density-matrix formalism", *Phys. Rev. D*, vol. 96, no. 1, pp. 015031, 2017.

[414] S. Eijima, M. Shaposhnikov, and I. Timiryasov, "Parameter space of baryogenesis in the $\nu$MSM", *JHEP*, vol. 07, pp. 077, 2019.

[415] Dietrich Bödeker and Dennis Schröder, "Equilibration of right-handed electrons", *JCAP*, vol. 05, pp. 010, 2019.

[416] J. Ghiglieri and M. Laine, "Smooth interpolation between thermal Born and LPM rates", *JHEP*, vol. 01, pp. 173, 2022.

[417] Juan Carlos D'Olivo, Jose F. Nieves, and Manuel Torres, "Finite temperature corrections to the effective potential of neutrinos in a medium", *Phys. Rev. D*, vol. 46, pp. 1172–1179, 1992.

[418] C. Quimbay and S. Vargas-Castrillon, "Fermionic dispersion relations in the standard model at finite temperature", *Nucl. Phys. B*, vol. 451, pp. 265–304, 1995.

[419] Shintaro Eijima, Mikhail Shaposhnikov, and Inar Timiryasov, "Freeze-in and freeze-out generation of lepton asymmetries after baryogenesis in the $\nu$MSM", *JCAP*, vol. 04, no. 04, pp. 049, 2022.

[420] A. Bazavov et al., "Chiral crossover in QCD at zero and non-zero chemical potentials", *Phys. Lett. B*, vol. 795, pp. 15–21, 2019.

[421] Loretta M. Johnson, Douglas W. McKay, and Tim Bolton, "Extending sensitivity for low mass neutral heavy lepton searches", *Phys. Rev. D*, vol. 56, pp. 2970–2981, 1997.

[422] Dmitry Gorbunov and Mikhail Shaposhnikov, "How to find neutral leptons of the $\nu$MSM?", *JHEP*, vol. 10, pp. 015, 2007, [Erratum: JHEP 11, 101 (2013)].

[423] Kyrylo Bondarenko, Alexey Boyarsky, Dmitry Gorbunov, and Oleg Ruchayskiy, "Phenomenology of GeV-scale Heavy Neutral Leptons", *JHEP*, vol. 11, pp. 032, 2018.

[424] Pilar Coloma, Enrique Fernández-Martínez, Manuel González-López, Josu Hernández-García, and Zarko Pavlovic, "GeV-scale neutrinos: interactions with mesons and DUNE sensitivity", *Eur. Phys. J. C*, vol. 81, no. 1, pp. 78, 2021.

[425] Dominik J. Schwarz and Maik Stuke, "Lepton asymmetry and the cosmic QCD transition", *JCAP*, vol. 11, pp. 025, 2009, [Erratum: JCAP 10, E01 (2010)].

[426] Dietrich Bödeker, Florian Kühnel, Isabel M. Oldengott, and Dominik J. Schwarz, "Lepton flavor asymmetries and the mass spectrum of primordial black holes", *Phys. Rev. D*, vol. 103, no. 6, pp. 063506, 2021.

[427] Duurt Johan Van der Hoek, "Massive neutrinos and their occurence in a left-right symmetric model", Master's thesis, Groningen U., 2007.

[428] N. G. Deshpande, J. F. Gunion, Boris Kayser, and Fredrick I. Olness, "Left-right symmetric electroweak models with triplet Higgs", *Phys. Rev. D*, vol. 44, pp. 837–858, 1991.

[429] Armen Tumasyan et al., "Search for a right-handed W boson and a heavy neutrino in proton-proton collisions at $\sqrt{s}$ = 13 TeV", *JHEP*, vol. 04, pp. 047, 2022.

[430] "Search for $\mathrm{Z}'$ bosons decaying to pairs of heavy Majorana neutrinos in proton-proton collisions at $\sqrt{s} = 13$ TeV", 2022.

[431] Georges Aad et al., "Search for heavy Majorana or Dirac neutrinos and right-handed W gauge bosons in final states with charged leptons and jets in pp collisions at $\sqrt{s} = 13$ TeV with the ATLAS detector", *Eur. Phys. J. C*, vol. 83, no. 12, pp. 1164, 2023.

[432] Goran Senjanović and Vladimir Tello, "Right Handed Quark Mixing in Left-Right Symmetric Theory", *Phys. Rev. Lett.*, vol. 114, no. 7, pp. 071801, 2015.

[433] A. Abada et al., "FCC-ee: The Lepton Collider: Future Circular Collider Conceptual Design Report Volume 2", *Eur. Phys. J. ST*, vol. 228, no. 2, pp. 261–623, 2019.

[434] M. Benedikt et al., "Future Circular Collider Feasibility Study Report: Volume 1, Physics, Experiments, Detectors", 4 2025.

[435] Stefan Antusch, Jan Hajer, and Johannes Rosskopp, "Simulating lepton number violation induced by heavy neutrino-antineutrino oscillations at colliders", *JHEP*, vol. 03, pp. 110, 2023.

[436] Max Aker et al., "Direct neutrino-mass measurement based on 259 days of KATRIN data", *Science*, vol. 388, no. 6743, pp. adq9592, 2025.

[437] A. G. Adame et al., "DESI 2024 VI: cosmological constraints from the measurements of baryon acoustic oscillations", *JCAP*, vol. 02, pp. 021, 2025.

[438] W. Elbers et al., "Constraints on Neutrino Physics from DESI DR2 BAO and DR1 Full Shape", 3 2025.

[439] Marcin Chrzaszcz, Marco Drewes, Tomás E. Gonzalo, Julia Harz, Suraj Krishnamurthy, and Christoph Weniger, "A frequentist analysis of three right-handed neutrinos with GAMBIT", *Eur. Phys. J. C*, vol. 80, no. 6, pp. 569, 2020.

[440] Igor Krasnov, "HNL see-saw: lower mixing limit and pseudodegenerate state", 7 2023.

[441] Ivan Esteban, M. C. Gonzalez-Garcia, Michele Maltoni, Thomas Schwetz, and Albert Zhou, "The fate of hints: updated global analysis of three-flavor neutrino oscillations", *JHEP*, vol. 09, pp. 178, 2020.

[442] R. Acciarri et al., "Long-Baseline Neutrino Facility (LBNF) and Deep Underground Neutrino Experiment (DUNE): Conceptual Design Report, Volume 2: The Physics Program for DUNE at LBNF", 12 2015.

[443] K. Abe et al., "Physics potential of a long-baseline neutrino oscillation experiment using a J-PARC neutrino beam and Hyper-Kamiokande", *PTEP*, vol. 2015, pp. 053C02, 2015.

[444] K. Abe et al., "Physics potentials with the second Hyper-Kamiokande detector in Korea", *PTEP*, vol. 2018, no. 6, pp. 063C01, 2018.

[445] J. Bian et al., "Hyper-Kamiokande Experiment: A Snowmass White Paper", in *Snowmass 2021*, 3 2022.

[446] Takehiko Asaka, Shintaro Eijima, and Hiroyuki Ishida, "Mixing of Active and Sterile Neutrinos", *JHEP*, vol. 04, pp. 011, 2011.

[447] Oleg Ruchayskiy and Artem Ivashko, "Experimental bounds on sterile neutrino mixing angles", *JHEP*, vol. 06, pp. 100, 2012.

[448] Marco Drewes, "Distinguishing Dirac and Majorana Heavy Neutrinos at Lepton Colliders", *PoS*, vol. ICHEP2022, pp. 608, 2022.

[449] Stefan Antusch, Eros Cazzato, and Oliver Fischer, "Displaced vertex searches for sterile neutrinos at future lepton colliders", *JHEP*, vol. 12, pp. 007, 2016.

[450] J. Angrik et al., "KATRIN design report 2004", 2 2005.

[451] Asmaa Abada, Giorgio Arcadi, Valerie Domcke, Marco Drewes, Juraj Klaric, and Michele Lucente, "Low-scale leptogenesis with three heavy neutrinos", *JHEP*, vol. 01, pp. 164, 2019.

[452] A. D. Dolgov, S. H. Hansen, G. Raffelt, and D. V. Semikoz, "Heavy sterile neutrinos: Bounds from big bang nucleosynthesis and SN1987A", *Nucl. Phys. B*, vol. 590, pp. 562–574, 2000.

[453] Oleg Ruchayskiy and Artem Ivashko, "Restrictions on the lifetime of sterile neutrinos from primordial nucleosynthesis", *JCAP*, vol. 10, pp. 014, 2012.

[454] Nashwan Sabti, Andrii Magalich, and Anastasiia Filimonova, "An Extended Analysis of Heavy Neutral Leptons during Big Bang Nucleosynthesis", *JCAP*, vol. 11, pp. 056, 2020.

[455] Alexey Boyarsky, Maksym Ovchynnikov, Oleg Ruchayskiy, and Vsevolod Syvolap, "Improved big bang nucleosynthesis constraints on heavy neutral leptons", *Phys. Rev. D*, vol. 104, no. 2, pp. 023517, 2021.

[456] Roberta Diamanti, Laura Lopez-Honorez, Olga Mena, Sergio Palomares-Ruiz, and Aaron C. Vincent, "Constraining Dark Matter Late-Time Energy Injection: Decays and P-Wave Annihilations", *JCAP*, vol. 02, pp. 017, 2014.

[457] Aaron C. Vincent, Enrique Fernandez Martinez, Pilar Hernández, Massimiliano Lattanzi, and Olga Mena, "Revisiting cosmological bounds on sterile neutrinos", *JCAP*, vol. 04, pp. 006, 2015.

[458] Vivian Poulin, Julien Lesgourgues, and Pasquale D. Serpico, "Cosmological constraints on exotic injection of electromagnetic energy", *JCAP*, vol. 03, pp. 043, 2017.

[459] Garv Chauhan, Shunsaku Horiuchi, Patrick Huber, and Ian M. Shoemaker, "Low-energy supernovae bounds on sterile neutrinos", *JCAP*, vol. 03, pp. 052, 2025.

[460] Nitsan Bar, Kfir Blum, and Guido D'Amico, "Is there a supernova bound on axions?", *Phys. Rev. D*, vol. 101, no. 12, pp. 123025, 2020.

[461] A. Aguilar-Arevalo et al., "Improved search for heavy neutrinos in the decay $\pi \to e\nu$", *Phys. Rev. D*, vol. 97, no. 7, pp. 072012, 2018.

[462] A. V. Artamonov et al., "Search for heavy neutrinos in $K^+ \to \mu^+\nu_H$ decays", *Phys. Rev. D*, vol. 91, no. 5, pp. 052001, 2015, [Erratum: Phys.Rev.D 91, 059903 (2015)].

[463] T. Yamazaki et al., "Search for Heavy Neutrinos in Kaon Decay", *Conf. Proc. C*, vol. 840719, pp. 262, 1984.

[464] G. Bernardi et al., "Search for Neutrino Decay", *Phys. Lett. B*, vol. 166, pp. 479–483, 1986.

[465] G. Bernardi et al., "FURTHER LIMITS ON HEAVY NEUTRINO COUPLINGS", *Phys. Lett. B*, vol. 203, pp. 332–334, 1988.

[466] Amanda M. Cooper-Sarkar et al., "Search for Heavy Neutrino Decays in the BEBC Beam Dump Experiment", *Phys. Lett. B*, vol. 160, pp. 207–211, 1985.

[467] Ryan Barouki, Giacomo Marocco, and Subir Sarkar, "Blast from the past II: Constraints on heavy neutral leptons from the BEBC WA66 beam dump experiment", *SciPost Phys.*, vol. 13, pp. 118, 2022.

[468] A. Vaitaitis et al., "Search for neutral heavy leptons in a high-energy neutrino beam", *Phys. Rev. Lett.*, vol. 83, pp. 4943–4946, 1999.

[469] P. Abreu et al., "Search for neutral heavy leptons produced in Z decays", *Z. Phys. C*, vol. 74, pp. 57–71, 1997, [Erratum: Z.Phys.C 75, 580 (1997)].

[470] F. Bergsma et al., "A Search for Decays of Heavy Neutrinos in the Mass Range 0.5-GeV to 2.8-GeV", *Phys. Lett. B*, vol. 166, pp. 473–478, 1986.

[471] Armen Tumasyan et al., "Search for long-lived heavy neutral leptons with displaced vertices in proton-proton collisions at $\sqrt{\mathrm{s}}$ =13 TeV", *JHEP*, vol. 07, pp. 081, 2022.

[472] Eder Izaguirre and Brian Shuve, "Multilepton and Lepton Jet Probes of Sub-Weak-Scale Right-Handed Neutrinos", *Phys. Rev. D*, vol. 91, no. 9, pp. 093010, 2015.

[473] Arindam Das, Partha Konar, and Arun Thalapillil, "Jet substructure shedding light on heavy Majorana neutrinos at the LHC", *JHEP*, vol. 02, pp. 083, 2018.

[474] Akitaka Ariga et al., "FASER's physics reach for long-lived particles", *Phys. Rev. D*, vol. 99, no. 9, pp. 095011, 2019.

[475] David Curtin et al., "Long-Lived Particles at the Energy Frontier: The MATHUSLA Physics Case", *Rept. Prog. Phys.*, vol. 82, no. 11, pp. 116201, 2019.

[476] Giulio Aielli et al., "Expression of interest for the CODEX-b detector", *Eur. Phys. J. C*, vol. 80, no. 12, pp. 1177, 2020.

[477] Stefan Antusch, Eros Cazzato, and Oliver Fischer, "Sterile neutrino searches at future $e^-e^+$, $pp$, and $e^-p$ colliders", *Int. J. Mod. Phys. A*, vol. 32, no. 14, pp. 1750078, 2017.

[478] J. Beacham et al., "Physics Beyond Colliders at CERN: Beyond the Standard Model Working Group Report", *J. Phys. G*, vol. 47, no. 1, pp. 010501, 2020.

[479] Marco Drewes, Juraj Klarić, and Jacobo López-Pavón, "New benchmark models for heavy neutral lepton searches", *Eur. Phys. J. C*, vol. 82, no. 12, pp. 1176, 2022.

[480] Jean-Loup Tastet, Oleg Ruchayskiy, and Inar Timiryasov, "Reinterpreting the ATLAS bounds on heavy neutral leptons in a realistic neutrino oscillation model", *JHEP*, vol. 12, pp. 182, 2021.

[481] Asmaa Abada, Pablo Escribano, Xabier Marcano, and Gioacchino Piazza, "Collider searches for heavy neutral leptons: beyond simplified scenarios", *Eur. Phys. J. C*, vol. 82, no. 11, pp. 1030, 2022.

[482] A. Granelli, K. Moffat, and S. T. Petcov, "Flavoured resonant leptogenesis at sub-TeV scales", *Nucl. Phys. B*, vol. 973, pp. 115597, 2021.

[483] Garv Chauhan and P. S. Bhupal Dev, "Interplay between resonant leptogenesis, neutrinoless double beta decay and collider signals in a model with flavor and CP symmetries", *Nucl. Phys. B*, vol. 986, pp. 116058, 2023.

[484] Cristiano Alpigiani et al., "An Update to the Letter of Intent for MATHUSLA: Search for Long-Lived Particles at the HL-LHC", 9 2020.

[485] Peiran Li, Zhen Liu, and Kun-Feng Lyu, "Heavy neutral leptons at muon colliders", *JHEP*, vol. 03, pp. 231, 2023.

[486] Oleksii Mikulenko and Mariia Marinichenko, "Measuring lepton number violation in heavy neutral lepton decays at the future muon collider", *JHEP*, vol. 01, pp. 032, 2024.

[487] Krzysztof Mekala, Jurgen Reuter, and Aleksander Filip Zarnecki, "Heavy neutrinos at future linear $e^+e^-$ colliders", *JHEP*, vol. 06, pp. 010, 2022.

[488] Kyrylo Bondarenko, Alexey Boyarsky, Juraj Klaric, Oleksii Mikulenko, Oleg Ruchayskiy, Vsevolod Syvolap, and Inar Timiryasov, "An allowed window for heavy neutral leptons below the kaon mass", *JHEP*, vol. 07, pp. 193, 2021.

[489] Marco Drewes, Juraj Klarić, and Philipp Klose, "On lepton number violation in heavy neutrino decays at colliders", *JHEP*, vol. 11, pp. 032, 2019.

[490] Frank F. Deppisch, P. S. Bhupal Dev, and Apostolos Pilaftsis, "Neutrinos and Collider Physics", *New J. Phys.*, vol. 17, no. 7, pp. 075019, 2015.

[491] G. Anamiati, M. Hirsch, and E. Nardi, "Quasi-Dirac neutrinos at the LHC", *JHEP*, vol. 10, pp. 010, 2016.

[492] J. D. Vergados, H. Ejiri, and F. Simkovic, "Theory of Neutrinoless Double Beta Decay", *Rept. Prog. Phys.*, vol. 75, pp. 106301, 2012.

[493] Stefano Dell'Oro, Simone Marcocci, Matteo Viel, and Francesco Vissani, "Neutrinoless double beta decay: 2015 review", *Adv. High Energy Phys.*, vol. 2016, pp. 2162659, 2016.

[494] J. D. Vergados, H. Ejiri, and F. Šimkovic, "Neutrinoless double beta decay and neutrino mass", *Int. J. Mod. Phys. E*, vol. 25, no. 11, pp. 1630007, 2016.

[495] Michelle J. Dolinski, Alan W. P. Poon, and Werner Rodejohann, "Neutrinoless Double-Beta Decay: Status and Prospects", *Ann. Rev. Nucl. Part. Sci.*, vol. 69, pp. 219–251, 2019.

[496] J. Schechter and J. W. F. Valle, "Neutrinoless Double beta Decay in SU(2) x U(1) Theories", *Phys. Rev. D*, vol. 25, pp. 2951, 1982.

[497] Martin Hirsch, Sergey Kovalenko, and Ivan Schmidt, "Extended black box theorem for lepton number and flavor violating processes", *Phys. Lett. B*, vol. 642, pp. 106–110, 2006.

[498] Mihai Horoi and Andrei Neacsu, "Towards an effective field theory approach to the neutrinoless double-beta decay", 6 2017.

[499] Amand Faessler, Marcela González, Sergey Kovalenko, and Fedor Šimkovic, "Arbitrary mass Majorana neutrinos in neutrinoless double beta decay", *Phys. Rev. D*, vol. 90, no. 9, pp. 096010, 2014.

[500] Mattias Blennow, Enrique Fernandez-Martinez, Jacobo Lopez-Pavon, and Javier Menendez, "Neutrinoless double beta decay in seesaw models", *JHEP*, vol. 07, pp. 096, 2010.

[501] Manimala Mitra, Goran Senjanovic, and Francesco Vissani, "Neutrinoless Double Beta Decay and Heavy Sterile Neutrinos", *Nucl. Phys. B*, vol. 856, pp. 26–73, 2012.

[502] J. Lopez-Pavon, S. Pascoli, and Chan-fai Wong, "Can heavy neutrinos dominate neutrinoless double beta decay?", *Phys. Rev. D*, vol. 87, no. 9, pp. 093007, 2013.

[503] J. Barea, J. Kotila, and F. Iachello, “Limits on sterile neutrino contributions to neutrinoless double beta decay”, *Phys. Rev. D*, vol. 92, pp. 093001, 2015.

[504] Takehiko Asaka, Hiroyuki Ishida, and Kazuki Tanaka, “Hiding neutrinoless double beta decay in the minimal seesaw mechanism”, *Phys. Rev. D*, vol. 103, no. 1, pp. 015014, 2021.

[505] Vincenzo Cirigliano, Wouter Dekens, and Sebastián Urrutia Quiroga, “Neutrino-less double beta decay in the $\nu$ Standard Model”, 5 2025.

[506] Marco Drewes and Shintaro Eijima, “Neutrinoless double $\beta$ decay and low scale leptogenesis”, *Phys. Lett. B*, vol. 763, pp. 72–79, 2016.

[507] Takehiko Asaka, Shintaro Eijima, and Hiroyuki Ishida, “On neutrinoless double beta decay in the $\nu$MSM”, *Phys. Lett. B*, vol. 762, pp. 371–375, 2016.

[508] Wouter Dekens, Jordy de Vries, Emanuele Mereghetti, Javier Menéndez, Pablo Soriano, and Guanghui Zhou, “Neutrinoless double-$\beta$ decay in the neutrino-extended standard model”, *Phys. Rev. C*, vol. 108, no. 4, pp. 045501, 2023.

[509] W. Dekens, J. de Vries, D. Castillo, J. Menéndez, E. Mereghetti, V. Plakkot, P. Soriano, and G. Zhou, “Neutrinoless double beta decay rates in the presence of light sterile neutrinos”, *JHEP*, vol. 09, pp. 201, 2024.

[510] Riccardo Barbieri and A. Dolgov, “Neutrino oscillations in the early universe”, *Nucl. Phys. B*, vol. 349, pp. 743–753, 1991.

[511] S. Gariazzo, P. F. de Salas, and S. Pastor, “Thermalisation of sterile neutrinos in the early Universe in the 3+1 scheme with full mixing matrix”, *JCAP*, vol. 07, pp. 014, 2019.

[512] Alexey Boyarsky, Maksym Ovchynnikov, Nashwan Sabti, and Vsevolod Syvolap, “When feebly interacting massive particles decay into neutrinos: The Neff story”, *Phys. Rev. D*, vol. 104, no. 3, pp. 035006, 2021.

[513] Hannah Rasmussen, Alex McNichol, George M. Fuller, and Chad T. Kishimoto, “Effects of an intermediate mass sterile neutrino population on the early Universe”, *Phys. Rev. D*, vol. 105, no. 8, pp. 083513, 2022.

[514] Francesco D’Eramo, Fazlollah Hajkarim, and Seokhoon Yun, “Thermal QCD Axions across Thresholds”, *JHEP*, vol. 10, pp. 224, 2021.

[515] Francesco D’Eramo, Eleonora Di Valentino, William Giarè, Fazlollah Hajkarim, Alessandro Melchiorri, Olga Mena, Fabrizio Renzi, and Seokhoon Yun, “Cosmological bound on the QCD axion mass, redux”, *JCAP*, vol. 09, pp. 022, 2022.

[516] Luca Caloni, Martina Gerbino, Massimiliano Lattanzi, and Luca Visinelli, “Novel cosmological bounds on thermally-produced axion-like particles”, *JCAP*, vol. 09, pp. 021, 2022.

[517] Luca Di Luzio, Jorge Martin Camalich, Guido Martinelli, José Antonio Oller, and Gioacchino Piazza, "Axion-pion thermalization rate in unitarized NLO chiral perturbation theory", *Phys. Rev. D*, vol. 108, no. 3, pp. 035025, 2023.

[518] David I. Dunsky, Lawrence J. Hall, and Keisuke Harigaya, "Dark Radiation Constraints on Heavy QCD Axions", *JHEP*, vol. 04, pp. 130, 2024.

[519] Marcin Badziak, Keisuke Harigaya, Michał Łukawski, and Robert Ziegler, "Thermal production of astrophobic axions", *JHEP*, vol. 09, pp. 136, 2024.

[520] Masahiro Ibe, Shin Kobayashi, Yuhei Nakayama, and Satoshi Shirai, "Cosmological constraint on dark photon from $N_{eff}$", *JHEP*, vol. 04, pp. 009, 2020.

[521] Jung-Tsung Li, George M. Fuller, and Evan Grohs, "Probing dark photons in the early universe with big bang nucleosynthesis", *JCAP*, vol. 12, pp. 049, 2020.

[522] Alberto Salvio, "Thermal production of massless dark photons", *JCAP*, vol. 07, pp. 035, 2023.

[523] Signe Riemer-Sørensen and Espen Sem Jenssen, "Nucleosynthesis Predictions and High-Precision Deuterium Measurements", *Universe*, vol. 3, no. 2, pp. 44, 2017.

[524] Zhen Hou, Ryan Keisler, Lloyd Knox, Marius Millea, and Christian Reichardt, "How Massless Neutrinos Affect the Cosmic Microwave Background Damping Tail", *Phys. Rev. D*, vol. 87, pp. 083008, 2013.

[525] Julien Lesgourgues, Gianpiero Mangano, Gennaro Miele, and Sergio Pastor, *Neutrino Cosmology*, Cambridge University Press, 2 2013.

[526] Daniel Baumann, "Primordial Cosmology", *PoS*, vol. TASI2017, pp. 009, 2018.

[527] B. A. Benson et al., "SPT-3G: A Next-Generation Cosmic Microwave Background Polarization Experiment on the South Pole Telescope", *Proc. SPIE Int. Soc. Opt. Eng.*, vol. 9153, pp. 91531P, 2014.

[528] F. Ge et al., "Cosmology From CMB Lensing and Delensed EE Power Spectra Using 2019-2020 SPT-3G Polarization Data", 11 2024.

[529] Erminia Calabrese et al., "The Atacama Cosmology Telescope: DR6 Constraints on Extended Cosmological Models", 3 2025.

[530] Peter Ade et al., "The Simons Observatory: Science goals and forecasts", *JCAP*, vol. 02, pp. 056, 2019.

[531] M. Abitbol et al., "The Simons Observatory: Science Goals and Forecasts for the Enhanced Large Aperture Telescope", 3 2025.

[532] MA Herrera and S Hacyan, "Relaxation time of neutrinos in the early universe", *Astrophysical Journal, Part 1 (ISSN 0004-637X), vol. 336, Jan. 15, 1989, p. 539-543.*, vol. 336, pp. 539–543, 1989.

[533] N. C. Rana and Banashree Mitra Seifert, "Effect of neutrino heating in the early universe on neutrino decoupling temperatures and nucleosynthesis", *Phys. Rev. D*, vol. 44, pp. 393–397, 1991.

[534] Scott Dodelson and Michael S. Turner, "Nonequilibrium neutrino statistical mechanics in the expanding universe", *Phys. Rev. D*, vol. 46, pp. 3372–3387, 1992.

[535] A. D. Dolgov and M. Fukugita, "Nonequilibrium effect of the neutrino distribution on primordial helium synthesis", *Phys. Rev. D*, vol. 46, pp. 5378–5382, 1992.

[536] Steen Hannestad and Jes Madsen, "Neutrino decoupling in the early universe", *Phys. Rev. D*, vol. 52, pp. 1764–1769, 1995.

[537] A. D. Dolgov, S. H. Hansen, and D. V. Semikoz, "Nonequilibrium corrections to the spectra of massless neutrinos in the early universe", *Nucl. Phys. B*, vol. 503, pp. 426–444, 1997.

[538] Nickolay Y. Gnedin and Oleg Y. Gnedin, "Cosmological neutrino background revisited", *Astrophys. J.*, vol. 509, pp. 11–15, 1998.

[539] A. D. Dolgov, S. H. Hansen, and D. V. Semikoz, "Nonequilibrium corrections to the spectra of massless neutrinos in the early universe: Addendum", *Nucl. Phys. B*, vol. 543, pp. 269–274, 1999.

[540] S. Esposito, G. Miele, S. Pastor, M. Peloso, and O. Pisanti, "Nonequilibrium spectra of degenerate relic neutrinos", *Nucl. Phys. B*, vol. 590, pp. 539–561, 2000.

[541] E. Grohs, G. M. Fuller, C. T. Kishimoto, M. W. Paris, and A. Vlasenko, "Neutrino energy transport in weak decoupling and big bang nucleosynthesis", *Phys. Rev. D*, vol. 93, no. 8, pp. 083522, 2016.

[542] Julien Froustey and Cyril Pitrou, "Incomplete neutrino decoupling effect on big bang nucleosynthesis", *Phys. Rev. D*, vol. 101, no. 4, pp. 043524, 2020.

[543] Jack J. Bennett, Gilles Buldgen, Pablo F. De Salas, Marco Drewes, Stefano Gariazzo, Sergio Pastor, and Yvonne Y. Y. Wong, "Towards a precision calculation of $N_{\text{eff}}$ in the Standard Model II: Neutrino decoupling in the presence of flavour oscillations and finite-temperature QED", *JCAP*, vol. 04, pp. 073, 2021.

[544] Duane A. Dicus, Edward W. Kolb, A. M. Gleeson, E. C. G. Sudarshan, Vigdor L. Teplitz, and Michael S. Turner, "Primordial Nucleosynthesis Including Radiative, Coulomb, and Finite Temperature Corrections to Weak Rates", *Phys. Rev. D*, vol. 26, pp. 2694, 1982.

[545] A. F. Heckler, "Astrophysical applications of quantum corrections to the equation of state of a plasma", *Phys. Rev. D*, vol. 49, pp. 611–617, 1994.

[546] N. Fornengo, C. W. Kim, and J. Song, "Finite temperature effects on the neutrino decoupling in the early universe", *Phys. Rev. D*, vol. 56, pp. 5123–5134, 1997.

[547] Robert E. Lopez and Michael S. Turner, "An Accurate Calculation of the Big Bang Prediction for the Abundance of Primordial Helium", *Phys. Rev. D*, vol. 59, pp. 103502, 1999.

[548] G. Mangano, G. Miele, S. Pastor, and M. Peloso, "A Precision calculation of the effective number of cosmological neutrinos", *Phys. Lett. B*, vol. 534, pp. 8–16, 2002.

[549] Jack J. Bennett, Gilles Buldgen, Marco Drewes, and Yvonne Y. Y. Wong, "Towards a precision calculation of the effective number of neutrinos $N_{\rm eff}$ in the Standard Model I: the QED equation of state", *JCAP*, vol. 03, pp. 003, 2020, [Addendum: JCAP 03, A01 (2021)].

[550] Steen Hannestad, "Oscillation effects on neutrino decoupling in the early universe", *Phys. Rev. D*, vol. 65, pp. 083006, 2002.

[551] Gianpiero Mangano, Gennaro Miele, Sergio Pastor, Teguayco Pinto, Ofelia Pisanti, and Pasquale D. Serpico, "Relic neutrino decoupling including flavor oscillations", *Nucl. Phys. B*, vol. 729, pp. 221–234, 2005.

[552] Pablo F. de Salas and Sergio Pastor, "Relic neutrino decoupling with flavour oscillations revisited", *JCAP*, vol. 07, pp. 051, 2016.

[553] Rasmus S. L. Hansen, Shashank Shalgar, and Irene Tamborra, "Neutrino flavor mixing breaks isotropy in the early universe", *JCAP*, vol. 07, pp. 017, 2021.

[554] Yuan-Zhen Li and Jiang-Hao Yu, "Revisiting primordial neutrino asymmetries, spectral distortions and cosmological constraints with full neutrino transport", 9 2024.

[555] Kensuke Akita and Masahide Yamaguchi, "A precision calculation of relic neutrino decoupling", *JCAP*, vol. 08, pp. 012, 2020.

[556] Julien Froustey, Cyril Pitrou, and Maria Cristina Volpe, "Neutrino decoupling including flavour oscillations and primordial nucleosynthesis", *JCAP*, vol. 12, pp. 015, 2020.

[557] Jeremiah Birrell, Cheng-Tao Yang, and Johann Rafelski, "Relic Neutrino Freeze-out: Dependence on Natural Constants", *Nucl. Phys. B*, vol. 890, pp. 481–517, 2014.

[558] Luke C. Thomas, Ted Dezen, Evan B. Grohs, and Chad T. Kishimoto, "Electron-Positron Annihilation Freeze-Out in the Early Universe", *Phys. Rev. D*, vol. 101, no. 6, pp. 063507, 2020.

[559] Claudio Coriano and Rajesh R. Parwani, "The Three loop equation of state of QED at high temperature", *Phys. Rev. Lett.*, vol. 73, pp. 2398–2401, 1994.

[560] Rajesh R. Parwani and Claudio Coriano, "Higher order corrections to the equation of state of QED at high temperature", *Nucl. Phys. B*, vol. 434, pp. 56–84, 1995.

[561] Barry A. Freedman and Larry D. McLerran, "Fermions and Gauge Vector Mesons at Finite Temperature and Density. 3. The Ground State Energy of a Relativistic Quark Gas", *Phys. Rev. D*, vol. 16, pp. 1169, 1977.

[562] Varouzhan Baluni, "Nonabelian Gauge Theories of Fermi Systems: Chromotheory of Highly Condensed Matter", *Phys. Rev. D*, vol. 17, pp. 2092, 1978.

[563] IA Akhiezer and SV Peletminskii, "Use of the methods of quantum field theory for the investigation of the thermodynamical properties of a gas of electrons and photons", *Zh. Eksp. Teor. Fiz.*, vol. 11, pp. 1316–1322, 1960.

[564] J. I. Kapusta and Charles Gale, *Finite-temperature field theory: Principles and applications*, Cambridge Monographs on Mathematical Physics. Cambridge University Press, 2011.

[565] Oleksandr Tomalak and Richard J. Hill, "Theory of elastic neutrino-electron scattering", *Phys. Rev. D*, vol. 101, no. 3, pp. 033006, 2020.

[566] Mattia Cielo, Miguel Escudero, Gianpiero Mangano, and Ofelia Pisanti, "Neff in the Standard Model at NLO is 3.043", *Phys. Rev. D*, vol. 108, no. 12, pp. L121301, 2023.

[567] G. Jackson and M. Laine, "QED corrections to the thermal neutrino interaction rate", *JHEP*, vol. 05, pp. 089, 2024.

[568] G. Jackson and M. Laine, "Neutrino-antineutrino production, annihilation, and scattering at MeV temperatures and NLO accuracy", 12 2024.

[569] S. Esposito, G. Mangano, G. Miele, I. Picardi, and O. Pisanti, "Radiative corrections to neutrino energy loss rate in stellar interiors", *Mod. Phys. Lett. A*, vol. 17, pp. 491–502, 2002.

[570] S. Esposito, G. Mangano, G. Miele, Ilenia Picardi, and O. Pisanti, "Neutrino energy loss rate in a stellar plasma", *Nucl. Phys. B*, vol. 658, pp. 217–253, 2003.

[571] Richard J. Hill and Oleksandr Tomalak, "On the effective theory of neutrino-electron and neutrino-quark interactions", *Phys. Lett. B*, vol. 805, pp. 135466, 2020.

[572] Eric Braaten and Daniel Segel, "Neutrino energy loss from the plasma process at all temperatures and densities", *Phys. Rev. D*, vol. 48, pp. 1478–1491, 1993.

[573] R. L. Workman et al., "Review of Particle Physics", *PTEP*, vol. 2022, pp. 083C01, 2022.

[574] P. L. Anthony et al., "Precision measurement of the weak mixing angle in Moller scattering", *Phys. Rev. Lett.*, vol. 95, pp. 081601, 2005.

[575] Alberto Sirlin and Andrea Ferroglia, "Radiative Corrections in Precision Electroweak Physics: a Historical Perspective", *Rev. Mod. Phys.*, vol. 85, no. 1, pp. 263–297, 2013.

[576] A. D. Dolgov, S. H. Hansen, S. Pastor, S. T. Petcov, G. G. Raffelt, and D. V. Semikoz, "Cosmological bounds on neutrino degeneracy improved by flavor oscillations", *Nucl. Phys. B*, vol. 632, pp. 363–382, 2002.

[577] Yvonne Y. Y. Wong, "Analytical treatment of neutrino asymmetry equilibration from flavor oscillations in the early universe", *Phys. Rev. D*, vol. 66, pp. 025015, 2002.

[578] Savely G. Karshenboim, "Precision physics of simple atoms: QED tests, nuclear structure and fundamental constants", *Phys. Rept.*, vol. 422, pp. 1–63, 2005.

[579] Jonathan L. Feng, Manoj Kaplinghat, Huitzu Tu, and Hai-Bo Yu, "Hidden Charged Dark Matter", *JCAP*, vol. 07, pp. 004, 2009.

[580] Benedict von Harling and Kalliopi Petraki, "Bound-state formation for thermal relic dark matter and unitarity", *JCAP*, vol. 12, pp. 033, 2014.

[581] Christiana Vasilaki and Kalliopi Petraki, "Radiation back-reaction during dark-matter freeze-out via metastable bound states", *JCAP*, vol. 06, pp. 027, 2024.

[582] Tobias Binder, Anastasiia Filimonova, Kalliopi Petraki, and Graham White, "Saha equilibrium for metastable bound states and dark matter freeze-out", *Phys. Lett. B*, vol. 833, pp. 137323, 2022.

[583] Tobias Binder, Laura Covi, and Kyohei Mukaida, "Dark Matter Sommerfeld-enhanced annihilation and Bound-state decay at finite temperature", *Phys. Rev. D*, vol. 98, no. 11, pp. 115023, 2018.

[584] M. Laine, O. Philipsen, P. Romatschke, and M. Tassler, "Real-time static potential in hot QCD", *JHEP*, vol. 03, pp. 054, 2007.

[585] A. Beraudo, J. P. Blaizot, and C. Ratti, "Real and imaginary-time Q anti-Q correlators in a thermal medium", *Nucl. Phys. A*, vol. 806, pp. 312–338, 2008.

[586] Fabio Dominguez and Bin Wu, "On dissociation of heavy mesons in a hot quark-gluon plasma", *Nucl. Phys. A*, vol. 818, pp. 246–263, 2009.

[587] Nora Brambilla, Jacopo Ghiglieri, Antonio Vairo, and Peter Petreczky, "Static quark-antiquark pairs at finite temperature", *Phys. Rev. D*, vol. 78, pp. 014017, 2008.

[588] Antonio Vairo, "Effective field theories for heavy quarkonium at finite temperature", *PoS*, vol. CONFINEMENT8, pp. 002, 2008.

[589] Miguel Angel Escobedo and Joan Soto, "Non-relativistic bound states at finite temperature (I): The Hydrogen atom", *Phys. Rev. A*, vol. 78, pp. 032520, 2008.

[590] Miguel Angel Escobedo and Joan Soto, "Non-relativistic bound states at finite temperature (II): the muonic hydrogen", *Phys. Rev. A*, vol. 82, pp. 042506, 2010.

[591] Seyong Kim and M. Laine, "On thermal corrections to near-threshold annihilation", *JCAP*, vol. 01, pp. 013, 2017.

[592] Simone Biondini, Nora Brambilla, Gramos Qerimi, and Antonio Vairo, "Effective field theories for dark matter pairs in the early universe: cross sections and widths", *JHEP*, vol. 07, pp. 006, 2023.

[593] T. Matsui and H. Satz, "$J/\psi$ Suppression by Quark-Gluon Plasma Formation", *Phys. Lett. B*, vol. 178, pp. 416–422, 1986.

[594] RG Sachs and M Goeppert-Mayer, "Calculations on a new neutron-proton interaction potential", *Physical Review*, vol. 53, no. 12, pp. 991, 1938.

[595] FJ Rogers, HC Graboske Jr, and DJ Harwood, "Bound eigenstates of the static screened coulomb potential", *Physical Review A*, vol. 1, no. 6, pp. 1577, 1970.

[596] M. A. Stroscio, "Positronium: Review of the Theory", *Phys. Rept.*, vol. 22, pp. 215–277, 1975.

[597] Maxim Pospelov and Adam Ritz, "Astrophysical Signatures of Secluded Dark Matter", *Phys. Lett. B*, vol. 671, pp. 391–397, 2009.

[598] John David March-Russell and Stephen Mathew West, "WIMPonium and Boost Factors for Indirect Dark Matter Detection", *Phys. Lett. B*, vol. 676, pp. 133–139, 2009.

[599] William Shepherd, Tim M. P. Tait, and Gabrijela Zaharijas, "Bound states of weakly interacting dark matter", *Phys. Rev. D*, vol. 79, pp. 055022, 2009.

[600] E. Beth and G. Uhlenbeck, "The quantum theory of the non-ideal gas. II. Behaviour at low temperatures", *Physica*, vol. 4, pp. 915–924, 1937.

[601] Dietrich Kremp, Manfred Schlanges, and Wolf-Dietrich Kraeft, *Quantum statistics of nonideal plasmas*, vol. 25, Springer Science & Business Media, 2005.

[602] Werner Ebeling, Wolf Kraeft, and Dietrich Kremp, *Theory of Bound States and Ionization Equilibrium in Plasmas and Solids*, 01 1976.

[603] S. Cassel, "Sommerfeld factor for arbitrary partial wave processes", *J. Phys. G*, vol. 37, pp. 105009, 2010.

[604] Sean Tulin, Hai-Bo Yu, and Kathryn M. Zurek, "Beyond Collisionless Dark Matter: Particle Physics Dynamics for Dark Matter Halo Structure", *Phys. Rev. D*, vol. 87, no. 11, pp. 115007, 2013.

[605] Andrea Mitridate, Michele Redi, Juri Smirnov, and Alessandro Strumia, "Cosmological Implications of Dark Matter Bound States", *JCAP*, vol. 05, pp. 006, 2017.

[606] Martin Beneke, Tobias Binder, Lorenzo De Ros, and Mathias Garny, "Enhancement of p-wave dark matter annihilation by quasi-bound states", *JHEP*, vol. 06, pp. 207, 2024.

[607] Bjorn Garbrecht and Thomas Konstandin, "Separation of Equilibration Time-Scales in the Gradient Expansion", *Phys. Rev. D*, vol. 79, pp. 085003, 2009.

[608] Kensuke Akita and Masahide Yamaguchi, "A Review of Neutrino Decoupling from the Early Universe to the Current Universe", *Universe*, vol. 8, no. 11, pp. 552, 2022.

[609] Magaret E. Carrington, De-fu Hou, and Markus H. Thoma, "Equilibrium and nonequilibrium hard thermal loop resummation in the real time formalism", *Eur. Phys. J. C*, vol. 7, pp. 347–354, 1999.

[610] Jose F. Nieves, Palash B. Pal, and David G. Unger, "Photon Mass in a Background of Thermal Particles", *Phys. Rev. D*, vol. 28, pp. 908, 1983.

[611] Andre Peshier, Klaus Schertler, and Markus H. Thoma, "One loop selfenergies at finite temperature", *Annals Phys.*, vol. 266, pp. 162–177, 1998.

[612] Hugo Schérer and Katelin Schutz, "Photon self-energy at all temperatures and densities in all of phase space", *JHEP*, vol. 11, pp. 139, 2024.

[613] M. Vanderhaeghen, J. M. Friedrich, D. Lhuillier, D. Marchand, L. Van Hoorebeke, and J. Van de Wiele, "QED radiative corrections to virtual Compton scattering", *Phys. Rev. C*, vol. 62, pp. 025501, 2000.

[614] A. Rebhan, "Hard thermal loops and QCD thermodynamics", in *Cargese Summer School on QCD Perspectives on Hot and Dense Matter*, 11 2001, pp. 327–351.

[615] Eric Braaten and Robert D. Pisarski, "Soft Amplitudes in Hot Gauge Theories: A General Analysis", *Nucl. Phys. B*, vol. 337, pp. 569–634, 1990.